THÈSE présentée par :

Yuhan ZHONG

soutenue le : **30 Juin 2023**

pour obtenir le grade de : **Docteur de l'université de Strasbourg**

Discipline/ Spécialité : **Physique**

New strategies to improve the transparency of photovoltaic spatial light modulators for self-powered dynamic glazing

---

THÈSE dirigée par :

Prof. HEISER Thomas	Professeur, Université de Strasbourg, France
Dr. BRINKMANN Martin	Directeur de Recherche CNRS, Institut Charles Sadron, Strasbourg, France

RAPPORTEURS :

Prof. MULLER Christian	Professor, Chalmers University of Technology, Sweden
Dr. DEMADRILLE Renaud	Directeur de Recherche CEA, Institut de Recherche Interdisciplinaire de Grenoble (IRIG), France

AUTRES MEMBRES DU JURY:

Prof. KACZMAREK Malgosia	Professor, University of Southampton, United Kingdom
Dr. BINIEK Laure	Chargée de Recherche CNRS, Institut Charles Sadron, Strasbourg, France

I have not failed. I've just found 10000 ways that won't work.

- *Thomas. A. Edison*

Acknowledgements

I really appreciate my lovely laboratories ICube and ICS where I spend a wonderful time in the past three years. Thanks to all of you who helped, supported and accompanied me during my PhD study.

I would like to express my sincere gratitude to my supervisor **Prof. Thomas HEISER**. I appreciate that he provides me an opportunity to work in such agreeable research environment. He led me to the photovoltaic materials world. We have abundant discussions during last three years, his guidance, trust, inspiration, patience and positive attitude brought me motivation and allowed me to improve my scientific research competence.

I also want to express my heartfelt gratefulness to my co-supervisor **Dr. Martin BRINKMANN**. I am really lucky to meet him six years ago, when I did my internship in ICS. At that time, he showed me what really scientific research should be, how to write a scientific report and how to give a nice presentation. All these have laid the foundation for my future PhD Study. During last three years, I not only learnt scientific knowledge from him, but also grew an independent thinking. He always encouraged me when I got failures of my experiments, allowing me to overcome the difficulties.

I would like to thank our perfect collaborator **Dr. Nicolas LECLERC** from ICPEES, who provided me precious polymers and organic molecules. He always has the patience to answer all my questions and help me to better understand the organic samples for fabricating PSLM devices. Very special thanks to **Laurent HERMANN** for the rubbing machine fabrication and maintenance at ICS. We have many interesting discussions during my PhD study. I would also like to thank **Nicolas ZIMMERMANN** from ICube for his kind help and technical support.

Thanks to my colleagues in ICube: **Dr. Dominique MULLER** for RBS measurements as well as fruitful discussions and collaborations; **Dr. Jérémy BARTRINGER** for optical measurements; **Dr. Nicolas BROUCKAERT** who taught me many experimental techniques at the beginning of my PhD study; **Dr. Sadiara FALL**, **Dr. Yaochen LIN**, **Dr. Emilie STEVELER**, **Dr. Patrick LEVEQUE**, **Stéphane ROQUES** for their valuable suggestions and technical support. To all my friends in our teams: **Dr. Jiang JING**, **Dr. Jing WANG**, **Dr. Amina LABIOD**, thank you for encouragement and support.

A great appreciation to my colleagues in ICS: **Dr. Anais DE MARIA** for her kind help on the NIR-UV-visible spectroscopy and internal sphere measurements; **Dr. Christophe CONTAL** for AFM

measurements; **Dr. Alain Carvalho** for SEM characterization and patiently answering my questions. I would strongly thank to my lovely office mates **Shubhradip GUCHAIT** for conductivity measurements, exchanging knowledge, encouragement as well as Madeleine. I sincerely hope that he will get whatever he wants in his career and life. Thanks to **Souhail ESSADIKI**, **Estelle FARGEOT** and **Antoine LEMAIRE** for funny discussions and support. I wish everything goes well for them in the future.

I also want to thank our collaborators from ICPEES: **Wenziz MUZUZU** for synthesizing the polymers and small molecules, many discussions and collaborations that promotes my experimental progress, **Dr. Chaima MAHMOUDI** who synthesized TAT-Cbz molecules, **Dr. Olivier BARDAGOT** who is my model of an excellent young researcher, I appreciate his suggestion, kind help and encouragement. I wish all the best for him.

I would like to thank our collaborators **Prof. Dimitri IVANOV** and **Dr. Ioannis MOUTSIOS** from IS2M for measurements and analyzing the polymer structure.

I am very grateful to collaborators from IPCMS: **Dr. Benoit HEINRICH** for DSC measurements and **Dr. Celine KIEFER** for her help on FTIR measurements.

I must thank **Sébastien SCHMITT**, **Nicolas COLLIN**, **Marina URBAN**, **Estelle BRUNETTE**, **Odile LEMBLE** and **Nathalie KOSTMANN** for all administrative documents during last three years.

I would like to thank **ITI HifunMat** for many interesting conferences and summer school that help me to improve scientific communications. Moreover, I acknowledge financial support from **ANR**.

Outside the lab, I want to thank my friend **Prof. Léon OTTEN**. We have many interesting discussions every week, I not only improved my language skills, but also learnt about biology, European history, politics, economics and culture and broadened my horizon. His presence and accompany make me a more colorful life in Strasbourg.

At last, thanks to **my parents**, my boyfriend **Florian** and **his parents**, they are always there and support me mentally. Your love encouraged me to explore the world and to do all the things that I want to do.

Yuhan ZHONG
钟雨含
22/09/2023
Bordeaux, France

Table of contents

List of abbreviations

A	Acceptor
AVT	Average visible transmittance
AFM	Atomic Force Microscopy
ACN	Acetonitrile
BHJ	Bulk heterojunction
CT	Charge transfer
CS	Charge-separated
CPI	Crossed-polarizer intensity
CB	Chlorobenzene
CTC	Charge transfer complex
D	Donor
DR	Dichroic ratio
DSC	Differential scanning calorimetry
D	Diffusion constant
EA	Electron affinity
EC	Electrochromic
ED	Electron diffraction
E_g	Band gap energy
ETL	Electron transporting layer
E_{Fn}	Electron quasi-Fermi energy level
E_{Fp}	Hole quasi-Fermi energy level
FF	Fill factor

F_r	Rubbing force
F_4TCNQ	2,3,5,6-tetrafluoro-7,7,8,8-tetracyanoquinodimethane
F_6TCNNQ	1,3,4,5,7,8-hexafluorotetracyanonaphthoquinodimethane
$FeCl_3$	Ferric chloride
FTIR	Fourier-transform infrared
HVAC	Heating, ventilation, air conditioning
HOMO	Highest occupied molecular orbital
HTL	Hole transporting layer
HR-TEM	High resolution transmission electron microscopy mode
IP	Ionization potential
ITO	Indium tin oxide
ICBA	Indene-C60-bisadduct
ICT	Integer charge transfer
ICD	Incremental concentration doping
I_{OFF}	Transmitted light intensity in the OFF state
I_{ON}	Transmitted light intensity in the ON state
J_{sc}	Short-circuit current density
J_m	Current density of point of maximum power
J_{obs}	Current density in dark
LOMO	Lowest unoccupied molecular orbital
LC	Liquid crystal
LCD	Liquid crystal device
l	Film thickness
MoO_3	Molybdenum trioxide

Mw	Weight average molecular weight
Mn	Number average molecular weight
Mo(tfd-COCF$_3$)$_3$	Molybdenum tris(1-(trifluoroacetyl)-2-(trifluoromethyl)ethane-1,2-dithiolene)
Magic bleu/MB	Tris(4-bromophenyl)ammoniumyl hexachloroantimonate
NUV	Near ultra-violet
n$_o$	Ordinary refractive index
n$_e$	Extraordinary refractive index
NLC	Nematic liquid crystal
NIR	Near infrared
NDI	Naphthalene diimide
NaPSS	Poly(sodium 4-styrenesulfonate)
OPV	Organic photovoltaic
OSC	Organic solar cell
OFET	Organic field-effect transistors
OLED	Organic light-emitting diodes
PC	Photochromic
PDLC	Polymer-dispersed liquid crystal
PEDOT: PSS	Poly(3,4-ethylenedioxythiophene): polystyrene sulfonate
PEIE	polyethyleneimine ethoxylated
PSLM	Photovoltaic spatial light modulator
PCE	Power conversion efficiency
P$_m$	Point of maximal power
P$_{in}$	Incident solar power
P3HT	Poly(3-hexylthiophene)

PC$_{60}$BM	[6,6]-phenyl-C61-butyric acid methyl ester
PBnDT-FTAZ	Poly (benzodithiophene-alt-dithienyl difluorobenzotriazole)
P(NDI2OD-T2)/ N2200	Poly {[N, N'-bis(2-octyldodecyl)-1,4,5,8-naphthalenedicarboximide-2,6-diyl]-alt-5,5'-(2,2'bithiophene)}
POL ⊥ R	Incident light polarization perpendicular to the rubbing direction
POL // R	Incident light polarization parallel to the rubbing direction
PTFE	Polytetrafluoroethylene
PSCs	Polymer semiconductors
R	Reflectance
R$_s$	Series resistance
R$_{sh}$	Shunt resistance
RMS	Root mean square
RBS	Rutherford Backscattering Spectroscopy
S	Order parameter
SEM	Scanning electron microscopy
T	Transmittance
TNLC	Twisted nematic liquid crystal
TC	Thermochromic
TCO	Transparent conducting oxide
TMO	Transition metal oxide
T$_m$	Melting point
T$_c$	Clearing temperature
T$_r$	Rubbing temperature
T$_A$	Annealing temperature
T-OSCs	Transparent organic solar cells

TAT-Cbz   Triazatruxene-carbazole

TEM   Transmission electron microscopy

T2   Bithiophene

UV-vis-NIR   Ultra-violet-visible-Near-infrared

V_{oc} Open-circuit voltage

V_{th} Fréedericksz voltage (threshold voltage)

V_{ph} Photovoltage

V_{LC} Voltage across the LC layer

V_{DC} Applied voltage

V_m Voltage of point of maximum power

WO_3 Tungsten (VI) oxide

ZOPV   Polarizing organic photovoltaic

ZnO   Zinc oxide

Δn   Birefringence

ɛ   Dielectric constant

Đ   polydispersity index

σ   Charge conductivity

Chapter 1. General introduction

The substantial growth of the world population and rapid development of the global economy have led to a huge energy demand.[1] According to the BP Statistical Review of World Energy, the world's primary energy consumption has increased from 156 EJ in 1965 to 595 EJ in 2021.[2] Among them, the oil demand, natural gas and coal consumption account for the largest part of primary energy consumption.[3] However, the combustion of fossil fuels results in global greenhouse gas emission (i.e., CO_2 emission), which causes a detrimental effect on the environment and contributes to global warming. Moreover, fossil fuels are nonrenewable resources. For these reasons, it is crucial to save energy while developing clean and renewable energy sources, such as solar, wind and geothermal energies.

End-user energy consumption is mainly divided into three sectors: transportation, industry and building.[4] Together with the growth of population, enhanced building services (such as hot water, light, cooking, heating etc.) and comfort levels have raised the energy use in buildings. Since 2004, the energy consumed by buildings is greater than that by industry and transportation sectors.[5] The buildings account for around 40% of the total primary energy consumption and 36% annual greenhouse gas emission.[6] Approximately 50% of building energy consumption is assigned to heating, ventilation and air conditioning (HVAC system).[7] One of the reasons for the strong demand of cooling systems is solar infrared light transmitted through the windows. Near infrared (NIR) light is located in the range of 700-2500 nm and represents around 50% of incident solar energy. Due to global climate change, cooling energy demands are predicted to exceed heating energy demands and increase by 72% around 2100.[8] Therefore, controlling heat transfer from NIR light and thus reducing the use of HVAC systems is an effective strategy for saving energy (i.e., improving energy efficiency) in buildings while maintaining high comfort levels.

Dynamic or "smart" windows have been designed to improve the energy efficiency of buildings by controlling reversibly and dynamically indoor solar irradiation. Dynamic windows are expected to block solar heat in summer and allow solar heating in winter.[9,10] In addition, smart glazing technologies have been extensively studied for applications in greenhouses, switchable sunglasses, windows for aircrafts, etc.[11] Many smart windows technologies have been recently developed. According to underlying optical modulation mechanisms, they can be mainly

classified as electrochromic, photochromic, thermochromic and liquid crystal devices.

An ideal smart window should display high energy efficiency, quick response time, good reversibility, stability and permit user control. However, none of these technologies can fulfill all these requirements. A new concept named photovoltaic spatial light modulator (PSLM) has been recently proposed.[12] This novel dynamic glazing system has the potential to overcome some of the bottlenecks that currently limit the integration of smart windows into buildings. A PSLM is composed of a liquid crystal light valve and an organic photovoltaic (OPV) unit. The OPV unit is capable of converting absorbed photons into voltage, enabling the device operation in a self-powered regime upon illumination.

The first PSLM device was fabricated in 2017 by T. Regrettier et al. at ICube, in collaboration with M. Kaczmarek from the University of Southampton. They observed a 20% autonomous drop in transmittance of the device under 0.1 W.cm^{-2} monochromatic light illumination. Since then, the working principle of PSLMs has been further studied and the device performance has been improved. Self-powered PSLMs were recently reported by T. Heiser et al.[12] Their results demonstrated that a PSLM can show a quick response time, a good reversibility and can be easily controlled by the users. Moreover, the drop in transmittance was shown to remain stable for more than 5 h. However, some challenging issues still exist and need to be addressed before applying PSLMs to smart windows, such as long-term stability, large-area device fabrication and low transparency in the OFF (or "clear") state. For instance, current PSLMs can only achieve approximately 9% average visible transmittance, which is insufficient for window applications. The low transparency arises from the optical absorption of external polarizers and of the organic PV layer integrated into the PSLM. The optical absorption of organic semiconductors can be modified through molecular engineering, making it possible to reduce visible light absorption by organic layers in PSLMs.

This thesis focuses on the improvement in transparency of PSLMs via three complementary methods: I) Using a near UV light-absorbing PV layer containing a high band gap donor and a fullerene acceptor for PSLM. A semi-transparent device is achieved and can operate in self-powered regime; II) Using the anisotropic optical PV layers as "internal polarizers" for PSLMs. They involve a fabrication step making use of high temperature rubbing. Based on such PV layers, the OSCs display a significant dichroic photovoltaic effect; and III) Replacing the

commercial external polarizers by oriented conducting polymer films. Combining a self-powered PSLM with oriented conducting polymers increases the transmittance in the visible region while limiting the optical modulation to NIR range. The final PSLM should display a high transmittance in the visible region, harvest UV light to generate the photovoltage, and, at the same time, allow to control NIR light (i.e., solar heating).

The thesis is accordingly organized in 7 chapters:

Chapter 1 introduces the purpose of this thesis research as well as the thesis structure.

Chapter 2 presents the state-of-the-art of various smart glazing technologies including electrochromic, photochromic, thermochromic and Liquid crystal devices and briefly summarizes their cons and pros.

Chapter 3 first describes the working principle of organic photovoltaics and liquid crystal light valves, which are the main building blocks of PSLM devices. Then, we explain the physical mechanisms underlying PSLM operation, show the performance of self-powered PSLMs achieved in a previous work and discuss the subsistent scientific challenges of the device, especially low transparence of the device in its OFF state. Different strategies are proposed to improve the transparency, each being described in detail in the following chapters.

Chapter 4 describes the strategy, that consists in using a semi-transparent PV layer in a PSLM. The PV layers are composed of new high band gap materials (carbazole-based molecules) and fullerene molecules, limiting photon absorption to the near UV. The optical and photovoltaic properties of these high band gap materials are first studied. Then, the optical response of a PSLM based on the semi-transparent PV layer is investigated.

Chapter 5 focuses on the fabrication and use of oriented PV layers that are considered as another efficient way of increasing the transparency of PSLM. The aligned PV layers should be capable of generating the photovoltage while polarizing visible light. They have been fabricated either by a combination of oriented polymer donors and diffused small molecular acceptors, or by direct orientation of flexible donor and acceptor polymer blend films. The alignment, structure/morphology and PV properties of the oriented PV layers are presented as a function of fabrication parameters in this chapter.

Chapter 6 explores the possibility to use oriented conducting polymer films as "NIR polarizers" for PSLMs, offering high transmittance in the visible region and anisotropic reflection and absorption in the NIR range. The "NIR polarizers" are fabricated by a combination of high temperature rubbing and sequential doping. The electrical and optical properties of oriented conducting films as well as the impacts of doping on the alignment and structure of the aligned polymers are studied by conductivity measurements, polarized UV-visible spectroscopy and electron diffraction. The optical modulation of a self-powered PSLM using such "NIR polarizers" is also shown in this chapter.

Chapter 7 presents the main conclusions of the thesis project and discusses its perspectives.

References

(1)   Omer, A. M. Energy, Environment and Sustainable Development. *Renew. Sustain. Energy Rev.* **2008**, *12* (9), 2265–2300.

(2)   British Petroleum. BP Statistical Review of World Energy, 2021.

(3)   Wang, H.; Wang, Y. Estimating per Capita Primary Energy Consumption Using a Novel Fractional Gray Bernoulli Model. *Sustainability* **2022**, *14* (4), 2431.

(4)   González-Torres, M.; Pérez-Lombard, L.; Coronel, J. F.; Maestre, I. R.; Yan, D. A Review on Buildings Energy Information: Trends, End-Uses, Fuels and Drivers. *Energy Rep.* **2022**, *8*, 626–637.

(5)   Pérez-Lombard, L.; Ortiz, J.; Pout, C. A Review on Buildings Energy Consumption Information. *Energy Build.* **2008**, *40* (3), 394–398.

(6)   D'Agostino, D.; Mazzarella, L. What Is a Nearly Zero Energy Building? Overview, Implementation and Comparison of Definitions. *J. Build. Eng.* **2019**, *21*, 200–212.

(7)   Ke, Y.; Zhou, C.; Zhou, Y.; Wang, S.; Chan, S. H.; Long, Y. Emerging Thermal-Responsive Materials and Integrated Techniques Targeting the Energy-Efficient Smart Window Application. *Adv. Funct. Mater.* **2018**, *28* (22), 1800113.

(8)   Isaac, M.; van Vuuren, D. P. Modeling Global Residential Sector Energy Demand for Heating and Air Conditioning in the Context of Climate Change. *Energy Policy* **2009**, *37* (2), 507–521.

(9)   Baetens, R.; Jelle, B. P.; Gustavsen, A. Properties, Requirements and Possibilities of Smart Windows for Dynamic Daylight and Solar Energy Control in Buildings: A State-of-the-Art Review. *Sol. Energy Mater. Sol. Cells* **2010**, *94* (2), 87–105.

(10)   Debije, M. G. Solar Energy Collectors with Tunable Transmission. *Adv. Funct. Mater.* **2010**, *20* (9), 1498–1502.

(11)   Ke, Y.; Chen, J.; Lin, G.; Wang, S.; Zhou, Y.; Yin, J.; Lee, P. S.; Long, Y. Smart Windows: Electro-, Thermo-, Mechano-, Photochromics, and Beyond. *Adv. Energy Mater.* **2019**, *9* (39), 1902066.

(12)   Fall, S.; Wang, J.; Regrettier, T.; Brouckaert, N.; Ibraikulov, O. A.; Leclerc, N.; Lin, Y.; Elhaj, M. I.; Komitov, L.; Lévêque, P.; Zhong, Y.; Brinkmann, M.; Kaczmarek, M.; Heiser, T. Self-Powered Dynamic Glazing Based on Nematic Liquid Crystals and Organic Photovoltaic Layers for Smart Window Applications. *ACS Appl. Mater. Interfaces* **2023**, *15* (3), 4267–4274.

Chapter 2. Scientific context

Dynamic glazing technologies

Dynamic glazing technologies have been developed rapidly in the last decades for improving the energy efficiency of buildings. A major component of dynamic glazing technologies are dynamic optical materials, whose transparency can be modulated by external stimulus such as electricity, light, heat, etc. Based on the different external stimulus and operating principles, these technologies can be categorized into electrochromic (EC), photochromic (PC), thermochromic (TC), polymer-dispersed liquid crystal (PDLC) devices, etc. Among them, EC and PDLC devices are considered as "active" systems, that can be controlled by an externally applied electrical voltage to address the user's demand. On the other hand, photochromism and thermochromism are regarded as "passive" mode, which can respond to respectively surrounding light intensity and temperature without requiring an external power supply.

In this chapter, we present the operational mechanism and characteristics of these four major categories of dynamic glazing technologies, and summarize the strategies for improving their performance using different materials and technologies. Finally, we also discuss their pros and cons, considering performance, installation costs, and environmental impact.

2.1 Electrochromic (EC) devices and materials

Electrochromic devices are able to change reversibly their optical properties due to redox processes as response to an applied electric field. Over the past decades, the EC devices have been widely used in information displays, smart windows and variable-reflectance mirrors.[1–4] A typical EC device is composed of five layers, as shown in **Figure 1**: an ion storage layer or anodic EC film (counter-electrode) and a cathodic EC film (working electrode) joined by an ion-conducting electrolyte, the three-layer stack being sandwiched between two glass substrates coated with transparent conducting oxide (TCO) layers. This device can be regarded as an 'electrical thin-film battery' with its optical absorption depending on the charging state.[4] When the voltage is applied to the TCO substrates, small cations such as Li^+ are intercalated into the cathodic EC layer, leading to a tinted state. Conversely, when the applied voltage is turned off, the ions are attracted to the ionic charge storage layer, resulting in a bleached state. The performance of an EC device is generally described by I) its switching time, i.e., how long does

the device take for performing a switching between two colored states; II) its cycling stability, that implies switching cycles without significant degradation; III) the operational driving voltage for visual colour change; IV) the optical contrast, which is an essential parameter to evaluate the intensity of color change in devices; V) the coloration efficiency (CE), that is defined as a ratio between the optical absorbance change (ΔA, or optical density change ΔOD) and inserted charge per unit area (ΔQ, $cm^2 C^{-1}$); as well as VI) its electrochemical stability.[5]

The electroactive materials used in EC devices have a strong impact on their performance and are mainly categorized into inorganic materials (metal oxide, metal complexes), organic materials (organic molecules, conjugated polymers) and hybrid organic-inorganic materials. In this section, we will briefly discuss transition metal oxides and organic EC materials.
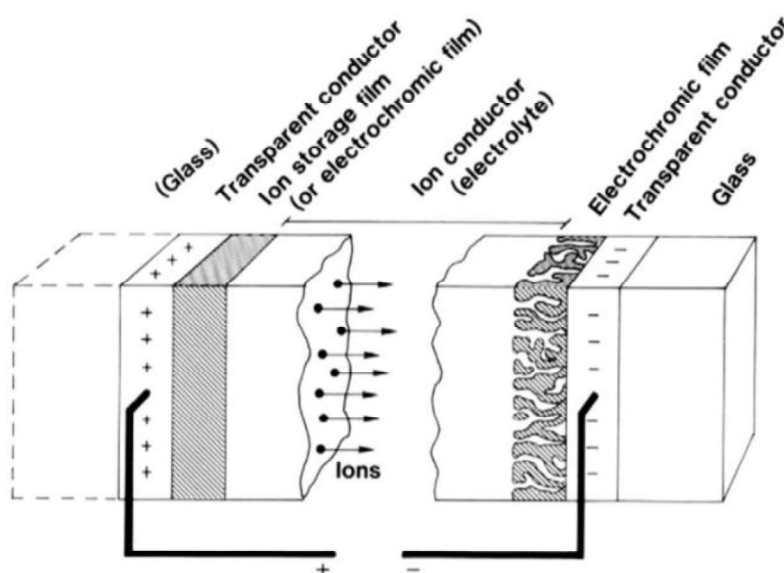
Figure 1. *Schematic illustration of a typical reversible ECD. Arrows represent the direction of ion movement at an applied electric field. From Ref [4].*

2.1.1 Transition metal oxides for EC applications

Transition metal oxides (TMOs) such as oxides of iridium, tungsten, cobalt, manganese, nickel, titanium and molybdenum are key inorganic materials for EC applications. In 1969, the EC effect in tungsten oxide film was firstly demonstrated by S.K.Ded.[6,7] Since then, WO_3 has attracted much research interest especially for smart windows. The EC characteristics of TMOs result from reversible redox reactions of the transition metal ions, involving injection/extraction of electrons and ions upon voltage application. Their EC performances are

mainly governed by the amount of the oxidized/reduced metal ions (i.e., coloration center) and how fast redox reactions take place. Indeed, the redox reactions of TMOs include a charge transfer process at the electrolyte-material interface and an ion diffusion-controlled process within the material lattice. Promoting and facilitating these processes can improve the EC performance.[8]

A high coloration efficiency means a large optical modulation with small charge insertion/extraction, enhancing long-term cycling stability. However, the coloration efficiencies of TMOs are typically rather low, therefore, a high electrical power is required to obtain the desired optical contrast in TMOs based ECDs.[9] Moreover, the ion-intercalation kinetic in TMOs is limited by the ion diffusion coefficients and diffusion path lengths. The former is influenced by the chemical and crystal structure of TMOs, and the latter is determined by the material's microstructure.[10] Hence, fabrication of TMOs with controlled nanostructures is expected to shorten the diffusion distance of ions, thus accelerating the switching kinetics, enhancing durability and finally improving EC performance. In the past decades, various types of TMO nanostructures such as nanorods, nanowires and nanotubes were synthesized by different deposition techniques. Doping the nanostructured TMO film with metal ions including Ni and Ti can further improve their EC properties. Xu et al synthesized nanostructured Ni-doped WO_3 film on ITO substrate via a seed-free hydrothermal technique and studied the influence of Ni-doping on the morphology, crystal structure and EC properties of WO_3 film, respectively.[11] Their results indicated that the nanostructure was significantly changed by Ni-doping. The WO_3 film with low Ni doping concentration displayed high optical modulation, as shown in **Figure 2a,b** (over 85% from 600 to 900 nm), high CE (60.5 $cm^2\,C^{-1}$ at 600 nm) and good cycling stability for about 5500 cycles. The optimized Ni-WO_3 film was used in ECD with a complementary NiO-based film, that shows color change from transparent to black. The maximum transmittance in the dark state is only 3.5% (**Figure 2c,d**). This dark device has emerged as a promising system for smart windows.
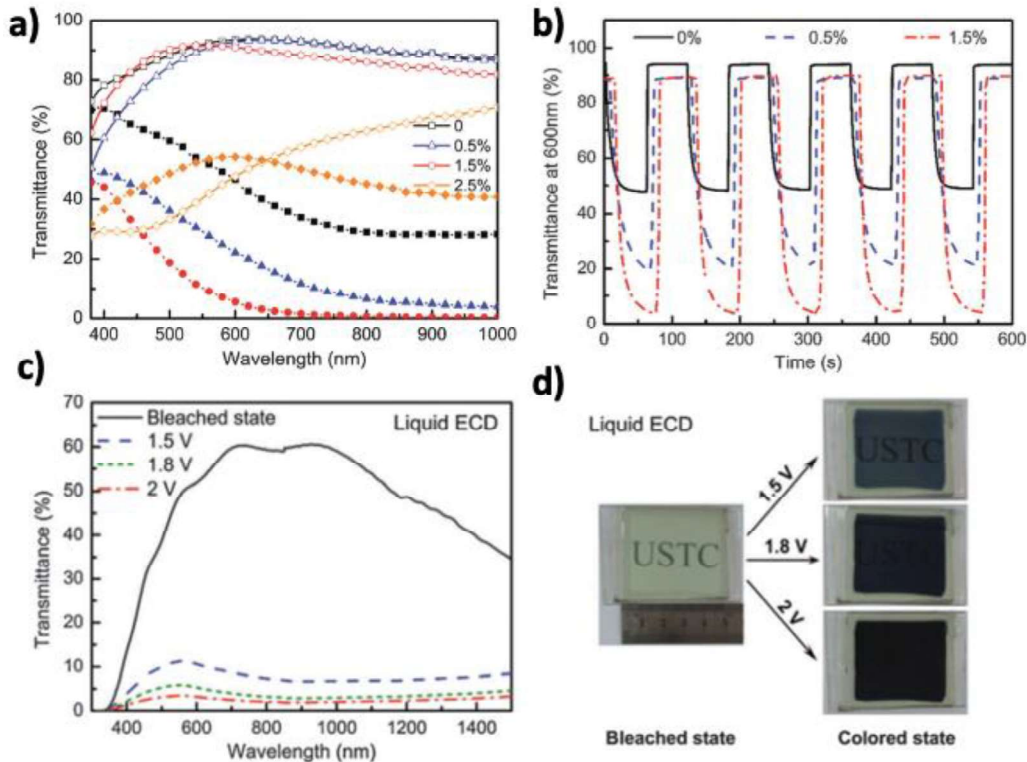
Figure 2. *a) Transmittance spectra of the Ni-WO₃ films for different Ni-doping concentration in the bleached (solid line) and colored (dotted line) state by applying +1V and -1.5V for 60s, respectively, in 0.1M LiClO₄-PC electrolyte with a three-electrode system. b) Optical transmittance response at 600nm of the Ni-WO₃ films applied +1V and -1.5V for 60s in 0.1M LiClO₄-PC electrolyte with a three-electrode system. c)Transmittance spectra of the complementary ECD assembled by 1.5% Ni-WO₃ and Li–Ti–NiO films in bleached (solid line) and colored (dotted lines) state at different applied voltages from 1.5 V to 2 V for 300 s. d) Corresponding photographs of ECD (5 cm x 5 cm) in the bleached state (left) and colored state (right) at different applied potential for 300 s. Reproduced from [11].*

2.1.2 Organic molecules and Conjugated polymers for EC application

A typical example of organic EC molecules is viologen that exhibits low switching voltage and high optical contrast.[12] The 4,4'-bipyridinium salts (viologens) possess three reversible redox states: V^{2+} (dication), $V^{+\bullet}$ (radical cation) and V^0 (neutral form). There are two successive electron transfer reactions: I) a colourless V^{2+} is reduced into a deep-blue $V^{+\bullet}$ whose high molar absorption coefficient is attributed to an intramolecular charge-transfer complexation, and, II) $V^{+\bullet}$ is further reduced into colorless V^0. However, the last reduction step has a poor reversibility since the generated V^0 is insoluble and thus not suitable for EC applications.[13] A viologen-based ECD using hydroquinone as an electron mediator to avoid the appearance of neutral form V^0

was reported by Vergaz et al.[14] Their results showed that a transmittance of 82.6% drops at 600 nm from bleached state to colored state with an applied voltage of 1.8 V. The optical response time is 3.6 s for coloring at 602 nm where the highest optical contrast is observed.

π-conjugated polymers such as polythiophenes (PTP), polypyrroles (PPy), polyaniline (PANI) and their derivatives are also widely used for EC application. Compared to the transition metal oxide, conjugated polymers require lower voltages and display higher coloration efficiencies with faster response times.[9,15,16] The mechanism of color change in conjugated polymers involves reversible redox doping/dedoping processes. The redox doping can be classified into two categories: p-type doping (oxidation) and n-type doping (reduction). In the neutral state, the conjugated polymers show semi-conducting characteristics. Upon doping, charge carriers are formed on the polymer backbone, while counterions are inserted into the polymer to neutralize the charge. Doping introduces two new localized electronic states within the bandgap, leading to the change in electrical and optical properties.

One advantage of conjugated polymers is their ability to be chemically modified by introducing functional groups, or fused aromatic rings to tailor their EC properties. In the past decades, many research groups on EC polymers focused on engineering the polymer chemical structure and related bandgap to realize color control in both doped and neutral states. A new series of conjugated polymers showing outstanding EC properties are poly-(3,4-alkylenedioxypyrrole)s (PXDOPs), reported by Reynolds et al.[17] In comparison with other p-type polymers such as poly(3-alkylthiophene)s, PPy and PEDOT, PXDOPS exhibit lower oxidation potential, which are easier to oxidatively dope into their conducting form. These new PPy derivatives are highly stable and present electrochromic behaviour with respect to multiple colors. Poly(3,4-ethylenedioxypyrrole) (PEDOP) is a representative PXDOP derivative with a band gap of 2.0 eV, it shows a red neutral state and a transmissive blue oxidized state. Poly(3,4-propylenedioxypyrrole) (PProDOP) whose monomer structure is slightly modified relative to that of PEDOP exhibits a change in color states with a band gap of 2.2 eV: an orange neutral state, an intermediate brown state, and a gray/blue oxidized state. Furthermore, poly(N-sulfonatopropoxy-ProDOP) (N-PrS-PProDOP) is synthesized with different substituent group at N atom referring to that of PProDOP.[18] The N-substitution in unit repeat leads to an increase in band gap ($\geq$ 3.0 eV) due to steric effects. As a result, this polymer is an anodically coloring material, that appears as completely transmissive and colorless in the neutral state and switches to an absorbing light gray oxidized state. The optical contrast of organic EC devices

can be improved by assembling a cathodically coloring polymer and an anodically coloring polymer in the same device. In this type of EC device, the applied voltage needs to achieve simultaneous switching of both EC materials. The group of John Reynold reported a dual polymer EC device (**Figure 3a**) with excellent optical contrast (**Figure 3b**), rapid switching rate (0.5 s to achieve full color change) and a very good cyclability.[19]

In summary, the conducting polymers as organic EC materials exhibit quick switching rate and high optical contrast. However, these materials generally show multiple coloration in the visible region that leads to unclear and low transparent states. In addition, the charged conjugated backbones are usually unstable under exposure to oxygen or moisture, and under high applied voltages or high temperatures. Most organic EC devices have shorter life cycles (≤ 1000 cycles)[20] relative to inorganic devices (≤ 20,000 cycles)[21] due to poor environmental and electrochemical stability of EC polymers.
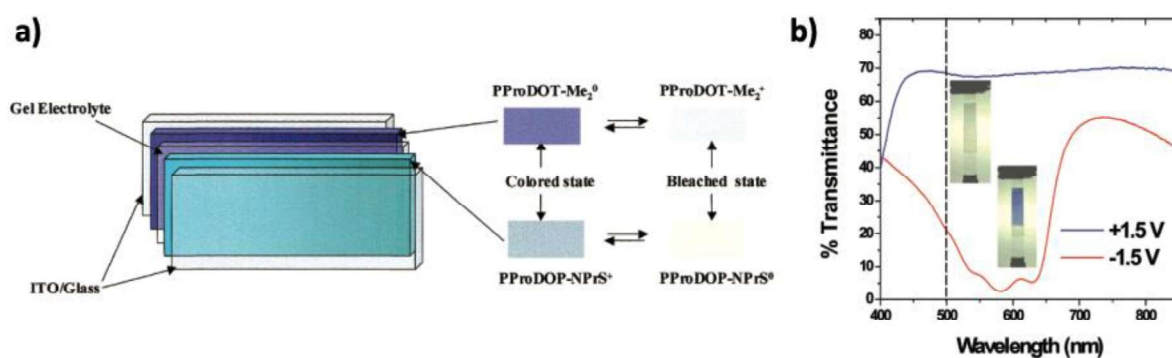
Figure 3. *a) Schematic illustration of a transmissive dual polymer ECD structure, the color representations (right) for two polymers both in bleached and colored states. b) Transmittance spectra and photographs of organic ECD assembled by the cathodically coloring polymer PProDOT-Me$_2$ and the anodically coloring polymer PProDOP-NPrS, switching between bleached and colored states. Adapted from*[19].

2.2 Photochromic (PC) materials and applications

Photochromic (PC) materials undergo reversible color changes in response to irradiation with UV/visible light. Thanks to their reversible photo-switchable characteristics, these materials have been extensively investigated for numerous applications including optical memories, data recording, molecular logic gates, transitional lenses, multi-photon devices, etc.[22-25] The obvious advantages of PC devices are that they do not need an external power supply and that they have therefore a simple device structure allowing for lower fabrication costs than EC

devices. An ideal PC material should display high coloration contrast with a quick switching speed and have a good photochemical stability. PC effects have been observed in both inorganic materials (such as WO_3, TiO_2, ZnO, Titanates, metal halide, etc.) and organic materials (such as dithienylethene, spiropyran, azobenzene, etc.).

AgCl particles incorporated into borosilicate glass was demonstrated to exhibit reversible photochromism.[26,27] The coloration under exposure to sunlight is attributed to the reduction reaction from Ag^+ ions to Ag^0 particles. These glasses containing AgCl have a fast response (few minutes) and have been widely used as PC lenses. Transition metal oxides such as WO_3 have a potential for large-scale applications (e.g., smart windows) owing to their good stability. Adachi et al fabricated a highly transparent PC composite material where WO_3 nanoparticles were dispersed into transparent (triethoxysilyl)propyl methacrylate/tetraethoxysilane xerogel matrix, while Li_2SO_4 was introduced to prompt the coloration reaction.[28] The color change in this system arises from the reduction of colorless W^{6+} ions to blue W^{5+} ions. Such composite materials show promising PC properties. However, the color change of many PC inorganic materials is limited to colorless/white to blue.[29] On the other hand, organic materials have attracted much attention for PC applications, since it is possible to yield PC properties in a wide range of wavelengths in the visible region.

In organic PC systems, the photo-induced color changes arise from cyclization or cycloreversion within the molecules, modifying the conjugation pathways and thus changing their optical and electronic properties. Among these organic materials, the spiro-compounds including spirooxazines and spiropyrans have been studied for major commercial applications in ophthalmic lenses. They exhibit good coloration properties and display high fatigue resistance.[30,31] The PC mechanism involves a photo-induced heterolytic cleavage of the C–O bond of the oxazine ring, that leads to a structural change, from the colorless spiro-form to the colored merocyanine form (**Figure 4**). Most of merocyanines are thermally unstable and can be bleached by heating or irradiation with visible light.[32] The incorporation of PC dyes into a polymer matrix results in better mechanical properties and thermal resistance.[33] However, the thermal fade speed of spiro-compounds is substantially slower in a rigid polymer matrix than that of the same dye in solution. This is probably due to a limited free volume in the polymer matrix that restricts the internal rotation of PC dyes for isomerization.[31] Such slow fading in ophthalmic lenses is undesirable. One possible solution for increasing the switching speed is to attach flexible oligomers with a low glass-transition temperature (T_g) to the PC dyes. Lewis

et al designed a PC dye-polydimethylsiloxane (PDMS) conjugated oligomer to increase rational mobility of dye in a rigid polymer matrix. Importantly, this method did not alter the electronic nature of the dye.[34] They measured the time ($t_{3/4}$) it takes for the optical density to reduce by 3/4 the initial optical density of the colored state. The results indicated that the fade rate of spirooxazine-PDMS conjugate ($t_{3/4}$=7s) is much faster as compared to that of unconjugated spirooxazine ($t_{3/4}$=110 s).

In summary, the color of many inorganic PC materials such as WO_3 can be easily controlled by modifying the light intensity.[29] Although these materials confer color change to a limited range, e.g., colorless to blue for WO_3, they are still promising materials for smart window applications due to less restrictions on the bleaching process. On the other hand, organic PC materials show a broader range of color change in the visible range. However, the majority of organic PC materials cannot get back to their original colors by only removing the UV light. Therefore, this feature limits their applications in smart windows. Organic PC materials and metal halide such as AgCl have been extensively studied for application in PC lenses, optical switches, etc.
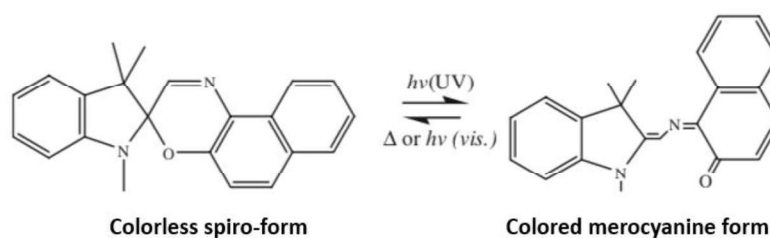
Figure 4. *Photochromism of Spirooxazine. Reproduced from*[31].

2.3 Thermochromic (TC) materials and applications

Thermochromism is defined as a reversible modulation of optical properties that is triggered by a temperature variation. Therefore, the TC devices are self-activated and energy saving. TC materials have been exploited in many areas such as microelectronics, data storage and intelligent architectural glazing.[35–38] A good temperature-responsive material should fulfill some requirements: I) an autonomous switching between transmitted and blocked solar radiation with large optical contrast, II) an appropriate transition temperature range of 30-40°C, III) outstanding durability and cycle life. Several types of TC materials such as inorganic

solids, organic small molecules, polymers and coordination complexes exhibit promising performances. Here, we will discuss shortly for two key TC materials: TMOs and polymers.

The most widely studied thermochromic TMOs is vanadium dioxide (VO_2), that undergoes a metal-insulator transition at a critical temperature (T_c). The crystal structures of VO_2 are shown in **Figure 5a**. Below T_c, VO_2 display an insulating monoclinic phase (M-phase) that is relatively infrared transparent. Above T_c, it presents a metallic tetragonal rutile structure (R-phase) that is infrared reflecting. Therefore, the structural transformation induces a change in electrical conductivity and an optical contrast in the IR region along with negligible changes in the visible region, enabling VO_2 to be very attractive for smart windows applications. The pure VO_2 films exhibit a high transition temperature (T_c =68°C), a limited solar energy regulation ability (ΔT_{sol} < ~ 10%) and an acceptable luminous transmittance (T_{lum}~ 40%).[39] ΔT_{sol} is defined as the difference in solar energy transmittance between the two phases. Many research groups have made efforts to overcome some bottlenecks for VO_2 used in smart windows by I) lowering T_c close to room temperature, II) improving T_{lum} and III) increasing ΔT_{sol}. Doping of VO_2 is an effective method to decrease T_c. Long's group recently fabricated W/Mg co-doped VO_2 thin films in order to improve the TC performance, as depicted in **Figure 5b**. Among them, the best performing film $V_{0.94}W_{0.02}Mg_{0.04}O_2$ exhibited a low T_c (~ 30°C), a high T_{lum} (~ 80%) and a modest ΔT_{sol} (~4%).[40] Nano/microscale engineering using porosity control, nanocomposites or multilayers can further optimize ΔT_{sol}.[37,41] In composite coatings derived from highly crystalline VO_2 nanoparticles (**Figure 5c**), ΔT_{sol} (22.3%) was significantly increased (**Figure 5d**) but accompanied by an increase in T_c, up to 91°C.[42]

The VO_2 films show a large modulation in the IR range, however, balancing ΔT_{sol}, T_{lum} and T_c remains very challenging. Another drawback of VO_2 based smart windows is their low resistance to oxidization.[43] An encapsulation layer is required to prevent oxidation from the environment, that probably leads to a change in their optical properties.
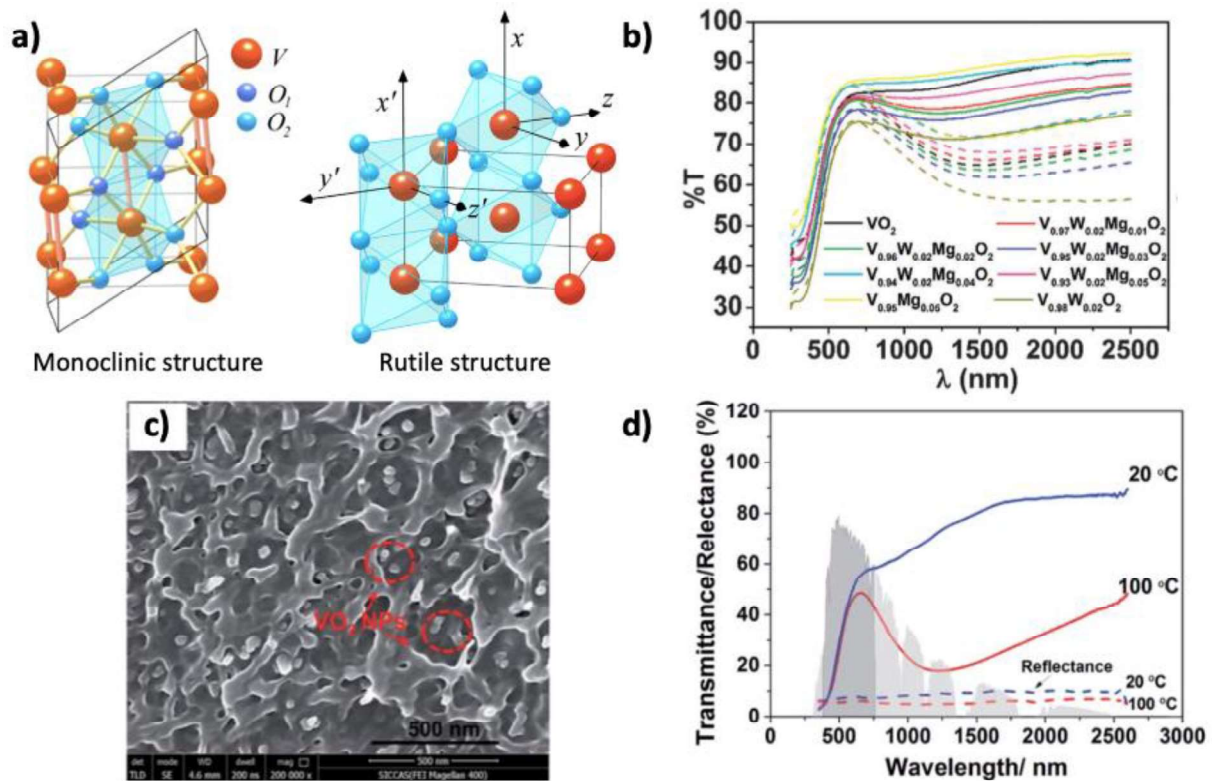
Figure 5. a) Crystal structure of VO$_2$. In monoclinic structure, two type of oxygen ions can be distinguished. In rutile structure, the red circles correspond to V^{4+} ions, the small blue circles are O^{2-} ions. Ref solid state TC materials. b) Transmittance spectra in the UV-Vis-NIR range for the pure VO$_2$ and W/Mg co-doped VO$_2$ films. The solid and dashed lines represent the spectra measured at 15°C and 90°C, respectively.[40] c) SEM images of VO$_2$/PU composite coating containing VO$_2$ nanoparticles synthesized at 300°C. d) Transmittance/Reflectance spectra of the composite coating measured at 20 and 100°C, respectively. The shadow represent the spectral distribution of solar energy. Adapted from[42].

Among organic TC materials, TC hydrogels that consist of a hydrophilic polymer with an aqueous-rich environment, have been regarded as promising candidates for energy-efficient smart windows. Their optical properties change upon a reversible hydrophilic-to-hydrophobic phase transition at a low critical solution temperature (LCST). As illustrated in **Figure 6a**, below the LCST, hydrogen bonds are formed between the polymer chains and the surrounding water molecules. Therefore, the polymers can be homogenously distributed in the matrix with a uniform refractive index. If the temperature increases and exceeds the LCST, hydrogen bonds are broken, polymer chains collapse and reduce their volume. The phase separation and polymer chain aggregation induce incident light scattering because of different refractive indexes between the polymer domains and the surrounding matrix.[44–46]

The TC hydrogels including polyampholyte hydrogels, hydroxypropyl cellulose and poly(N-iso-propylacrylmide) (PNIPAm) have been mostly studied. Zhou et al reported PNIPAm hydrogel based smart windows with a very large ΔT_{sol} and high T_{lum}.[38] In their works, the PNIPAm hydrogel was sandwiched between two glass substrates. The thickness of hydrogels has a strong impact on the TC properties. With an optimal thickness, the PNIPAm hydrogel showed a high T_{lum} (87.9%) at room temperature, an acceptable T_{lum} (59.9%) at 40°C and a good ΔT_{sol} $_{20-40°C}$ (20.4%). The switching times of this smart window are 1 min both for indoors and outdoors. Good TC performances were maintained after 20 cycles. However, ΔT_{sol} in PNIPAm hydrogel contains a large modulation in the visible region and a moderate modulation in the IR range. In order to enhance the IR modulation and thus improve the total optical modulation, hybrid VO$_2$-hydrogel thermochromic materials have been developed by the same research group (**Figure 6b**).[47] The hybrid materials exhibited a high ΔT_{sol} $_{20-80°C}$ (34.7%) and an acceptable average T_{lum} (62.6%). Compared to the pure VO$_2$ nanoparticles and pure hydrogel (**Figure 6c**), ΔT_{sol} in the hybrid system was significantly improved. Moreover, ΔT_{sol} and T_{lum} at 80°C for hybrid VO$_2$-hydrogel with a thickness of 100 μm remained stable up to 20 cycles (**Figure 6d**).
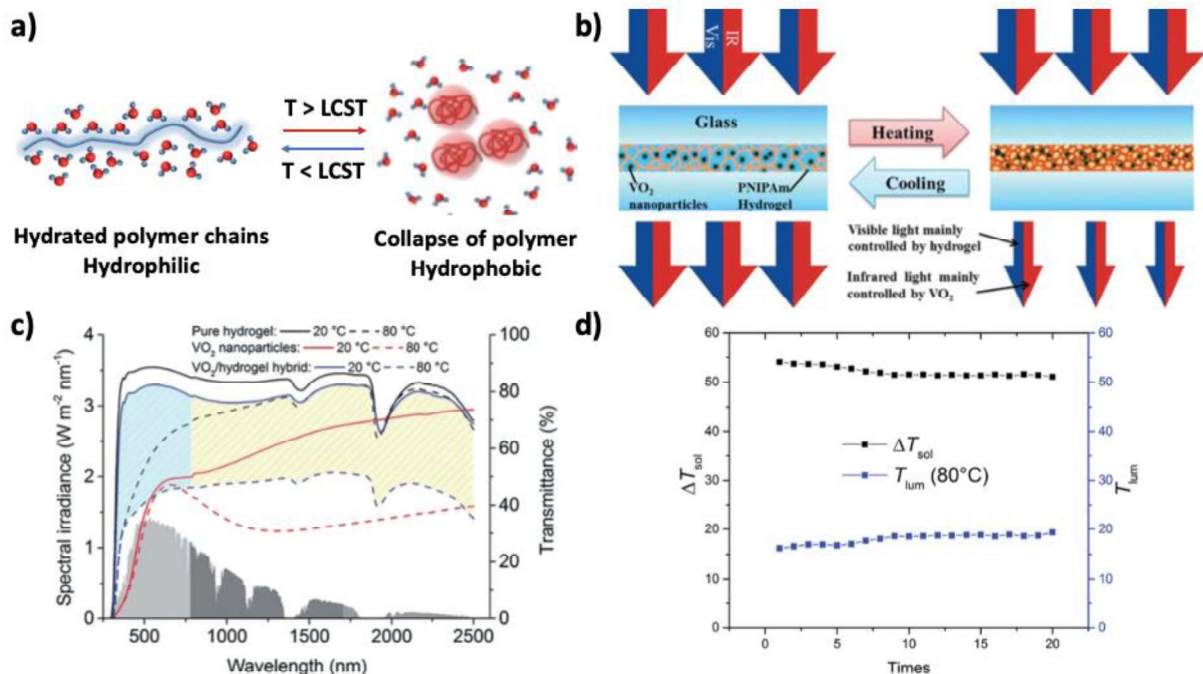
Figure 6. *a) Schematic representation of thermo-responsive polymer chains behavior below and above LCST.[46] b) Solar modulation mechanism of PNIPAm/VO$_2$ hybrid smart windows with a sandwiched structure. c)Transmittance spectra in UV-Vis-NIR range of pure PNIPAm hydrogel (black), VO$_2$ nanoparticles (red) and*

PNIPAm/VO₂ hybrid hydrogel (blue) at 20 and 80°C. The shadow represents the spectral distribution of solar energy. The cyan area highlights the visible transmission difference, and the yellow area is the IR transmission difference of PNIPAm/VO₂ hybrid hydrogel. d) Cycling stability measurements of PNIPAm/VO₂ hybrid film with a thickness of 100 µm switching between 20 and 80°C. Adapted from[47].

To summarize, regarding inorganic TC materials, VO₂ films show a large transmittance contrast in the IR range with a high T_c of 68°C. TC hydrogels show a larger optical modulation in the visible range than VO₂ pure system. Therefore, new hybrid organic-inorganic TC device are able to maximize the solar energy saving, opening a new research direction for smart windows.

2.4 Polymer-dispersed liquid crystal (PDLC)

Liquid crystals are able to modulate optical properties including polarization states and light intensity upon application of an external stimulus (e.g., light, electric field or temperature). Electrically-driven LC devices usings polymer-dispersed liquid crystals (PDLC) have attracted significant research interest for applications in smart glazing systems. Unlike typical EC devices, where optical switching arises from electrochemical processes, LC devices change light scattering or transmission by electrically controlled LC alignment. However, the voltage required for operating PDLC devices (~10 V) is much higher than that needed to drive typical EC devices (< 3 V). [29]

PDLC is a key material used in commercialized LC-based electrically-driven smart windows, and is composed of micro-sized LC domains, commonly in the form of droplets, embedded in a polymer matrix.[48] In the OFF state (i.e., without electric field), the director of LC domains is randomly oriented, leading to a refractive index mismatch between the LC droplets and the surrounding polymer matrix. As a result, the incoming visible light is scattered and the PDLC film appears milky white. In the ON state i.e., upon application of an external electric to the PDLC film, LC molecules reorient in a preferential direction. At this point, if the ordinary refractive index of LC domains and the refractive index of polymer matrix are identical, the PDLC film becomes transparent.[49] When the applied electric field is removed, the LC domains return to their initial orientation due to surface energy.[50] A PDLC device for developing smart glazing applications should have a high contrast ratio, a low threshold voltage and a short switching time.

Many research groups demonstrated that using dichroic dye-doped LC can enhance the contrast ratio of PDLC devices.[49,51–53] The dye generally possess a rod-like molecular structure, showing a strong anisotropic optical absorption. When the dichroic dye is dissolved in LC droplets, its long molecular axis aligns along the LC director. In the OFF state, the randomly arranged LC molecules induce the isotropic orientation of dye molecules. In this case, the overall extinction coefficient in LC droplets is equal to the isotropic extinction coefficient (ε) of the dyes. In the ON state, the orientation of dyes follows the LC director, that is usually normal to the substrate. The LC droplets display a perpendicular ε of dyes that is less than isotropic ε, leading to weak incident light absorption. However, some dichroic dyes are not only dissolved in LC droplets but also in the polymer matrix. The dyes in the polymer matrix have a fixed random distribution state, even under applied voltage, that influence the light absorption and scattering of PDLC device. Kim et al have proposed a core-shell structured encapsulation technique in order to isolate dichroic dyes with LC in microcapsules and separate dyes from polymer matrix.[54] In their work, the monodispersed microcapsules consist of dye/LC cores and polyurethane/polyurea shells were fabricated through membrane emulsification and interfacial polymerization. The structure and electro-optical switching of dye-doped PDLC device are illustrated in **Figure 7**. The contrast ratio (CR) is an important parameter reflecting a switching-state yield, which is defined as the ratio of maximal transmittance in the ON state and minimal transmittance in the OFF state at a defined wavelength. The dye doped-PDLC device utilizing LC/dye microcapsules exhibited a CR higher than 120 at 600 nm with a maximal transmittance of 90% at 700 nm, which is a promising device for smart glazing applications.
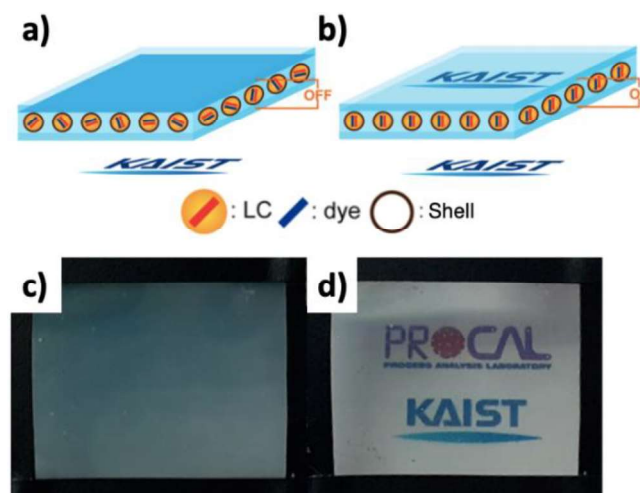
Figure 7. *Schematic illustration of dye-doped PDLC device in a) the OFF state (opaque state) and b) the ON state (transparent state). Photographs of dye-doped PDLC device in c) the OFF state and d) the ON state. From ref [54]*

2.5 Conclusion

The advantages and disadvantages of EC, PC, TC and PDLC devices are summarized in Table 1. As to the switching time, PDLC devices have a fast switching speed (<60 ms)[55,56] , while EC, PC and TC devices can perform an optical switch within less than a few minutes. Among them, PDLC devices and EC windows have attracted most attention because they allow user control. They are already available on the market, but suffer from relatively high fabrication costs.[56] Moreover, PDLC devices need higher driving voltages as compared to EC devices. Photochromic materials have been widely used for transitional lenses. Since the PC cannot be controlled by users to meet personal preferences, and because their optical switching speed strongly depends on the incident light intensity, their development in smart windows is still limited. Likewise, TC materials are not user-controllable and generally show a lower maximum transmittance in the visible range compared to EC materials. So far, none of these technologies can perfectly meet all the conditions for an ideal smart window (including fast switching speed, user control, high energy efficiency, good stability and reversibility). There are still strong challenges for the development of these technologies to make them compatible with the constraints imposed for large scale applications in buildings.

In this context, a new device has been developed, called photovoltaic spatial light modulator (PSLM), opening a new direction for self-powered smart window applications. The PSLM has a potential to overcome some of the bottlenecks that limit the integration of smart windows into buildings. Its structure, operational mechanism, advantages as well as some issues need to be addressed will be presented in next chapter.

Table 1. *Summary about cons and pros of EC, PC, TC and PDLC devices.*

	Advantages	Disadvantages
EC	- Users controlled - Active modulation in a broad spectral range - Excellent optical modulation - Good cycling stability	- Electric supply demand - Relatively high fabrication costs because of complicated device structure
PC	- Self-activated with UV irradiation - Energy saving - Low cost for installation owing to simple device configuration	- Lack of user control - Dependent-light intensity responsive materials
TC	- Self-powered with temperature changes - Energy saving - Less cost due to simple configuration	- Lack of user control - A limited maximum visible light transmittance
PDLC	- Users controlled - Very fast response time - High transparency in the ON state	- High-power requirements relative to EC devices - High costs for fabrication

References

(1)   Granqvist, C. G. Electrochromic Tungsten Oxide "lms: Review of Progress 1993}1998. *Sol. Energy Mater.* **2000**.

(2)   Kim, J.; Myoung, J. Flexible and Transparent Electrochromic Displays with Simultaneously Implementable Subpixelated Ion Gel-Based Viologens by Multiple Patterning. *Adv. Funct. Mater.* **2019**, *29* (13), 1808911.

(3)   Alesanco, Y.; Viñuales, A.; Palenzuela, J.; Odriozola, I.; Cabañero, G.; Rodriguez, J.; Tena-Zaera, R. Multicolor Electrochromics: Rainbow-Like Devices. *ACS Appl. Mater. Interfaces* **2016**, *8* (23), 14795–14801.

(4)   Granqvist, C. G. Electrochromics for Smart Windows: Oxide-Based Thin Films and Devices. *Thin Solid Films* **2014**, *564*, 1–38.

(5)   Rai, V.; Singh, R. S.; Blackwood, D. J.; Zhili, D. A Review on Recent Advances in Electrochromic Devices: A Material Approach. *Adv. Eng. Mater.* **2020**, *22* (8), 2000082.

(6)   Deb, S. K. A Novel Electrophotographic System.

(7)   Deb, S. K. Optical and Photoelectric Properties and Colour Centres in Thin Films of Tungsten Oxide. *Philos. Mag.* **1973**, *27* (4), 801–822.

(8)   Thakur, V. K.; Ding, G.; Ma, J.; Lee, P. S.; Lu, X. Hybrid Materials and Polymer Electrolytes for Electrochromic Device Applications. *Adv. Mater.* **2012**, *24* (30), 4071–4096.

(9)   Mortimer, R. J. Electrochromic Materials. *Annu. Rev. Mater. Res.* **2011**, *41* (1), 241–268.

(10)   Lee, S.-H.; Cheong, H. M.; Tracy, C. E.; Mascarenhas, A.; Pitts, J. R.; Jorgensen, G.; Deb, S. K. Alternating Current Impedance and Raman Spectroscopic Study on Electrochromic A-WO3 Films. *Appl. Phys. Lett.* **2000**, *76* (26), 3908–3910.

(11)   Zhou, J.; Wei, Y.; Luo, G.; Zheng, J.; Xu, C. Electrochromic Properties of Vertically Aligned Ni-Doped WO$_3$ Nanostructure Films and Their Application in Complementary Electrochromic Devices. *J. Mater. Chem. C* **2016**, *4* (8), 1613–1622.

(12)   Chen, P.-Y.; Chen, C.-S.; Yeh, T.-H. Organic Multiviologen Electrochromic Cells for a Color Electronic Display Application: Article. *J. Appl. Polym. Sci.* **2014**, *131* (13), n/a-n/a.

(13)   Bird, C. L.; Kuhn, A. T. Electrochemistry of the Viologens. *Chem. Soc. Rev.* **1981**, *10* (1), 49.

(14)   Vergaz, R.; Barrios, D.; Sánchez-Pena, J. M.; Pozo-Gonzalo, C.; Salsamendi, M.; Pomposo, J. A. Impedance Analysis and Equivalent Circuit of an All-Plastic Viologen Based Electrochromic Device. *Displays* **2008**, *29* (4), 401–407.

(15)   Amb, C. M.; Dyer, A. L.; Reynolds, J. R. Navigating the Color Palette of Solution-Processable Electrochromic Polymers. *Chem. Mater.* **2011**, *23* (3), 397–415.

(16)   Balan, A.; Baran, D.; Toppare, L. Benzotriazole Containing Conjugated Polymers for Multipurpose Organic Electronic Applications. *Polym. Chem.* **2011**, *2* (5), 1029–1043.

(17)   Schottland, P.; Zong, K.; Gaupp, C. L.; Thompson, B. C.; Thomas, C. A.; Giurgiu, I.; Hickman, R.; Abboud, K. A.; Reynolds, J. R. Poly(3,4-Alkylenedioxypyrrole)s: Highly Stable Electronically Conducting and Electrochromic Polymers. *Macromolecules* **2000**, *33* (19), 7051–7061.

(18)   Sönmez, G.; Schwendeman, I.; Schottland, P.; Zong, K.; Reynolds, J. R. N-Substituted Poly(3,4-Propylenedioxypyrrole)s: High Gap and Low Redox Potential Switching Electroactive and Electrochromic Polymers. *Macromolecules* **2003**, *36* (3), 639–647.

(19)   Schwendeman, I.; Hickman, R.; Sönmez, G.; Schottland, P.; Zong, K.; Welsh, D. M.; Reynolds, J. R. Enhanced Contrast Dual Polymer Electrochromic Devices. *Chem. Mater.* **2002**, *14* (7), 3118–3122.

(20)   Christiansen, D. T.; Reynolds, J. R. A Fruitful Usage of a Dialkylthiophene Comonomer for Redox Stable Wide-Gap Cathodically Coloring Electrochromic Polymers. *Macromolecules* **2018**, *51* (22), 9250–9258.

(21)   Liang, H.; Li, R.; Li, C.; Hou, C.; Li, Y.; Zhang, Q.; Wang, H. Regulation of Carbon Content in MOF-Derived

Hierarchical-Porous NiO@C Films for High-Performance Electrochromism. *Mater. Horiz.* **2019**, *6* (3), 571–579.

(22)   Gust, D.; Andréasson, J.; Pischel, U.; Moore, T. A.; Moore, A. L. Data and Signal Processing Using Photochromic Molecules. *Chem Commun* **2012**, *48* (14), 1947–1957.

(23)   Mori, K.; Ishibashi, Y.; Matsuda, H.; Ito, S.; Nagasawa, Y.; Nakagawa, H.; Uchida, K.; Yokojima, S.; Nakamura, S.; Irie, M.; Miyasaka, H. One-Color Reversible Control of Photochromic Reactions in a Diarylethene Derivative: Three-Photon Cyclization and Two-Photon Cycloreversion by a Near-Infrared Femtosecond Laser Pulse at 1.28 Mm. *J. Am. Chem. Soc.* **2011**, *133* (8), 2621–2625.

(24)   Dong, H.; Zhu, H.; Meng, Q.; Gong, X.; Hu, W. Organic Photoresponse Materials and Devices. *Chem Soc Rev* **2012**, *41* (5), 1754–1808.

(25)   Ebisawa, F.; Hoshino, M.; Sukegawa, K. Self-holding Photochromic Polymer Mach–Zehnder Optical Switch. *Appl. Phys. Lett.* **1994**, *65* (23), 2919–2921.

(26)   Zayat, M.; Einot, D.; Reisfeld, R. Reversible Photochromism of Sol-Gel SiO2 : AgCl Films. **1997**.

(27)   Armistead, W. H.; Stookey, S. D. Photochromic Silicate Glasses Sensitized by Silver Halides: Their Characteristic of Changing Color Reversibly, in Combination with Other Properties, Suggests Many Uses. *Science* **1964**, *144* (3615), 150–154.

(28)   Adachi, K.; Tokushige, M.; Omata, K.; Yamazaki, S.; Iwadate, Y. Kinetics of Coloration in Photochromic Tungsten(VI) Oxide/Silicon Oxycarbide/Silica Hybrid Xerogel: Insight into Cation Self-Diffusion Mechanisms. *ACS Appl. Mater. Interfaces* **2016**, *8* (22), 14019–14028.

(29)   Ke, Y.; Chen, J.; Lin, G.; Wang, S.; Zhou, Y.; Yin, J.; Lee, P. S.; Long, Y. Smart Windows: Electro-, Thermo-, Mechano-, Photochromics, and Beyond. *Adv. Energy Mater.* **2019**, *9* (39), 1902066.

(30)   Marevtsev, V. S.; Zaichenko, N. L. Peculiarities of Photochromic Behaviour of Spiropyrans and Spirooxazines. *J. Photochem. Photobiol. Chem.* **1997**, *104* (1–3), 197–202.

(31)   Such, G.; Evans, R. A.; Yee, L. H.; Davis, T. P. Factors Influencing Photochromism of Spiro-Compounds Within Polymeric Matrices. *J. Macromol. Sci. Part C Polym. Rev.* **2003**, *43* (4), 547–579.

(32)   Tamai, N.; Miyasaka, H. Ultrafast Dynamics of Photochromic Systems. *Chem. Rev.* **2000**, *100* (5), 1875–1890.

(33)   Hagen, J. P.; Becerra, I.; Drakulich, D.; Dillon, R. O. Effect of Antenna Porphyrins and Phthalocyanines on the Photochromism of Benzospiropyrans in Poly(Methyl Methacrylate) Films. *Thin Solid Films* **2001**, *398–399*, 104–109.

(34)   Evans, R. A.; Hanley, T. L.; Skidmore, M. A.; Davis, T. P.; Such, G. K.; Yee, L. H.; Ball, G. E.; Lewis, D. A. The Generic Enhancement of Photochromic Dye Switching Speeds in a Rigid Polymer Matrix. *Nat. Mater.* **2005**, *4* (3), 249–253.

(35)   Saeli, M.; Piccirillo, C.; Parkin, I. P.; Ridley, I.; Binions, R. Nano-Composite Thermochromic Thin Films and Their Application in Energy-Efficient Glazing. *Sol. Energy Mater. Sol. Cells* **2010**, *94* (2), 141–151.

(36)   Lee, M.-J.; Park, Y.; Suh, D.-S.; Lee, E.-H.; Seo, S.; Kim, D.-C.; Jung, R.; Kang, B.-S.; Ahn, S.-E.; Lee, C. B.; Seo, D. H.; Cha, Y.-K.; Yoo, I.-K.; Kim, J.-S.; Park, B. H. Two Series Oxide Resistors Applicable to High Speed and High Density Nonvolatile Memory. *Adv. Mater.* **2007**, *19* (22), 3919–3923.

(37)   Warwick, M. E. A.; Binions, R. Advances in Thermochromic Vanadium Dioxide Films. *J Mater Chem A* **2014**, *2* (10), 3275–3292.

(38)   Zhou, Y.; Cai, Y.; Hu, X.; Long, Y. Temperature-Responsive Hydrogel with Ultra-Large Solar Modulation and High Luminous Transmission for "Smart Window" Applications. *J Mater Chem A* **2014**, *2* (33), 13550–13555.

(39)   Li, S.-Y.; Niklasson, G. A.; Granqvist, C. G. Thermochromic Fenestration with VO2-Based Materials: Three Challenges and How They Can Be Met. *Thin Solid Films* **2012**, *520* (10), 3823–3828.

(40)   Wang, N.; Liu, S.; Zeng, X. T.; Magdassi, S.; Long, Y. Mg/W-Codoped Vanadium Dioxide Thin Films with Enhanced Visible Transmittance and Low Phase Transition Temperature. *J. Mater. Chem. C* **2015**, *3*

(26), 6771–6777.

(41) Wang, S.; Owusu, K. A.; Mai, L.; Ke, Y.; Zhou, Y.; Hu, P.; Magdassi, S.; Long, Y. Vanadium Dioxide for Energy Conservation and Energy Storage Applications: Synthesis and Performance Improvement. *Appl. Energy* **2018**, *211*, 200–217.

(42) Chen, Z.; Gao, Y.; Kang, L.; Cao, C.; Chen, S.; Luo, H. Fine Crystalline VO2 Nanoparticles: Synthesis, Abnormal Phase Transition Temperatures and Excellent Optical Properties of a Derived VO2 Nanocomposite Foil. *J. Mater. Chem. A* **2014**, *2* (8), 2718.

(43) Ke, Y.; Zhou, C.; Zhou, Y.; Wang, S.; Chan, S. H.; Long, Y. Emerging Thermal-Responsive Materials and Integrated Techniques Targeting the Energy-Efficient Smart Window Application. *Adv. Funct. Mater.* **2018**, *28* (22), 1800113.

(44) Jain, K.; Vedarajan, R.; Watanabe, M.; Ishikiriyama, M.; Matsumi, N. Tunable LCST Behavior of Poly(N-Isopropylacrylamide/Ionic Liquid) Copolymers. *Polym. Chem.* **2015**, *6* (38), 6819–6825.

(45) Schild, H. G.; Tirrell, D. A. Microcalorimetric Detection of Lower Critical Solution Temperatures in Aqueous Polymer Solutions. *J. Phys. Chem.* **1990**, *94* (10), 4352–4356.

(46) de la Rosa, V. R.; Woisel, P.; Hoogenboom, R. Supramolecular Control over Thermoresponsive Polymers. *Mater. Today* **2016**, *19* (1), 44–55.

(47) Zhou, Y.; Cai, Y.; Hu, X.; Long, Y. VO $_2$ /Hydrogel Hybrid Nanothermochromic Material with Ultra-High Solar Modulation and Luminous Transmission. *J. Mater. Chem. A* **2015**, *3* (3), 1121–1126.

(48) Bronnikov, S.; Kostromin, S.; Zuev, V. Polymer-Dispersed Liquid Crystals: Progress in Preparation, Investigation, and Application. *J. Macromol. Sci. Part B* **2013**, *52* (12), 1718–1735.

(49) Eun Jung, J.; Lee, G. H.; Eun Jang, J.; Hwang, K. Y.; Ahmad, F.; Jamil, M.; Jin Woo, L.; Jae Jeon, Y. Optical Property Enhancement of Dye-PDLC Using Active Reflector Structure. *J. Appl. Polym. Sci.* **2012**, *124* (1), 873–877.

(50) Bouteiller, L.; Barny, P. L. Polymer-Dispersed Liquid Crystals: Preparation, Operation and Application. *Liq. Cryst.* **1996**, *21* (2), 157–174.

(51) Kumar, P.; Neeraj; Kang, S.-W.; Lee, S. H.; Raina, K. K. Analysis of Dichroic Dye-Doped Polymer-Dispersed Liquid Crystal Materials for Display Devices. *Thin Solid Films* **2011**, *520* (1), 457–463.

(52) Deshmukh, R. R.; Malik, M. K. Effect of Dichroic Dye on Phase Separation Kinetics and Electro-Optical Characteristics of Polymer Dispersed Liquid Crystals. *J. Phys. Chem. Solids* **2013**, *74* (2), 215–224.

(53) Jung, J. E.; Lee, G. H.; Jang, J. E.; Hwang, K. Y.; Ahmad, F.; Muhammad, J.; Woo Lee, J.; Jeon, Y. J. Optical Enhancement of Dye-Doped PDLC by Additional Dye-LC Layer Coating. *Opt. Mater.* **2011**, *34* (1), 256–260.

(54) Kim, M.; Park, K. J.; Seok, S.; Ok, J. M.; Jung, H.-T.; Choe, J.; Kim, D. H. Fabrication of Microcapsules for Dye-Doped Polymer-Dispersed Liquid Crystal-Based Smart Windows. *ACS Appl. Mater. Interfaces* **2015**, *7* (32), 17904–17909.

(55) Luo, L.; Liang, Y.; Feng, Y.; Mo, D.; Zhang, Y.; Chen, J. Recent Progress on Preparation Strategies of Liquid Crystal Smart Windows. *Crystals* **2022**, *12* (10), 1426.

(56) Casini, M. Active Dynamic Windows for Buildings: A Review. *Renew. Energy* **2018**, *119*, 923–934.

Chapter 3. Scientific background

Photovoltaic spatial light modulators (PSLMs) are composed of two parts. One is an organic photovoltaic multilayer similar to an organic solar cell (OSC) but without the top electrode; another is similar to the twisted nematic liquid crystal (TNLC) cell. In this chapter, we will first describe the working principle of an OSC, a TNLC cell, and then the operational mechanism of PSLMs. We will present self-powered PSLMs from previous work and discuss scientific and technical challenges in current devices.

3.1 Organic photovoltaic devices

In the last decades, organic semiconductors have been widely used in numerous applications including photodetectors[1,2], organic field-effect transistors (OFET)[3,4], organic light-emitting diodes (OLED)[5] as well as OSC[6,7] owing to their flexibility, low cost, large-area printing via roll-to-roll processing. The organic photovoltaic unit integrated into PSLMs can generate a photovoltage upon illumination, avoiding the use of external power supply. Therefore, studying the organic semiconductor properties and understanding the working principle of OSC is crucial to improve PSLM performance.

3.1.1 Electronic structure of an organic semiconductor

Organic semiconductors are carbon-based materials, possessing a π-conjugated molecular structure that involves an alternation of single (σ) and double (π) bonds between carbon atoms. It is well known that each carbon atom can contribute four electrons to form covalent bonds. In the conjugated molecules, the carbon atoms adopt a sp^2-hybridization: three electrons respectively from 2s, $2p_x$ and $2p_y$ orbitals hybridize forming three sp^2-hybridized orbitals with equal energy, as illustrated in **Figure 1a**. The fourth electron from the $2p_z$ orbital does not participate in the hybridization and appears at a higher energy than the hybridized orbitals. The three sp^2-hybrid orbitals of each carbon atom are used to form strong σ bonds, which are coplanar and separated by an angle of 120° (**Figure 1b**). The $2p_z$ orbitals of neighboring carbon atoms overlap to form π bonds that are perpendicular to the hybrid orbital plane. The π bonds are weaker relative to σ bonds, and π electrons can be delocalized over a group of atoms along the molecular backbone. The delocalization distance is referred to as conjugation length. A longer conjugation length results in better intramolecular charge transport. However, chemical

and planarity defects of the molecular backbone generally restrict the conjugation length in organic materials.

The interaction between $2p_z$ orbitals yields the π bonding orbital and π^* anti-bonding orbital. The bonding orbital is referred to as the highest occupied molecular orbital (HOMO) and the anti-bonding orbital is called lowest unoccupied molecular orbital (LUMO). In a solid organic semiconductor, the LUMO and HOMO levels distribution is analogous to the conduction and valence bands found in inorganic semi-conductors, respectively. The difference in the energy between the HOMO and the LUMO levels is defined as the energy bandgap (E_g). When the conjugation length increases, the band gap is reduced (**Figure 1c**). In the case of an energy band gap lower than 3 eV, the organic material shows semiconducting properties.
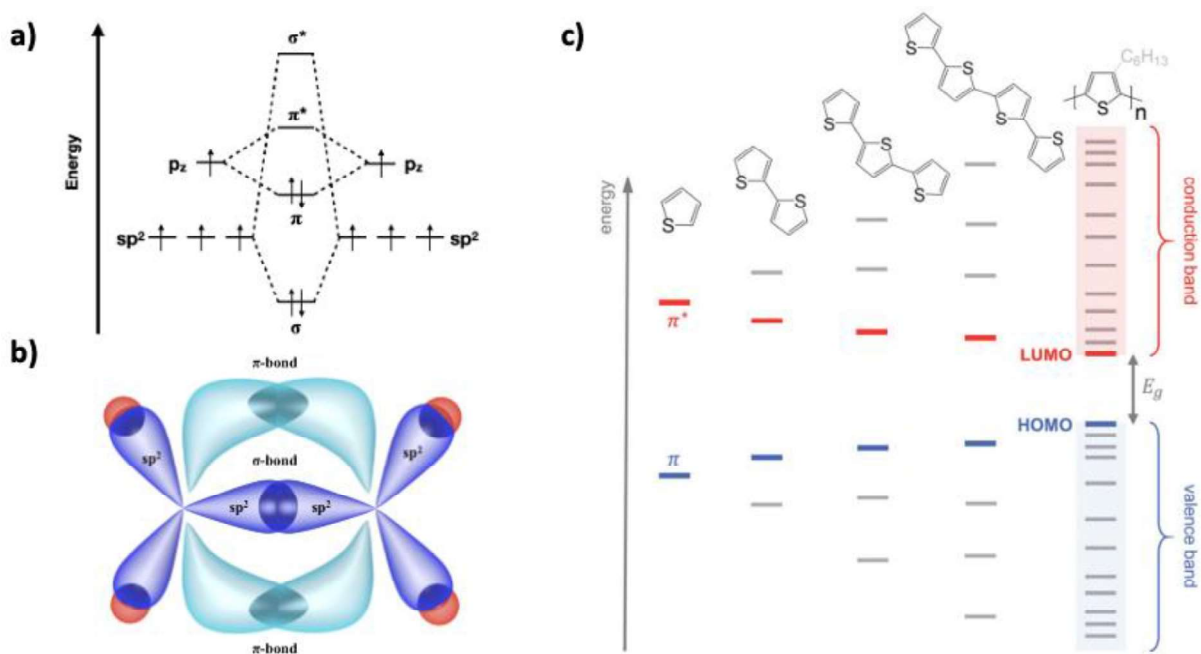
Figure 1. a) Energy level diagram of C-C bonding in a sp^2 hybridized system. b) Schematic illustration of hybridized orbitals and chemical bonding in ethylene C_2H_4 molecule. Reproduced from[8]. c) Evolution of HOMO, LUMO levels and bandgap (E_g) as a function of the amount of thiophene repeating units. 'Conduction band' and 'valence band' are bordered by LUMO and HOMO, respectively. Adapted from [9].

3.1.2 Operation of an organic solar cell

In an OSC, the photovoltaic layer is typically composed of two organic semiconductors: an electron donor (D) and an electron acceptor (A). The energy offset between the frontier orbital energy levels of D and A molecules offers a driving force to promote exciton dissociation. The

HOMO and LUMO levels can be estimated from their ionization potential (IP) and electron affinity (EA), respectively (**Figure 2**). EA is the amount of energy released for an electron transfer from the vacuum level to the LUMO level. IP is defined as the minimal energy required to remove an electron from the HOMO level. Comparing the energy levels of D and A, D has a lower IP than A, and A has a higher EA. Selecting the D and A with appropriated energy levels is critical to the efficient operation of OSC.
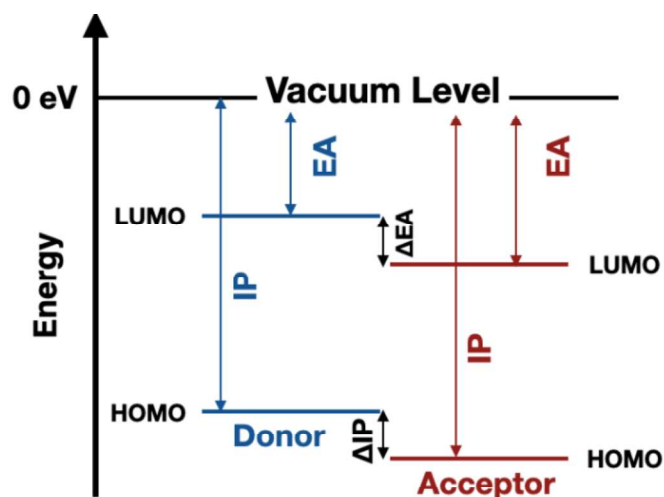
Figure 2. *Energy level diagram of electron-donor and electron-acceptor. The difference in EA and in IP between donor and acceptor are ΔEA and ΔIP, respectively.*

The working principle of an organic solar cell involves four steps as follows (**Figure 3**): I) Exciton generation upon photon absorption; II) Exciton diffusion and dissociation into free charge carriers at the D/A interface; III) Charge transport towards the electrodes; and finally, IV) charge extraction.
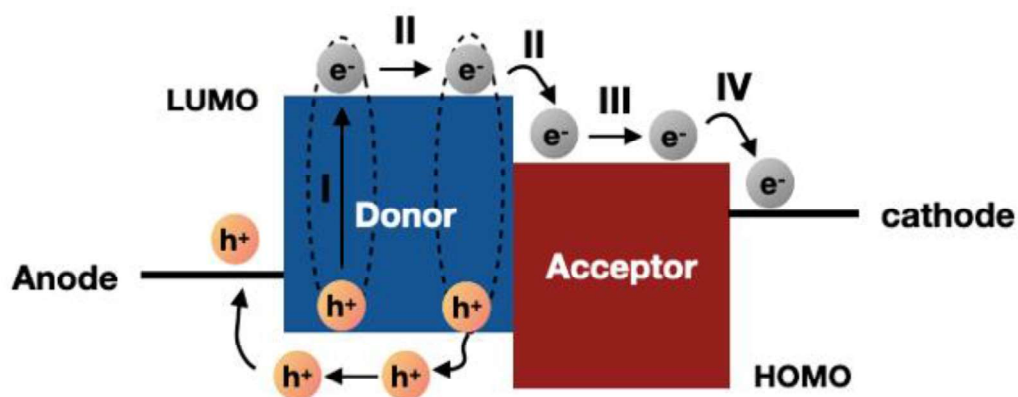
Figure 3. *Working principle of organic solar cells with four main steps upon illumination.*

I) Exciton generation: Organic semiconductors frequently have high molar absorption coefficients (typically around 10^5 cm^{-1}).[10] Hence, an organic thin film with only 100~200 nm thickness is sufficient to absorb most of the incident photons. Upon illumination, photons with energy equal or higher than E_g are absorbed by the organic semiconductor, forming bound electron-hole pairs referred to as excitons.

II) Exciton diffusion and dissociation: The photogenerated excitons will diffuse to the D/A interface where dissociation into charge carriers occurs. The distance to reach the interface should be less than the exciton diffusion length, which is defined as the average exciton diffusion distance before recombination. In inorganic semiconductors, the exciton dissociation can be easily achieved by thermal energy at room temperature due to a low exciton binding energy of a few meV. In organic semiconductors, the dielectric constant ($\mathcal{E}$=~3) is lower relative to that of inorganic semiconductors ($\mathcal{E}$>10).[10] Therefore, the electron and hole wavefunctions are more localized, giving rise to strong coulombic interactions between electron-hole pairs and a high exciton binding energy (100-1400 meV).[11,12] Thermal energy is thus not sufficient to dissociate excitons into free charge carriers. One approach for exciton dissociation and charge generation reported by Tang et al consisted in using a heterojunction composed of a bilayer of two different organic semiconductors with appropriate energy levels (i.e., D and A).[13] Since then, donor-acceptor bulk heterojunctions, composed of a blend of D and A molecules, became the basis of organic solar cells. If the energy offset between D and A is large enough to overcome the exciton binding energy, a charge transfer (CT) can take place at the D/A interface. The CT is an intermediate state between strongly bound excitons and free charge carriers. In the CT state, the electron-hole pair is still influenced by the coulombic interaction, but can be subsequently dissociated into a charge-separated (CS) state due to the weaker binding energy compared with the initial exciton. In the CS state, free electrons are located in the LUMO of the acceptor, and can drift/diffuse towards the cathode. On the contrary, free holes reside in the HOMO of the donor and can be collected at the anode.

III) Charge transport: The charge transport can be performed by diffusion or drift. The former results from carrier concentration gradients within the solar cell. The latter arises from the built-in electric field created by the anode and the cathode. The drift speed of charge carriers (i.e., charge mobility) and diffusion constant can be influenced by the molecular weight, the morphologies and the crystal structure (like crystalline, semi-crystalline, disordered). In most organic semiconductors, the charge mobility is highest along the backbone (intrachain) and

the π-π stacking (interchain) directions, and lowest along the direction of side chains.[14–16] Furthermore, since intermolecular interactions are due to weak Van Der Waals forces, charge carriers are generally rather localized on one or a few molecules, and intermolecular transport is achieved by a thermally activated hopping process. The charge mobility is a key factor for OSC performance. A high charge mobility results in a fast charge extraction, preventing electron-hole recombination and thereby showing good photovoltaic performance of solar cells.

IV) Charge collection: Eventually, free charge carriers are collected at the respective electrodes. The electrode materials have a strong impact on the charge extraction processes. The work function of the metal electrode is the energy difference between the vacuum level and its Fermi level. In order to achieve a high efficiency in the charge extraction, the energy barrier at the active layer/interface leading to charge accumulation should be minimized. Consequently, the work function of the anode is expected to match the HOMO of D, while the work function of the cathode is expected to be aligned with the LUMO of A. Furthermore, electron and hole transporting layers are often deposited between the active layer and the electrodes. They can be considered as 'buffer' layers used to avoid charge collection at the wrong electrodes and thus lower the device performance. Many research groups demonstrated that electron transporting layers (ETL) such as ZnO, TiO_x efficiently enhance electron collection.[17–20] Also hole transporting layers (HTL) such as MoO_3 have been used efficiently to modify the work function of electrodes and form good ohmic contacts.[21]

3.1.3 Organic Solar cell architecture

Active layers with a D/A bilayer or a bulk heterojunction (BHJ) have been widely used in photovoltaic devices. The D/A bilayer heterojunction concept was initially proposed by Tang et al.[13] Such bilayer devices contain a single and well-defined interface between D and A (**Figure 4a**). Thus, the separated electrons and holes can be easily transported to the respective electrodes with a low risk of charge recombination.[19] However, the exciton diffusion length is short in organic semiconductors (typically 1~10 nm).[22–24] Most excitons are thus generated far from the D/A interface and may recombine or be trapped before reaching the interface. One solution consists to decrease the thickness of the active layer, so that more excitons can diffuse to the D/A interface before recombination. However, in ultra-thin films, the weak light

absorption leads to a reduced quantity of photogenerated excitons.[25] The BHJ avoids this bottleneck by making most excitons be generated close to the D/A interface. The first BHJ solar cell was reported by Heeger et al.[26] Their results indicated that blending D and A in the form of an active layer can improve the energy conversion efficiency considerably. The BHJ consists of interpenetrating networks of D and A, enhancing charge generation due to the larger D/A interfacial area (**Figure 4b**). Ideally, the domain size of both D and A should be small enough to ensure efficient exciton diffusion to the interface, and large enough to facilitate charge transport and reduce bimolecular recombination.[27] The domain size can be controlled by modifying the molecular structure (e.g., side chains or substituents), employing solvent additives, thermal annealing, etc. Optimizing the morphology of the BHJ is necessary to achieve high OSC performances.

A typical OSC is composed of five layers: hole and electron transporting layers are deposited on each side of the active layer. This three-layer stack is sandwiched between two electrodes. The bottom electrode of a solar cell is generally transparent to ensure good light absorption in the active layer. Indium-tin-oxide (ITO) was used as transparent bottom electrode in this thesis. According to which type of charge carriers (electrons or holes) are collected by the ITO bottom electrode, the OSC architecture can be categorized into "standard" structure and "inverted" structure, as shown in **Figure 4 c,d.** In the standard structure, the ITO electrode whose work function is modified by a HTL like Poly(3,4-ethylenedioxythiophene): polystyrene sulfonate (PEDOT: PSS) is responsible for hole collection.[28] A metal electrode such as Al or Ca/Al with low work function is used as a top contact for electron extraction. However, Al can be easily oxidized in air, leading to a poor stability of solar cells. On the other hand, in the case of inverted architectures, the working function of ITO can be significantly reduced by a thin layer of ethoxylated polyethyleneimine (PEIE), enabling electron collection.[29] Meanwhile, the holes are collected at metal top electrodes with high working function such as silver (Ag) or gold (Au). MoO_3 is usually used as a HTL to minimize recombination at the interface between the active layer and the electrode.
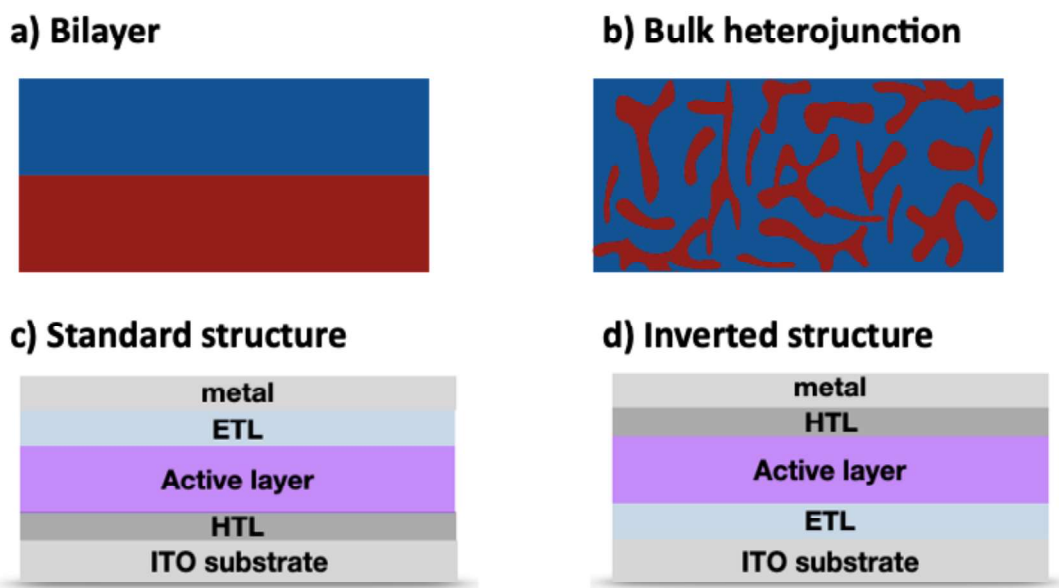
Figure 4. Schematic representation of two different photovoltaic layers: a) bilayer and b) bulk heterojunction. The organic solar cells were fabricated based on c) the standard structure or on d) the inverted structure.

3.1.4 Current-voltage characteristics

The J-V characteristics are extensively used to quantitively evaluate the solar cell efficiency. An example for J-V curves of OSC measured in the dark and upon illumination are shown in **Figure 5**. The power conversion efficiency (PCE) is the most intuitive parameter to represent the solar cell performance. The PCE is defined as the ratio of the maximal electrical power generated by the solar cell (P_m) to the incident solar power (P_{in}).

$$\eta(\%) = \frac{P_m}{P_{in}} \times 100\%$$

Eq. 3. 1
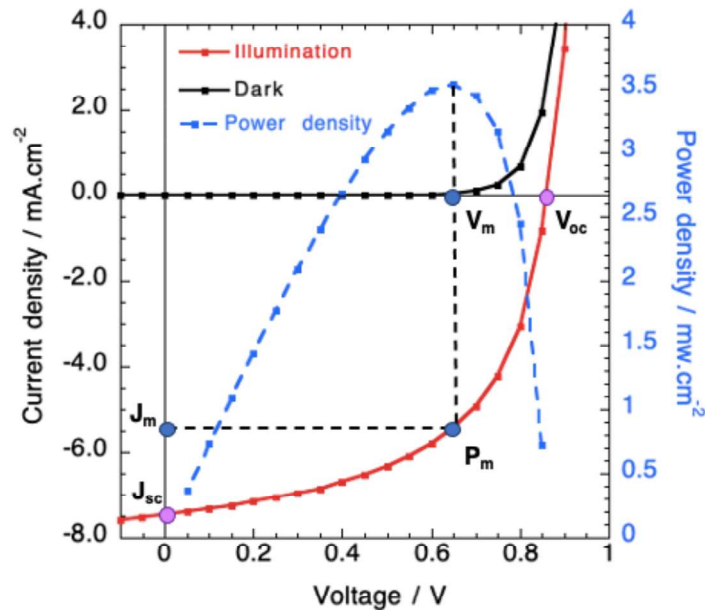
Figure 5. *J-V characteristics of an OSC investigated in this thesis. The OSC was measured in dark (black line) and upon illumination (red line), respectively. The blue dashed line corresponds to the power density of the OSC with its maximum power point (P_m) at around 0.65 V (V_m). The purple circles represent the open circuit voltage V_{oc} and the short circuit current density J_{sc}.*

The P_m can be determined by measuring the open-circuit voltage (V_{oc}), the short-circuit current density (J_{sc}) and the fill factor (FF).

The V_{oc} is the voltage when no current flows through the solar cell upon illumination, which is also the maximum voltage generated by the solar cell that can be provided to an external circuit. In general, V_{oc} is directly related to the energy gap between the electron (E_{Fn}) and the hole (E_{Fp}) quasi-Fermi energy levels. It can be expressed as follows[30]:

$$V_{oc} = \frac{1}{q}\left(E_{Fn} - E_{Fp}\right) \qquad\qquad Eq.\ 3.\ 2$$

where q is the elementary charge. E_{Fn}-E_{Fp} is generally significantly smaller than the effective bandgap of the BHJ, defined by the difference between the LUMO of the acceptor and the HOMO of the donor. It is well-known that organic semiconductors are highly disordered materials. Structural disorder results in site energy fluctuations in the HOMO or LUMO energy levels. The energy bands therefore take the form of a Gaussian distribution.[31] In this case, the gap tail states (near band-edge) downshift the electron quasi Fermi-level and upshift the hole quasi Fermi-level, reducing V_{oc}.[32] In addition to energetic disorder, V_{oc} is influenced by other parameters such as the energy of the charge transfer state, photogenerated carrier density, etc.

The J_{sc} is the current density produced by the solar cell in short-circuit conditions. It is directly proportional to the number of photons absorbed in the active layer. Hence, enhancing the light absorption coefficient or decreasing the band gap of the organic semiconductor can improve J_{sc}. Furthermore, the morphology is also an important factor to optimize J_{sc}. As mentioned before, if the length scale of phase separation in the bulk heterojunction is comparable to the exciton diffusion length, charge generation is enhanced and J_{sc} is increased. The Fill factor (FF) is defined as the ratio of maximum output power of OSC to the ideal product of V_{oc} and J_{sc}.

$$FF = \frac{V_m \times J_m}{V_{oc} \times J_{sc}}$$

Eq. 3. 3

Where V_m and J_m can be obtained by estimating the maximum power density of the OSC, as depicted in **Figure 5**. The FF represents how efficiently the photogenerated charge carriers are extracted out of the OSC. Hence, key factors limiting the FF are due to current/voltage losses, that can be quantified by the series resistance (R_s) and the shunt resistance (R_{sh}). Rs originates from the bulk resistance of all materials in the device as well as their contact with each other, reducing the current flow. R_{sh} denotes the leakage current induced by pinholes, aggregates in the films, traps or edges of the device.[33,34] Reducing R_s or enhancing R_{sh} (i.e., diminish the leakage current) improves charge collection and optimizes the FF and the PCE.[35–38]

According to equation 3.1 and 3.3, the PCE can be ultimately expressed as:

$$\eta = \frac{V_{oc} \times J_{sc} \times FF}{P_{in}}$$

Eq. 3. 4

Standard testing condition are used to determine the PCE, consisting of an incident light density of 100 mW.cm^{-2} with an AM 1.5G solar spectrum and a testing temperature of 25°C.

3.2 Liquid crystals (LCs)

Liquid crystals (LCs) possess both the fluidity of a liquid and the anisotropic properties of a crystal. Hence, LC phases appear between the crystalline solid state and the isotropic liquid state.[39] One of LC categories is thermotropic LC whose phase is controlled by temperature. Depending on the shape and the arrangement of thermotropic LC molecules, they have been subdivided into nematic, smectic, columnar phases, etc. Among them, the nematic liquid crystal (NLC) is extensively used in liquid crystal displays (LCD), and is also employed for our PSLM devices.

3.2.1 Nematic liquid crystals (NLCs) and twisted LC configuration

Nematic liquid crystal (NLC) molecules have a longitudinal, rod-like structure that is generally composed of elongated rigid geometry (e.g., aromatic cycles) with one or several flexible tail chains (e.g., hydrocarbon groups). An example of NLC molecular structures was illustrated in **Figure 6a**. The rigid part provides a certain degree of order, while the flexible tail chains offer the mobility to the molecules. NLC phase occurs as a function of temperature variation. As shown in **Figure 6b**, below the melting temperature (T_m), a crystalline solid is formed with 3D periodic order in the molecular arrangement. Above the clearing temperature (T_c), an isotropic liquid is formed with a random distribution of molecular orientations. The nematic phase (i.e., mesophase) exists between T_m and T_c. It is thermodynamically stable in this domain of temperature. The nematic LC molecules possess long-range orientational order with their long axis aligned in a preferred direction.[40] The average direction of all molecules is represented by a vector $\vec{n}$ called director. Unlike crystalline solids where each molecule strictly aligns along certain crystallographic directions in the crystals, in the nematic phase individual molecules slightly deviate from the director.
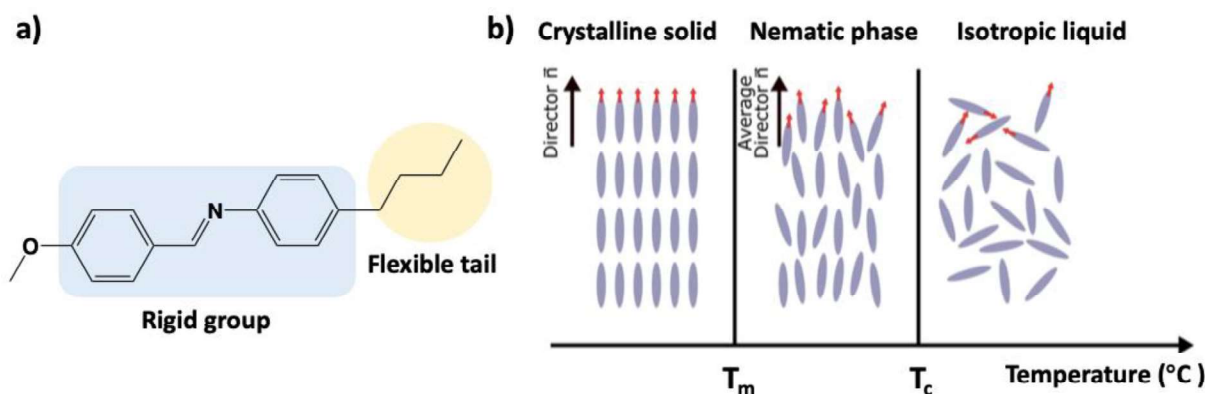
Figure 6. a) Chemical structure of 4-methoxylbenzyli-dene-4'-butylaniline (MBBA). b) Nematic LC molecules states as a function of temperature. Reproduced from [41].

The conventional twisted nematic liquid crystal (TNLC) was discovered by Schadt and Helfrich in 1970.[42] In this context, "twisted" means that the molecules are directionally oriented and stacked in a helical mode, with each layer rotated at a slight angle compared to the neighboring ones (**Figure 7**). In this report, the NLC molecules were deposited between two rubbed and 'crossed' electrodes. The LC director is constrained and aligns along the rubbing direction at each of the electrode surface. This phenomenon is attributed to the "anchoring" force. The anchoring force to fix LC molecules on the electrode or polymer surface originates from their molecular interaction.[43] Since anchoring effects exist on both sides of the two crossed alignment surface, LC molecules finally rotate 90° from one substrate to other one.

Schadt et al further showed that only a small voltage (~3V) was necessary to change the LC orientation, from a twisted to a homeotropic configuration, which is significantly lower than for other LC configurations (commonly 5-8 V).
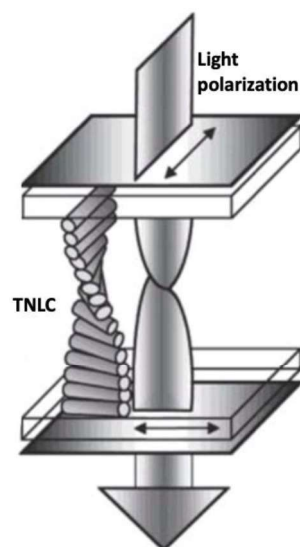
Figure 7. *Schematic illustration of a LC cell with 90° twist in a nematic liquid crystal. Adapted from[44].*

3.2.2 LC orientation control

TNLC cells require a well-defined LC orientation. An oriented organic polymer film over the glass substrate can help LC molecules to exhibit a uniform alignment. It can be achieved via the unidirectional rubbing of the polymer film, using a machine which consists of a rotating cylinder covered by microfiber cloth (**Figure 8**). The rubbing parameters such as rubbing force between rotating cylinder and the surface of film can be adjusted to optimize the LC alignment. The orientation of LC molecules along the rubbing direction can be attributed to the presence of anisotropic order in polymer chains or the reduced distortion energy of NLC molecules fitting in microscopically grooved surface created by the rubbing.[43,45–47] Increasing the rubbing force leads to a better polymer alignment and more pronounced anisotropic optical properties (The P3HT polymers oriented under different rubbing forces will be shown in chapter 5). However, a strong rubbing force might cause a damage of BHJ layer below the AL. Consequently, a "soft" rubbing method (i.e., using a relatively low rubbing force) is generally used to orient the organic alignment layer, creating aligned polymer chains on the top-surface of the films with a low roughness.

The poly(3-hexylthiophene) (P3HT) as a flexible polymer was used as LC alignment layer in this thesis. The rubbed P3HT polymer has a good thermal stability, good film forming properties, is commercially available and can induce high-quality LC alignments.[48]
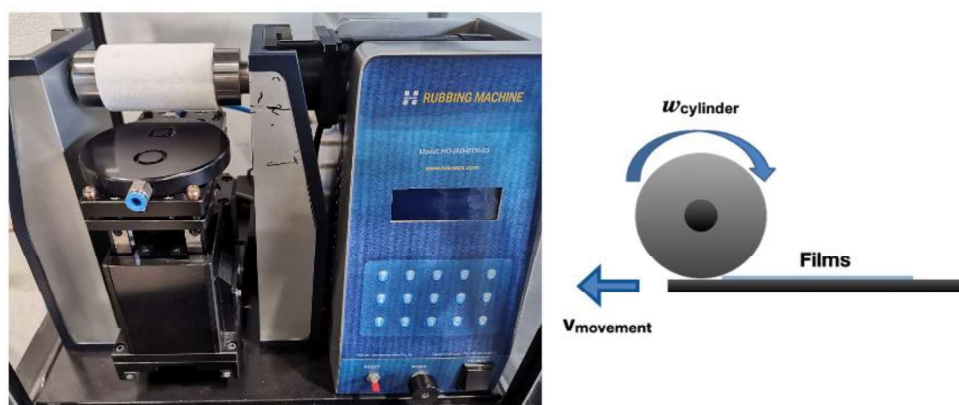
Figure 8. *Photograph and schematic view of the commercial rubbing machine (Holmarc). During the rubbing process, the cylinder will contact the surface of the film and rub the film surface at a constant rotation speed **ω** film moves at a constant speed **V**_{movement} under the rotating cylinder.*

3.2.3 Optical activity of NLC and TNLC molecules

Unlike the liquid phase that appears clear, the nematic phase appears milky due to its birefringence and light scattering properties. A nematic LC molecule possesses an optical axis such that all the directions perpendicular to it are optically equivalent. In a planar configuration (i.e., when both alignment layers of a LC cell are parallel to each other), uniaxial nematic molecules produce two different refractive indexes: ordinary (n_o) and extraordinary (n_e) refractive indexes. The ordinary light polarization is perpendicular to the optical axis, whereas the extraordinary light polarization is parallel to the optical axis. The difference between n_o and n_e defines the birefringence ($\Delta n = n_e - n_o$).

When linearly polarized light travels through the nematic LC molecules, it can be considered as a vectorial sum of extraordinary and ordinary rays. Two polarizations have different refractive indexes ($n_o \neq n_e$), and thus travel at different velocities through the LC ($n = \frac{c}{v}$, where n is refractive index, c and v are light velocities in medium and vacuum, respectively). Typical nematic LC have a positive birefringence ($\Delta n = 0.05 \sim 0.5$).[40] The phase difference between two polarizations leads to a transformation from linearly polarized input light to elliptically polarized output light. The polarization at the output of the LC medium depends on the film thickness, the birefringence of the LC layer, the incident light polarization and the light wavelength.

Within TNLC cells, the director is forced to twist by 90° between the two crossed alignment

substrates within the LC cell. It has been shown that, as the incident light polarization propagates through the TNLC, the light polarization follows the twist of LC molecules, giving rise to a phase difference of $\pi/2$ at the output.[42,44,49]

3.2.4 Dielectric Anisotropy of NLC molecules

The change in LC orientation by an electric field depends on the LC electrical dipole moment. In some NLC molecules, the presence of differently electronegative atoms along the molecular backbone generates a permanent electric dipole. Other NLC molecules do not have permanent dipoles, but electrical dipoles are induced by the electric field. When a high enough electric field is applied to LC molecules, the permanent or induced electric dipoles will align along the electric field leading to a change of LC orientation.

According to the chemical structure, the electric dipole can be parallel or perpendicular to the long axis of the molecules. In the former case, the dielectric constant along the molecular long axis ($\varepsilon_{//}$) is larger than that perpendicular to the molecular long axis ($\varepsilon_{\perp}$). Hence, the dielectric anisotropy defined as $\Delta\varepsilon = \varepsilon_{//} - \varepsilon_{\perp}$ is positive (**Figure 9a**). On the contrary, the latter case leads to a negative dielectric anisotropy due to $\varepsilon_{//} < \varepsilon_{\perp}$ (**Figure 9b**).
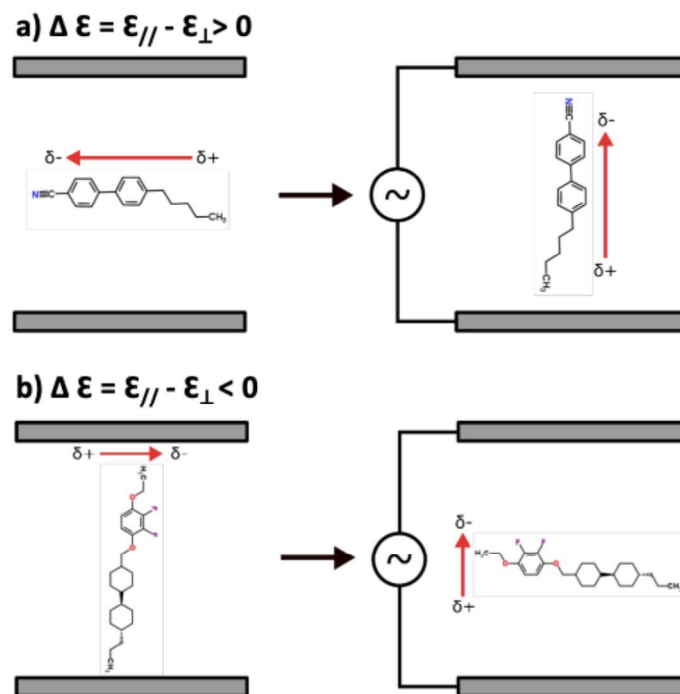
Figure 9. *Schematic illustration for NLC molecules orientation before (on the left) and after (on the right) the application of an external electric field in the case of a) $\Delta\varepsilon > 0$ and b) $\Delta\varepsilon < 0$. Reproduced from[41].*

3.2.5 Operation of TNLC cells

When a voltage is applied to the TNLC cells, the electric field appears across the TNLC layer. Except for LC molecules closest to substrate surface, which are exposed to strong anchoring forces, the bulk nematic LC molecules align parallel to the electric field, if the applied voltage exceeds a threshold value called Fréedericksz voltage (V_{th}). Above V_{th}, the TNLC molecules reorient and take up a homeotropic orientation. More specifically, the Fréedericksz transition voltage is defined as the threshold voltage applied to LC molecules so that LC orientation starts to change. It depends on the physical properties of the LC molecules and the anchoring strength between LC molecules and the substrate surface. If LC molecules have a high dielectric anisotropy and a relative weaker anchoring force, the threshold voltage will be low. In addition, sometimes a small angle between LC molecules and substrate plane is formed and referred to as pre-tilt angle. This angle will also reduce the threshold voltage or increase the switching speed.

In a twisted nematic light valve, the TNLC cell is placed between two crossed polarizers (**Figure 10**). Without the applied voltage, the incident light polarization is rotated 90° by the twisted LC molecules and passes through the second polarizer. When applying a voltage above the threshold value to the TNLC cell, the LC molecules change from the twisted state to the homeotropic state. In this case, the incident light will propagate along the optical axis of the nematic LC molecules. As mentioned above, the polarizations perpendicular to the optical axis have the same refractive indexes ($n_o = n_e$), leading to no optical activity. As a result, the light polarization remains unchanged and is blocked by the second polarizer.
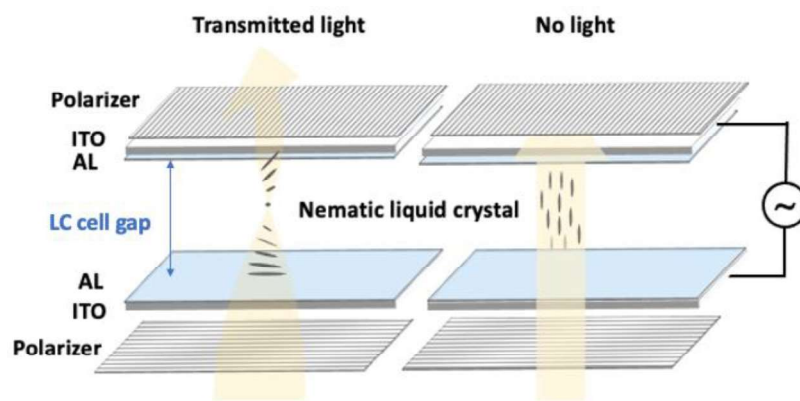
Figure 10. *Schematic illustration for TNLC light valve before (on the left) and after (on the right) the application of voltage upon illumination.*

A spacer is used to confer a uniform cell gap and has a strong impact on the operation of the device. Indeed, there exists a competition between anchoring forces and electric field to control the LC orientation. If the thickness of the TNLC layer is ultrathin, the LC director is dominated by strong anchoring forces. Therefore, less LC molecules can modify their orientation under the electric field. If the TNLC layer is fairly thick, the LC alignment in the center of the layer cannot be controlled by anchoring, probably modifying the birefringence of TNLC layer and thus influencing the transmittance of the device.

3.3 Photovoltaic spatial light modulators (PSLM)

3.3.1 PSLM device structure and working principle

The PSLM device can be divided into two parts: I) TNLC cell, which is responsible to modulate the optical properties, and II) an organic photovoltaic multilayer capable of generating the electric field upon illumination. As illustrated in **Figure 11**, this device consists of a twisted nematic liquid crystal, sandwiched between two ITO substrates coated with alignment layers (ALs). The alignment layers are mutually perpendicular, enabling the LC molecules to twist by 90° from one side to the side. The OPV multilayer is positioned between the LC layer and one of the ITO substrates. It includes an HTL, a BHJ and an ETL. Under illumination, the BHJ generates free electron-hole pairs, which are separated by diffusion/drift under the influence of a build-in voltage and the presence of carrier selective interfaces. The electrons and holes will reach at ETL and HTL respectively, creating a voltage drop across the multilayer stack referred to as photovoltage (V_{ph}). One of the alignment layers is produced by directly rubbing the HTL in contact with the LC layer or by adding an oriented polymer layer on top of the HTL (e.g., a rubbed P3HT layer).

The PSLM operates between a polarizer and an analyzer. The incident light is linearly polarized by the polarizer, which is oriented parallel to the LC directors at the illuminated surface. As depicted in **Figure 11a**, in the open-circuit condition (OFF state or clear state), photogenerated holes and electrons accumulate in the HTL and ETL, respectively. No electric field is produced across the LC layer. Consequently, the light polarization is rotated 90° by LC molecules, passing through the analyzer that is perpendicular to the initial polarizer. This leads to a transparent state. In the case both ITO substrates are short-circuited (ON state or dark state), as shown in **Figure 11b**, the electrons can be transferred to the opposite ITO substrate. The voltage drops

across the LC layer, and matches roughly the photovoltage generated by the BHJ layer. If the photovoltage exceeds the Fréedericksz transition voltage (V_{th}), the LC molecules start to change orientation, resulting in a decrease of the device transmittance. Since the photovoltage amplitude is influenced by local light intensity, the device response is spatially resolved.[48]
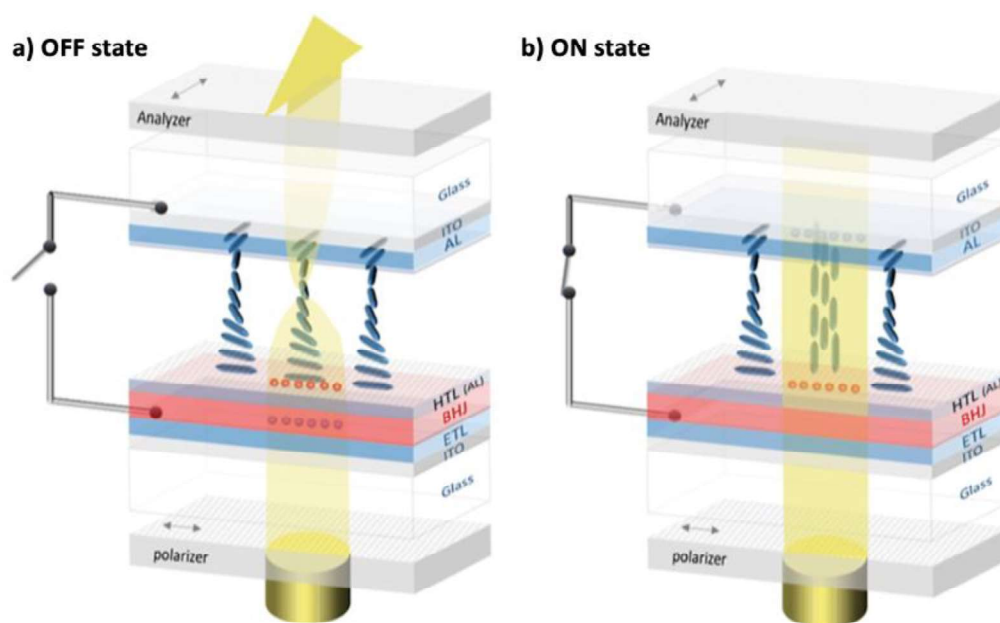
Figure 11. *Schematic illustration of PSLM devices in a) OFF state and b) ON state. Red circles correspond to the holes and blue circles to electrons. Reproduced from*[48].

3.3.2 Proof-of-principle

A first set of devices based on P3HT and indene-C60-bisadduct (ICBA) were fabricated, using a customized NLC (HVT6897).[48] The P3HT is a common donor used in organic electronics, and ICBA is a fullerene derivative used as an acceptor. In order to highlight the physical mechanism during PSLM operation, the devices were characterized by crossed-polarizer intensity (CPI) measurements. This technique measures the transmitted light intensity as a function of an applied voltage, using an AM 1.5G solar simulator, filtered by various light attenuators, as a variable light source. In this case, as the photovoltage generated by P3HT/ICBA layer ($V_{ph}<V_{oc}$ =0.83 V) is lower than the V_{th} of HVT6897 (2.3 V), an additional external voltage is required to change the device transmittance. **Figure 12** shows the normalized transmittance of the device as a function of the applied DC voltage. The PSLM response strongly depends on the incident light intensity and on the polarity of the applied voltage. Under low incident light intensity, the

applied voltage where the transmittance starts to drop is comparable to V_{th} of NLC. This is consistent with the fact that no photovoltage is generated in the system at this low intensity. With increasing light intensity, the CPI curves shift. This result can be understood by considering that the voltage across the LC layer (V_{LC}) is set by the applied voltage (V_{DC}) and the photovoltage (V_{ph}) such as $V_{LC} = V_{DC} \pm V_{ph}$. In the case of positive polarity ($V_{LC} = V_{DC} + V_{ph}$), the applied voltage and photovoltage have the same direction. The photovoltage increases with increasing incident light intensity. Hence, the threshold value can be reached at lower applied voltage. Conversely, in the case of negative polarity ($V_{LC} = V_{DC} - V_{ph}$), higher applied voltage will be required to change the LC orientation. This phenomenon is attributed to the photovoltaic effect. Moreover, the CPI curves shift by 0.7 V between the high and low intensities. This value is close to the V_{oc} produced by the corresponding P3HT/ICBA based solar cell. It is slightly lower than V_{oc} due to the incident light attenuation by the absorptive polarizer. This first device demonstrated the physical principle underlying PSLM device operation. However, the photovoltage remains below the threshold value and thus does not allow an autonomous operation.
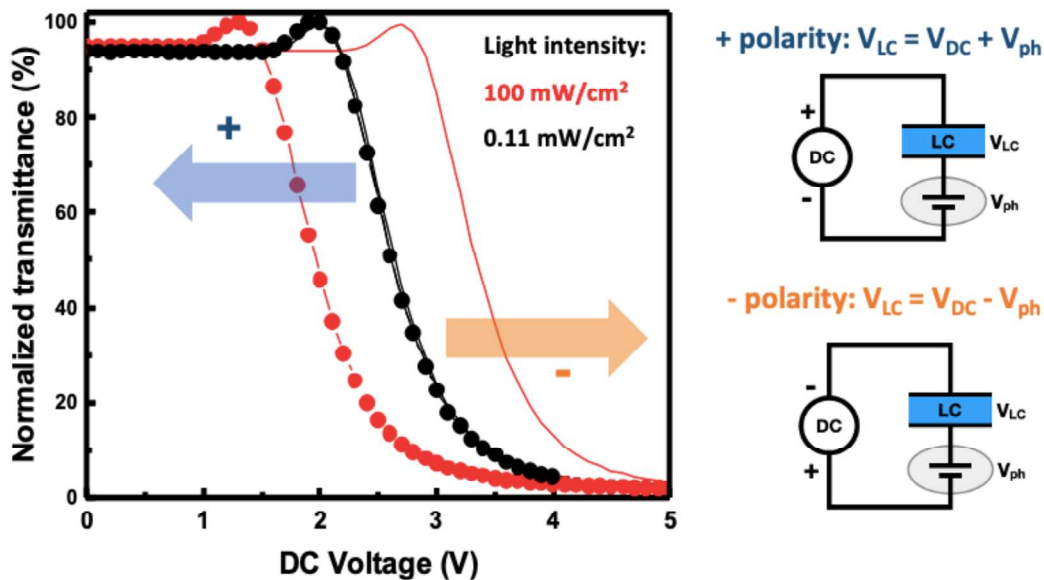
Figure 12. *Normalized transmittance as a function of DC voltage for a P3HT/ICBA based PSLM device measured under various light intensities and DC voltage polarities (including positive polarity + and negative polarity-). The normalized transmittance is estimated as a ratio of transmittance in ON state over maximum transmittance. Reproduced from[48].*

3.3.3 Self-powered PSLM

To achieve a self-powered PSLM device, the photovoltage delivered by the BHJ should be larger than the threshold voltage of the LC molecules. Based on this requirement, two solutions were proposed as follows: I) using organic multilayers that generate larger photovoltages; II) selecting a nematic LC with lower Fréedericksz transition voltage. The photovoltage was increased by introducing a tandem structure composed of two identical BHJ layers in series. For instance, solar cells based on the P3HT/ICBA (**Figure 13a**) with such a tandem structure (**Figure 13b**) can produce a V_{oc} of 1.45 V, much higher than a single structure (0.83 V). Another option is to keep a single structure but employ D and A materials capable of producing a higher V_{oc}, such as PM6/ICBA. PM6 is a fluorinated low-bandgap polymer (**Figure 13a**), that can be blended with ICBA to achieve a solar cell with a $V_{oc} \approx 1$ V. In addition, QYTN004 LC molecules were used in self-powered PSLM owing to its low threshold voltage (0.64 V).
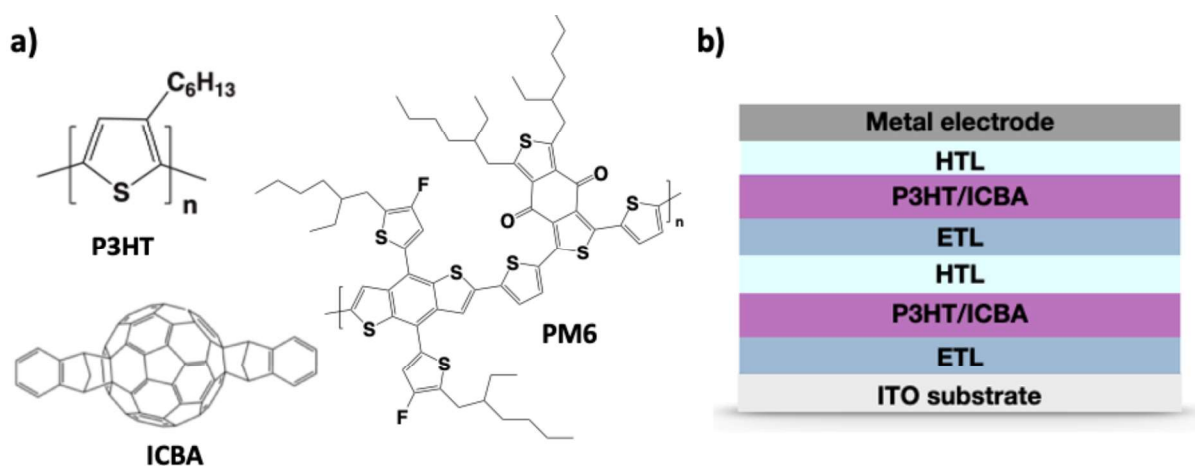
Figure 13. *a) Chemical structures of donors (P3HT and PM6) and ICBA acceptor. b) Schematic illustration of an OSC based on the P3HT/ICBA tandem structure.*

Figure 14a,b depict the normalized transmittance of PSLM devices based on a tandem P3HT/ICBA and on a single PM6/ICBA as a function of incident light intensity. In parallel, the photovoltages delivered by different BHJ layers under various light intensities were estimated by measuring the voltage drop occurring between the two ITO substrates in the OFF state. Both figures show that the photovoltages increase with light intensity and exceed the threshold value at high enough intensities. As expected, the LC molecules start to change the orientation for $V_{ph} > 0.84$ V, leading to a drop in transmittance. The response of a PSLM based

on a single PM6/ICBA layer shows a lower threshold voltage compared to that of PSLM based on a tandem structure, probably due to different LC anchoring strengths on top of the PV multilayers. The results indicate that both types of PSLMs are self-powered and the photovoltages delivered by BHJ layers are able to induce the LC homeotropic orientation under light intensity of 100 mW/cm^2 (i.e., one sun irradiance)

In order to further achieve user-controlled PSLM operation, a variable resistor R_s can be inserted and connected in series with a PSLM device, playing a role of a 'voltage divider' (**Figure 14c**). One fraction of the generated photovoltage drops across R_s, while the remaining fraction drops across the LC layer, impacting the LC orientation. Hence, users can obtain their preferred transmittance (from ~0% to maximum transmittance of PSLM in the OFF state, e.g., an AVT of 9% for PM6-based PSLM) of this device by adjusting the magnitude of the resistance R_s under sun illumination.

Switching speed is another key parameter to describe smart glazing technology performance. The response time of a PSLM has been investigated by measuring its transmittance switching between OFF state and ON state under a constant illumination. For a single junction PM6/ICBA based PSLM device, the normalized transmittance decreases from 90% to 10% after 540 ms and vice versa after 2.2 s. Furthermore, the response of the device remains stable during at least 150 ON/OFF cycles under one sun illumination, showing a good reversibility (**Figure 14d**). Comparing to the other reported user-controlled dynamic glazing including EC, PC and TC devices (Chapter 2), our PSLM devices are much faster.
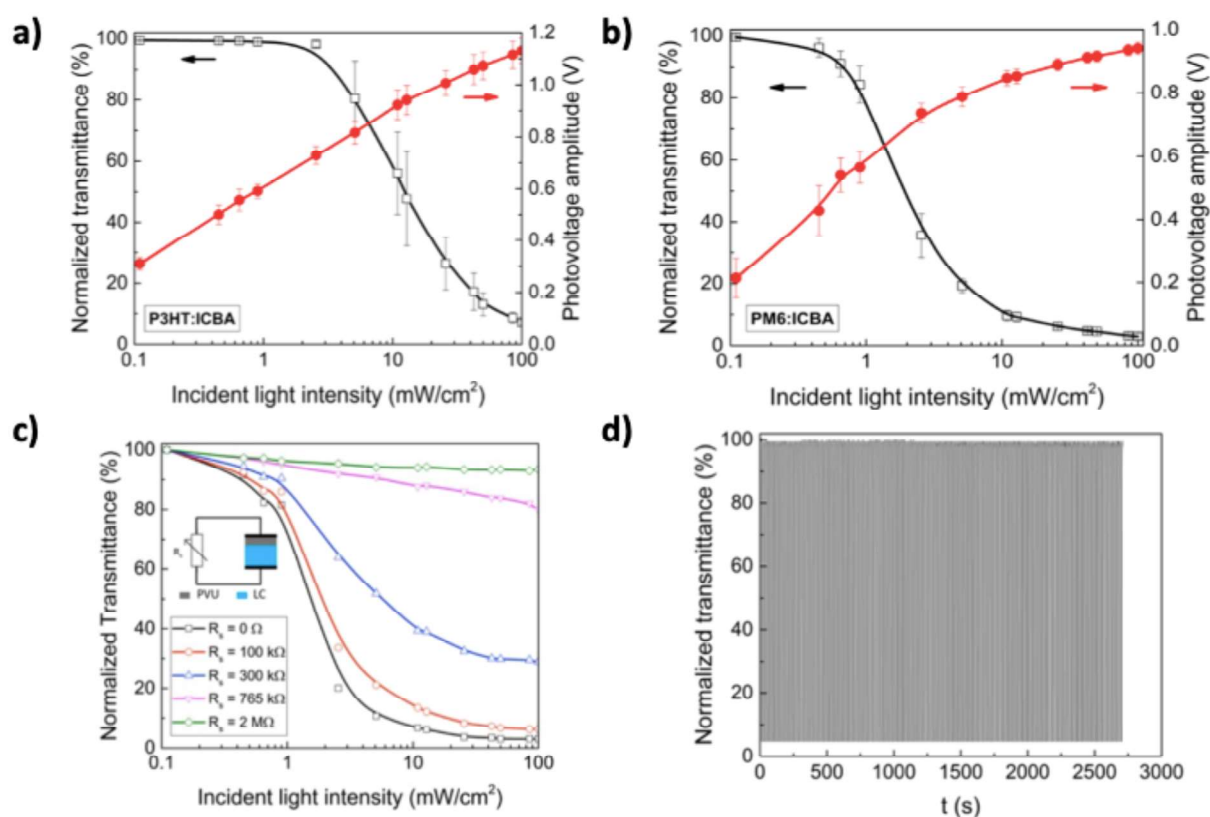
Figure 14. *Normalized transmittance (black lines) in ON state and photovoltage measured in OFF state as a function of incident light intensities for a) a PSLM device based on P3HT/ICBA tandem structure and b) a PM6-based PSLM. c) Normalized transmittance of PM6-based PSLM versus light intensities, with different resistors inserted between both ITO contacts. d) Normalized transmittance of PM6-based PSLM during periodic switching at least 150 ON/OFF cycles. Adapted from[48]*

It is important to point out that the wavelength range for which the transmittance of PSLM can be modulated is dependent on the polarizers. **Figure 15** shows the transmittance of two polarizers in parallel (black lines) and in perpendicular (red lines) without PSLM, as well as the spectral responses of a PM6-based PSLM using different polarizers, measured by switching between the OFF (blue lines) and ON states (green lines) upon illumination. The wire-grid polarizers (**Figure 15a**) are capable of operating both in the visible and near-infrared (NIR) regions, permitting an autonomous transmittance modulation of the PSLM in the same spectral range. Whereas flexible plastic polarizers (**Figure 15b**) that can only operate in the range of 400~800 nm, restrict the optical modulation of the PSLM to the visible range. Thus, the spectral response of a PSLM can be modified by changing the polarizers. More interestingly, using wire-grid polarizers allows the NIR transmittance of PSLM decreasing from around 20%

to less than 1%. This result demonstrates that PSLMs are promising devices for smart windows applications to reduce solar heating and improve the energy efficiency of buildings.
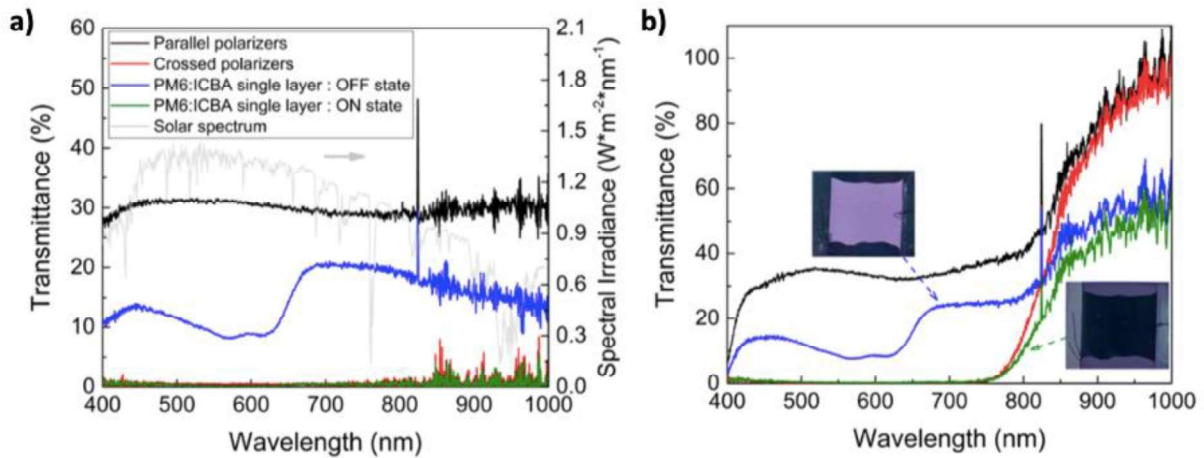
Figure 15. *Transmittance of PM6/ICBA based PSLM in OFF state (blue lines) and ON state (green line) using a) wire-grid polarizers and b) flexible plastic polarizers. The grey line shows a solar spectrum. The reference corresponds to the transmittance of two polarizers which are perpendicular (red lines) and parallel (black lines). Reproduced from[48]*

3.4 Scientific challenges

The PSLM devices have an autonomous operation with a fast response time and good reversibility. Their transmittance can be also easily tuned to fulfil the user's requirements, as shown in **Figure 14c**. However, there are still some bottlenecks to be overcome before PSLMs can be applied as smart windows. The scientific and technical challenges can be mainly classified into three points: I) better control of the LC/AL interface; II) lower impact of ionic contamination in the LC layer, which have a detrimental effect on the long-term stability of PSLMs and III) Higher transparency of PSLMs in the OFF state.

I) LC/AL interface: The optical-electro properties of a PSLM are influenced by the pre-tilt angle between the LC molecules and the AL. The pre-tilt angle can lower the threshold voltage and induce a faster response time. On the other hand, the transmittance of the device in the OFF state is impacted by a large pre-tilt angle. The pre-tilt angle depends on the intermolecular interactions between AL and LC layers, which in turn are influenced by the rubbing process. It is important to prepare the AL in a reproducible manner that controls surface roughness and orientation. In this context, our collaborator Nicolas Brouckaert from the university of

Southampton has developed a model to extract spatially resolved pre-title angles from cross-polarizer intensity measurements. Such data are necessary to better understand the correlation between pre-tilt angle and the nature of AL, and will contribute to a better control of the LC/AL interface.

II) LC ionic conductivity: It is well known that the LC layer commonly possesses residual ions. Even highly purified LC might get ion contamination from adhesives and AL during PSLM fabrication. When a DC voltage is applied to the PSLM, ions will drift towards the electrodes, leading to charge accumulation at the AL/LC interface that screens the electric field. This results in a hysteresis effect in the response of the PSLM. Since residual ions are known to have a negative effect on the long-term stability of LC devices, several methods have been suggested to reduce ion contamination or accumulation at the interfaces. For example, nanoparticles can be added into the LC layer to trap ions and decrease the ionic conductivity.[50] Another possibility, which is currently explored at ICUBE, consists in using semi-conducting AL layers. It has indeed been observed that these layers are able to neutralize the accumulated ions and thus considerably attenuate the impact of the ions on the PSLM response. The underlying mechanism remains however unclear and is the topic of on-going research at ICUBE.

III) Low transparency in the OFF state: As depicted in **Figure 15**, one major bottleneck of PSLM is their low transmittance in the visible range in the OFF state. The external polarizers of a PSLM absorb more than 50% of the incident light, while only the transmittance of the remaining part can be modulated by the PSLM. Moreover, part of the remaining light is absorbed by the AL and BHJ layers to generate the photovoltage, ultimately leading to a maximum transmittance in the OFF state of less than 20%. Thus, the optical absorptions of the polarizers, BHJ and AL have a strong impact on the transparency in the OFF state. An ideal AL used for a PSLM should be fully transparent, have a LC-orienting ability, and allow the neutralization of residual ions in the LC layer. Numerous studies and investigations are still required to identify the most suitable ALs to be integrated into PSLMs.

In this thesis, we focused only on optimizing the BHJ and polarizers to enhance the transmittance of PSLMs in the OFF state.

3.5 Context of the thesis

The transparency of PSLMs can be improved by I) selecting the BHJ that limit photon

absorption to the near UV; II) using oriented photovoltaic materials as "internal polarizer", to avoid the use of external polarizers (the BHJ with anisotropic optical properties is expected to polarize the incident light and also convert the absorbed light to a photovoltage); and III) investigating polarizers that operate in the IR range and show high transmittance in the visible region (**Figure 16**). Ideally, the PSLM should be transparent in the visible range, absorbing the UV light for self-powered operation, while controlling NIR light.
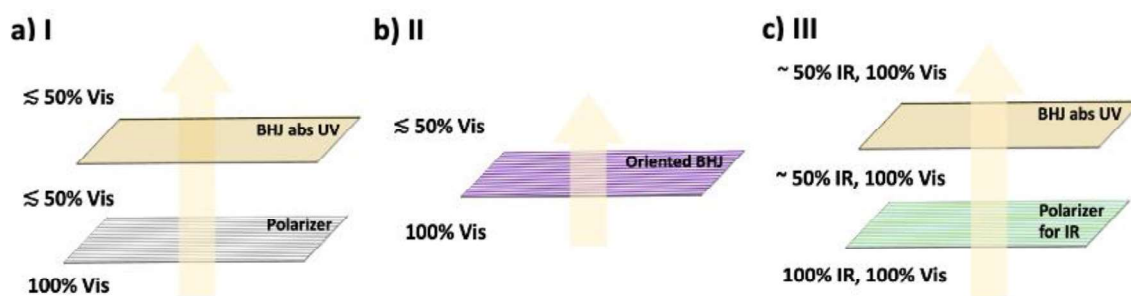
Figure 16. *Schematic representation for various methods to improve the transparency of PSLM: a) Selecting high band gap materials, b) Orienting the BHJ and c) Using IR polarizers.*

In order to achieve a more transparent PSLM according to method (I), we selected and investigated a new small molecular donor with a wide bandgap that limits optical absorption to the near UV range. The results will be discussed in the next chapter.

References

(1) Huang, J.; Lee, J.; Vollbrecht, J.; Brus, V. V.; Dixon, A. L.; Cao, D. X.; Zhu, Z.; Du, Z.; Wang, H.; Cho, K.; Bazan, G. C.; Nguyen, T. A High-Performance Solution-Processed Organic Photodetector for Near-Infrared Sensing. *Adv. Mater.* **2020**, *32* (1), 1906027.

(2) Wu, Y.; Fukuda, K.; Yokota, T.; Someya, T. A Highly Responsive Organic Image Sensor Based on a Two-Terminal Organic Photodetector with Photomultiplication. *Adv. Mater.* **2019**, *31* (43), 1903687.

(3) Durban, M. M.; Kazarinoff, P. D.; Luscombe, C. K. Synthesis and Characterization of Thiophene-Containing Naphthalene Diimide n-Type Copolymers for OFET Applications. *Macromolecules* **2010**, *43* (15), 6348–6352.

(4) Tao, J.; Sun, W.; Lu, L. Organic Small Molecule Semiconductor Materials for OFET-Based Biosensors. *Biosens. Bioelectron.* **2022**, *216*, 114667.

(5) Salehi, A.; Fu, X.; Shin, D.; So, F. Recent Advances in OLED Optical Design. *Adv. Funct. Mater.* **2019**, *29* (15), 1808803.

(6) Wöhrle, D.; Meissner, D. Organic Solar Cells. *Adv. Mater.* **1991**, *3* (3), 129–138.

(7) Xue, R.; Zhang, J.; Li, Y.; Li, Y. Organic Solar Cell Materials toward Commercialization. *Small* **2018**, *14* (41), 1801793.

(8) Bubnova, O. *Thermoelectric Properties of Conducting Polymers*; Department of Science and Technology, Linköping University: Norrköping, 2013.

(9) Kroon, R.; Mengistie, D. A.; Kiefer, D.; Hynynen, J.; Ryan, J. D.; Yu, L.; Müller, C. Thermoelectric Plastics: From Design to Synthesis, Processing and Structure–Property Relationships. *Chem. Soc. Rev.* **2016**, *45* (22), 6147–6164.

(10) Dyer-Smith, C.; Nelson, J.; Li, Y. Organic Solar Cells. In *McEvoy's Handbook of Photovoltaics*; Elsevier, 2018; pp 567–597.

(11) Knupfer, M. Exciton Binding Energies in Organic Semiconductors. *Appl. Phys. A* **2003**, *77* (5), 623–626.

(12) Clarke, T. M.; Durrant, J. R. Charge Photogeneration in Organic Solar Cells. *Chem. Rev.* **2010**, *110* (11), 6736–6767.

(13) Tang, C. W. Two-layer Organic Photovoltaic Cell. *Appl. Phys. Lett.* **1986**, *48* (2), 183–185.

(14) Tremel, K.; Fischer, F. S. U.; Kayunkid, N.; Pietro, R. D.; Tkachov, R.; Kiriy, A.; Neher, D.; Ludwigs, S.; Brinkmann, M. Charge Transport Anisotropy in Highly Oriented Thin Films of the Acceptor Polymer P(NDI2OD-T2). *Adv. Energy Mater.* **2014**, *4* (10), 1301659.

(15) Hamidi-Sakr, A.; Biniek, L.; Fall, S.; Brinkmann, M. Precise Control of Lamellar Thickness in Highly Oriented Regioregular Poly(3-Hexylthiophene) Thin Films Prepared by High-Temperature Rubbing: Correlations with Optical Properties and Charge Transport. *Adv. Funct. Mater.* **2016**, *26* (3), 408–420.

(16) Xue, X.; Chandler, G.; Zhang, X.; Kline, R. J.; Fei, Z.; Heeney, M.; Diemer, P. J.; Jurchescu, O. D.; O'Connor, B. T. Oriented Liquid Crystalline Polymer Semiconductor Films with Large Ordered Domains. *ACS Appl. Mater. Interfaces* **2015**, *7* (48), 26726–26734.

(17) Kuwabara, T.; Nakayama, T.; Uozumi, K.; Yamaguchi, T.; Takahashi, K. Highly Durable Inverted-Type Organic Solar Cell Using Amorphous Titanium Oxide as Electron Collection Electrode Inserted between ITO and Organic Layer. *Sol. Energy Mater. Sol. Cells* **2008**, *92* (11), 1476–1482.

(18) Waldauf, C.; Morana, M.; Denk, P.; Schilinsky, P.; Coakley, K.; Choulis, S. A.; Brabec, C. J. Highly Efficient Inverted Organic Photovoltaics Using Solution Based Titanium Oxide as Electron

Selective Contact. *Appl. Phys. Lett.* **2006**, *89* (23), 233517.

(19) Wang, D. H.; Choi, D.-G.; Park, O. O.; Park, J. H. Solution-Processable Polymer Based Photovoltaic Devices with Concentration Graded Bilayers Made via Composition Control of a Poly(3-Hexylthiophene)/[6,6]-Phenyl C61-Butyric Acidmethyl Ester. *J. Mater. Chem.* **2010**, *20* (23), 4910.

(20) Liang, Z.; Zhang, Q.; Jiang, L.; Cao, G. ZnO Cathode Buffer Layers for Inverted Polymer Solar Cells. *Energy Environ. Sci.* **2015**, *8* (12), 3442–3476.

(21) Tao, C.; Ruan, S.; Zhang, X.; Xie, G.; Shen, L.; Kong, X.; Dong, W.; Liu, C.; Chen, W. Performance Improvement of Inverted Polymer Solar Cells with Different Top Electrodes by Introducing a MoO3 Buffer Layer. *Appl. Phys. Lett.* **2008**, *93* (19), 193307.

(22) Shaw, P. E.; Ruseckas, A.; Samuel, I. D. W. Exciton Diffusion Measurements in Poly(3-Hexylthiophene). *Adv. Mater.* **2008**, *20* (18), 3516–3520.

(23) Menke, S. M.; Holmes, R. J. Exciton Diffusion in Organic Photovoltaic Cells. *Energy Env. Sci* **2014**, *7* (2), 499–512.

(24) Mikhnenko, O. V.; Blom, P. W. M.; Nguyen, T.-Q. Exciton Diffusion in Organic Semiconductors. *Energy Environ. Sci.* **2015**, *8* (7), 1867–1888.

(25) Abdulrazzaq, O. A.; Saini, V.; Bourdo, S.; Dervishi, E.; Biris, A. S. Organic Solar Cells: A Review of Materials, Limitations, and Possibilities for Improvement. *Part. Sci. Technol.* **2013**, *31* (5), 427–442.

(26) Yu, G.; Gao, J.; Hummelen, J. C.; Wudl, F.; Heeger, A. J. Polymer Photovoltaic Cells: Enhanced Efficiencies via a Network of Internal Donor-Acceptor Heterojunctions. *Science* **1995**, *270* (5243), 1789–1791.

(27) Genene, Z.; Mammo, W.; Wang, E.; Andersson, M. R. Recent Advances in N-Type Polymers for All-Polymer Solar Cells. *Adv. Mater.* **2019**, *31* (22), 1807275.

(28) Zhang, Y.; Chen, L.; Hu, X.; Zhang, L.; Chen, Y. Low Work-Function Poly(3,4-Ethylenedioxylenethiophene): Poly(Styrene Sulfonate) as Electron-Transport Layer for High-Efficient and Stable Polymer Solar Cells. *Sci. Rep.* **2015**, *5* (1), 12839.

(29) Zhou, Y.; Fuentes-Hernandez, C.; Shim, J.; Meyer, J.; Giordano, A. J.; Li, H.; Winget, P.; Papadopoulos, T.; Cheun, H.; Kim, J.; Fenoll, M.; Dindar, A.; Haske, W.; Najafabadi, E.; Khan, T. M.; Sojoudi, H.; Barlow, S.; Graham, S.; Brédas, J.-L.; Marder, S. R.; Kahn, A.; Kippelen, B. A Universal Method to Produce Low–Work Function Electrodes for Organic Electronics. *Science* **2012**, *336* (6079), 327–332.

(30) Shockley, W.; Queisser, H. J. Detailed Balance Limit of Efficiency of *P-n* Junction Solar Cells. *J. Appl. Phys.* **1961**, *32* (3), 510–519.

(31) Yuan, J.; Zhang, C.; Qiu, B.; Liu, W.; So, S. K.; Mainville, M.; Leclerc, M.; Shoaee, S.; Neher, D.; Zou, Y. Effects of Energetic Disorder in Bulk Heterojunction Organic Solar Cells. *Energy Environ. Sci.* **2022**, *15* (7), 2806–2818.

(32) Elumalai, N. K.; Uddin, A. Open Circuit Voltage of Organic Solar Cells: An in-Depth Review. *Energy Environ. Sci.* **2016**, *9* (2), 391–410.

(33) Qi, B.; Wang, J. Fill Factor in Organic Solar Cells. *Phys. Chem. Chem. Phys.* **2013**, *15* (23), 8972.

(34) Jao, M.-H.; Liao, H.-C.; Su, W.-F. Achieving a High Fill Factor for Organic Solar Cells. *J. Mater. Chem. A* **2016**, *4* (16), 5784–5801.

(35) Yu, J.; Zang, Y.; Li, H.; Huang, J. Fill Factor Enhancement of Organic Solar Cells Based on a Wide Bandgap Phosphorescent Material and C60. *Thin Solid Films* **2012**, *520* (21), 6653–6657.

(36) Stubhan, T.; Li, N.; Luechinger, N. A.; Halim, S. C.; Matt, G. J.; Brabec, C. J. High Fill Factor Polymer Solar Cells Incorporating a Low Temperature Solution Processed WO$_3$ Hole Extraction Layer. *Adv.*

Energy Mater. **2012**, *2* (12), 1433–1438.

(37) Stubhan, T.; Ameri, T.; Salinas, M.; Krantz, J.; Machui, F.; Halik, M.; Brabec, C. J. High Shunt Resistance in Polymer Solar Cells Comprising a MoO3 Hole Extraction Layer Processed from Nanoparticle Suspension. *Appl. Phys. Lett.* **2011**, *98* (25), 253308.

(38) Stubhan, T.; Salinas, M.; Ebel, A.; Krebs, F. C.; Hirsch, A.; Halik, M.; Brabec, C. J. Increasing the Fill Factor of Inverted P3HT:PCBM Solar Cells Through Surface Modification of Al-Doped ZnO via Phosphonic Acid-Anchored C60 SAMs. *Adv. Energy Mater.* **2012**, *2* (5), 532–535.

(39) Bisoyi, H. K.; Li, Q. Liquid Crystals: Versatile Self-Organized Smart Soft Materials. *Chem. Rev.* **2022**, *122* (5), 4887–4926.

(40) Andrienko, D. Introduction to Liquid Crystals. *J. Mol. Liq.* **2018**, *267*, 520–541.

(41) Thomas, R. Optically addressed light modulators using an organic photovoltaic layer.

(42) Schadt, M.; Helfrich, W. VOLTAGE-DEPENDENT OPTICAL ACTIVITY OF A TWISTED NEMATIC LIQUID CRYSTAL. *Appl. Phys. Lett.* **1971**, *18* (4), 127–128.

(43) Nemoto, F.; Nishiyama, I.; Takanishi, Y.; Yamamoto, J. Anchoring and Alignment in a Liquid Crystal Cell: Self-Alignment of Homogeneous Nematic. *Soft Matter* **2012**, *8* (45), 11526.

(44) Kirsch, P.; Bremer, M. Nematic Liquid Crystals for Active Matrix Displays: Molecular Design and Synthesis. *Angew. Chem.* **2000**, *39* (23), 4216–4235.

(45) Geary, J. M.; Goodby, J. W.; Kmetz, A. R.; Patel, J. S. The Mechanism of Polymer Alignment of Liquid-crystal Materials. *J. Appl. Phys.* **1987**, *62* (10), 4100–4108.

(46) Cheng, J.; Boyd, G. D. The Liquid-crystal Alignment Properties of Photolithographic Gratings. *Appl. Phys. Lett.* **1979**, *35* (6), 444–446.

(47) Berreman, D. W. Solid Surface Shape and the Alignment of an Adjacent Nematic Liquid Crystal. *Phys. Rev. Lett.* **1972**, *28* (26), 1683–1686.

(48) Fall, S.; Wang, J.; Regrettier, T.; Brouckaert, N.; Ibraikulov, O. A.; Leclerc, N.; Lin, Y.; Elhaj, M. I.; Komitov, L.; Lévêque, P.; Zhong, Y.; Brinkmann, M.; Kaczmarek, M.; Heiser, T. Self-Powered Dynamic Glazing Based on Nematic Liquid Crystals and Organic Photovoltaic Layers for Smart Window Applications. *ACS Appl. Mater. Interfaces* **2023**, *15* (3), 4267–4274.

(49) Kawamoto, H. The History of Liquid-Crystal Displays. *Proc. IEEE* **2002**, *90* (4), 460–500.

(50) Garbovskiy, Y.; Glushchenko, I. Nano-Objects and Ions in Liquid Crystals: Ion Trapping Effect and Related Phenomena. *Crystals* **2015**, *5* (4), 501–533.

Chapter 4. Semi-transparent organic photovoltaics

4.1 Motivation

High band gap organic materials have been developed to enhance the transmittance of solar cells.[1,2] Moreover, larger band-gaps are expected to yield higher V_{oc}. Therefore, integrating such materials into PSLMs should improve the transparency and sensitivity of the devices. It is important to note that V_{oc} is the most crucial parameter for an autonomous operation of PSLM, the photocurrent and fill-factor being only essential to the device response time. In other words, a PSLM does not require photovoltaic layers that show photovoltaic performance at the state-of-the-art, leading to a greater choice of materials suitable for PSLMs.

In this chapter, the fabrication and properties of a semi-transparent PSLM using a photovoltaic layer composed of a small molecular donor TAT-Cbz and an electron acceptor $PC_{60}BM$, that exhibit a moderate PCE but rather high V_{oc} and high transparency in the visible, are reported. The transmittance and optical response of the devices will be investigated and compared to other PSLM devices.

4.2 State-of-the-art

In recent years, transparent organic solar cells (T-OSCs) have attracted more and more attention for many potential applications including smart window technologies, building-integrated photovoltaics and agro-photovoltaics.[3–5] The BHJ layer in T-OSCs is required to exhibit high transparency in the visible range. Therefore, the average visible transmittance (AVT) is one of the key parameters to evaluate the T-OSCs performance. It is defined as the brightness of T-OSC as perceived by human eyes, can be determined according to the following equation[6]:

$$AVT = \frac{\int T(\lambda)P(\lambda)S(\lambda)d\lambda}{\int P(\lambda)S(\lambda)d\lambda} \qquad Eq.\ 4\ .1$$

Where T is transmittance, P is the human eyes photonic response (380 nm-780 nm), S is solar radiance spectrum (AM 1.5G) and λ is the wavelength.

One of strategies followed to achieve efficient T-OSCs has been to use photoactive materials that harvest mostly either NIR or near ultraviolet (NIR) light. Since a high fraction (51%) of solar energy is located in the NIR range, the theoretical PCE produced by NIR absorbers can be as high as that of solar cells harvesting only visible light (**Figure 1**). [5] Sun et al recently reported

highly T-OSCs based on a polymer donor (PDTP-DFBT) and a non-fullerene acceptor (FOIC), both with low bandgaps (E_g <1.4 eV).[7] After optimizing the top electrode, the transparent device exhibited an AVT of 61.5% and a PCE of 3.5%. In addition, Durrant et al also fabricated a visibly transparent OSC using both NIR photon harvesting donor (DPP2T) and acceptor (IEICO-4F). This device with an ultrathin Ag top electrode (8 nm) displays a PCE of 5.7 % and a visible transmittance reaching 60%.[8] A higher PCE produced by NIR-absorbing OSC was reported by Zhan et al.[9] They used PTB7-Th polymer as donor and IHIC as acceptor, achieving a PCE of approximately 10% with an AVT of 36%. The NIR-absorbing OSCs has proven to not only show an acceptable transmittance (35~65%) in the visible range but also achieve a good PV efficiency (4~10%).
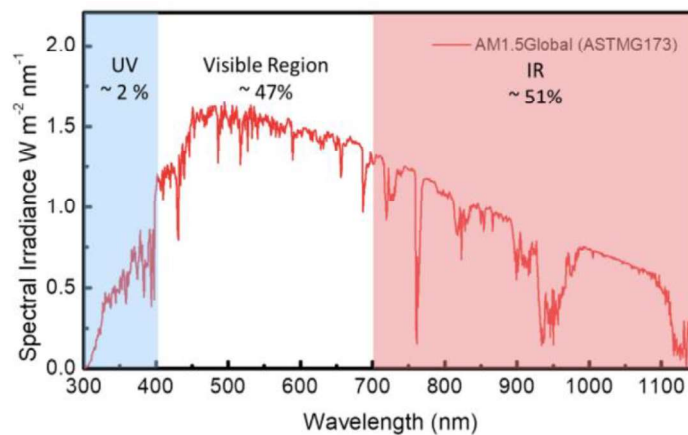
Figure 1. The solar emission spectrum and distribution of solar energy in different range including ultraviolet (UV), visible and infrared region. Reproduced from [5]

Although only 2% of solar energy is distributed within the UV range, making NUV absorbers to generate less charge carriers, they still have been regarded as promising materials for smart windows applications. Indeed, the target of controlled-natural heating smart windows such as PSLM devices is to dynamically regulate NIR light. As described in chapter 3, a PV layer in PSLM generates the electric field by absorbing one part of the incident light, while the remaining part of light passes through the LC layer, whose optical properties can be modulated. In other words, PSLM devices do not regulate the light absorbed by the PV layer. Selecting NUV absorbers for power generation ensures that all NIR light will not be absorbed by PV layers and can be controlled by the PSLM.

NUV photon harvesting solar cells are expected to yield high V_{oc} due to the wider band gaps.

Loo et al. reported NUV bilayer solar cells fabricated by thermal evaporation[1] and composed of contorted hexabenzocoronene derivatives are used as either donor (D) or acceptor (A1 or A2) and possess wide bandgaps (2.7~3.0 eV). The chemical structure of D, A1 and A2 are shown in **Figure 2a**. Their devices can generate large V_{oc} (1.63 V for D/A1 and 1.46 V for D/A2) and display high transmittance in the visible range (> 80% in **Figure 2b**), with PCE around 1.3~1.5%. It is worth mentioning that unlike NIR-absorbing solar cells, whose performance reduces with increasing area of solar cell, the performance of solar cells based on D/A1 remains unchanged even when the area is increased by an order of magnitude. The authors ascribed the scalability of the NUV solar cells to lower resistive power losses and the absence of pinholes in the amorphous active layer. The resistive power loss per unit area is proportional to R_s and J_m (i.e., current density at maximum-power point). Since NUV solar cell deliver higher voltages and lower currents than NIR devices, the resistive power losses are reduced.

Furthermore, Vandewal et al showed that a NUV solar cell based on the blend of high band gap BF-DPB donor and high band gap B4PYMPM acceptor (**Figure 2a**) generates a V_{oc} as high as 2 V.[2] This blend was deposited on the substrate through thermal evaporation. Using the same acceptor blended with NPB donor (**Figure 2a**), Spoltore et al reported a transparent OSC produces a V_{oc} of 1.96 V and exhibited an AVT of 60.3% with a PCE of 0.23%.[10]

To the best of my knowledge, the NUV photon harvesting PV layers with the appropriate energy levels can generally produce a higher photovoltage ($V_{oc} \leq 2$ V)[2] than that delivered by many NIR or visible light-absorbing OSCs ($V_{oc} \leq 1$ V).[11] Therefore, they should be promising materials used in PSLMs to achieve an autonomous operation and improve the transparency of devices. Nowadays, many current NUV solar cells were fabricated by thermal evaporation of active layers in a vacuum system.[1,2,10,12] In this work, we decided to use NUV BHJ that can be deposited from solution in order to keep the elaboration procedure of PSLM devices as simple as possible. TAT-Cbz small molecules with a wide bandgap were designed by STELORG consortium, which has high solubility in common organic solvents such as chloroform and methylene chloride.
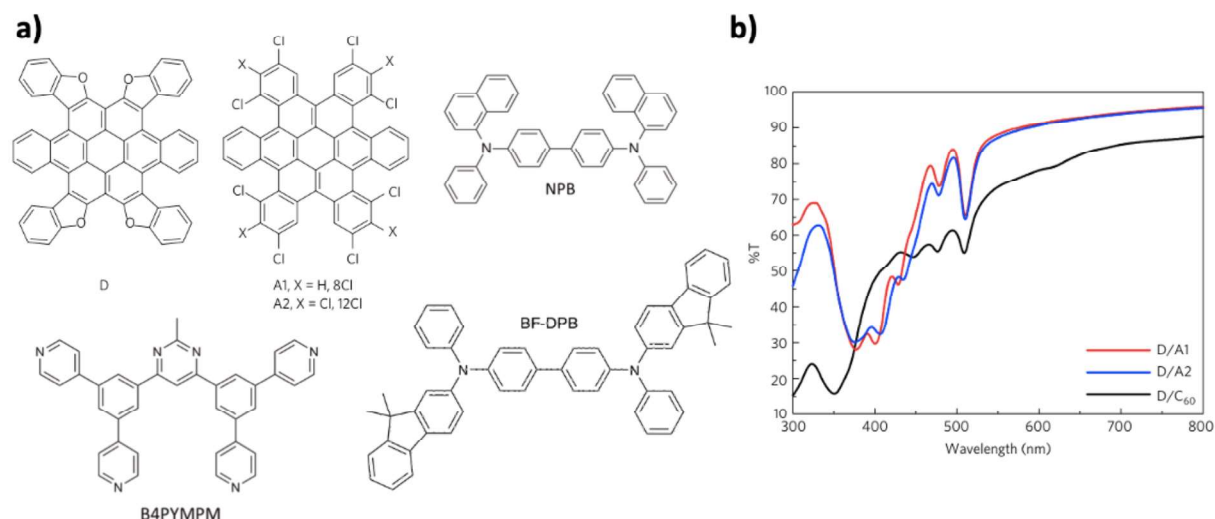
Figure 2. *a) Chemical structures of contorted hexabenzocoronene derivatives used as donor (D) and acceptors (A1 and A2) as well as other wide bandgap materials (B4PYMPM acceptors, NPB and BF-DPB donors).Reproduced from*[1,2,10] *b) Transmittance spectra of photoactive layers composed of D/A1 (red), D/A2 (blue) and D/C$_{60}$ (black). C$_{60}$ is a type of fullerene. The active layer D/C$_{60}$ is used as a reference to compare with the new wide bandgap materials D/A1 and D/A2. Adapted from*[1]

4.3 Materials and methods

High band gap material

A planar dumbbell-shaped molecular electron donor TAT-Cbz was designed and synthesized by Dr. Chaima Mahmoudi under the supervision of Dr. Nicolas Leclerc at Institute de chimie et procédés pour l'énergie, l'environnement et la santé (ICPPES). As illustrated in Figure 3, this small molecule consists of two triazatruxene (TAT) end-groups, bridged by a π-conjugated carbazole (Cbz) unit. The TAT unit contains three alkyl chains at nitrogen atoms, allowing the small molecule to have high solubility. Both TAT and Cbz are electron-donating groups, resulting in the absence of intermolecular charge transfer and thus forming a high bandgap.
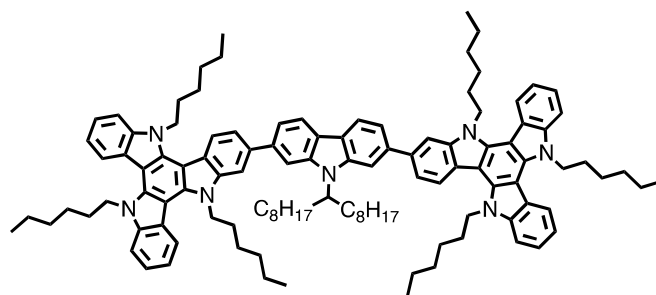
Figure 3. *Chemical structure of TAT-Cbz.*

Semi-transparent organic solar cell fabrication

The solar cells based on the TAT-Cbz were fabricated with a standard structure as follows: glass/patterned ITO/PEDOT:PSS/TAT-Cbz:PC$_{60}$BM/Ca/Al and an inverted structure as follows: glass/patterned ITO/PEIE/TAT-Cbz:PC$_{60}$BM/P30 or MoO$_3$/Ag. An example of inverted structure is illustrated in **Figure 4a**. The patterned ITO coated glass substrates were cleaned by soap, deionized water, acetone, and isopropyl alcohol, respectively, in ultrasonic bath at 45°C for 15 mins. After that, the patterned ITO substrates were further cleaned by UV ozone for 30 mins. For standard structure, a PEDOT: PSS (30~40 nm) layer was spin coated at 5000 rpm for 60 s. A part of the PEDOT:PSS film was removed with the water followed by an annealing step at 140 °C for 30 mins. For inverted structure, a PEIE (7~10 nm) layer was first deposited on the ITO substrate by spin coating at 5000 rpm for 60s, then cleaned with isopropyl alcohol from the part of substrate (**Figure 4a**) and finally thermal annealed at 100°C for 10min. The TAT-Cbz/PC$_{60}$BM (~142 nm) layer was spin-coated at 1000 rpm for 120 s from filtrated chloroform solution (TAT-Cbz:PC$_{60}$BM with a weight ratio of 2:3, total concentration of 15 mg/mL). The chloroform solution was stirred at room temperature for around 24 h. A part of the PV layer was removed with dichlorobenzene (**Figure 4a**). Both annealing step and deposition of BHJ were performed under a nitrogen atmosphere. The Ca (20 nm)/Al (120 nm) bilayers or MoO$_3$ (7 nm)/Ag (120 nm) bilayers were thermally evaporated on the top of BHJ in vacuum (pressure $\leq 1 \times 10^{-6}$ mbar). Each device possesses four diodes, and the active areas (12 mm^2) of each diode is well defined by a shadow mask during the J-V measurements. The photograph of TAT-Cbz-based OSC is illustrated in **Figure 4b**.
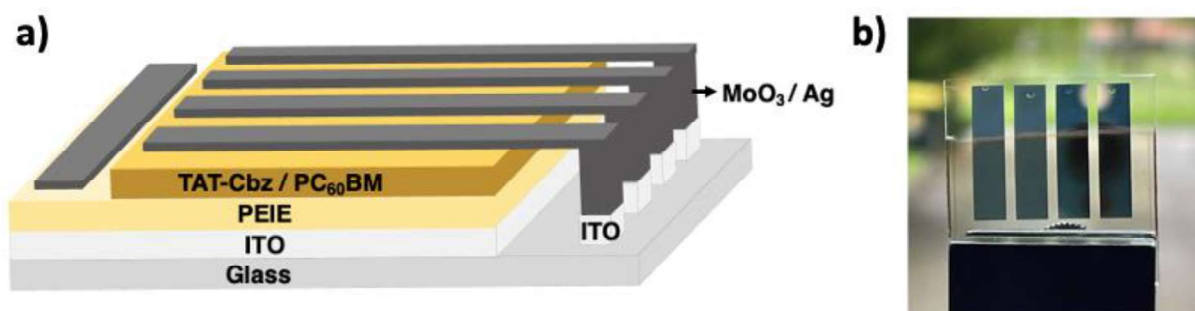
Figure 4. a) Schematic illustration of OSC based on the TAT-Cbz with an inverted structure and b) Photograph of this full OSC. The dark gray parts correspond to the sliver electrodes.

For these materials used in the fabrication of OSCs, $PC_{60}BM$ was purchased from Solenne B.V. and used as electron acceptor. PEIE as ETL was purchased from Sigma-Aldrich. P30 from Avantama is a product blended PEDOT: PSS with MoO_3, used as HTL. Other types of PEDOT: PSS formulations used for this chapter are AI4083 and HTL solar from Heraeus. Their chemical structures were shown in **Figure 5**. A commercial LC QYTN004 was purchased from Qingdao QY Liquid Crystal Co. The chloroform and chlorobenzene were purchased from Sigma-Aldrich. All the commercial organic materials were used as received. The adhesive for assembling process of PSLM was purchased from Cospheric. ITO-coated glass substrates with the surface of 2 x 2 cm^2 were purchased from Lumet.
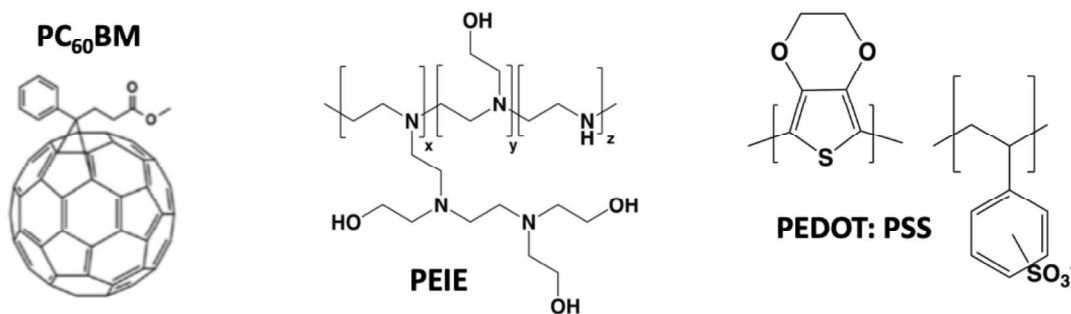
Figure 5. *Chemical structures of PCBM acceptors, PEIE (ETL) and PEDOT: PSS (HTL).*

PSLM devices based on the high band gap materials

The PSLM configuration based on TAT-Cbz is the following: glass/ITO/PEIE/TAT-Cbz: $PC_{60}BM$/P30/PEDOT: PSS/P3HT/LC/P3HT/ITO/glass. The cleaning step for the glass substrates coated with full ITO and the preparation of PEIE/TAT-Cbz: $PC_{60}BM$ layer are same as for the manufacturing of full solar cells, except that part of organic layers does not to be removed.

A thin layer of P30 was spin-coated at 4000 rpm for 120s on the top of active layer, followed by an HTL-solar PEDOT: PSS layer (100 nm) that was deposited at 4000 rpm. The film was dried in vacuum (pressure $\leq$ 1x10^{-7} mbar) for at least 3h. Then, a P3HT layer was spin coated at 4000 rpm from 5 mg/mL chlorobenzene solution and put the film again in vacuum overnight. This layer is used as liquid crystal alignment layer. Once the P3HT film is well dried, the sample was gently rubbed at room temperature by a commercial rubbing machine (Holmarc). The rubbing condition including rubbing cycles, rubbing pressure were explored to induce a high-quality LC alignment. The rubbing pressure between rotating cylinder and surface of films can be

adjusted by increasing or decreasing the height of a plate to support the film. This height can be progressively adjusted by "steps" and each "step" corresponds to few micrometers. A higher height results in a stronger applied force of rotating cylinder on the polymer films. A simple LC light valve (ITO/P3HT/LC/P3HT/ITO) was fabricated to determine the quality of LC alignment. We placed the device between two polarizers in parallel and in perpendicular. For crossed polarizers, if the LC molecules are well-aligned, a homogenously dark state can be observed.

The PSLM device was fabricated by assembling one part (glass/ITO/PEIE/TAT-Cbz: $PC_{60}BM$/P30/PEDOT: PSS/P3HT) with another part (glass/ITO/P3HT). A UV-curable adhesive mixed with 7.75 μm SiO_2 spacers was used to assemble the two parts, setting the thickness of LC layer. The rubbing directions of both P3HT layers are perpendicular to each other for creating a LC twisted configuration. In order to dry this adhesive, the device covered with a mask was placed under UV light for around 15 mins. The mask can effectively protect the organic layers and avoid their degradation. The cell was finally filled with LC by capillarity action, heated at 80°C for 2mins and then slowly cooled to room temperature. Except for rubbing and device assembling process, all the preparation steps of PSLM devices were achieved under nitrogen atmosphere.

Ultraviolet (UV)-visible spectroscopy

The UV-visible spectroscopy was used to measure quantitively the optical absorption or reflectance of materials in solution and in thin films. This technique generally consists of a radiation source, a monochromator, an adjustable sample holder and a photodetector. During the measurements, the monochromator disperses the light source so that the light of a given wavelength passes through the sample and reaches the detector. The UV-Vis spectrophotometer records the transmittance (T) as a function of wavelength, where T is defined as the ratio of transmitted light intensity at given wavelength (I) to the incident light intensity (I_0). If the reflectance and non-specular light diffusion are negligible, the absorbance (A) can be expressed by the following equation:

$$A = log_{10} \frac{I_0}{I}$$

Eq. 4. 2

Moreover, the optical bandgap ($E_{g, opt}$) can be estimated from the wavelength at the onset of absorption (λ_{onset}), using the following equation:

$$E_{g,opt} = \frac{hc}{\lambda_{onset}} \approx \frac{1240}{\lambda_{onset}}$$

Eq. 4. 3

Where h is plank constant (6.62×10^{-34} J.s), c is speed of light in vacuum (3×10^{8} m.s^{-1}).

The absorption spectra of TAT-Cbz in thin films and in solution were previously measured on a Shimadzu UV-2600 by Dr. Nicolas Leclerc.

Internal integrating sphere

The transmittance of TAT-Cbz/PC$_{60}$BM was measured using a Cary 5000 (Agilent) UV-Vis-NIR spectrophotometer equipped with an integrating sphere (Internal Diffuse Reflectance Accessory DRA 2500). The sample was placed in entrance port of integrating sphere and measured through a 1 x 1 cm^2 square aperture fixed on a homemade sample holder. The transmitted light is fully captured in the integrating sphere with an incidence angle of 3°. A glass substrate is used as reference. Transmission spectra are recorded in the range of 350 nm to 800 nm.

J-V characteristics measurements

The current-voltage characteristics measurement was performed in the dark and under illumination using a LabView-controlled Keithley 2400. The illumination is provided by an ABET Technologies Sun 3000 solar simulator equipped with an AM 1.5G filter. The illumination power (100 mW/cm^2) is calibrated via a reference silicon solar cell. The measurement is done under nitrogen atmosphere.

The photovoltaic parameters V_{oc}, J_{sc}, FF and PCE along with R_s and R_{sh} were estimated via a LabView software. The J-V curves of solar cells and the corresponding parameters are described in more detail in Chapter 3.

Switching time and transmittance of PSLMs

The switching time was measured using a set-up composed of the solar simulator as light source, two wire-grid polarizers (Thorlabs WP25L-VIS as the polarizer and WP25M-UB as the analyzer) oriented perpendicularly to each other, a silicon photodiode and a current pre-amplifier (**Figure 5**). During the measurements, the PSLM is placed between polarizer and analyzer. The optical axe of the polarizer was set parallel to the LC directors at the illuminated surface. When switching between the OFF state and the ON state, a change in transmittance as a function of time was monitored. The normalized transmittance is defined as a ratio of the current measured as a function of time and its value in the OFF state (prior to switching).
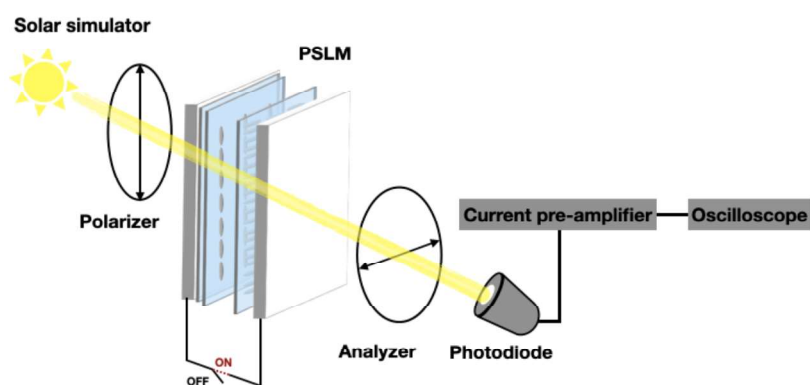
Figure 5. *Experimental set-up for the switching time measurements.*

The transmittance measurement was performed by using the same set-up, except for the photodiode and pre-amplifier, which were replaced by a spectrometer (BWTEK Inc) (**Figure 6**). The transmittance spectrum was recorded in the range of 400 to 1100 nm.
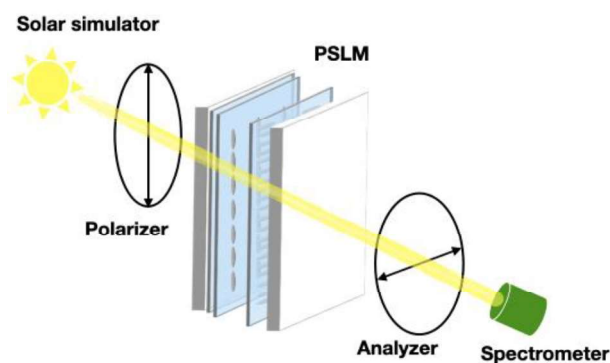
Figure 6. *Experimental set-up for transmittance measurements in the OFF state.*

4.4 Results and discussion

4.4.1 Optical properties of donors and photovoltaic layers

The UV-visible absorption spectra for TAT-Cbz in solution and in thin films are depicted in **Figure 7a**. Both spectra show several absorbance bands in NUV range only. In solution, the lower-energy absorption peak at around 382 nm can be assigned to the 0-0 transition, from HOMO to LUMO level, corresponding to the electron mainly delocalized over central carbazole and the surrounding indole units.[12] The second higher-energy absorption band at around 320 nm is attributed to the transition from the energy level below the HOMO to LUMO and the transition from HOMO to the energy level above the LUMO.[12] In thin films, the absorption spectra are slightly red-shifted (~12 nm) which can be ascribed to the intermolecular coupling in solid state. The bathochromic shift results in an onset of film absorption at 441 nm, corresponding to an energy band-gap of 2.8 eV for TAT-Cbz films.[12]
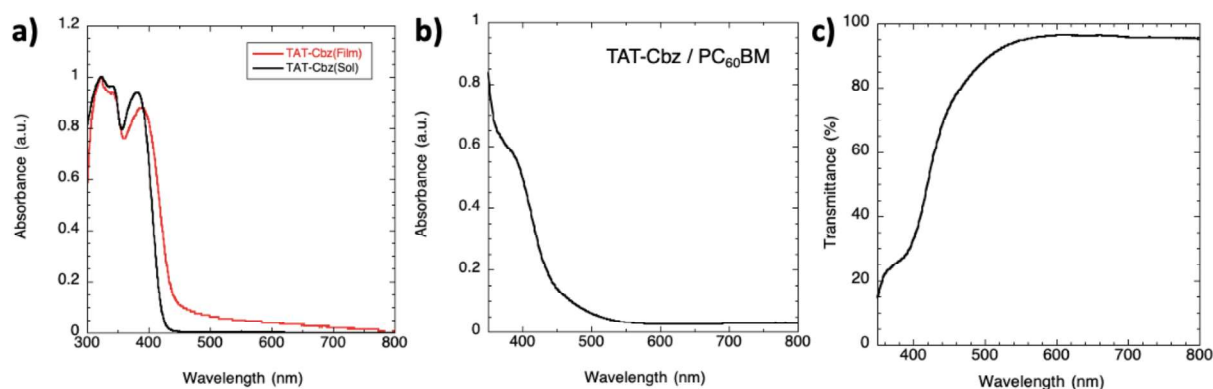
Figure 7. *a) Normalized UV-vis absorption spectra of TAT-Cbz in thin films (red) and in dichloromethane solution (black) with a concentration of 10^{-6} mol. L^{-1}. b) Absorption spectra of TAT-Cbz/$PC_{60}BM$ photoactive layers. The thickness of this film is (142±3) nm. c) Transmittance spectra of same PV layers in b).*

The NUV light harvesting BHJ was achieved by blending TAT-Cbz with $PC_{60}BM$ whose maximum absorption is also located in UV range. The absorption and transmittance spectra of the BHJ layer with a thickness of 142 nm are shown in **Figure 7b,c**. The most visible absorption only occurs at 400-500 nm. The results indicated that the photovoltaic layer is highly transparent in the visible region with an AVT of 86.4%.[12]

4.4.2 Photovoltaic properties

In order to determine the voltage that can be produced by TAT-Cbz and $PC_{60}BM$ in a PSLM device, full solar cells were fabricated with standard and inverted structures and characterized by J-V measurements (**Figure 8**). P30 containing PEDOT:PSS and MoO_3 will be used as HTL in PSLM. Therefore, an inverted structure of OSC with P30 was also measured. The important photovoltaic parameters are summarized in **Table 1**.

Table 1. Photovoltaic parameters of TAT-Cbz-based solar cell with standard and inverted structures.

	Solar cell configuration	V_{oc} (V)	J_{SC} (mA.cm^{-2})	FF (%)	PCE (%)
Inverted structure	**1.** ITO/PEIE/TAT-Cbz:PC$_{60}$BM/MoO$_3$/Ag	0.86±0.01	0.39±0.01	36±1	0.12±0.01
	2. ITO/PEIE/TAT-Cbz:PC$_{60}$BM/P30/Ag	0.83±0.01	0.42±0.01	35±1	0.12±0.01
Standard structure	**3.** ITO/PEDOT: PSS/TAT-Cbz:PC$_{60}$BM/Ca/Al	0.83±0.02	0.40±0.01	38±1	0.13±0.01
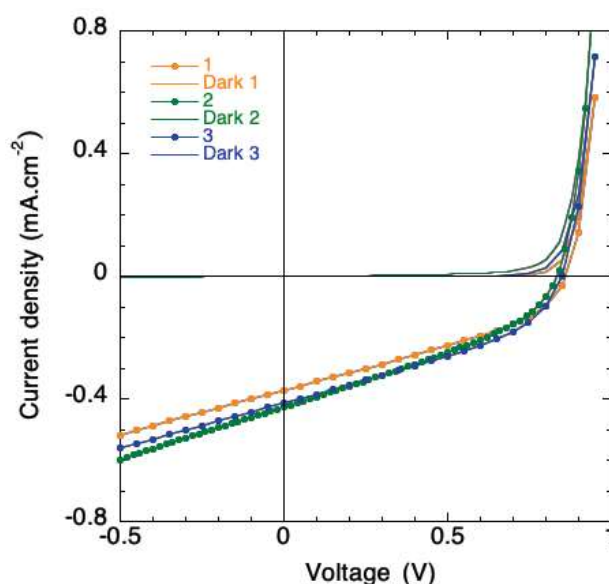
Figure 8. *J-V characteristics of solar cells based on TAT-Cbz/PC$_{60}$BM with inverted structures (orange and green) and standard structure (blue). The solar cells were measured in dark (lines) and upon AM 1.5G illumination (circles), respectively.*

We studied solar cells using both standard and inverted device structures, since several reports on fullerene-based BHJ solar cells have reported a vertical phase separation that can have a strong impact on the photovoltaic performances.[13,14,15,16] In the case of TAT-Cbz, the FF, J_{sc} and PCE are similar for both standard and inverted structures suggesting that TAT-Cbz and $PC_{60}PM$ domains are distributed homogenously along the vertical direction in the BHJ layer.

The rather low performance (PCE of 0.12~0.13%) is mainly caused by low J_{sc} and FF values. The former can be attributed in part to the limited photon absorption, while the latter points out poor charge collection, presumably due to low charge carrier mobility and/or carrier recombination. This is corroborated by the significant increase in current density observed under reverse bias. The strong dependence of photogenerated current density on the applied voltage represents inefficient charge extraction, which is in-line with measured low FF.

The V_{oc} is mainly related to the difference between HOMO level of TAT-Cbz and LUMO level of $PC_{60}BM$,[17] independently of the device structure. The V_{oc} generated by TAT-Cbz/$PC_{60}BM$ (0.83~0.86 V) is higher than the V_{th} of QYTN004 LC (0.64 V). Although the active layer does not exhibit a good photovoltaic performance, the V_{oc} is high enough to modify the LC orientation, fulfilling the requirements of self-powered PSLM devices. In order to achieve a semi-transparent PSLM, the high band gap materials will be integrated into the devices.

4.4.3 PSLMs based on TAT-Cbz

The PVU with an inverted structure ITO/PEIE/BHJ/PEDOT: PSS has been used in the fabrication of PSLMs. PEDOT: PSS is a transparent conducting polymer, which is not only extensively used as HTL but also is investigated as an electrode for organic devices.[18–21]In PSLMs, it can be regarded as a 'top electrode' with a lower conductivity relative to ITO electrode but is sufficient for PSLM operation. However, a conductive ETL is not still found to integrate into PSLMs, restricting the development of PSLMs based on the standard structure. For this reason, all the PSLMs we currently fabricate are of an inverted structure.

For fabrication of semi-transparent PSLM, P30 and HTL solar will be deposited on the BHJ layer followed by a thermal annealing to remove residual solvents. Therefore, the impact of thermal annealing on the photovoltage (V_{ph}) delivered by TAT-Cbz/$PC_{60}BM$ was first studied. The photovoltaic unit of PSLM was tested under different annealing temperatures by J-V measurements. The device preparation is similar to an uncompleted solar cell fabrication

lacking of the metal top electrode (**Figure 9**). The conductive PEDOT:PSS (HTL solar) as a "top electrode" is sufficient for the electrical contact. The photovoltage delivered by PV layer is independent on the surface of the device, thus it can be determined by J-V measurements. The average values corresponding to each condition were summarized in **Table 2**.

The V_{ph} decreases slightly with the annealing temperature up to 100°C and reduces more pronouncedly at 120°C. Possible reasons for the voltage loss are less charge generation (due to larger domain sizes) and/or interface degradation.[22,23] To avoid premature degradation of the photovoltaic unit, the HTL and AL (deposited on the top of the semi-transparent BHJ layer) were dried by storage under vacuum at room temperature instead of thermal annealing.

Table 2. Photovoltage of semi-transparent photovoltaic unit under different annealing conditions.

	Annealing condition	V_{ph} (V)
	-	0.85±0.01
	50°C for 10min	0.85±0.01
Photovoltaic unit of PSLM:	80°C for 10min	0.84±0.01
ITO/PEIE/TAT-Cbz:PC$_{60}$BM/P30/HTL Solar	100°C for 10min	0.84±0.01
	120°C for 10min	0.77±0.01
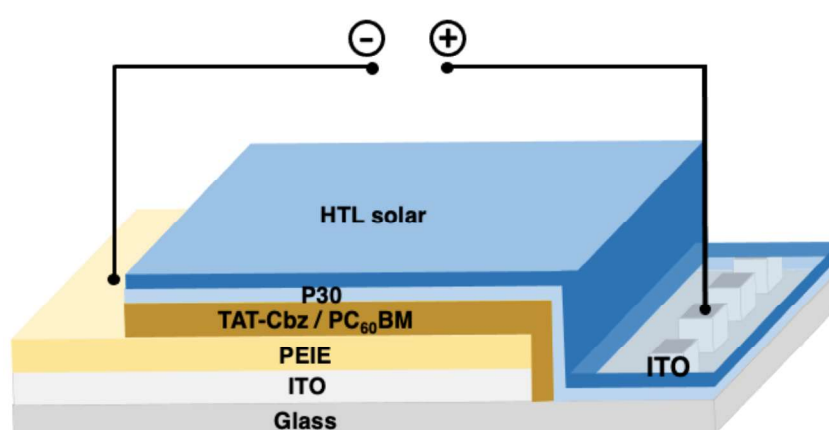
Figure 9. Schematic illustration of an uncompleted OSC lacking of the top electrode (with a cell configuration of glass/patterned ITO/PEIE/TAT-Cbz:PC$_{60}$BM/P30/HTL solar) measured by J-V measurements.

The semi-transparent PSLM architecture is illustrated in **Figure 10a**, which consists of semi-transparent PV unit, P3HT alignment layer and twisted LC molecules. The device was placed between two crossed polarizers. Under 1 sun illumination, the photovoltage was estimated to approximately 0.65 V, by measuring directly the voltage drop occurring between both ITO contacts in the OFF state. The reduced photovoltage, in comparison to V_{oc} of a full solar cell, is mainly due to the external polarizer, which reduces the light intensity reaching the BHJ.

The optical response of the PSLM was probed by switching between the ON state and the OFF state during illumination. The **Figure 10b** shows a drop of 32% in transmittance from the OFF state to the ON state, demonstrating that TAT-Cbz-based device can operate in a self-powered regime. The amplitude of the PSLM response is smaller in comparison to the other PSLM devices (based for instance on a tandem P3HT/ICBA or on a single PM6/ICBA photovoltaic unit), as a consequence of the lower photovoltage delivered by TAT-Cbz/PC_{60}BM, which is insufficient to induce the LC homeotropic orientation fully.

The semi-transparent PSLM can operate automatically even though TAT-Cbz based OSCs display low PV performance. However, does the low photocurrent have an influence on the response time? In order to better understand the correlation between the photocurrent on the response time of PSLM. We estimated the response time of semi-transparent PSLM and compared with that of PM6-based PSLM. The PM6-based OSCs (J_{sc} = 6.74 mA.cm^{-2}) are capable of producing a much higher photocurrent than that delivered by OSCs based on the TAT-Cbz (J_{sc} = 0.39 mA.cm^{-2}).

The response time of a PSLM can be defined as the time it takes for the device to switch from the maximum to the minimum transmittance (switching-on time) or vice versa (switching-off time). The switching-on time (~2.2 s) is much faster than the switching-off time (~98.5 s). This phenomenon was also observed in most LCD.[24–26] Since the device turns on by responding to the application of a voltage, while the applied electric field is removed, the LC molecules simply relaxes back to the initial state. The lower the anchoring force, the longer the switching OFF time can be.

In addition, the normalized transmittance decreases from 100% to 90% in 890 ms which is 22 times longer than for PM6-based device (40 ms).

The response time of a PSLM can be expected to be related to the transient current generated by the photoactive layers, which determines the time required to reach the maximum voltage drop across the LC layer. As shown in the inset of **Figure 10b**, a simplified electrical circuit

model of PSLM is composed of total impedances of ITO, AL, photovoltaic unit (Z_R) in series with the impedance of LC layer and the photocurrent (I_{ph}). The LC impedance consists of a capacitor (C) in parallel with a resistor (R_{LC}). The response time of PSLM is determined by the time (Δt) needed to charge the capacitor. For PSLMs that are fabricated using the same LC molecules and rubbing conditions, the amount of charge stored in the capacitor (ΔQ), corresponding to drop of 10% in transmittance, should be similar. We may write:

$$\Delta Q = \int_0^{\Delta t} I(t)dt \;\rightarrow\; \Delta t = \frac{\Delta Q}{\langle I \rangle} \qquad\qquad Eq.4.4$$

where *I(t)* is the photocurrent delivered by the photovoltaic unit once the device is switched to the ON state. While it is not straightforward to estimate the time-evolution of the current, it is reasonable to assume as a first approximation that its time-averaged value (*<I>*) is proportional the photocurrent delivered by the photovoltaic cell (based on the same BHJ) under short-circuit conditions. Thus, the larger the short-circuit current, the smaller Δt should be. This is corroborated by the ratio of the short-circuit currents delivered by both types of solar cells under AM1.5 illumination ($J_{sc\,(PM6)}$/ $J_{sc\,(TAT-Cbz)} \approx 17$) which matches roughly the inverse ratio of response times ($\Delta t_{TAT-Cbz}$/ $\Delta t_{PM6} = 22$)

Overall, we may conclude that the low photocurrent delivered by TAT-Cbz does not impede the self-powered operation of the devices, but results only in a long switching time.
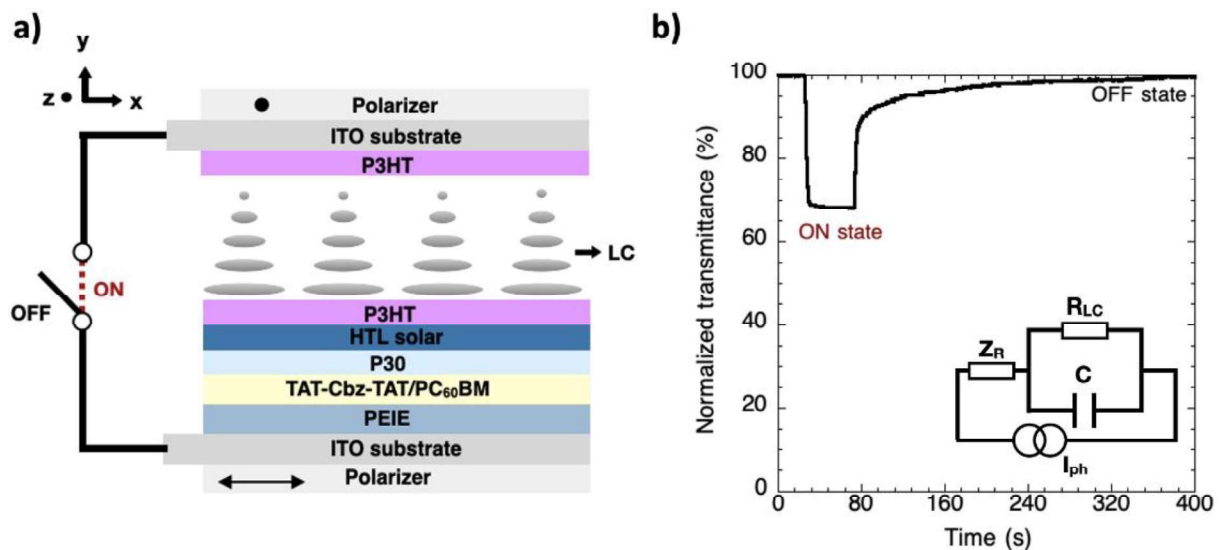
Figure 10. a) Schematic representation of semi-transparent PSLM based on high band gap materials. The device is placed between two mutually perpendicular polarizers. b) Normalized transmittance of semi-transparent PSLM switching between the OFF state and the ON state as a function of time. The inset is a simplified electric circuit model of PSLM.

Figure 11a depicts the transmittance spectra of PSLMs based on the different PV layers in the OFF state. The transmittance is fairly low for PSLM based on tandem structure that contains two PV multilayers in series. As results, more visible light is absorbed by tandem structure as compared to a single PV layer. The PSLM based on PM6/ICBA shows a minimum transmittance at around 600 nm, that corresponds to the maximum absorption of PM6 donor.[27] The results demonstrated that the transparency of PSLMs is strongly influence by the absorption of PV layers. Using the NUV absorbing PV layer TAT-Cbz/$PC_{60}BM$ leads to a significant improvement in transparency. The strong absorption between 500 and 650 nm is due to the P3HT polymer used as AL. The pictures of PSLMs based on the tandem structure and on the TAT-Cbz/$PC_{60}BM$ in the OFF state were given in Figure 10b, highlighting the higher transmittance in the visible range for TAT-Cbz-based PSLM.

According to the transmittance spectra, the AVT of PSLMs and of two polarizers in parallel were estimated by *eq.4.1*. The results corresponding the PSLMs based on various photovoltaic layers are summarized in **Table 3**. It is important to note that the maximum transmittance of a PSLM is currently limited to around 28% by the absorption of both external polarizers. The OFF-state transparency of a PSLM based on TAT-Cbz is significantly higher than that of PSLMs based on either PM6/ICBA or tandem P3HT/ICBA photovoltaic layers, as the AVT increases from 9% to 15%. Selecting a more transparent AL than P3HT can thus further improve the transparency of PSLMs. Moreover, using polarizers that operate only in the IR range while being more transparent in the visible (provided such polarizers exist), may also significantly improve the transmittance in the OFF state.

Table 3. AVT of two oriented parallel polarizers and PSLMs based on different photoactive layers in the OFF state.

	AVT (%)
Two polarizers in parallel	28.39
Tandem structure P3HT/ICBA	7.15
PM6/ICBA	9.24
TAT-Cbz/$PC_{60}BM$	14.87
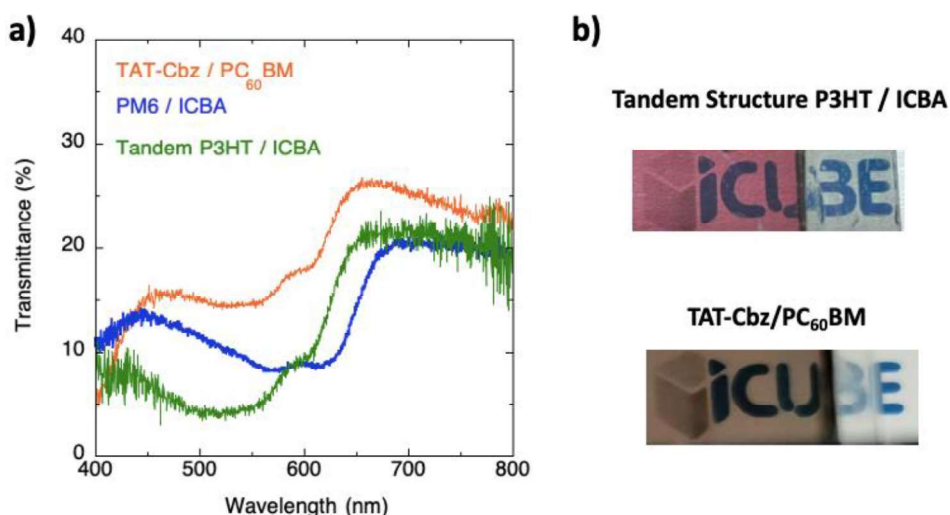
Figure 11. a) Transmission spectra of PSLMs based on high band gap materials (orange), P3HT/ICBA tandem structure (green) and PM6/ICBA (blue) in the OFF state. The PSLMs are placed between two crossed polarizers (Thorlabs WP25L-VIS and WP25M-UB). b) Photographs of PSLMs based on high band gap materials and P3HT/ICBA tandem structure with polarizers in the OFF state.

4.5 Conclusion

In this chapter, we have investigated the optical and photovoltaic properties of a new high band gap material TAT-Cbz and the optical response of PSLM device based on the high band gap materials. The PV layer composed of TAT-Cbz and $PC_{60}BM$ shows a high transmittance in the visible range. Using such highly transparent PV layer, the transparence of PSLMs in the OFF state was improved from 9% to 15%. The transmittance can be further improved by using more transparent alignment layer. In addition, the photovoltage delivered by TAT-Cbz/$PC_{60}BM$ is high enough to turn the LC orientation. We demonstrated that semi-transparent PSLM have a self-powered operation, even though the full solar cell based on TAT-Cbz exhibits low PCE (0.12-0.13 %). The V_{oc} is crucial for autonomous operation of PSLM.

Table 3 shows that external polarizers limit the transmitted light intensity of PSLM in the OFF state. As mentioned before (chapter 3), one of the methods for increasing the transmittance is to use an oriented BHJ that shows the highly anisotropic optical properties. Such anisotropic BHJ may play a role of 'internal polarizer' while simultaneously generating the photovoltage to control the LC orientation. In the ideal case, 50% of the incident light would no more absorbed by the polarizer, leading thus to a significant boost in the device transmittance. The

work dedicated to the fabrication of such oriented BHJ layers will be presented in the next chapter.

References

(1)   Davy, N. C.; Sezen-Edmonds, M.; Gao, J.; Lin, X.; Liu, A.; Yao, N.; Kahn, A.; Loo, Y.-L. Pairing of Near-Ultraviolet Solar Cells with Electrochromic Windows for Smart Management of the Solar Spectrum. *Nat. Energy* **2017**, *2* (8), 17104.

(2)   Ullbrich, S.; Benduhn, J.; Jia, X.; Nikolis, V. C.; Tvingstedt, K.; Piersimoni, F.; Roland, S.; Liu, Y.; Wu, J.; Fischer, A.; Neher, D.; Reineke, S.; Spoltore, D.; Vandewal, K. Emissive and Charge-Generating Donor–Acceptor Interfaces for Organic Optoelectronics with Low Voltage Losses. *Nat. Mater.* **2019**, *18* (5), 459–464.

(3)   Tai, Q.; Yan, F. Emerging Semitransparent Solar Cells: Materials and Device Design. *Adv. Mater.* **2017**, *29* (34), 1700192.

(4)   Traverse, C. J.; Pandey, R.; Barr, M. C.; Lunt, R. R. Emergence of Highly Transparent Photovoltaics for Distributed Applications. *Nat. Energy* **2017**, *2* (11), 849–860.

(5)   Chang, S.-Y.; Cheng, P.; Li, G.; Yang, Y. Transparent Polymer Photovoltaics for Solar Energy Harvesting and Beyond. *Joule* **2018**, *2* (6), 1039–1054.

(6)   Lunt, R. R. Theoretical Limits for Visibly Transparent Photovoltaics. *Appl. Phys. Lett.* **2012**, *101* (4), 043902.

(7)   Xie, Y.; Xia, R.; Li, T.; Ye, L.; Zhan, X.; Yip, H.; Sun, Y. Highly Transparent Organic Solar Cells with All-Near-Infrared Photoactive Materials. *Small Methods* **2019**, *3* (12), 1900424.

(8)   Lee, J.; Cha, H.; Yao, H.; Hou, J.; Suh, Y.-H.; Jeong, S.; Lee, K.; Durrant, J. R. Toward Visibly Transparent Organic Photovoltaic Cells Based on a Near-Infrared Harvesting Bulk Heterojunction Blend. *ACS Appl. Mater. Interfaces* **2020**, *12* (29), 32764–32770.

(9)   Wang, W.; Yan, C.; Lau, T.; Wang, J.; Liu, K.; Fan, Y.; Lu, X.; Zhan, X. Fused Hexacyclic Nonfullerene Acceptor with Strong Near-Infrared Absorption for Semitransparent Organic Solar Cells with 9.77% Efficiency. *Adv. Mater.* **2017**, *29* (31), 1701308.

(10)   Jia, X.; Baird, E. C.; Blochwitz-Nimoth, J.; Reineke, S.; Vandewal, K.; Spoltore, D. Selectively Absorbing Small-Molecule Solar Cells for Self-Powered Electrochromic Windows. *Nano Energy* **2021**, *89*, 106404.

(11)   Yao, H.; Ye, L.; Hou, J.; Jang, B.; Han, G.; Cui, Y.; Su, G. M.; Wang, C.; Gao, B.; Yu, R.; Zhang, H.; Yi, Y.; Woo, H. Y.; Ade, H.; Hou, J. Achieving Highly Efficient Nonfullerene Organic Solar Cells with Improved Intermolecular Interaction and Open-Circuit Voltage. *Adv. Mater.* **2017**, *29* (21), 1700254.

(12)   Mahmoudi, C.; Muzuzu, W.; Fall, S.; Zhong, Y.; Mélart, C.; Lévêque, P.; Heiser, T.; Jaballah, N. S.; Majdoub, M.; Leclerc, N. Near Ultra-Violet Absorbers for Transparent Organic Solar Cells. *Dyes Pigments* **2022**, *207*, 110752.

(13)   Chintala, R.; Tait, J. G.; Eyben, P.; Voroshazi, E.; Surana, S.; Fleischmann, C.; Conard, T.; Vandervorst, W. Insights into the Nanoscale Lateral and Vertical Phase Separation in Organic Bulk Heterojunctions via Scanning Probe Microscopy. *Nanoscale* **2016**, *8* (6), 3629–3637.

(14)   Wang, K.; Liu, C.; Meng, T.; Yi, C.; Gong, X. Inverted Organic Photovoltaic Cells. *Chem. Soc. Rev.* **2016**, *45* (10), 2937–2975.

(15)   Campoy-Quiles, M.; Ferenczi, T.; Agostinelli, T.; Etchegoin, P. G.; Kim, Y.; Anthopoulos, T. D.; Stavrinou, P. N.; Bradley, D. D. C.; Nelson, J. Morphology Evolution via Self-Organization and Lateral and Vertical Diffusion in Polymer:Fullerene Solar Cell Blends. *Nat. Mater.* **2008**, *7* (2), 158–164.

(16)   Xu, Z.; Chen, L.-M.; Yang, G.; Huang, C.-H.; Hou, J.; Wu, Y.; Li, G.; Hsu, C.-S.; Yang, Y. Vertical Phase

Separation in Poly(3-Hexylthiophene): Fullerene Derivative Blends and Its Advantage for Inverted Structure Solar Cells. *Adv. Funct. Mater.* **2009**, *19* (8), 1227–1234.

(17) Dennler, G.; Scharber, M. C.; Brabec, C. J. Polymer-Fullerene Bulk-Heterojunction Solar Cells. *Adv. Mater.* **2009**, *21* (13), 1323–1338.

(18) Levermore, P. A.; Chen, L.; Wang, X.; Das, R.; Bradley, D. D. C. Fabrication of Highly Conductive Poly(3,4-Ethylenedioxythiophene) Films by Vapor Phase Polymerization and Their Application in Efficient Organic Light-Emitting Diodes. *Adv. Mater.* **2007**, *19* (17), 2379–2385.

(19) Ouyang, J.; Chu, C.-W.; Chen, F.-C.; Xu, Q.; Yang, Y. High-Conductivity Poly(3,4-Ethylenedioxythiophene):Poly(Styrene Sulfonate) Film and Its Application in Polymer Optoelectronic Devices. *Adv. Funct. Mater.* **2005**, *15* (2), 203–208.

(20) Na, S.-I.; Kim, S.-S.; Jo, J.; Kim, D.-Y. Efficient and Flexible ITO-Free Organic Solar Cells Using Highly Conductive Polymer Anodes. *Adv. Mater.* **2008**, *20* (21), 4061–4067.

(21) Huang, J.; Miller, P. F.; Wilson, J. S.; de Mello, A. J.; de Mello, J. C.; Bradley, D. D. C. Investigation of the Effects of Doping and Post-Deposition Treatments on the Conductivity, Morphology, and Work Function of Poly(3,4-Ethylenedioxythiophene)/Poly(Styrene Sulfonate) Films. *Adv. Funct. Mater.* **2005**, *15* (2), 290–296.

(22) Menke, S. M.; Ran, N. A.; Bazan, G. C.; Friend, R. H. Understanding Energy Loss in Organic Solar Cells: Toward a New Efficiency Regime. *Joule* **2018**, *2* (1), 25–35.

(23) Rosenthal, K. D.; Hughes, M. P.; Luginbuhl, B. R.; Ran, N. A.; Karki, A.; Ko, S.; Hu, H.; Wang, M.; Ade, H.; Nguyen, T. Quantifying and Understanding Voltage Losses Due to Nonradiative Recombination in Bulk Heterojunction Organic Solar Cells with Low Energetic Offsets. *Adv. Energy Mater.* **2019**, *9* (27), 1901077.

(24) Melnyk, O.; Garbovskiy, Y.; Bueno-Baques, D.; Glushchenko, A. Electro-Optical Switching of Dual-Frequency Nematic Liquid Crystals: Regimes of Thin and Thick Cells. *Crystals* **2019**, *9* (6), 314.

(25) Lee, H.; Yang, S.; Lee, J.-H.; Soo Park, Y. Improvement of the Relaxation Time and the Order Parameter of Nematic Liquid Crystal Using a Hybrid Alignment Mixture of Carbon Nanotube and Polyimide. *Appl. Phys. Lett.* **2014**, *104* (19), 191601.

(26) Oh-e, M.; Kondo, K. Response Mechanism of Nematic Liquid Crystals Using the In-plane Switching Mode. *Appl. Phys. Lett.* **1996**, *69* (5), 623–625.

(27) Xiao, L.; Wu, X.; Ren, G.; Kolaczkowski, M. A.; Huang, G.; Tan, W.; Ma, L.; Liu, Y.; Peng, X.; Min, Y.; Liu, Y. Highly Efficient Ternary Solar Cells with Efficient Förster Resonance Energy Transfer for Simultaneously Enhanced Photovoltaic Parameters. *Adv. Funct. Mater.* **2021**, *31* (41), 2105304.

Chapter 5 Oriented photovoltaic layers

5.1 Motivation

As demonstrated in the previous chapters, the PSLM architecture implies the use of light polarizers. We have therefore used commercial polarizers. They display a dichroic ratio (DR) of extinction coefficients of 800:1 to 1000:1. However, smart window applications do not require such a high dichroic ratio.[1] Indeed, it can be shown (Annex) that if the incident light polarization through the PSLM can accurately be rotated by 90°C, the amplitude of optical modulation between OFF state and ON state is given by:

$$\frac{I_{OFF}}{I_{ON}} = \frac{\left(1+\frac{1}{DR}\right)^2 \times DR}{4}$$

Eq. 5. 1

where I_{OFF} is the transmitted light intensity in the OFF state and I_{ON} is the light intensity in the ON state. As a result, a modulation by a factor of 3 in the PSLM transmittance requires a polarizer with a DR of only 10. To date, several research groups managed to produce aligned semiconductor polymer films with DR≥10 and this is in particular the case for the method of high temperature rubbing (HTR).[2–4] In addition, it has been demonstrated that it is possible to produce oriented photovoltaic (PV) layers.[5,6] Such aligned OPV cells show dichroic photovoltaic effects as well as polarized absorption in a large spectral range. Therefore, orienting the photovoltaic (PV) layer containing π-conjugated semiconductor polymers is an interesting strategy to replace the external polarizers and to improve the transparency of PSLMs.

In this chapter, we present some results that demonstrate how to use HTR to prepare PV layers with polarized absorption and a dichroic photovoltaic effect. To this aim, we first present results related to the improvement of the method of HTR. In particular, we focus on a new rubbing machine that allows to control precisely the applied force of the rotating cylinder on the polymer film. We show how the orientation and the film structure are modified by the applied force during rubbing. In a second part, we apply this method to the fabrication of aligned PV devices. We have tested two PV cell architectures: I) a bilayer structure composed of oriented P3HT and the acceptor $PC_{60}BM$ and II) an oriented heterojunction composed of rubbed blends of an electron donor polymer (PBnDT-FTAZ) and an electron acceptor material (N2200) (**Figure 1**). We have investigated what are the conditions that lead to high orientation in these devices and how to prepare OPV cells that show a dichroic photovoltaic effect.
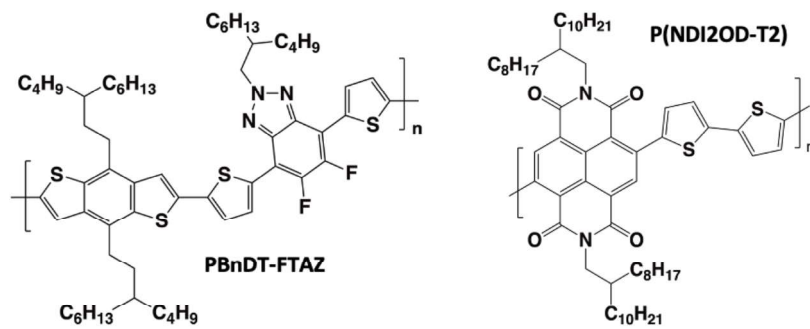
Figure 1. *Chemical structure of PBnDT-FTAZ donor and P(NDI2OD-T2) acceptor.*

5.2 State-of-the-art

a) High temperature rubbing

Orienting conjugated semiconducting polymers can enhance their charge transport due to intrinsically anisotropic electrical properties.[7,8] In addition, the alignment can also increase polarized luminescence and electroluminescence of semiconducting polymers.[9–11] Therefore, various alignment strategies of conjugated polymers have been developed including friction transfer, dip-coating, stretching, directional epitaxial growth, rubbing, etc.[2,4,11–13] Among them, rubbing was frequently used to orient PV layers for fabrication of polarizing OSCs or polarization photodetector.[5,6] Moreover, rubbing has also widely been used in the fabrication of LCD for aligning polyimide layers to control LC alignment.[14,15]

The orientation of conjugated polymers can be achieved by either manually or mechanically unidirectional rubbing with a velvet cloth. During the rubbing process, a shear force is applied to the surface of the films and thus the polymer chains align along the rubbing direction. The level of alignment can be quantified by a 3D order parameter S which is defined as (DR-1)/(DR+2).[4] DR is the dichroic ratio that can be determined by measuring the absorbances at a defined wavelength for incident light polarization parallel (//) and perpendicular ($\perp$) to the rubbing direction (DR=$A_{//}$/$A_{\perp}$). If S=0, the polymer chain orientations are isotropically distributed in plane. On the contrary, if S=1, the polymer chains are perfectly aligned in the film plane.

The influence of mechanical rubbing on the P3HT-based transistor performance was reported by Heil et al.[16] They observed increased charge mobilities for oriented P3HT films with a DR of 5.1, and the P3HT alignment slightly improved by an additional annealing step after rubbing.

The high temperature mechanical rubbing method was recently proposed to further improve orientation of polymer films by Brinkmann's group. In this case, the temperature of the polymer films is controlled during the rubbing process. Biniek et al reported that high in-plane alignment of the conjugated polymer poly(2,5-bis(3-dodecyl-2-yl)- thieno[3,2-b] thiophene) (C_{12}-pBTTT) was obtained by rubbing at 50 °C ≤ T_r ≤ 125 °C.[3] **Figure 2a,b** shows the evolution of the DR as a function of T_r and polarized UV-vis spectra at T_r=125°C. These results demonstrate that increasing the rubbing temperature can significantly enhance the level of orientation of polymer films. The authors attributed the improved alignment to the disordering of side chains at higher T_r, and thus increased plasticity of C_{12}-PBTTT films. Interestingly, increasing the rubbing temperature from room temperature to 125°C causes a change in the orientation of the crystalline domains, from edge-on to face-on. The aligned C_{12}-PBTTT films with pure face-on orientation show highly anisotropic charge transport properties ($\mu_{///}/\mu_{\perp}$ = 70). Furthermore, controlling crystal size in oriented P3HT films by modifying the rubbing temperature was reported by Hamidi-Sakr et al.[4] With increasing T_r, they observed a significant improvement in the alignment (**Figure 2c**) as well as enhanced crystallinity in P3HT films. The P3HT films possess a semi-crystalline structure that consists of alternating crystalline lamellae and amorphous zones. For 144 °C ≤ T_r ≤ 217 °C, the lamellar periodicity gradually increased from 13 to 25 nm due to increased crystal size along its chain direction.

In addition to rubbing temperature, the molecular weight (M_w) has also a strong impact on the level of orientation. Biniek et al used high temperature rubbing to successfully align different π-conjugated systems (i.e., p- and n-type semiconducting homopolymers such as P3HT and alternating copolymers such as P(NDI2OD-T2)).[17] In this reference, the evolution of DR for P3HT polymer with different M_w as a function of T_r was reported (**Figure 2d**). At room temperature, low- M_w P3HT display a high orientation whereas the high- M_w P3HT polymers were poorly oriented. A higher rubbing temperature is required for high- M_w P3HT polymers in order to achieve a high DR. The same phenomenon was observed for C_{12}-PBTTT polymer with different molecular weights. Consequently, their results indicate that both the rubbing temperature and the molecular weight distribution of the polymers are key parameters to control the level of orientation.

Yet, the impact of the force (pressure) during rubbing on the resulting alignment and structure of PSC films has not been investigated in details. Fortunately, in the course of this thesis, we had the chance to develop a new HTR machine that allows for a precise pressure (force) control

during the rubbing of the films. We will accordingly present the major results concerning the impact of rubbing pressure on the film orientation and structure.
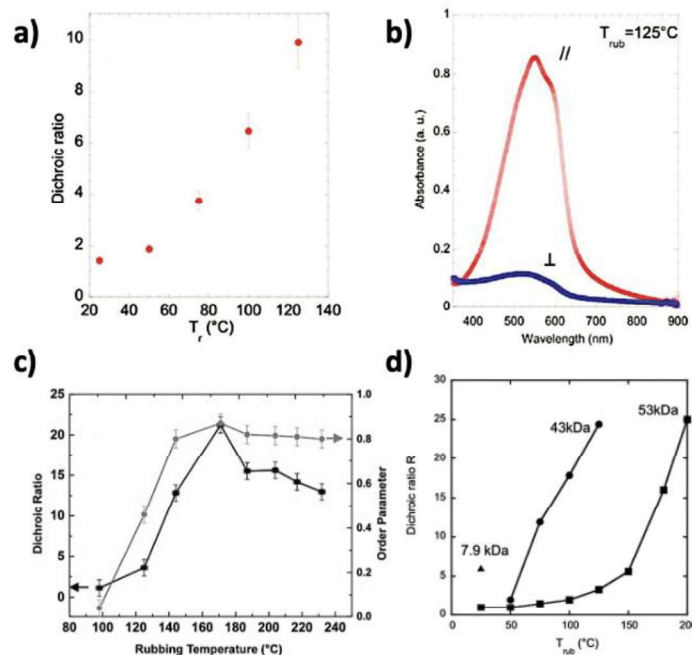
Figure 2. *a) Evolution of DR at 550 nm for the oriented C_{12}-pBTTT thin films as a function of rubbing temperature T_r. b) Polarized UV-vis spectra of the C_{12}-pBTTT films rubbed at 125°C for incident light polarization parallel and perpendicular to the rubbing direction. Reproduce from[3] c) Dependence of DR at 610 nm and order parameter for the aligned P3HT films as a function of rubbing temperature. Reproduce from[4] d) Evolution of DR at 605 nm for oriented P3HT films with different molecular weights (from 7.9 KDa to 53 KDa) as a function of rubbing temperature. Reproduced from[17]*

b) Oriented photovoltaic layers for applications

The first oriented organic solar cells fabricated using polymer rubbing were initially reported by Vohra et al.[18] They demonstrated that the photovoltaic performance of solar cells were enhanced by a soft rubbing the P3HT films prior to $PC_{60}BM$ deposition. As compared to the unrubbed P3HT films, I) rubbed P3HT polymers were less dissolved during the $PC_{60}BM$ deposition, II) $PC_{60}BM$ molecules diffused better into rubbed P3HT polymer matrix, and III) rubbing P3HT films displayed a reorientation of the crystallites from edge-on to face-on configuration, resulting in a better charge transport along the vertical direction in the solar cells. Therefore, the graded bilayer solar cell based on the rubbed P3HT films (J_{sc} =10.48 mA.cm^{-2}, FF =59.40 %) significantly increase J_{sc} and FF as compared to that with non-rubbed

P3HT polymers (J_{sc} =9.94 mA.cm^{-2}, FF =52.57 %). Furthermore, oriented active layers have been used by Yang and coworkers to achieve a polarizing organic photovoltaic (ZOPV) cell (The authors used 'ZOPV' rather than 'POPV' to avoid confusion with polymer organic photovoltaics), with the objective to improve the energetic efficiency of liquid crystal displays (by recovering part of the backlight in displays) (LCD). The ZOPV devices are designed by Yang and co-workers with a standard structure as follows: ITO/TiO$_2$:CsCO$_3$/oriented P3HT/PC$_{60}$BM/PEDOT:PSS/top electrode. They are integrated into LCDs and serve at the same time as polarizers and photovoltaic (PV) devices.[5]

The rubbed P3HT films showed highly anisotropic optical absorption (**Figure 3a**). To fabricate the solar cell, the PC$_{60}$BM acceptor was deposited by spin coating on the top of the oriented P3HT films, filling the cracks and pin-holes created by mechanical rubbing. Polarized UV-vis spectroscopy demonstrated that the diffusion of PC$_{60}$BM molecules does affect neither the P3HT molecular orientation nor the packing of P3HT chains. The quasi-bilayer films ultimately have a high DR of approximately 11.3 at 604 nm (**Figure 3b**). The ZOPV devices based on the inverted quasi-bilayer structure (**Figure 3c**) showed a dichroic photovoltaic effect with a $J_{sc//}$/ $J_{sc\perp}$ ratio of 3.54 (**Figure 3d**).
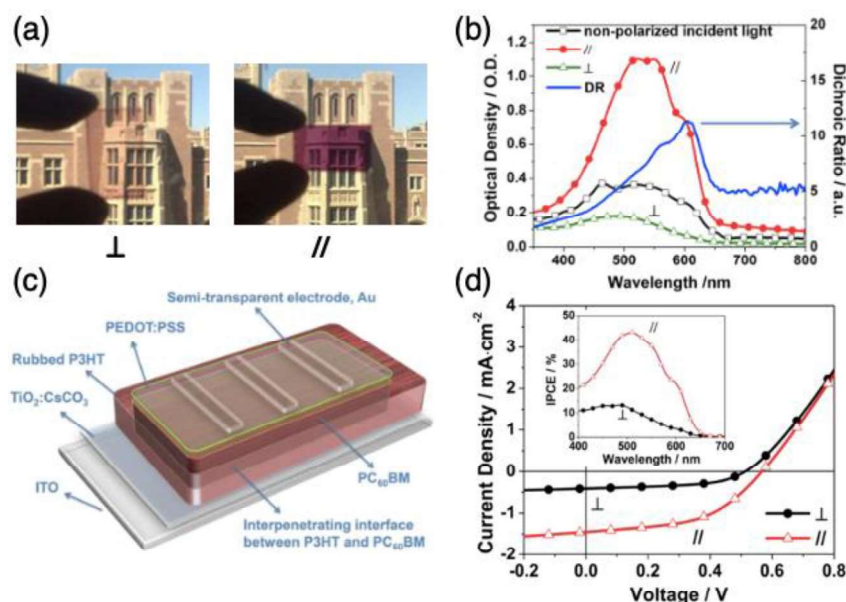
Figure 3. a) Images of a rubbed P3HT film for the light polarization perpendicular (⊥) or parallel (//) to the rubbing direction. b) Polarized UV-visible absorption spectra of quasi-bilayer P3HT-PC$_{60}$BM. The incident light polarization is parallel (//) or perpendicular (⊥) to the rubbing direction. c) ZOPV device structure based on the inverted quasi-bilayer. d) Dichroic J-V characterization of ZOPV device in c). The intensity of polarized incident light is around 33 mW/cm^2. Inset: polarized IPCE spectra. Reproduced from [5]

Recently, O'Connor and coworkers reported a record in-plane alignment of bulk heterojunction films used in polarization sensitive photodetectors. In such a device, the incident light polarization is converted to an electrical signal that is used as signal output.[6] The key factors for polarization sensitive photodetectors are I) the photocurrent anisotropy and II) the electrical responsivity upon illumination. The authors focused on the BHJ composed of PBnDT-FTAZ and poly {[N, N'-bis(2-octyldodecyl)-1,4,5,8-naphthalenedicarboximide-2,6-diyl]-alt-5,5'-(2,2'bithiophene)} P(NDI2OD-T2), also known as N2200. The BHJ layers were rubbed with a velvet cloth and annealed at high temperature (**Figure 4a**). Their results indicated that the film alignment was significantly enhanced after thermal annealing of the rubbed blend films (**Figure 4b**). For PBnDT-FTAZ of low molecular weight, the maximum DR was close to 17 (**Figure 4c**). Semi-transparent organic photodiodes based on the well-aligned films were fabricated with an inverted organic photovoltaic architecture (**Figure 4d**). A high dichroic photovoltaic effect was observed in the J-V characteristic measurements for incident light polarization parallel and perpendicular to the rubbing direction (**Figure 4e**). As shown in **Figure 4f**, the spectral responsivity indicated that detectors have a large photocurrent ratio of 15 while maintaining responsivity above 20 mA/W.

It is important to note that these results were reported for detectors with very small active surfaces (0.0314 cm^2) possibly to avoid pine-hole effects that occur in rubbed blend films (vide infra).
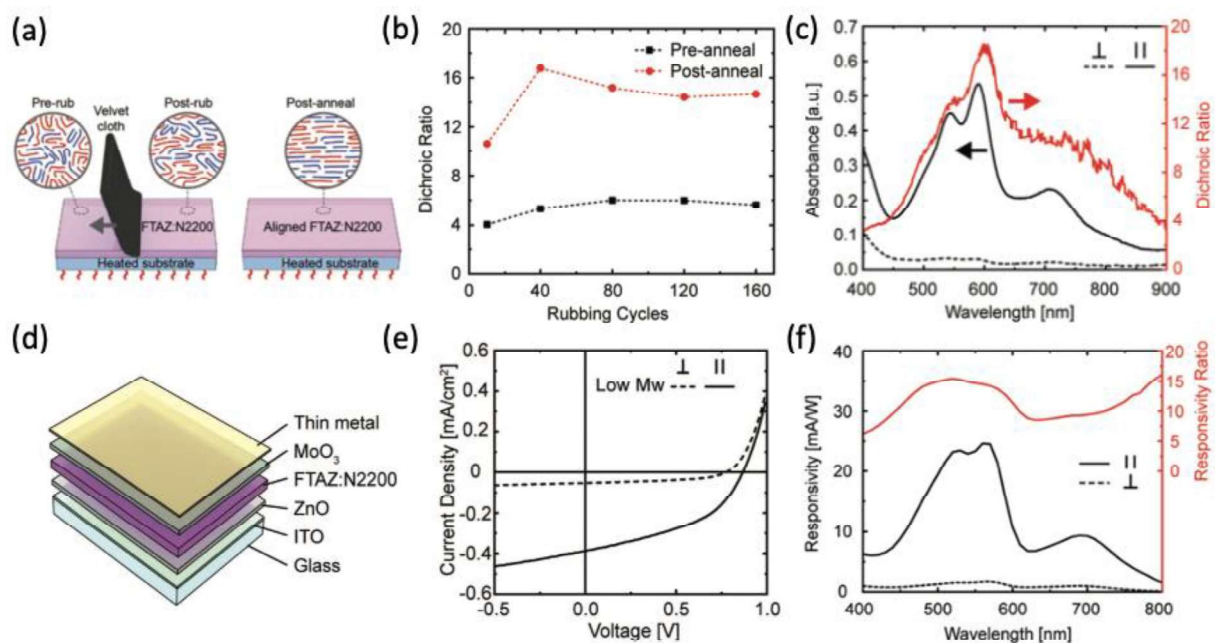
Figure 4. a) Schematic illustration of FTAZ-N2200 polymers blend alignment procedure. b) The DR at a wavelength of 595nm as a function of rubbing cycles for pre-annealed and post-annealed FTAZ-N2200 blend films. c) Polarized UV-visible absorption spectra and corresponding DR for aligned (40 rubbing cycles) and annealed films (at 275°C for 5 min) with the rubbing direction parallel (//) and perpendicular (⊥) to the incident light polarization. d) Polarization sensitive photodiode detector device structure. e) J-V characteristics for photodiode detector device in under optimal alignment conditions. Responsivity (f) and responsivity ratio (e) of a polarized photodiode detector for parallel and perpendicular directions of the incident light polarization. Adapted from[6].

Both polarized OSCs and photodetectors show anisotropic optical properties as well as dichroic photovoltaic effects. In our case, the main idea is to produce aligned BHJ that display a dichroic photovoltaic effect that would be beneficial when integrated into the PSLM. Such layers may play the twofold role of light polarizer and OPV cell that generate the voltage necessary to switch the device. It makes therefore sense to use such oriented P3HT/PC_{60}BM bilayer and aligned FTAZ:N2200 blend films for the fabrication of PSLMs. In publications discussed above, the orientation of PV layers was performed by rubbing 40~80 times by hand with a velvet cloth a polymer film maintained onto a hot plate. To make the fabrication process more reproducible, a high temperature rubbing machine is used in this thesis. It consists of two main parts (**Figure 5**): I) a rotating cylinder covered with a microfiber cloth mounted on a support that can controls the applied force of the cylinder/cloth on a polymer film and II) a translating and heating stage onto which the polymer film is mounted. Most importantly, the pressure between the rotating cylinder/cloth and the surface of polymer films can be controlled during the rubbing processes with the help of a pressure sensor. The impact of rubbing force on the level of orientation and the structure of the P3HT films was first studied. Second, we investigated the possibility to produce oriented PV cells to be integrated in PSLMs using this new rubbing machine. We used two strategies: I) oriented P3HT/PC_{60}BM bilayer structures and II) aligned heterojunctions composed of PBnDT-FTAZ and P(NDIT2OD-T2).

5.3 Polarized OSCs based on the oriented P3HT/PC_{60}BM bilayer structure

In this section, we first investigated the impact of rubbing force on the roughness, the level of orientation and the crystal structure of oriented P3HT films. Then, the PC_{60}BM layer is deposited on the top of oriented P3HT polymers, creating a quasi-bilayer structure. We studied the anisotropic optical and PV properties of the quasi-bilayer and the impact of rubbing force

on the PV dichroic effect.

5.3.1 Experimental section

Materials and film preparation

Regio-regular P3HT was purchased from Merck (M_w= 43.6 KDa, Đ = 1.8). ZnO was purchased from Sigma-Aldrich. In order to study the impact of pressure on the P3HT alignment, the P3HT layer was spin coated at 2500 rpm for 30s from chlorobenzene solution with a concentration of 20 mg. mL^{-1}. Then, the film was annealed at 150°C for 10 min.

Rubbing procedure

The rubbing machine was fabricated at the Institute Charles Sadron, as illustrated in **Figure 5**. In the home-made rubbing machine, the diameter of rotating cylinder (C) is 4 cm. During the rubbing process, its rotation speed (ω) is ~600 rpm. The samples placed on a hot plate (i.e., sample holder) move at a steady speed (v) of 1 cm/s under the rotating cylinder. The rubbing temperature of the samples can be modified from room temperature to 240°C. Before rubbing, the temperature of the samples as allowed to stabilize for ~ 1 min. Moreover, the rubbing force can be controlled in the range of 5.39-12.29 N.
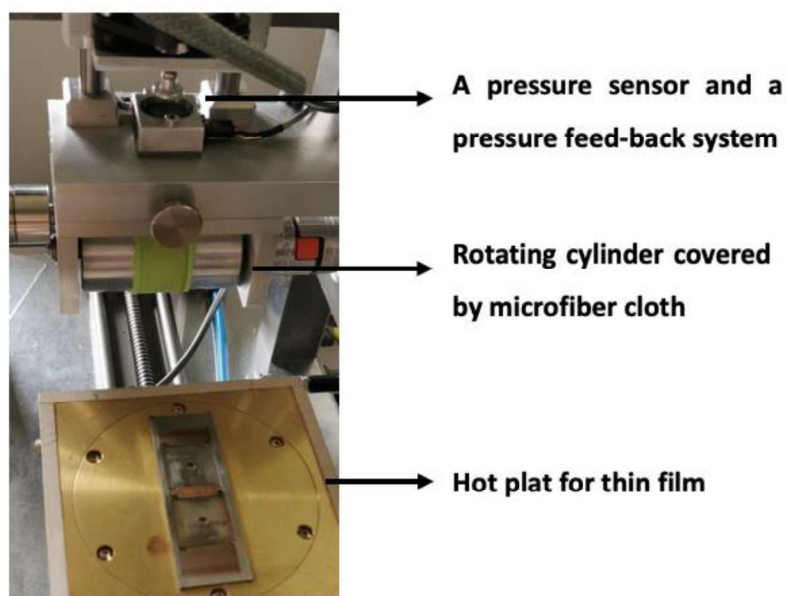
Figure 5. Photograph of the mechanical rubbing machine fabricated at Institut Charles Sadron.

A key parameter for orientation is the rubbing length R_d, which can be considered as the total

rubbing length of microfiber cloth in contact with substrate and defined by the following equation:

$$R_d = \frac{(\pi C \omega + v)N}{v}$$
Eq.5.2

Where N corresponds to the number of cycles. The P3HT films were oriented under different forces (7.36-12.26 N). Other rubbing parameters (including N=1 and T_r=150°C) were constant. The rubbing process was achieved under ambient air conditions.

Solar cell fabrication

Inverted structure: OSC based on the non-oriented PV layer were prepared as a reference (glass/ITO/PEIE/non-oriented P3HT/PC$_{60}$BM/PEDOT:PSS/Al). PEIE (~7 nm) was spin-coated on the clean ITO substrates and annealed at 100°C for 10 min. The P3HT layer (See film preparation) was deposited on the PEIE layer. Then, a 0.5 wt% solution PC$_{60}$BM in DCM was deposited on the top of non-oriented P3HT layer by spin coating at 4500 rpm for 20 s. DCM is a poor solvent for P3HT.[19] The films were annealed at 150 °C for 5 min. PEDOT:PSS (Al 4083) solution was spin coated at 4000 rpm for 60s and annealed at 80 °C for 2 min. The device fabrication was eventually completed by the thermal evaporation of Al (100 nm) as a top electrode.

Standard structure: The OSC configurations is: glass/ITO/PEDOT:PSS/non-oriented or oriented P3HT/PC$_{60}$BM/ZnO /Ag. The deposition of PEDOT: PSS (Al 4083) and Ag were performed following the methodology described in Chapter 4. For the non-oriented P3HT film, the PV bilayer was prepared in the same way as the inverted structure. For the oriented P3HT film, the P3HT layer was spin coated directly onto the PEDOT: PSS layer followed by rubbing. After that, PC$_{60}$BM molecules were deposited onto the oriented P3HT film to fill some pin-holes or/and scratches. The ZnO (7~10 nm) was spin coated at 5000 rpm for 60 s and annealed at 100 °C for 10 min.

Polarized UV–Vis–NIR Absorption

The level of film orientation was investigated by a Varian Cary 5000 spectrometer equipped with a light polarizer (350-2500 nm). The polarizer is placed between the incident light source and the sample. The angle of light polarization was measured with respect to the rubbing direction (0° corresponding to the light polarization POL//R and 90° corresponding to the light

polarization POL⊥R). The polarized absorbance spectra were recorded in the range of 350-900 nm with the spectral resolution of 1 nm.

Atomic force microscopy (AFM) characterization

AFM is widely used to measure the topography surface of the thin films. The AFM images of oriented films were obtained using Bruker multimode 8 (Peak Force Tapping technologies) with Nanoscope V controller using ScanAsyst-Air tips (0.4 N.m^{-1}). This measurement was performed by Christophe Contal at the Institute Charles Sadron. The images were treated with Nanoscope Analysis software.

TEM analysis

For TEM sample preparation, the oriented polymer films were coated with a thin amorphous carbon film using an Edwards Auto306 evaporator. The films were removed from the NaPSS-coated glass substrate by floating on distilled water and recovered on TEM copper grids. The thermal annealing was directly performed on the TEM grids. The structural analysis of the aligned films was achieved in bright field, high resolution and diffraction modes by a CM12 Philips microscope (120 kV) equipped with a MVIII (Soft Imaging System) camera.

J-V characterization

The J-V measurements for OSC based on the non-aligned PV layers were performed following the methodology described in Chapter 4. For testing polarized organic photovoltaic devices, a linear polarizer (AP42-008T-PSA from American Polarizers Inc.) was placed between the incident light source and the samples. The samples were measured for the incident light polarization parallel and perpendicular to the rubbing direction.

5.3.2 Results and discussion

a) Influence of rubbing force on the roughness of oriented P3HT films

In order to study the impact of the rubbing force (F_r) on the roughness of oriented films, the P3HT polymers were rubbed at 150°C at different rubbing forces and were investigated by atomic force microscopy (AFM). As shown in **Figure 6a-d**, some material on the surface was removed by the velvet cloth during the rubbing process, even at a relatively low force (F_r =7.36 N). In addition, the AFM height images do not show a significant difference. We plotted the

root mean square (RMS) roughness of rubbed films as a function of F_r (**Figure 6e**). The error bar was obtained by measuring different areas on a sample. The large error bars imply that the oriented films have an inhomogeneous topography surface. The RMS values slightly increases with increasing the rubbing pressure, but taking into account the errors, these values are very closed. This result suggests that the rubbing force does not have a strong influence on the roughness of films. Even for F_r =7.36 N, the RMS value already reaches around 17 nm. The roughness is likely associated with the surface roughness properties of the velvet cloth. A smoother velvet cloth might induce a smoother oriented film surface. The impact of F_r on the level of orientation and crystal structure of P3HT was further studied by polarized UV-visible spectroscopy and electron diffraction.
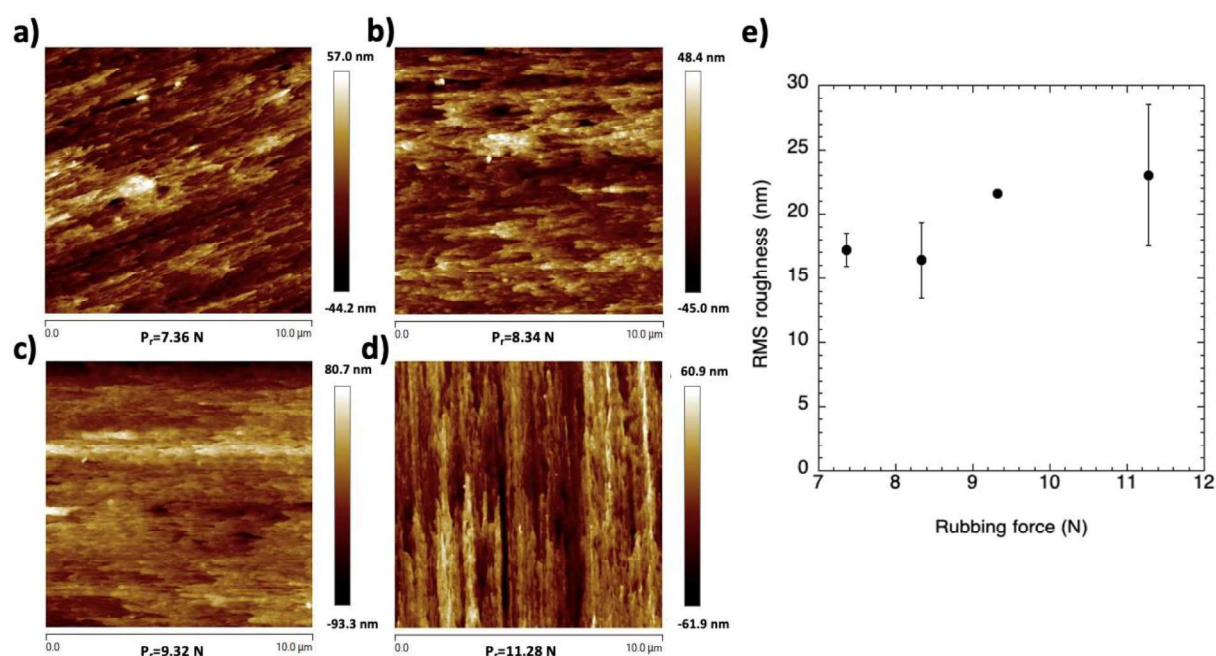
Figure 6. *AFM height images of P3HT films oriented at 150°C at different rubbing force: a) 7.36 N, b) 8.34 N, c) 9.32 N and d) 11.28 N. All scan areas are 10 µm x 10 µm. e) Evolution of the RMS roughness as function of rubbing force.*

b) Influence of rubbing force on the P3HT orientation/structure

Figure 7a depicts the polarized UV-vis absorption spectra for P3HT films oriented with a rubbing force of 10.29 N and measured for incident light polarization parallel (//) and perpendicular (⊥) to the rubbing direction. For POL//R, the spectrum shows a typical vibronic structure with components A_{0-2}, A_{0-1} and A_{0-0} centered at 520, 555 and 602 nm, respectively.

They correspond to electronic transitions from the ground state S_0 (v=0, v is vibrational state) to the first excited state S_1 (v=0,1,2). The pronounced vibronic structure is related to the conjugation length i.e., the length of planarized chain segments in the P3HT crystals. In strong contrast, the absorption spectrum for POL⊥R shows a single broad peak. Its maximum absorption is located around 500 nm. It is similar to the absorption of coiled P3HT in solution and indicates thus that the P3HT chains in the amorphous phase have a disordered non-planarized chain conformation.[20] In addition, in the amorphous zones, the twists of P3HT polymers break π-conjugation along the chains, thus resulting in a large distribution of conjugation lengths.[4]

The evolution of normalized absorption spectra for POL//R as a function of F_r is shown in **Figure 7b**. For comparison, the absorption spectra are normalized to maximum peak of A_{0-1}. At F_r=7.35 N (black lines), the vibronic components A_{0-1} and A_{0-2} are obvious, however, the A_{0-0} component is of poor intensity. With increasing F_r, the intensity of the 0-2 component decreases and the 0-0 contribution increases. In our case, the P3HT polymers display weak H-aggregate-like behavior due to the low intensity of the 0-0 component compared to that of A_{0-1} and A_{0-2}. Spano et al proposed that the H-aggregate model is 1D, taking into account the interchain exciton delocalization along the π stacking direction but neglecting the exciton delocalization in the chain direction.[21] The ratio A_{0-0}/A_{0-1} reflects the level of order in P3HT, which is associated with the free exciton bandwidth W for H-aggregates following the equations:

$$\frac{A_{0-0}}{A_{0-1}} = (\frac{1-0.24W/E_p}{1+0.073W/E_p})^2 \ and \ W = \frac{\left(1-\sqrt{\frac{A_{0-0}}{A_{0-1}}}\right)E_p}{0.073\sqrt{\frac{A_{0-0}}{A_{0-1}}}+0.24} \qquad Eq.5.3$$

Where W is related to the nearest-neighbor interchain coulombic coupling J_0 (W=4J_0). E_p represents the coupling strength between intramolecular vibrations electronic transitions, the former corresponds to symmetric C=C stretching of the thiophene ring (0.18 eV). As shown in **Figure 7d**, increasing F_r leads to the larger ratio of A_{0-0}/A_{0-1}. An increase ratio of A_{0-0}/A_{0-1} results in a decrease of W. Clark et al. and Hamidi-Sakr et al. demonstrated that the reduced W relates to an increase in effective conjugation length.[4,22] The present results imply that increasing F_r induces a more planarized and better ordered polymer chain. For POL⊥R, a blue shift can be observed with increasing F_r in **Figure 7c**. Since the spectra POL⊥R is dominated by the amorphous zone of P3HT, such blue shift suggests that the chains are more disordered in

the amorphous zones as F_r increases.

Figure 7e shows the evolution of DR and S at 557 nm as a function of F_r. The level of alignment is significantly improved by applying higher F_r to the polymer films. When F_r > 10.29 N, DR reaches a plateau close to 10. Accordingly, the increased DR with F_r is also consistent with larger planarized chain segments at higher F_r. Similarly to the rubbing temperature, the rubbing force has a significant impact on chain alignment and P3HT crystallization.
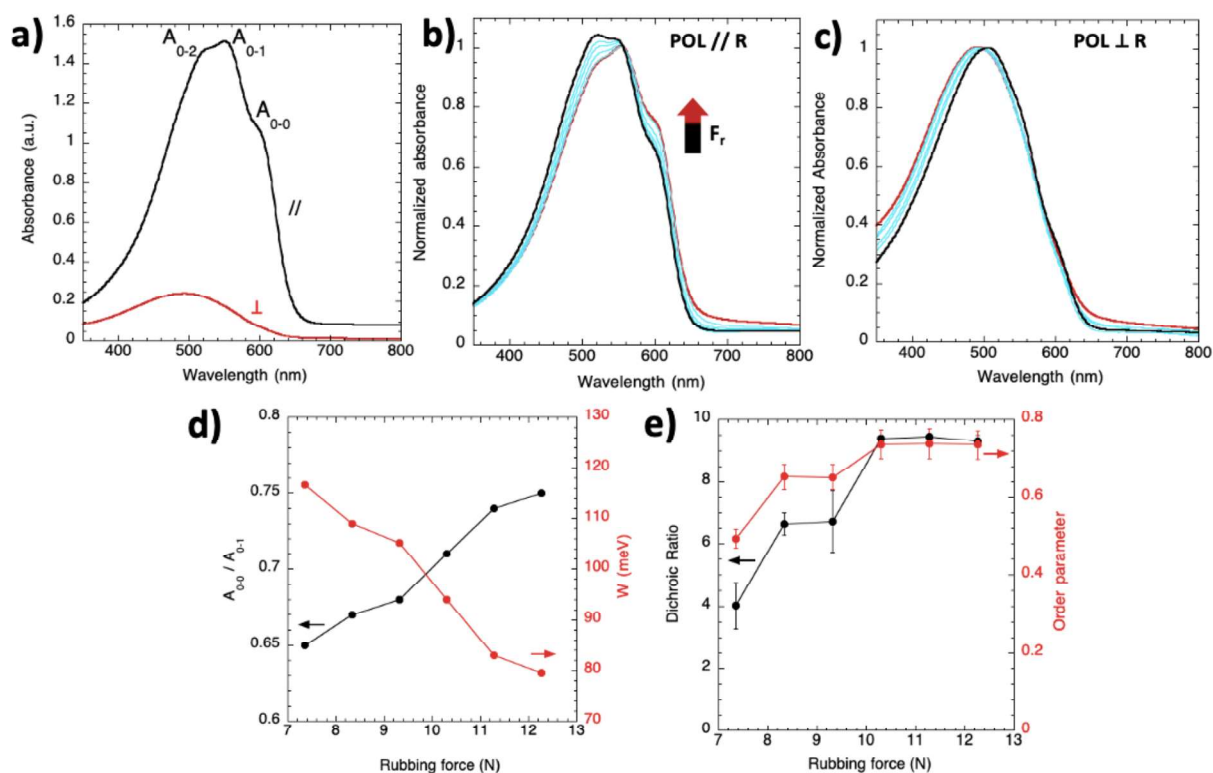
Figure 7. *Polarized UV-vis spectra of oriented P3HT films rubbed at 10.29 N (T_r= 150°C). The films are measured parallel (//) and perpendicular (⊥) to the rubbing direction. Evolution of the UV-vis spectra of P3HT films rubbed at different F_r for the incident light polarization parallel b) and perpendicular c) to the rubbing direction. The rubbing force varies from 7.36 N (dark lines) to 12.26 N (red lines). d) Evolution of the ratio between A_{0-0} at 555 nm and A_{0-1} at 602 nm (dark dots) and evolution of the exciton bandwidth W (red dots) as a function of rubbing force. e) Dependence of dichroic ratio DR (dark dots) and order parameter S (red dots) as a function of rubbing force.*

Electron diffraction (ED) helps us to further investigate the structural variation of rubbed films under different F_r. **Figure 8a-d** depict the characteristic ED patterns *versus* F_r and **Figure 8e** shows the intensity profile along the equator of the ED patterns *versus* increasing F_r. In the ED patterns, the 1 0 0, 0 2 0 and 0 0 2 reflections correspond to the distance between polymer

chains separated by alkyl side chains (d_{100}), π-stacking (d_{020}) and the length of the thiophene repeat unit along polymer backbone (d_{002}), respectively. For F_r= 7.35 N, the h 0 0 reflections (h= 1,2,3) as well as 0 2 0 Scherrer ring with weak intensity are present, indicating a coexistence of face-on and non-aligned edge-on crystal domains in the rubbed films. The non-oriented edge-on crystals give rise to a ring-like 0 2 0 reflection. For this rubbing force, the 0 0 2 reflection along the meridian is absent. This result indicates that the thiophene backbones are oriented along the rubbing direction but without a well-defined translational order along the chain direction C_{P3HT} between π-stacked thiophene groups.[13] In other words, for F_r= 7.35 N, the oriented film has a structure that is similar to the so-called smectic-like form of P3HT. When F_r increases from 7.35 N to 12.26 N, the intensity of the h 0 0 reflections increases, the 0 0 2 reflection emerges while the 0 2 0 reflection progressively disappears. The Scherrer-like ring of non-oriented P3HT disappears also. For $F_r \geq$ 8.34 N, the presence of the 0 0 2 reflection implies improved crystalline order along the polymer backbone i.e., the semi-crystalline form of P3HT is obtained. This result is in line with the observed evolution of the absorption spectra showing a larger A_{0-0}/ A_{0-1} ratio at increased F_r. At $F_r \geq$ 10.29 N, the absence of the 0 2 0 reflection suggests that the initial edge-on crystals are fully transformed to aligned face-on domains. The P3HT crystallites with face-on orientation should confer a better charge transport along the π-stacking direction that is normal to the film plane and thus should improve the photovoltaic performance in OSCs.
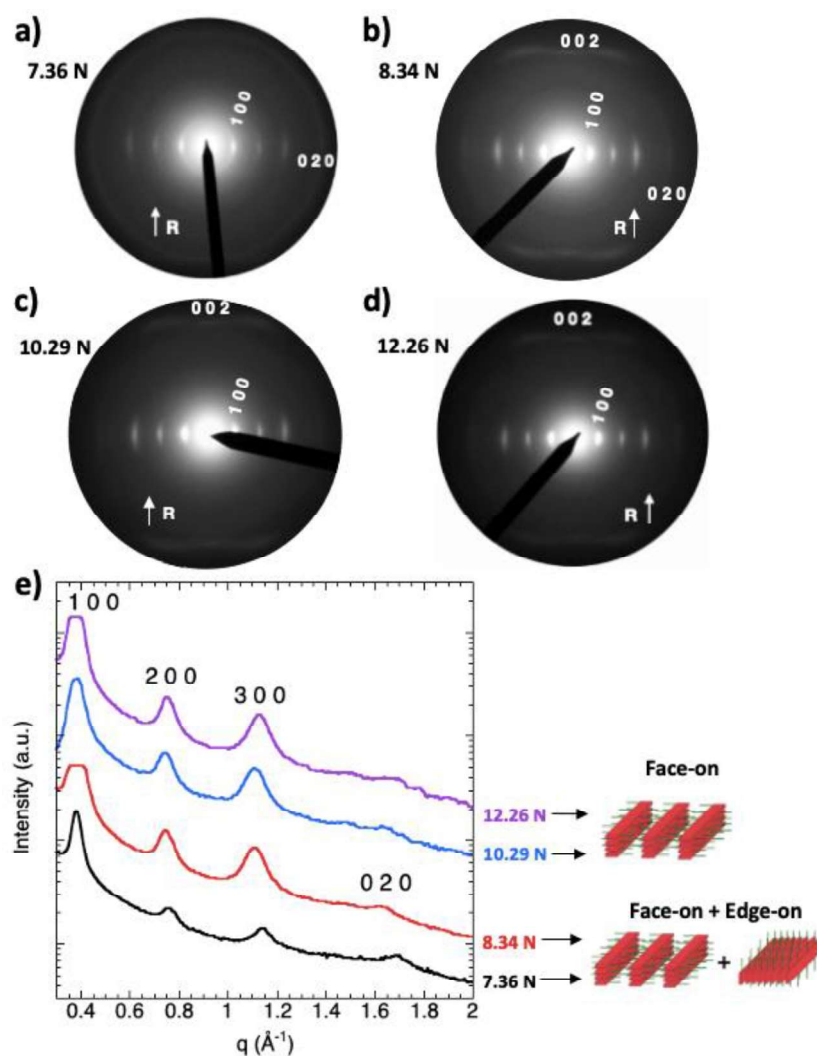
Figure 8. *a-d) ED patterns of oriented P3HT films prepared at different rubbing forces (T_r=150°C). The rubbing direction R is indicated by a white arrow. The most intense reflections have been indexed. e) Intensity profile along the equator of the ED patterns in a-d). Schematic illustration of crystal orientation as function of rubbing force is shown on the right.*

c) Fabrication of polarized OSCs with a bilayer structure

Oriented P3HT films show highly anisotropic optical properties that can be well controlled by playing with the rubbing temperature and the rubbing force. In order to achieve an efficient operation of solar cells, P3HT polymers were initially aligned at low F_r (7.36 N). Then, we deposited a thin $PC_{60}BM$ film from a solution in DCM atop the rubbed P3HT films to prepare a bilayer structure. The $PC_{60}BM$ film has two roles: I) it is an electron-accepting layer and II) it can fill some pinholes or scratches created by mechanical rubbing (**Figure 9a**). After that, the films were annealed at 150°C. In this case, the $PC_{60}BM$ molecules are expected to diffuse into

the P3HT polymer matrix forming an interpenetrated quasi-bilayer structure.[5] To confirm whether the deposition of $PC_{60}BM$ has an influence on the P3HT alignment, the oriented P3HT polymers and quasi-bilayer $PC_{60}BM$/oriented P3HT films are measured by polarized UV-vis spectroscopy (**Figure 9b**). After deposition of $PC_{60}BM$ molecules and thermal annealing, the P3HT molecular chains retain their orientation in despite of a slight reduction of DR from ~4 to ~3. This result is attributed to the $PC_{60}BM$ molecules diffusing preferentially into the amorphous regions of P3HT after annealing, leading to a moderate impact on the P3HT crystals.[23,24] After studying the optical properties of the quasi-bilayer films, their photovoltaic properties was investigated by integrating the films into OSCs.
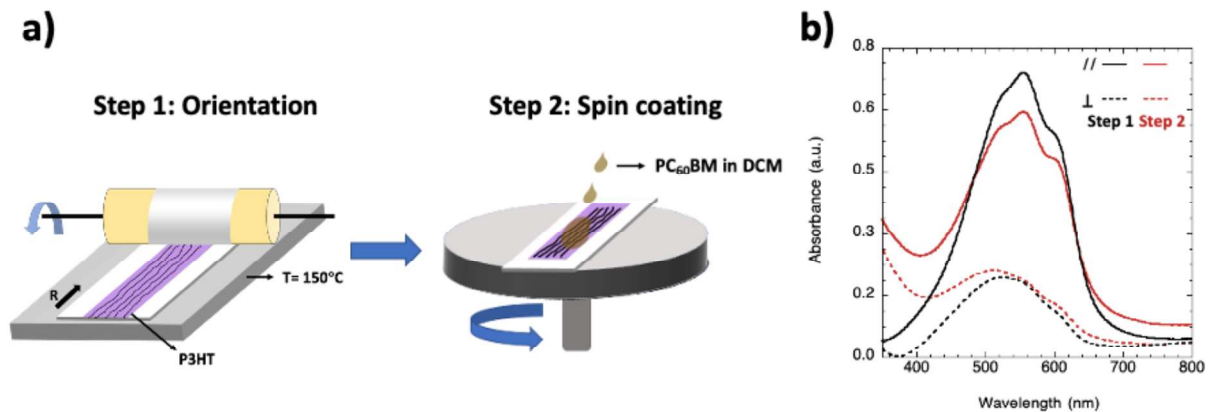
Figure 9. *a) Two-step preparation of quasi-bilayer structure. At first step, P3HT films is rubbed at 150°C at 7.36 N. The second step is to deposit the $PC_{60}BM$ molecules from a solution in DCM on the top of the oriented P3HT film. b) Polarized UV-vis spectra of oriented P3HT films in step 1 (dark lines) and of quasi-bilayer structure in step 2 (red lines).*

Based on a previous inverted quasi-bilayer structure of OSCs fabricated by Zhu at al[5], an OSC with the configuration of ITO/PEIE/non-aligned P3HT/$PC_{60}BM$/PEDOT: PSS/Al was initially prepared as a reference and characterized by J-V measurements under dark and illumination (**Figure 10a**). However, an S-shaped J-V curve was observed. The S-shaped curve results from the carrier accumulation in the OSC that alters the electric field distribution inside the device.[25] This can be explained by the fact that $PC_{60}BM$ molecules are located far from the cathode interface resulting in an imbalance of charge extraction rates at the electrodes[26] or that the pure $PC_{60}BM$ layer on the lower surface of the anode prevents the efficient hole collection. As compared to the previous reported OSCs configuration (ITO/TiO_2:Cs_2CO_3/non-aligned

P3HT/PC$_{60}$BM/PEDOT: PSS/Al), we used a different electron transporting layer to fabricate the OSCs with inverted structure. Therefore, we suspect that the PEIE and TiO$_2$:Cs$_2$CO$_3$ transporting layers might display different physicochemical affinities with PC$_{60}$BM and P3HT. Xu et al demonstrated that in a P3HT/ PC$_{60}$BM blend film, the PC$_{60}$BM tend to accumulate on the Cs$_2$CO$_3$ layer due to a strong dipole-dipole interaction.[27]

In order to avoid the S-shaped curves, we fabricated the OSCs with a standard structure based on the non-aligned P3HT polymers (as reference device) as well as on the P3HT films rubbed at different P$_r$. The important PV parameters were summarized in **Table 1**. The reference device was measured under unpolarized light, which exhibits a V$_{oc}$ of 0.58 V and a J$_{sc}$ of 6.99 mA.cm^{-2}, as shown in **Figure 10b**. To test anisotropic devices, a linear polarizer was placed between the AM 1.5G light source and the devices, introducing an incident light polarization. The devices (**Figure 10c**) were measured for incident light polarization parallel and perpendicular to the rubbing direction.

Table 1. *Photovoltaic parameters summary for non-aligned PV layer and for PV layer composed of P3HT films oriented at different rubbing forces.*

F$_r$ (N)	Test condition	V$_{oc}$ (V)	J$_{SC}$ (mA.cm^{-2})	FF (%)	PCE (%)
0	Unpolarized light	0.58 ± 0.01	6.99 ± 0.08	54.0 ± 0.4	2.19 ± 0.04
7.36	//	0.51 ± 0.01	1.09 ± 0.04	41.3 ± 9.5	0.22 ± 0.06
	⊥	0.47 ± 0.04	1.03 ± 0.02	39.2 ± 10.6	0.20 ± 0.06
7.84	//	0.50 ± 0.01	0.67 ± 0.11	50.4 ± 4.0	0.17 ± 0.04
	⊥	0.47 ± 0.02	0.57 ± 0.11	43.6 ± 4.4	0.12 ± 0.04
8.34*	//	0.46	0.67	65.1	0.17
	⊥	0.45	0.46	50.6	0.16

*4 diodes based on the oriented P3HT (F$_r$=8.34 N) were measured, three diodes show a significant leakage current, only one diode works.

Figure 10d depicts the evolution of J-V curves as a function of F$_r$ applied to P3HT polymers. In comparison with the devices based on the non-oriented P3HT polymers, the photocurrents delivered by polarized OSCs decrease obviously. Indeed, the commercial polarizer used for J-V

measurements can absorb over 50% of the incident light, leading to a significant decrease in the intensity of the incident light. In addition, the mechanical rubbing usually causes a thickness reduction of the P3HT layers, thereby lowering the photon absorption in the active layer. Consequently, the photocurrents should be lower than half the photocurrent delivered by the reference device.

At F_r=7.36 N, the J-V responses for POL//R and POL⊥R are very close. By further increasing the rubbing force, the solar cells display a better dichroic photovoltaic effect. Importantly, the V_{oc} measured for POL//R and POL⊥R is almost unchanged, whereas the J_{sc} becomes anisotropic. At F_r=7.84 N, $J_{sc//}$ = 0.67 mA.cm^{-2} and $J_{sc⊥}$ = 0.57 mA.cm^{-2}, yielding a J_{sc} ratio of ~1.2. The $J_{sc//}$ is larger than $J_{sc⊥}$, since more photon can be absorbed and converted to current for POL//R. However, the J_{sc} ratio is lower than DR (~3). This result is presumably due to depolarization by light reflection on a rough electrode surface. In the ideal case, a perfectly smooth metal surface reflects the polarized light in the specular direction, therefore, the reflected light is still polarized. However, in our case, the grooves on the surface of oriented P3HT polymers might result in a rough surface of the Ag electrode deposited on the top of the active layer. As the polarized light is reflected or scattered by the rough surface, the incident polarization will change.[28,29] The depolarized light will be reabsorbed by the active layer, reducing its anisotropic properties. When F_r increased to 8.34 N, the ratio of $J_{sc//}$ (0.67 mA.cm^{-2}) to $J_{sc⊥}$ (0.46 mA.cm^{-2}) is ~1.5. This result indicates that a larger rubbing force leads to a more pronounced dichroic photovoltaic effect. However, the V_{oc} was decreased as compared to that observed at higher F_r. This reduced V_{oc} results from a higher leakage current. A thin layer of PC$_{60}$BM is apparently not sufficient to fill the deep scratches of the rubbed P3HT films for the highest rubbing force.
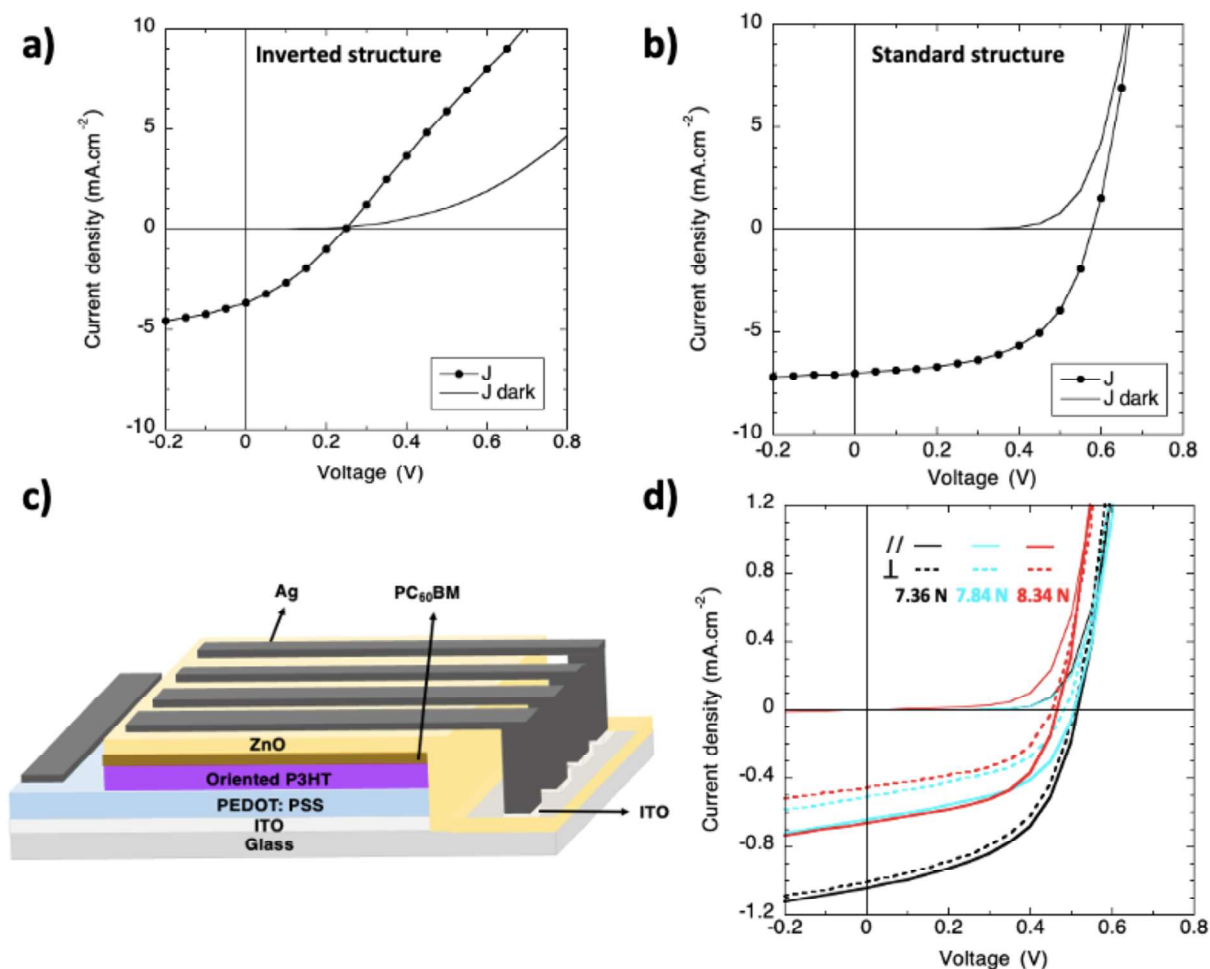
Figure 10. *J-V characterization of OSCs based on the non-aligned PV layer with a) an inverted structure and b) a standard structure measured in dark (grey lines) and upon illumination with 100 mW.cm^{-2} (dark lines). c) Schematic illustration of an OSC based on oriented P3HT/PC$_{60}$BM film with the standard structure. d) Dichroic J-V characterization of PV layers containing P3HT polymers rubbed at different F$_r$: 7.36 N (dark), 7.84 N (light blue) and 8.34 N (red). The aligned PV layers were measured in dark (fine lines) and for the incident light polarization parallel (lines) and perpendicular (dotted lines) to the rubbing direction.*

In this part, the polarized OSCs with standard structure was achieved, showing a DR of 3 and J$_{sc}$ ratio of 1.5. However, the photovoltage produced by the oriented P3HT/PC$_{60}$BM bilayer is lower than V$_{th}$. Moreover, the PSLM devices require an inverted structure of the OSC. Since an appropriate conductive electron transporting layer has not been found to build up a standard structure in the PSLMs. We conclude that the oriented bilayer structure is poorly adapted for PSLM applications.

In the following section, we will describe an alternative strategy to fabricate polarized OSCs for PSLM applications. Instead of the bilayer structure of the OSC, we will focus on OSCs based on

aligned films of the blend PBnDT-FTAZ donor plus the N2200 acceptor. The PBnDT-FTAZ is a 'weak donor-strong acceptor' polymer that consists of benzodithiophene (BnDT) and fluorinated benzotriazole (FTAZ) units.[30] The N2200 polymer is a very classical n-type alternated copolymer composed of the naphthalene diimide (NDI) unit and bithiophene (T2) unit.[31] The choice for the polymers is guided by: I) the fact that FTAZ and N2200 polymers show complementary spectral absorption ranges, II) appropriate energy levels as well as III) good thermomechanical properties suited for high-T rubbing. Most importantly, the FTAZ/N2200 blend films display high alignment upon rubbing.[32]

5.4. Polarized OSCs based on the aligned blend films of PBnDT-FTAZ:N2200

We first present the results relative to the alignment of the FTAZ:N2200 blends and demonstrate how it is possible to align both polymers by a combination of rubbing and thermal annealing. We also investigate the impact of alignment conditions on the structure of the blend films. In particular, N2200 is known to show a specific polymorphism that depends on the temperature of rubbing and annealing. We will investigate how both parameters rubbing temperature (T_r) and annealing temperature (T_A) affect the structure in FTAZ:N2200 blends. In a further section we describe their anisotropic PV properties.

5.4.1 Experimental section

Materials and film preparation

The PBnDT-FTAZ and P(NDIT2OD-T2) polymers were synthesized by Wenziz Muzuzu and Dr. Nicolas Leclerc at ICPEES. Both of FTAZ and N2200 polymers used in the blends have a high weight average molecular weight (M_w). The molecular parameters of FTAZ and melting point of N2200 are show in **Table 2**. In our case, the Mw and the number average molecular weight (M_n) of N2200 could not be accurately determined mainly due to the aggregation in the Size exclusion chromatography (SEC) columns. This phenomenon implies that the acceptor probably has very high molecular weight. Melting points were determined by differential scanning calorimetry (DSC) (Figure S1 in Annex). It is noteworthy that we do not observe a pronounced peak for DSC curves of FTAZ even at 400°C.

Table 2. *Molecular parameters including M_w, M_n and polydispersity index (Đ) of FTAZ and melting point (T_m) of N2200.*

	M_w (kg.mol^{-1})	M_n (kg.mol^{-1})	Đ	T_m (°C)
PBnDT-FTAZ	102	62	1.65	> 400°C ?
N2200	-	-	-	297

For preparation of neat polymer films, the PBnDT-FTAZ and P(NDIT2OD-T2) solution were separately prepared with a concentration of 6 mg/mL in chlorobenzene. The solutions were heated at 90°C for 24 h. The PBnDT-FTAZ layers were deposited on the glass substrate by spin coating at 2000 rpm for 60 s. The neat P(NDIT2OD-T2) films were spin coated at 1000 rpm for 60s. All films were dried by annealing at 135°C for 15 min after spin coating.

For preparation of blend films, the PBnDT-FTAZ and P(NDIT2OD-T2) polymers with a 1:1 weight ratio were dissolved in chlorobenzene solution with a total concentration of 20 mg/mL. The blend solution was heated at 90°C for 24 h and filtrated before spin coating. The BHJ layer (~ 92 nm) was spin coated at 2000 rpm for 60 s and subsequently annealed at 135°C for 10 min to remove the residual solvent. All film preparations (solution preparation, spin coating and annealing steps) were performed in glove box.

Rubbing and thermal annealing process

To study the impact of rubbing temperature on the film alignment, the neat polymer films and FTAZ:N2200 films were aligned at various rubbing temperatures (160, 180 and 200°C). The other rubbing parameters are constant, including 2 rubbing cycles and F_r=7.36 N. After rubbing step, the thermal annealing of PBnDT-FTAZ, N2200 polymers as well as the blend films were performed in a Linkam hot stage under inert atmosphere at the required temperature (250, 275, 300 or 325 °C). The annealing duration is 5 min. Both heating and cooling rates were 30 °C.min^{-1}.

Solar cell fabrication

The solar cells based on the aligned PBnDT-FTAZ and N2200 polymers were fabricated with an inverted structure as follows: glass/ITO/ZnO/ aligned PBnDT-FTAZ: N2200/ floated PBnDT-FTAZ: N2200/MoO$_3$/Ag. The transporting layers (ZnO and MoO$_3$) and electrode (Ag) were deposited

following the same methodology mentioned before. The FTAZ:N2200 layers were deposited on the top of ZnO and rubbed at 200°C. In order to avoid the leakage current caused by the pinholes in oriented films, a thin FTAZ:N2200 layer was deposited on the top of aligned films by a floating method. To prepare the thin layer, clean glass substrates were first coated with a thin film of 10 wt% NaPSS aqueous solution (poly(sodium 4-styrenesulfonate)) by spin-coating at 3000 rpm for 45 s. A thin FTAZ:N2200 layer (~35 nm) was then spin coated on top of the NaPSS layer from a concentration of 6mg/mL in CB solution. The films were slowly immersed in water to dissolve the NaPSS sacrificial layer. Floated films of PBnDT-FTAZ:N2200 were collected on the partially complete device stack (glass/ITO/ZnO/ aligned PBnDT-FTAZ: N2200). Then, thermal annealing was achieved under the optimized conditions (T_A=300°C for 5 min, with a heating rate of 30°C/min and cooling rate of 10 °C/min).

HR-TEM analysis

The HR-TEM images for oriented blends of PBnDT-FTAZ and N2200 polymers were performed in a modified low-dose mode to avoid beam damage of thin organic films. The detailed low-dose method to obtain HR-TEM images is described in reference[33].

Scanning electron microscope (SEM) characterization

SEM is widely used to study the surface topography, crystalline structure and chemical composition of materials. The measurements were performed by Alain Carvalho using Hitachi FEG (Field Emission guns)-SEM SU-8010 at the Institute Charles Sadron. The SEM operates with a primary electron energy of 5 kV, the incident electron beam is radiated to the materials and scans the surface. The interaction of the low-energy electron beam with the materials produces secondary electrons and some backscattered electrons. The secondary electrons can only escape from the near-surface of the materials, providing a topographic information. Meanwhile, backscattered electrons are collected by the secondary electron detectors, thus some compositional contrast is also present in the SEM images.

5.4.2 Results and discussion

### a) Identification of optimal rubbing conditions

In a first step, we determined the optimal rubbing conditions for the polymers and for their blends (with a 1:1 weight ratio of FTAZ and N2200). For the means of comparison, the PBnDT-FTAZ and N2200 polymers were separately aligned at various rubbing temperatures to identify the optimal alignment parameters. Then, the study was conducted on PBnDT-FTAZ: N2200 blends to identify if rubbing differs from the single components. Most importantly, the rubbing temperature (T_r) that is required must correspond to the highest orientation of both FTAZ and N2200.

Figure 11a depicts polarized absorption spectra of neat FTAZ films oriented at different T_r. The spectra POL//R shows evident vibronic structures including A_{0-1} and A_{0-0} peaked at 540 and 585 nm, respectively. At T_r= 160°C, the intensities of the 0-0 and 0-1 components are almost equivalent. Interestingly, when T_r increased to 180°C, the 0-1 component is obviously reduced, leading to an increase of the ratio A_{0-0}/A_{0-1}. This result implies that increasing T_r gives rise to a longer conjugation length of FTAZ. Moreover, the film alignment was significantly improved with a DR of 4 at 585 nm (**Figure 11b**). However, a higher T_r results in a slight decrease of DR. As a result, the optimal rubbing temperature to orient FTAZ polymers is close to 180°C.

Previous investigations by Untilova et al. showed that the best T_r for N2200 is observed for T_r= 240°C with DR=3.3. In our case, T_r= 200°C, leads to DR = 3.1. **Figure 11c** shows polarized absorption spectra of neat N2200 polymers oriented at an optimal rubbing temperature (T_r = 200°C). Two main absorption bands are visible: one maximum absorbance at around 390 nm is assigned to the π- π* transition; another peak at around 700 nm corresponds to a charge transfer (CT) transition along the polymer backbone. For POL//R, the low-energy CT band mainly contains a band absorption at 700 nm and two shoulders at 640 and 800 nm, respectively. The aligned N2200 polymers display polarized absorption with a DR of 3.2 at 700 nm.

For FTAZ:N2200 blend films, the impact of rubbing temperature on the film alignment can be observed in **Figure 11d**. For POL//R, the ratio A_{0-0}/A_{0-1} of FTAZ is larger at a higher rubbing temperature, which is similar to that observed in oriented neat FTAZ polymers. Increasing T_r results in better planarization of FTAZ backbones. The DR of N2200 and FTAZ in blends as a function of rubbing temperature are given in **Figure 11e**. The alignment of both of FTAZ and

N2200 can be improved by increasing the rubbing temperature. However, the DR values are still modest even for T_r= 200°C: DR=4.2 for FTAZ and DR=3.6 for N2200. A higher rubbing temperature might cause physical damage to the films. As demonstrated in a previous publication[6], a thermal annealing step after rubbing can further optimize the FTAZ:N2200 film alignment. Therefore, we explored the possibility to improve alignment of neat polymers and their blends by combining rubbing and thermal annealing after rubbing.
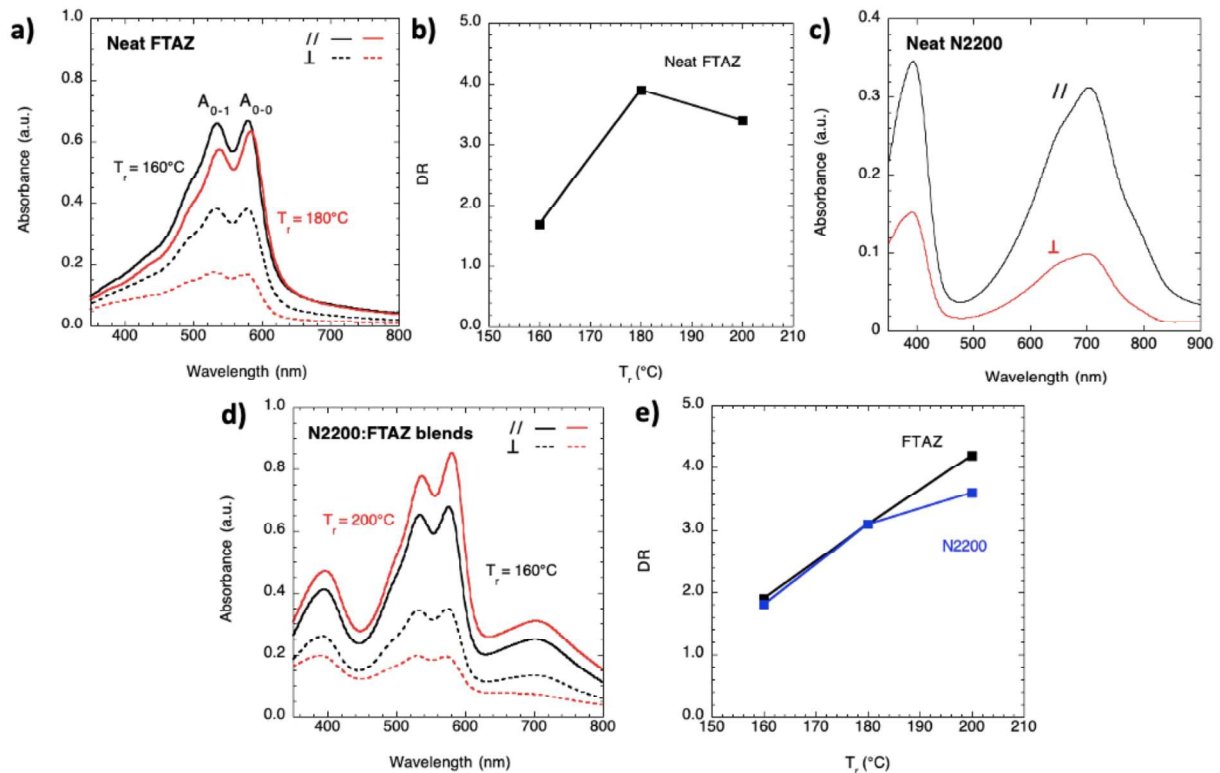
Figure 11. *a) Polarized UV-vis spectra of FTAZ films at different rubbing temperatures: T_r= 160°C (black) and T_r= 180°C (red). The incident light polarization is parallel (solid lines) and perpendicular (dotted lines) to the rubbing direction. b) Evolution of DR at 585 nm for aligned FTAZ films as a function of rubbing temperature. c) Polarized UV-vis spectra of N2200 polymers aligned at an optimal rubbing condition (T_r= 200°C, F_r=7.36 N). d) Polarized UV-vis spectra of FTAZ:N2200 films at different rubbing temperature: T_r= 160°C (black) and T_r= 200°C (red). e) Evolution of DR at 700 nm for rubbed N2200 films (blue) and DR at 585 nm for aligned FTAZ films (black) versus rubbing temperature.*

b) Impact of thermal annealing on orientation of blend films

Optimal thermal annealing conditions (annealing temperature T_A and duration) were identified to orient the polymers and blend films. The impact of thermal annealing on the

alignment of FTAZ, N2200 and their blends was studied by polarized UV-vis spectroscopy (**Figure 12 and Figure 13**). The results indicates that DR can be significantly increased upon thermal annealing for all films.

For pure FTAZ, a maximum DR of ~9 was observed at T_A= 250°C for 5 min. (**Figure 12a**). A higher annealing temperature leads to a decrease in DR. As depicted in **Figure 12b**, the ratio of A_{0-0}/A_{0-1} was reduced for films annealed at 250°C, implying a slightly shorter conjugation length. For pure N2200 polymers, a progressive increase in DR from 3 to 5 was observed as T_A was increased from 250 to 325°C (5 min) (**Figure 12c**). For T_A>325°C, the DR of films starts to decrease. At 325°C, T_A is higher than T_m (**Table 2**), the melting of N2200 crystals occurs, causing the loss of alignment. **Figure 12d** shows the absorption spectra for aligned N2200 films before and after thermal annealing. After annealing, the CT band shows a more pronounced vibronic structure. The absorption band at 640 nm is greatly enhanced, whereas the absorption at 800 nm is reduced. The variation of low-energy band is likely due to the presence of different categories of aggregates in N2200 films. According to the different stacking modes, the N2200 aggregates are classified into two polymorphs (**Figure 12e**): I) form I is composed of a segregated stacking of NDI and T2 units; II) form II corresponds to a mixed stacking of NDI and T2 units, which is caused by a ~c/2 shift between successive π-stacked chains.[34] The characteristic signatures of form I and form II in UV-vis spectra were reported by Brinkmann et al. Form I involves a shoulder at 800 nm, and form II is characterized by a prominent absorption band at 640 nm. In our case, the spectra for polymers rubbed at 200°C indicate that the films consist mainly of form I. The spectra for oriented films annealed at 325 °C are typical of a dominant form II. Therefore, we concluded that the thermal annealing leads to a transformation of form I into form II which is thermodynamically more stable.
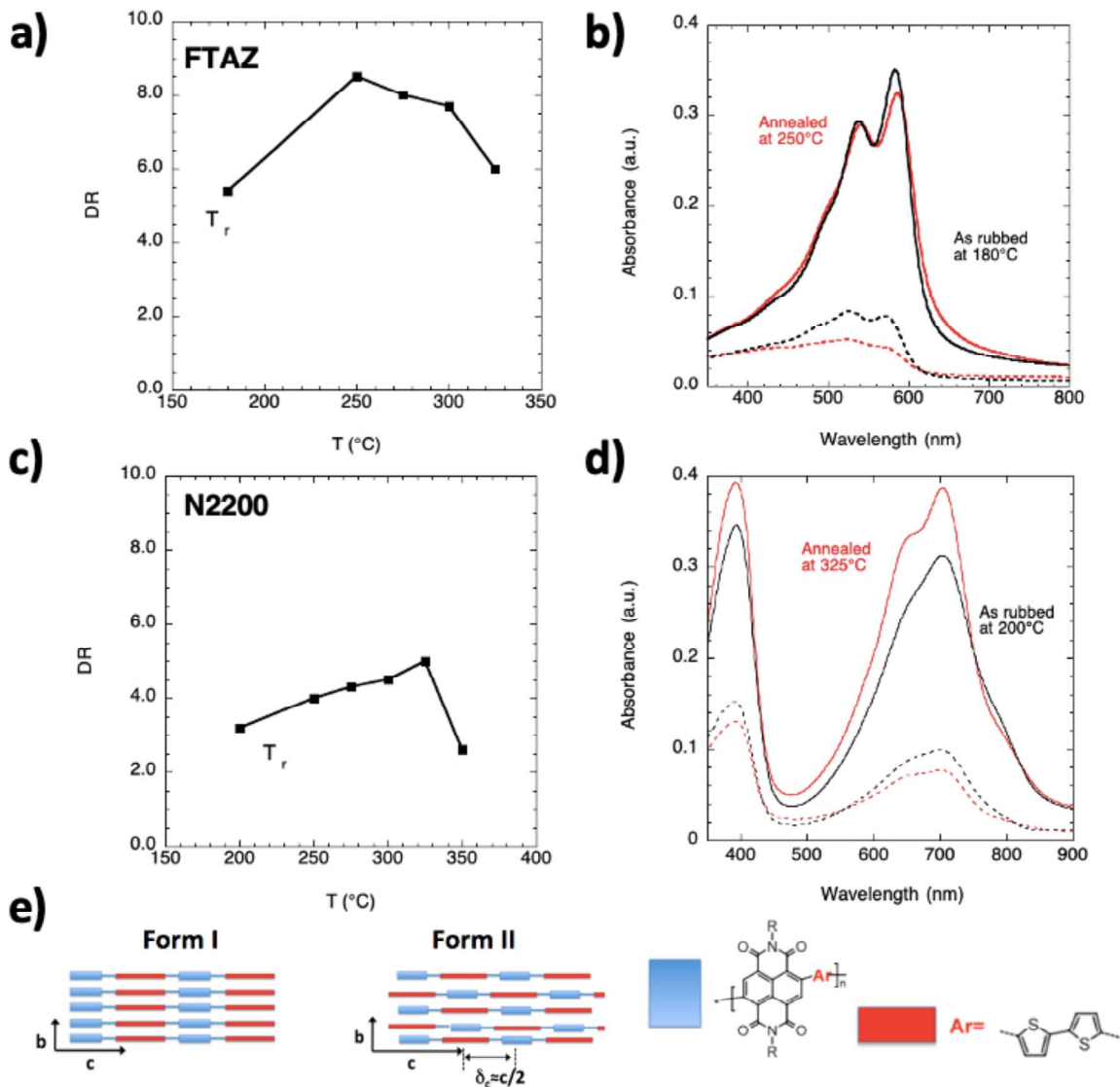
Figure 12. *a) Evolution of DR at 585 nm for aligned FTAZ films as a function of the post-rubbing annealing temperature. The FTAZ films were rubbed at 180 °C (T_r) before annealing. b) Polarized UV-vis spectra of rubbed FTAZ films under different annealing conditions: no-annealing (black) and annealing (red) at 250 °C. c) Evolution of DR at 700 nm for rubbed N2200 films as a function of annealing temperature. The oriented films were first rubbed at 200 °C. d) Polarized UV-vis spectra of oriented N2200 films before annealing (black) and after annealing (red) with an optimal temperature of 325 °C. e) Schematic illustration for polymorphs of N2200 polymers: Form I containing the segregated stacking of NDI (light blue) and T2 (red) units and Form II composed of mixed stacking of two units. Reproduced from [34]*

For FTAZ: N2200 blend films, a DR of FTAZ can reach approximately 14 after optimal annealing (T_A= 325 °C for 5 min), this is a 3.6-fold improvement over non-annealed films (**Figure 13a**). The DR of N2200 polymers slightly increase also from 4 to 6 after annealing. For T_A ≥ 325°C, the DR of blends decreases drastically. In particular, the DR of N2200 is lower than that of the

rubbed film. Therefore, the reduced alignment is related to the melting of N2200. Interestingly, rubbing leads to similar degrees of alignment for both polymers, but annealing results in a greater improvement in orientation for FTAZ. The polarized absorption spectra for rubbed blend films before and after annealing at 325 °C are given in **Figure 13b**. The annealed films are dominated by form II of N2200 due to the presence of band at 640 nm, similar to that observed in annealed pure N2200 films.
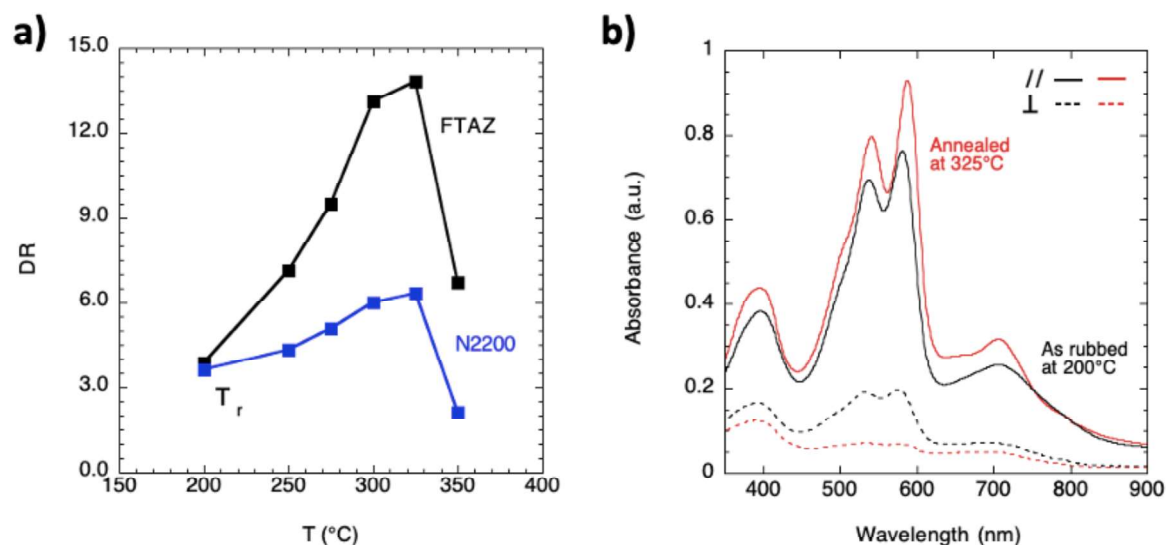
Figure 13. *a) Evolution of DR at 585 nm for aligned FTAZ polymers as well as DR at 706 nm for oriented N2200 polymers in blend films versus annealing temperature. The FTAZ/N2200 blend films were rubbed at 200 °C (T_r) before annealing. b) Polarized UV-vis spectra of rubbed blend films under different annealing conditions: as-rubbed (black) and after annealing (red) at 325 °C.*

c) Impact of T_r and T_A on the structure of aligned blend films

Electron diffraction was used to probe the film structure *versus* alignment parameters (T_r, T_A) for neat and blend films to further understand the variation of crystalline structure pre-and post-annealing. In a second step, Low dose High-resolution transmission electron microscopy (HRTEM) was also used to visualize the nanomorphology in the rubbed blend films.

Figure 14a,b depicts the ED patterns for neat aligned FTAZ films before and after thermal annealing. The pre-anneal and post-anneal d_{hkl} values of the reflections are summarized in **Table 3**. The oriented FTAZ film shows a relatively low crystallinity manifested by a single equatorial 1 0 0 reflection with an inter-chain distance d_{100}=19.26 Å, suggesting a preferential face-on crystal orientation. After thermal annealing, the ED patterns show additional
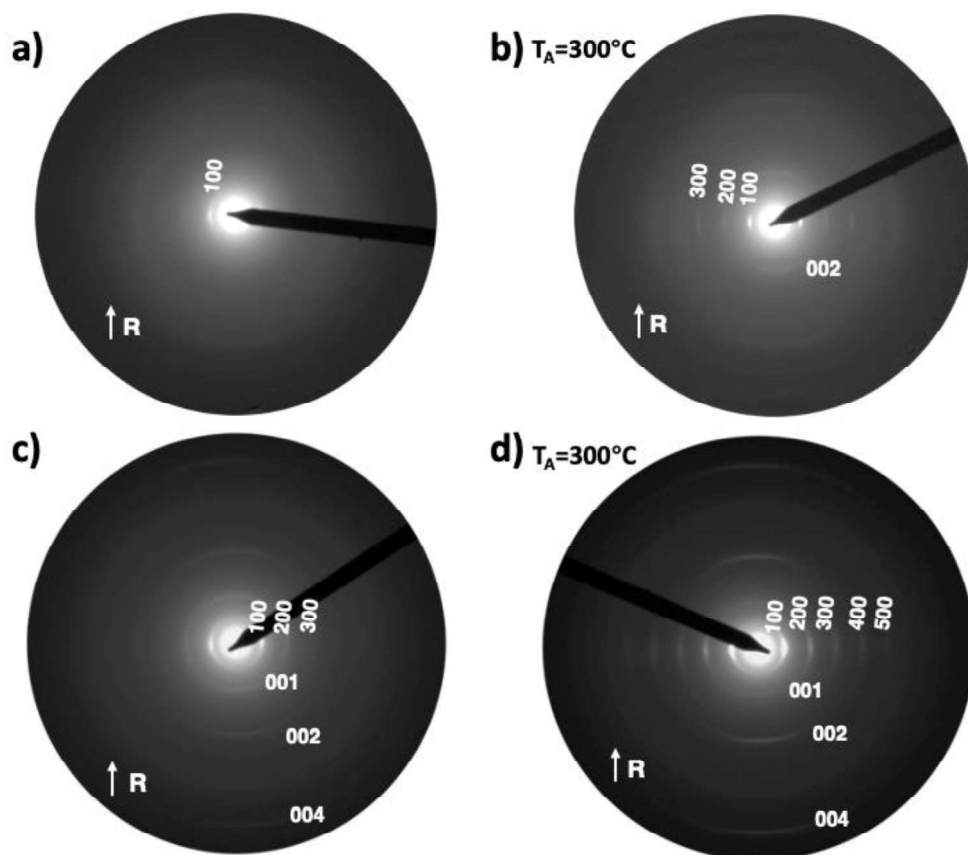
reflections such as h 0 0 (h=1,2,3) and the meridional 0 0 2 (**Figure 14b**). The results imply that rubbed FTAZ polymers contains mainly disordered domains with poor order that is nicely improved upon thermal annealing at 300°C. In particular, the appearance of 2 0 0 and 3 0 0 reflections indicates improved order in the side chain direction of FTAZ domains, as observed for annealed P3HT for instance.[35] In addition, thermal annealing further improves in-plane orientation of FTAZ domains as the angular spread of the 1 0 0 reflection is reduced as compared to the as-rubbed films (**Figure 14a**).

The ED pattern of the as-rubbed N2200 films presents h 0 0 reflections (h=1,2,3) along the equator as well as 0 0 l reflections (l=1,2,4) along the meridian (**Figure 14c**). The h 0 0 reflections correspond to an inter-chain distance of 25.68 Å along the side chain direction (d_{100}), the 0 0 l reflections correspond to the monomer repeat unit along the polymer backbone with a period of 13.34 Å. These values are close to these reported in previous publications.[34,36] The absence of the equatorial 0 2 0 reflection indicates that crystalline domains have a face-on orientation.

ED analysis of the films after thermal annealing at 300°C indicates that the face-on orientation of crystalline N2200 domains (**Figure 14d**) is preserved. The d_{hkl} values of the reflections from **Figure 14c,d** are collected in **Table 3**. As compared to as-rubbed films, the ED pattern after annealing shows brighter and sharper h 0 0 reflections (h=1,2,3,4), suggesting that crystallinity is significantly increased. Furthermore, **Figure 14c** shows that the intensity of meridional 0 0 l reflections follows the sequences $I_{001} > I_{002}$ and $I_{001} > I_{004}$. This indicates that as-rubbed N2200 films are made of form I. The strong intensity of the 0 0 1 reflection is the fingerprint of segregated stacking of NDI and T2 units in form I. In strong contrast, after thermal annealing, the intensity sequence in **Figure 14d** is different: $I_{001} < I_{002} \approx I_{004}$. This implies that form I was transformed into form II upon annealing as observed by UV-vis spectroscopy. The intensity of the 0 0 1 reflection is remarkably reduced in form II films of N2200, this is a fingerprint of form II N2200 films with a mixed stacking of NDI and T2 units. Annealing results also in small changes of lattice parameters (**Table 3**). The results are in line with polarized UV-vis spectra of N2200 polymers.

Table 3. *Reticular distances obtained from ED patterns of oriented PBnDT-FTAZ and N2200 films in Figure 14.*

		h k l	**Pre-anneal d$_{hkl}$ (Å)**	**Post-anneal d$_{hkl}$ (Å)**
Neat PBnDT-FTAZ	Equatorial reflections	1 0 0	19.26	19.07
		2 0 0	-	9.35
		3 0 0	-	6.23
	Meridional reflection	0 0 2	-	9.09
Neat N2200	Equatorial reflections	1 0 0	25.68	25.02
		2 0 0	13.21	12.55
		3 0 0	8.58	8.39
		4 0 0	-	6.26
		5 0 0	-	5.07
	Meridional reflections	0 0 1	13.34	13.79
		0 0 2	6.82	7.02
		0 0 4	3.65	3.51

Figure 14. *ED patterns of aligned FTAZ films a) as-rubbed at 180°C and b) after annealing at 300°C for 5 min and of oriented N2200 films c) as-rubbed at 200°C and d) after annealing at 300°C for 5 min. R is rubbing direction.*

Let us now consider the impact of thermal annealing on the structure of the blend films. **Figure 15** depicts ED patterns for aligned blend films as rubbed and after annealing. The reticular distances of the main reflections are collected in **Table 4**. For aligned blend films (**Figure 15a**), only reflections of N2200 polymers corresponding to form I are visible. In particular, the 1 0 0 of FTAZ is absent in the blend films, indicating that crystallization and ordering of FTAZ is difficult in the blends in the presence of N2200. N2200 seems thus to hamper ordering of FTAZ. Interestingly, after thermal annealing at 300°C (**Figure 15b**), the 1 0 0 and 0 0 1 reflections of FTAZ become visible beside those of N2200. As expected, thermal annealing at 300°C induces the structural modification form I $\rightarrow$ form II of N2200. Most importantly, both N2200 and FTAZ show a face-on orientation of crystalline domains after thermal annealing. Such an orientation of crystals is expected to lead to efficient charge transport in an OSC. The section profiles of ED patterns along the equatorial direction for neat and blend films are shown in **Figure 15c, d.** After thermal annealing, the intensities of the reflections in neat films and in blend films are obviously enhanced. However, the reflections of blend films are not exactly the superposition of reflections of neat N2200 and FTAZ films. This result implies that the ordering of donor and acceptor upon annealing is influenced by their interaction in the blends.

Table 4. *Reticular distances obtained from ED patterns of blend films in Figure 15a,b.*

Polymer in blends		*h k l*	Pre-anneal d_{hkl} (Å)	Post-anneal d_{hkl} (Å)
PBnDT-FTAZ donor	Equatorial reflection	1 0 0	-	18.80
	Meridional reflection	0 0 2	-	9.71
N2200 acceptor	Equatorial reflections	1 0 0	22.78	24.72
		2 0 0	-	12.54
	Meridional reflections	0 0 1	13.95	-
		0 0 2	7.00	7.00
		0 0 4	3.52	3.53
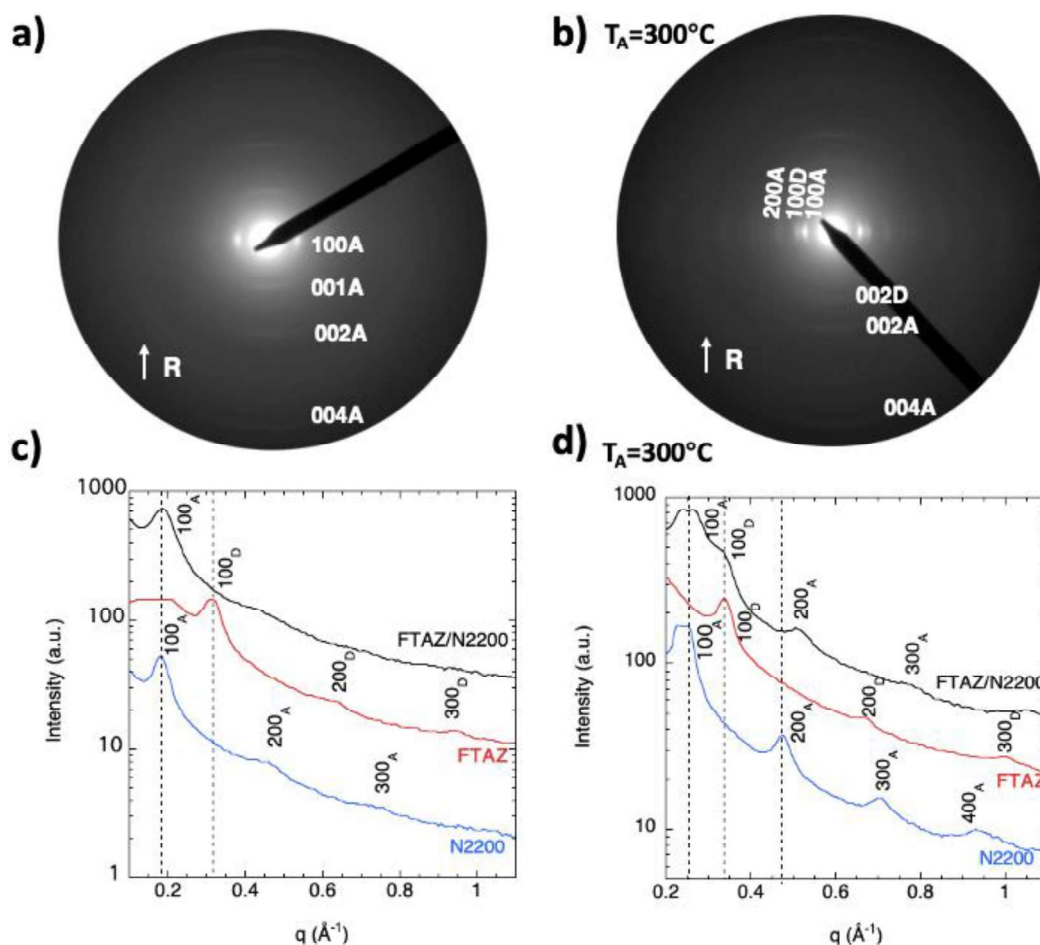
Figure 15. *ED patterns of FTAZ:N2200 blend films a) as-rubbed at 200°C and b) after annealing at 300°C for 5 min. The index A stands for N2200 whereas the index D for FTAZ. The arrow R indicates the rubbing direction (polymer chains direction). Intensity profiles along the equator of the ED pattern for oriented FTAZ, N2200, and FTAZ:N2200 blend films c) as-rubbed at 200°C and d) after annealing at 300 °C.*

d) Impact of T$_r$ and T$_A$ on the film nanomorphology

HR-TEM in low dose was used to visualize the different crystalline domains of FTAZ and N2200 in blend films as well as their in-plane alignment. This method allows also to estimate in-plane dimensions of the nano-crystalline domains of N2200 and FTAZ. The crystalline domain size has a significant influence on the charge transport and thus on the OSCs performance. As demonstrated in previous publications, low dose HR-TEM allows to visualize face-on oriented domains of the polymers P3HT and N2200 because of the contrast existing between electron-dense layers of sulfur-containing polymer backbones and layers of side chains.[4,34] In our case, both FTAZ and N2200 show crystalline domains with a face-on orientation, making it possible to observe them by HR-TEM.

Figure 16 depicts HR-TEM images for blend films rubbed at 200 °C and subsequently annealed at 300°C. The HR-TEM images show fringed patterns with two different periodicities, that correspond to oriented FTAZ and N2200 domains in the films. The observed periodicities correspond to the distances d_{100} between adjacent polymer backbones separated by side chains, also observed in the ED patterns. According to ED, the crystalline domains of the two polymers can be distinguished in HR-TEM images since FTAZ shows d_{100}=1.9 nm *versus* 2.4-2.5 nm for N2200. The periodic patterns of nano-crystals are also observed in the fast Fourier transformation (FFT) of HR-TEM images, as shown in the inset of **Figure 16**. Two close spots are visible in the FFT, they correspond to the 1 0 0 reflections of N2200 and of FTAZ.

The size of crystalline domain of donors and acceptors can be extracted from the HR-TEM images. The average length of FTAZ stem in crystals is (15 ± 1) nm, and its average crystal size along the side chain direction is (10 ± 1) nm. The N2200 polymers possess an average stem length of (14 ± 1) nm in crystalline domains and an average crystal size of (16 ± 3) nm along the side chain direction. The results indicate that the average crystal domain size of N2200 is slightly larger than that of FTAZ, which is consistent with the higher crystallinity of N2200 observed in ED patterns.

- PBnDT-FTAZ ($d_{100} \approx$ 1.9 nm)   - N2200 (d_{100} = 2.4 ~ 2.5 nm)
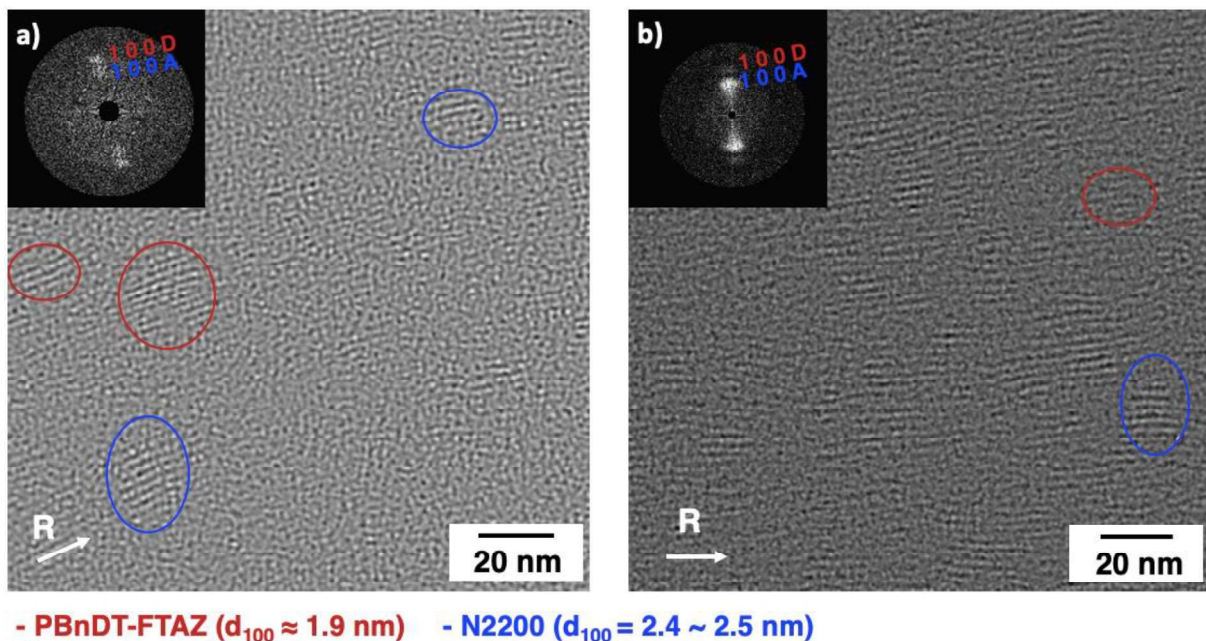
Figure 16. a) and b) HR-TEM images measured in two zones of FTAZ:N2200 blend films after rubbing at 200 °C followed by thermal annealing at 300 °C. The red and blue circles outline the crystalline domains of FTAZ and N2200 polymers, respectively. R is the rubbing direction, i.e., the polymer chain direction. The insets correspond to the fast Fourier transform of the HR-TEM images. A and D labels are used for N2200 and FTAZ, respectively.

**e) Fabrication of aligned heterojunctions of FTAZ/N2200**

The highly oriented blend films were integrated into OSCs with an inverted architecture (glass/ITO/ZnO/oriented FTAZ: N2200/MoO$_3$/Ag). The active layer was directly deposited on the top of a ZnO/ITO substrate, then aligned by rubbing and annealed at 300 °C (optimal condition). In order to confirm if the high temperature affects the operation of the OSCs, we first fabricated OSCs based on non-oriented active layers annealed at different temperatures: 135 °C (as a reference) and 300 °C (as a sample). The J-V characteristics of the devices measured under darkness and under illumination are shown in **Figure 17a**. The PV parameters are summarized in **Table 5**. The reference cell exhibits a V$_{oc}$ of 0.87 V, a J$_{sc}$ of 8.42 mA.cm^{-2} and a good maximum power conversion efficiency (PCE = 4.02 %). For the OSCs annealed at 300 °C (red lines), the V$_{oc}$ (0.87 V) remains constant. However, a significant decrease in J$_{sc}$ (2.06 mA.cm^{-2}) is observed and results in a lower PCE (0.70 %). The reduced photocurrent suggests a pronounced phase separation between donors and acceptors during annealing.[6] Although the annealed films show a modest photovoltaic performance, the unchanged photovoltage is larger than the LC threshold voltage, which is necessary to enable the fabrication of self-powered PSLM devices.

The OSCs based on the aligned active layer were prepared with optimal rubbing and annealing conditions. However, the J-V curves show a leakage current probably due to scratches created by mechanical rubbing (**Figure 17b**). The leakage current results in a loss in V$_{oc}$.

The output current density J (I, V) can be expressed as[37]:

$$J(I,V) = J_{obs}(V) - J_{ph}$$

<div align="right">*Eq.5.4*</div>

Where J$_{obs}$(V) is current density under dark as a function of applied voltage. J$_{ph}$ is photocurrent density delivered by PV layers. If J (I, V) =0, J$_{ph}$ is equal to J$_{obs}$ (V=V$_{oc}$). The leakage current does not influence on the J$_{ph}$ but gives rise to a low R$_{sh}$ and an increase in J$_{obs}$ (V), implying that a lower applied voltage is required for J$_{ph}$ = J$_{obs}$. Thus, V=V$_{oc}$ is decreased.
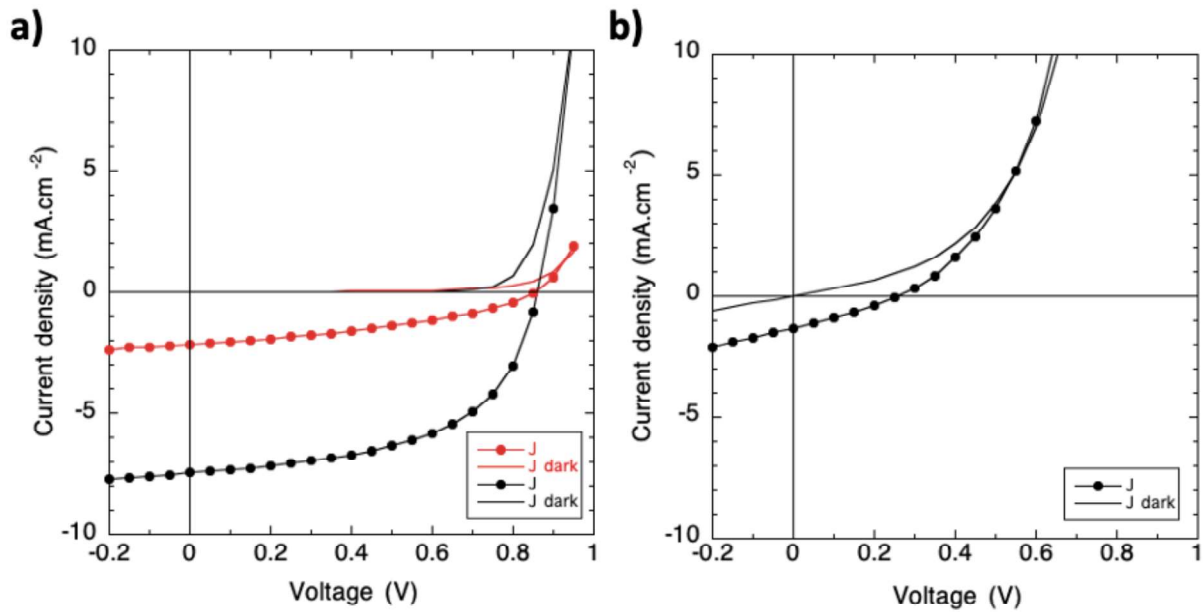
Figure 17. *a) J-V characterization of OSCs based on a non-aligned FTAZ/N2200 film (black lines) and on the film annealed at 300 °C for 5 min (red lines). The OSCs measured in dark and upon standard 1.5 AM illumination (100 mW.cm⁻²). b) J-V characteristics of OSC based on the oriented FTAZ/N2200 PV layer under dark (black lines) and standard 1.5 AM illumination (black circles).*

Table 5. *PV parameters for OSCs annealed at 135°C for 15 min and at 300 °C for 5 min.*

Annealing conditions	V_{oc} (V)	J_{SC} (mA.cm⁻²)	FF (%)	PCE (%)
135°C for 15 min	0.87 ± 0.01	8.42 ± 0.32	54.6 ± 0.2	4.02 ± 0.17
300°C for 5 min	0.87 ± 0.01	2.06 ± 0.05	38.6 ± 0.5	0.70 ± 0.01

In order to determine the cause of the leakage current, the surface topography of rubbed films on the ZnO (7~10 nm)/ITO substrate was investigated by scanning electron microscope (SEM). As shown in **Figure 18**, the compositional contrast implies that the oriented films rupture down to the substrate. Since ZnO/ITO substrate containing heavier elements such as Zn and In relative to C, N, S, H in polymers leads to more backscattered electrons being collected and thus a brighter field in images. It is concluded that the mechanical rubbing process causes a physical damage of the oriented films including scratches (**Figure 18a**) and pin-holes (**Figure 18b**). In addition, **Figure 18b** appears to be an aggregate of polymer film carried away by friction transfer the rubbing cloth.
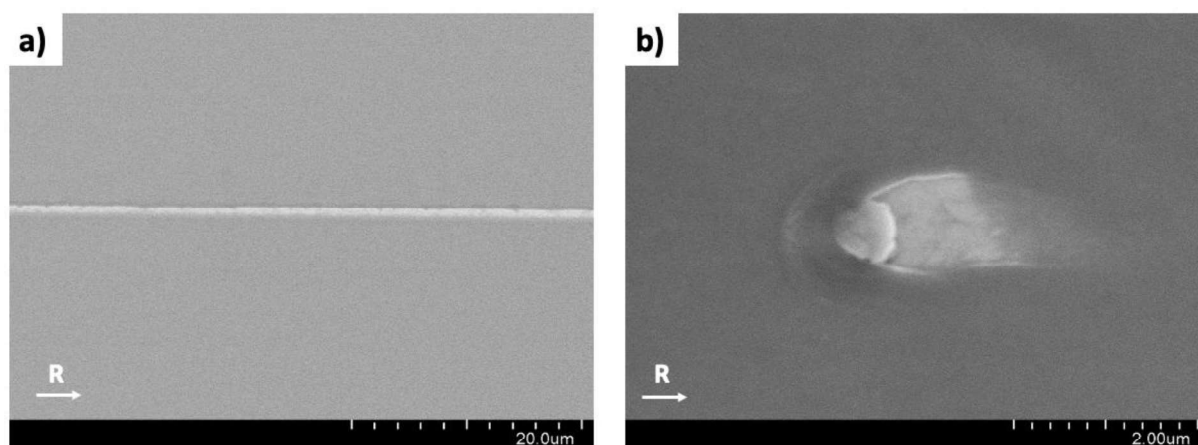
Figure 18. *SEM images of a rubbed FTAZ:N2200 film on the top of ZnO/ITO substrate measured at different scales a) and b).*

Rubbing and thermal annealing of FTAZ:N2200 blends results in high orientation of both polymers. However, the surface of the films presents some pin-holes and scratches that are responsible for leakage currents. We therefore developed a new strategy to avoid pin-holes. As shown in **Figure 19a**, a very thin non-oriented FTAZ-N2200 layer was deposited on the top of the rubbed FTAZ-N2200 film by floating. A thermal annealing of 300°C was subsequently applied to the films to smoothen the interface between non-aligned and the rubbed BHJ layers. The DR of FTAZ and N2200 polymers were determined following each step (including rubbing, floating and annealing). From **Figure 19b**, it is clear that the degree of alignment was reduced after addition of a non-aligned top layer. Through the thermal annealing, the films ultimately show the anisotropic optical properties with DR values of ~4 for FTAZ and of ~2 for N2200 (**Figure 19c**). The improvement in overall orientation of the film is attributed to I) an increase in DR for the rubbed films or II) to an epitaxial effect such that the bottom rubbed film induces some orientation of the top non-aligned layer along the rubbing direction. Additional experiments using GIWAXS are in progress to confirm this epitaxial orientation of the top layer by the rubbed bottom one.
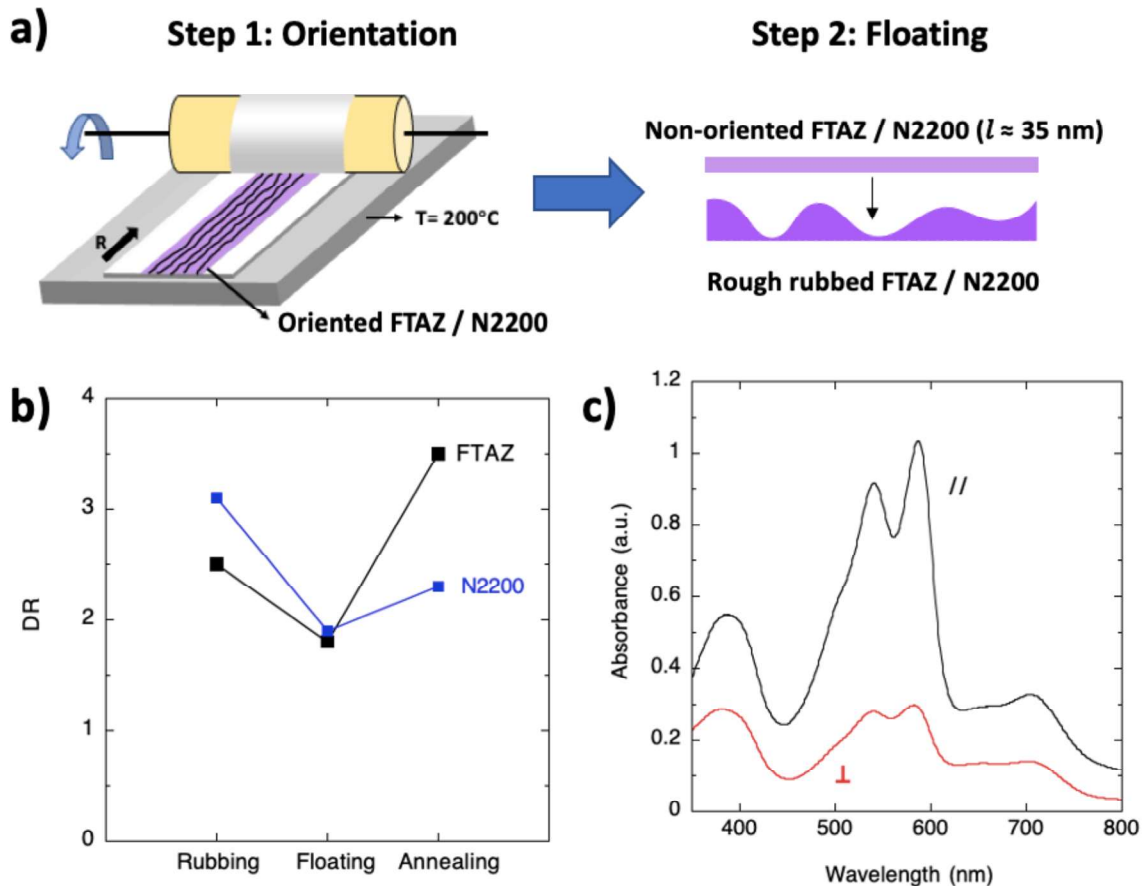
Figure 19. *a) New strategy to prepare aligned PV layers avoiding pin-holes. The FTAZ: N2200 film were first rubbed at 200°C. In a second step, a non-aligned FTAZ: N2200 film with a thickness of around 35 nm was floated atop the oriented blend film. b) Evolution of DR at 585 nm for aligned FTAZ polymers (black dot) as well as of DR at 706 nm for oriented N2200 polymers (blue dot) in blend films at each step to prepare floated PV layer on the oriented PV layer. c) Polarized UV-vis spectra for oriented FTAZ: N2200/ floated FTAZ: N2200 films after thermal annealing.*

A reference OSC based on a non-oriented FTAZ/N2200 film and a floated FTAZ/N2200 film was first fabricated. The reference device was tested under unpolarized AM 1.5G illumination, showing a PCE of 1.27% with V_{oc}=0.85 V, J_{sc}=3.55 mA.cm^{-2} and FF=41.5% (**Figure 20b**). The FF is similar to that of OSCs based on a single FTAZ/N2200 layer (FF=38.6%) in **Figure 17a**. The constant FF values suggest that floating a non-oriented FTAZ/N2200 film atop a rubbed blend film followed by the thermal annealing treatment does not cause more interfacial resistances in OSCs.

The oriented PV layers composed of the aligned FTAZ/N2200 film covered with a floated FTAZ/N2200 film were integrated into an OSC (**Figure 20a**). In the inset of **Figure 20c**, the pictures of the polarized solar cell for POL//R and POL⊥R points out the absorbance anisotropy.

The device was measured under polarized light parallel and perpendicular to the rubbing direction. A photocurrent anisotropy with a J_{sc} ratio of approximately 1.5 was observed. Although the J_{sc} ratio and DR of active layers are as large as those observed in OSCs based on oriented P3HT, the FTAZ/N2200 produces a higher photovoltage ($V_{oc} \approx 0.79$ V) and provides an available inverted structure for PSLM devices. Unfortunately, the integration of oriented PV layers into PSLMs have not yet been performed due to limited time.

Table 6. *PV parameters for OSCs based on the non-aligned PV layer (reference) and on the oriented PV layer (sample).*

	Test condition	V_{oc} (V)	J_{SC} (mA.cm^{-2})	FF (%)	PCE (%)
Reference	Unpolarized light	0.85 ± 0.01	3.55 ± 0.24	41.5 ± 1.4	1.27 ± 0.13
Sample	//	0.79 ± 0.01	0.85 ± 0.07	37.4 ± 0.7	0.25 ± 0.02
	⊥	0.77 ± 0.01	0.56 ± 0.04	40.2 ± 1.3	0.17 ± 0.01
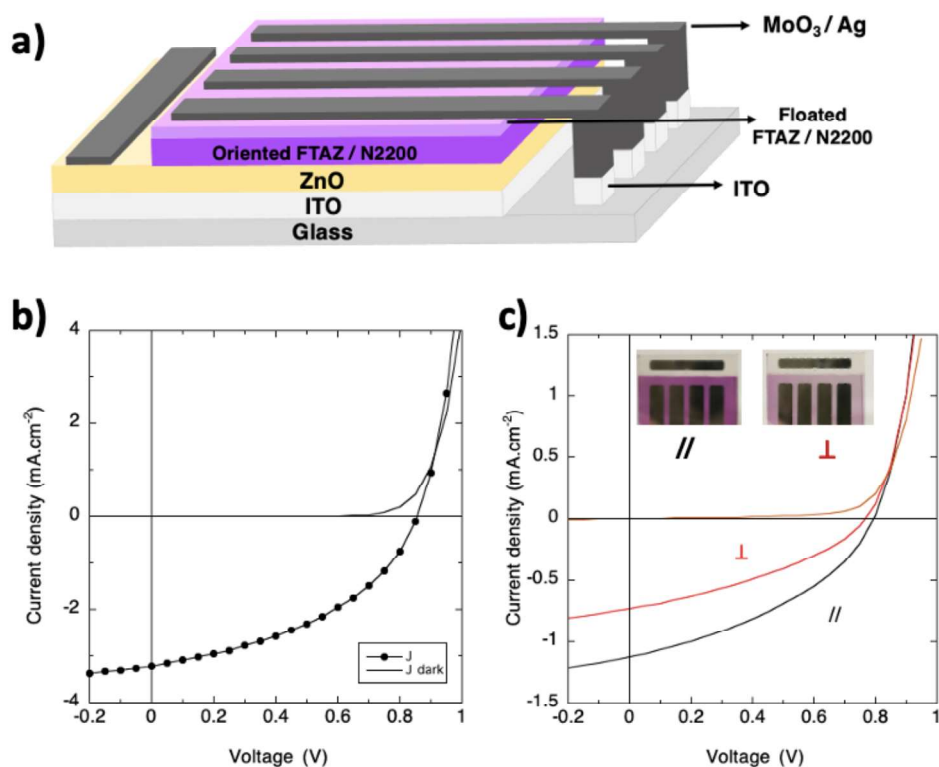
Figure 20. *a) Schematic illustration of polarized OSCs based on the oriented FTAZ/N2200 layer covered with a floated non-oriented FTAZ/N2200 layer. J-V characterization of OSC based on b) the non-aligned FTAZ: N2200/ floated FTAZ: N2200 films as a reference and c) the oriented FTAZ: N2200/ floated FTAZ: N2200 films as a sample. The reference was measured under dark and standard 1.5 AM illumination. The sample was tested in the dark and with polarizers under illumination. Inset: photos of a polarized solar cell for POL//R and POL⊥R.*

5.5 Conclusion

In this chapter, oriented PV layers could be achieved via rubbing P3HT polymers at 150°C followed by a deposition of $PC_{60}BM$ molecules. We discovered that the alignment and crystal structure of oriented P3HT films is largely influenced by the rubbing force. With increasing the rubbing force, the level of orientation is obviously enhanced and a transformation of edge-on to face-on crystal orientation is observed. The $PC_{60}BM$ molecules diffuse into the aligned P3HT polymer matrix upon annealing, forming a quasi-bilayer structure while maintaining the alignment of P3HT. Based on the quasi-bilayer structure, the polarized solar cells showed anisotropic optical and PV properties. Although increasing F_r leads to a more pronounced dichroic PV effect, the quality of the films is reduced probably due to more pinholes created by the mechanical rubbing. This causes a leakage current and decreases the generated photovoltage, which is no more sufficient to modify the LC orientation. Moreover, the quasi-bilayer standard structure is poorly adapted for PSLM applications. Since a suitable conducting HTL has not been found to integrate into PSLMs.

For these reasons, we exploited a different type of oriented PV layers containing PBnDT-FTAZ and N2200 polymers aligned by high temperature rubbing. The thermal annealing after rubbing gives rise to a large improvement of film alignment. Interestingly, according to distinct d_{100} periodicity of the two polymers, aligned crystalline domains of FTAZ and N2200 in blend films could be clearly observed in HR-TEM images. However, the quality of mechanically rubbed films is still problematic, when integrating such PV layer into solar cells, short circuits are caused by scratches and pinholes during rubbing. The local active area can be applied to polarization photodetector. However, it is insufficient for smart windows application. In order to avoid the leakage current in the whole device, a non-oriented FTAZ:N2200 thin layer is deposited on the top of oriented blend films to fill some scratches. The solar cells based on two PV layers eventually show a J_{sc} ratio of 1.5 and a DR of 4 while an active area attaining 0.12 cm^2 that is around 4 times larger than the active area measured in previous publication (**Table 7**).[6]

Table 7. *A comparison of our oriented OSCs with that reported in previous publication.*

	Reference[6]	Our results
Rubbing condition	T_r = 160°C, 40 rubbing cycles, by hand	T_r = 200°C, 1 rubbing cycle, by mechanical rubbing machine
DR of PV layer integrated into OSCs	17	4
$Jsc_{//}$ / $Jsc_{\perp}$	6.4	1.5
Active area for J-V measurements	0.0314 cm^2	0.12 cm^2

References

(1) Fall, S.; Wang, J.; Regrettier, T.; Brouckaert, N.; Ibraikulov, O. A.; Leclerc, N.; Lin, Y.; Elhaj, M. I.; Komitov, L.; Lévêque, P.; Zhong, Y.; Brinkmann, M.; Kaczmarek, M.; Heiser, T. Self-Powered Dynamic Glazing Based on Nematic Liquid Crystals and Organic Photovoltaic Layers for Smart Window Applications. *ACS Appl. Mater. Interfaces* **2023**, *15* (3), 4267–4274.

(2) Li, Q.; Yao, Z.; Lu, Y.; Zhang, S.; Ahmad, Z.; Wang, J.; Gu, X.; Pei, J. Achieving High Alignment of Conjugated Polymers by Controlled Dip-Coating. *Adv. Electron. Mater.* **2020**, *6* (6), 2000080.

(3) Biniek, L.; Leclerc, N.; Heiser, T.; Bechara, R.; Brinkmann, M. Large Scale Alignment and Charge Transport Anisotropy of PBTTT Films Oriented by High Temperature Rubbing. *Macromolecules* **2013**, *46* (10), 4014–4023.

(4) Hamidi-Sakr, A.; Biniek, L.; Fall, S.; Brinkmann, M. Precise Control of Lamellar Thickness in Highly Oriented Regioregular Poly(3-Hexylthiophene) Thin Films Prepared by High-Temperature Rubbing: Correlations with Optical Properties and Charge Transport. *Adv. Funct. Mater.* **2016**, *26* (3), 408–420.

(5) Zhu, R.; Kumar, A.; Yang, Y. Polarizing Organic Photovoltaics. *Adv. Mater.* **2011**, *23* (36), 4193–4198.

(6) Schrickx, H. M.; Sen, P.; Booth, R. E.; Altaqui, A.; Burleson, J.; Rech, J. J.; Lee, J.; Biliroglu, M.; Gundogdu, K.; Kim, B. J.; You, W.; Kudenov, M. W.; O'Connor, B. T. Ultra-High Alignment of Polymer Semiconductor Blends Enabling Photodetectors with Exceptional Polarization Sensitivity. *Adv. Funct. Mater.* **2022**, *32* (2), 2105820.

(7) Jimison, L. H.; Toney, M. F.; McCulloch, I.; Heeney, M.; Salleo, A. Charge-Transport Anisotropy Due to Grain Boundaries in Directionally Crystallized Thin Films of Regioregular Poly(3-Hexylthiophene). *Adv. Mater.* **2009**, *21* (16), 1568–1572.

(8) Sirringhaus, H.; Wilson, R. J.; Friend, R. H.; Inbasekaran, M.; Wu, W.; Woo, E. P.; Grell, M.; Bradley, D. D. C. Mobility Enhancement in Conjugated Polymer Field-Effect Transistors through Chain Alignment in a Liquid-Crystalline Phase. *Appl. Phys. Lett.* **2000**, *77* (3), 406–408.

(9) Grell, M.; Bradley, D. D. C. Polarized Luminescence from Oriented Molecular Materials. *Adv. Mater.* **1999**, *11* (11), 895–905.

(10) Memon, W. A.; Zhang, Y.; Zhang, J.; Yan, Y.; Wang, Y.; Wei, Z. Alignment of Organic Conjugated Molecules for High-Performance Device Applications. *Macromol. Rapid Commun.* **2022**, *43* (14), 2100931.

(11) Chen, X. L.; Bao, Z.; Sapjeta, B. J.; Lovinger, A. J.; Crone, B. Polarized Electroluminescence from Aligned Chromophores by the Friction Transfer Method. *Adv. Mater.* **2000**, *12* (5), 344–347.

(12) O'Connor, B.; Kline, R. J.; Conrad, B. R.; Richter, L. J.; Gundlach, D.; Toney, M. F.; DeLongchamp, D. M. Anisotropic Structure and Charge Transport in Highly Strain-Aligned Regioregular Poly(3-Hexylthiophene). *Adv. Funct. Mater.* **2011**, *21* (19), 3697–3705.

(13) Hartmann, L.; Tremel, K.; Uttiya, S.; Crossland, E.; Ludwigs, S.; Kayunkid, N.; Vergnat, C.; Brinkmann, M. 2D Versus 3D Crystalline Order in Thin Films of Regioregular Poly(3-Hexylthiophene) Oriented by Mechanical Rubbing and Epitaxy. *Adv. Funct. Mater.* **2011**, *21* (21), 4047–4057.

(14) van Aerle, N. A. J. M.; Tol, A. J. W. Molecular Orientation in Rubbed Polyimide Alignment Layers Used for Liquid-Crystal Displays. *Macromolecules* **1994**, *27* (22), 6520–6526.

(15) Itoh, S.; Hirosawa, I. Observation of an Optical Anisotropy of Rubbed Polyimide Film on Actual LCD Panel. *Mol. Cryst. Liq. Cryst. Sci. Technol. Sect. Mol. Cryst. Liq. Cryst.* **2001**, *367* (1), 745–752.

(16) Heil, H.; Finnberg, T.; von Malm, N.; Schmechel, R.; von Seggern, H. The Influence of Mechanical Rubbing on the Field-Effect Mobility in Polyhexylthiophene. *J. Appl. Phys.* **2003**, *93* (3), 1636–1641.

(17) Biniek, L.; Pouget, S.; Djurado, D.; Gonthier, E.; Tremel, K.; Kayunkid, N.; Zaborova, E.; Crespo-Monteiro, N.; Boyron, O.; Leclerc, N.; Ludwigs, S.; Brinkmann, M. High-Temperature Rubbing: A Versatile Method to Align π-Conjugated Polymers without Alignment Substrate. *Macromolecules* **2014**, *47* (12), 3871–3879.

(18) Vohra, V.; Arrighetti, G.; Barba, L.; Higashimine, K.; Porzio, W.; Murata, H. Enhanced Vertical Concentration Gradient in Rubbed P3HT:PCBM Graded Bilayer Solar Cells. *J. Phys. Chem. Lett.* **2012**, *3* (13), 1820–1823.

(19) Lee, K. H.; Schwenn, P. E.; Smith, A. R. G.; Cavaye, H.; Shaw, P. E.; James, M.; Krueger, K. B.; Gentle, I. R.; Meredith, P.; Burn, P. L. Morphology of All-Solution-Processed "Bilayer" Organic Solar Cells. *Adv. Mater.* **2011**, *23* (6), 766–770.

(20) Crossland, E. J. W.; Rahimi, K.; Reiter, G.; Steiner, U.; Ludwigs, S. Systematic Control of Nucleation Density in Poly(3-Hexylthiophene) Thin Films. *Adv. Funct. Mater.* **2011**, *21* (3), 518–524.

(21) Spano, F. C.; Silva, C. H- and J-Aggregate Behavior in Polymeric Semiconductors. *Annu. Rev. Phys. Chem.* **2014**, *65* (1), 477–500.

(22) Clark, J.; Silva, C.; Friend, R. H.; Spano, F. C. Role of Intermolecular Coupling in the Photophysics of Disordered Organic Semiconductors: Aggregate Emission in Regioregular Polythiophene. *Phys. Rev. Lett.* **2007**, *98* (20), 206406.

(23) Chen, D.; Liu, F.; Wang, C.; Nakahara, A.; Russell, T. P. Bulk Heterojunction Photovoltaic Active Layers via Bilayer Interdiffusion. *Nano Lett.* **2011**, *11* (5), 2071–2078.

(24) Treat, N. D.; Brady, M. A.; Smith, G.; Toney, M. F.; Kramer, E. J.; Hawker, C. J.; Chabinyc, M. L. Interdiffusion of PCBM and P3HT Reveals Miscibility in a Photovoltaically Active Blend. *Adv. Energy Mater.* **2011**, *1* (1), 82–89.

(25) Qi, B.; Wang, J. Fill Factor in Organic Solar Cells. *Phys. Chem. Chem. Phys.* **2013**, *15* (23), 8972.

(26) Finck, B. Y.; Schwartz, B. J. Understanding the Origin of the S-Curve in Conjugated Polymer/Fullerene Photovoltaics from Drift-Diffusion Simulations. *Appl. Phys. Lett.* **2013**, *103* (5), 053306.

(27) Xu, Z.; Chen, L.-M.; Yang, G.; Huang, C.-H.; Hou, J.; Wu, Y.; Li, G.; Hsu, C.-S.; Yang, Y. Vertical Phase Separation in Poly(3-Hexylthiophene): Fullerene Derivative Blends and Its Advantage for Inverted Structure Solar Cells. *Adv. Funct. Mater.* **2009**, *19* (8), 1227–1234.

(28) Polarization of Scattering by Rough Surfaces.

(29) Bergström, D.; Powell, J.; Kaplan, A. F. H. The Absorption of Light by Rough Metal Surfaces—A Three-Dimensional Ray-Tracing Analysis. *J. Appl. Phys.* **2008**, *103* (10), 103515.

(30) Price, S. C.; Stuart, A. C.; Yang, L.; Zhou, H.; You, W. Fluorine Substituted Conjugated Polymer of Medium Band Gap Yields 7% Efficiency in Polymer–Fullerene Solar Cells. *J. Am. Chem. Soc.* **2011**, *133* (12), 4625–4631.

(31) Yan, H.; Chen, Z.; Zheng, Y.; Newman, C.; Quinn, J. R.; Dötz, F.; Kastler, M.; Facchetti, A. A High-Mobility Electron-Transporting Polymer for Printed Transistors. *Nature* **2009**, *457* (7230), 679–686.

(32) Sen, P.; Yang, R.; Rech, J. J.; Feng, Y.; Ho, C. H. Y.; Huang, J.; So, F.; Kline, R. J.; You, W.; Kudenov, M. W.; O'Connor, B. T. Panchromatic All-Polymer Photodetector with Tunable Polarization Sensitivity. *Adv. Opt. Mater.* **2019**, *7* (4), 1801346.

(33) Brinkmann, M.; Rannou, P. Molecular Weight Dependence of Chain Packing and Semicrystalline Structure in Oriented Films of Regioregular Poly(3-Hexylthiophene) Revealed by High-Resolution Transmission Electron Microscopy. *Macromolecules* **2009**, *42* (4), 1125–1130.

(34) Brinkmann, M.; Gonthier, E.; Bogen, S.; Tremel, K.; Ludwigs, S.; Hufnagel, M.; Sommer, M.

Segregated *versus* Mixed Interchain Stacking in Highly Oriented Films of Naphthalene Diimide Bithiophene Copolymers. *ACS Nano* **2012**, *6* (11), 10319–10326.

(35) Salammal, S. T.; Mikayelyan, E.; Grigorian, S.; Pietsch, U.; Koenen, N.; Scherf, U.; Kayunkid, N.; Brinkmann, M. Impact of Thermal Annealing on the Semicrystalline Nanomorphology of Spin-Coated Thin Films of Regioregular Poly(3-Alkylthiophene)s as Observed by High-Resolution Transmission Electron Microscopy and Grazing Incidence X-Ray Diffraction. *Macromolecules* **2012**, *45* (13), 5575–5585.

(36) Tremel, K.; Fischer, F. S. U.; Kayunkid, N.; Pietro, R. D.; Tkachov, R.; Kiriy, A.; Neher, D.; Ludwigs, S.; Brinkmann, M. Charge Transport Anisotropy in Highly Oriented Thin Films of the Acceptor Polymer P(NDI2OD-T2). *Adv. Energy Mater.* **2014**, *4* (10), 1301659.

(37) Jao, M.-H.; Liao, H.-C.; Su, W.-F. Achieving a High Fill Factor for Organic Solar Cells. *J. Mater. Chem. A* **2016**, *4* (16), 5784–5801.

Chapter 6 Highly oriented conducting polymer films for PSLM applications

6.1 Motivation

Controlling solar heating (i.e., NIR light) through smart windows should be an effective way to improve the energy efficiency of buildings.[1] The NIR light intensity modulation could be achieved by combining a self-powered PSLM with commercial polarizers operating in the NIR region (See Chapter 3). However, these commercial polarizers are able to polarize not only NIR light but also visible light. Over 50% visible light is absorbed by the polarizers, reducing the transparency of the devices. Selecting polarizers with high transmittance in the visible range and strong NIR light polarization would be an elegant approach to enhance the transparency of PSLM devices. This chapter focuses accordingly on the possibility to introduce oriented polymer films with high NIR polarization into PSLM devices.

Doping highly oriented polymers such as P3HT or PBTTT has been demonstrated to reduced visible light absorption and generate anisotropic optical properties in the NIR region.[2–4] Therefore, such films have a potential to act as 'NIR polarizers' for PSLMs to modulate NIR light. In addition to optical properties, the doped oriented polymers also exhibit excellent charge conductivity.[2,5–7] The combination of high charge conductivity and reduced visible light absorption makes such doped polymer films promising materials to replace expensive and brittle ITO electrodes that are currently used in many electronic devices as well as our PSLM devices.

In this chapter, we focused on aligned P3HT films doped with magic blue (MB) that is a strong oxidant. The anisotropic electric and optical properties of MB-doped films are first investigated. In order to further understand the doping mechanism, we determined the amount of MB contained in the P3HT films and followed the structural changes induced by MB doping in rubbed P3HT films. A comparative study on structure-property correlations in P3HT doped with different dopants (MB, F_4TCNQ, $FeCl_3$, F_6TCNNQ, and $Mo(tdf-COCF_3)_3$) is presented. We test the optical modulation of the self-powered PSLM using MB-doped oriented polymer films. For NIR-controllable smart glazing systems, the NIR reflectivity of materials is essential to ensure the stability of devices. For this reason, the reflectance of MB-doped oriented films is also discussed.

6.2 Introduction

6.2.1 Doping mechanism

Doping of conjugated polymers leads to a remarkable increase of electrical conductivity as reported in the seminal work by Shirakawa and coworkers in 1977.[8] This interesting discovery initiated an extensive and systematic research on doped semiconducting polymers which can be widely used in organic electronic devices and thermoelectric application.[9–13] Doping is defined as the addition of impurities into a pure semiconductor in order to shift the energy levels, reduce the band gap and thus improve the electrical performance of the semiconductor. The doping of conjugated polymers can be achieved by either ion transfer (acid-base doping) or electron transfer (redox doping). In the case of redox doping, the electronic interaction between the conjugated polymer and the dopant occurs either following an integer charge transfer (ICT) mechanism or via the formation of a hybrid charge transfer complex between the polymer and the dopant (CTC).[14] The ICT mechanism involves a complete electron transfer from the HOMO level of the conjugated polymer to the LUMO level of dopants (p-type doping) or from the HOMO level of the dopant to the LUMO of the conjugated polymer (n-type doping). The charge carriers in polymers are either coulombically bound to the dopant counterions or free to move in the polymer matrix to ensure charge transport. The CTC is associated with the partial transfer between the conjugated polymers and the molecular dopants. It results from a hybridization of corresponding frontier molecular orbitals of the polymer and the dopant, leading to the creation of new local HOMO and LUMO states. In this chapter, we focus essentially on p-type redox doping. An energy offset (i.e., $EA_{dopant} > IP_{polymer}$) is favorable for effective p-type doping. Doping p-type conjugated polymers such as P3HT (IP≈4.8 eV) with F_4TCNQ (EA≈5.2 eV) has been demonstrated to involve an integer electron transfer (ICT).[5,14]

An example of chemical structures of P3HT, polaron and bipolaron as well as their energy level diagrams is shown in **Figure 1**. If an electron can be transferred from the polymer backbone to the molecular dopant, a radical cation is generated on the polymer chain and delocalized over several repeat units, inducing a local lattice distortion. Such a radical cation is referred to as positive polaron. The positive polaron with the presence of two localized electronic states within the bandgap leads to two sub-gap transitions P2 and P1 located in the NIR and mid-infrared (MIR) range, respectively. If oxidation is further pushed, another electron is removed from the polymer backbone, producing a positive bipolaron that contains two positive charges

on a distorted chain. In this case, only one sub-gap transition BP in MIR range is allowed from quantum chemical calculations. The formation of different charge carriers depends on the oxidation level.[15] In addition, the bipolaron is believed to be generally less mobile than the polaron.
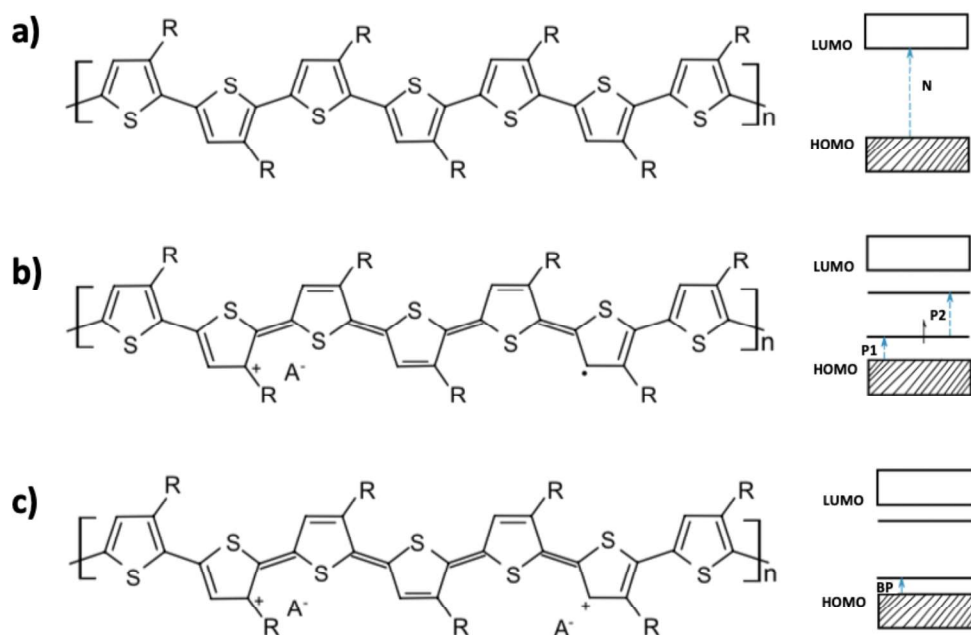
Figure 1. *The chemical structures and the energy level diagrams of a) pristine P3HT polymers, the corresponding b) positive polaron and c) positive bipolaron. A⁻ represents dopant anions and R stands for the side chain (C_6H_{13}). N is the neural polymer transition. P1 and P2 are polaronic transitions. BP denotes bipolaronic transition. Reproduced from[15].*

6.2.2 State-of-the-art for doping aligned conjugated polymers

a) Electric and optical properties

As compared to semiconducting polymers, most conducting polymers show a high level of disorder due to the random distribution of dopant molecules in the polymer matrix.[16–19] This structural disorder of "classical" conducting polymers (PANI, PEDOT:PSS, polypyrrol, etc..) hampers the efficiency of charge transport. Conversely, crystallization and order are well mastered in PSCs such as P3HT or PBTTT. Hence, an elegant method to produce highly ordered conducting polymers consists in doping PSCs. In addition, the orientation of semi-conducting and conducting polymers is an effective method to improve charge transport due to the intrinsic anisotropic charge transport of PSCs. The beneficial effect of orientation on charge

transport in sequentially doped P3HT was demonstrated by Hamidi-Sakr et al.[5] They proposed to produce highly oriented conducting polymer films by the combination of HTR followed by a soft doping method based on spin-coating or dip-coating in a solution of the dopant in an orthogonal solvent. The aligned P3HT films doped with F_4TCNQ (in ambient conditions) exhibits a charge conductivity of 22 S.cm^{-1} in the rubbing direction ($\sigma_{//}$). This is 3-4 times larger than the conductivity measured for non-oriented films. Since this seminal work, the optical and electrical properties of aligned P3HT films doped with various dopant molecules have been further investigated in the perspective to understand the correlations between dopant geometry, doping conditions and the resulting transport properties in aligned PSC films.

Doping oriented P3HT films with F_4TCNQ and F_6TCNNQ was recently reported by Untilova et al.[4] Higher charge conductivities ($\sigma_{//}$= 287 S.cm^{-1} for F_4TCNQ and $\sigma_{//}$= 521 S.cm^{-1} for F_6TCNNQ) were achieved using the incremental concentration doping method (ICD) performed in a glovebox (contrary to the original experiments of Hamidi-Sakr et al. performed in ambient and leading thus to lower charge conductivities). The ICD protocol is such that the oriented films were doped by successive dipping in dopant solutions of increasing concentration, preserving the high degree of order of undoped films. In this way, the dopant molecules enter progressively the lattice of the PSC preserving the pristine order of the PSCs to the extent possible. The polaronic absorption and film alignment was confirmed by polarized UV-vis-NIR spectroscopy (**Figure 2a**). The oriented films were measured for incident light polarization parallel (POL//R) and perpendicular (POL⊥R) to the rubbing direction. For POL//R, the doping with both F_4TCNQ and F_6TCNNQ leads to the presence of P1 and P2 polaronic band in the NIR range along the rubbing direction. The absorption peak at 570 nm is assigned to the neutral polymer (N). For POL⊥R, the absorption peaks at 413, 690, and 770 nm correspond to characteristic bands of the F_4TCNQ^- anions. The main F_6TCNNQ^- anion absorption bands are centered at 864, 988 and 1143 nm. The results suggest that the doping mechanism for P3HT doped with F_4TCNQ and F_6TCNNQ follows integer charge transfer (ICT). Moreover, both F_4TCNQ and F_6TCNNQ anions are oriented with their molecular long axis perpendicular to the P3HT chain direction. The spectra for POL⊥R which is dominated by the amorphous fraction of P3HT, does not show polaronic signatures seen in the spectra for POL//R. This indicates that the amorphous zones of P3HT are marginally doped with F_4TCNQ and F_6TCNNQ since charge transfer between dopants and coiled polymer chains is more difficult.

The situation for aligned P3HT sequentially doped with stronger oxidants such as $FeCl_3$ and

Mo(tfd-COCF$_3$)$_3$ is different.[2,6] **Figure 2a** shows the polaronic bands (P1 and P2) of oriented P3HT polymer doped with FeCl$_3$ and Mo(tfd-COCF$_3$)$_3$ for POL//R and POL⊥R. The results indicated an effective doping with stronger oxidants in both crystalline and amorphous phases of P3HT. The conductivities along the rubbing direction for FeCl$_3$ and Mo(tfd-COCF$_3$)$_3$ are 570 and 509 S.cm^{-1}, respectively. Noteworthy, at high doping concentration of FeCl$_3$, the absorption of neutral P3HT in the visible range is almost fully bleached. Therefore, the FeCl$_3^-$ doped P3HT films are almost optically transparent with a light blue color. However, the dichroic ratio of P1 and P2 band decreases with increasing FeCl$_3$ doping concentration, and this loss of orientation is probably due to loss of P3HT crystallinity and alignment.

All polarized UV-vis spectra in Figure 2 show that the aligned P3HT films are effectively doped with these dopants molecules while maintaining the polymer alignment induced by rubbing. Therefore, the anisotropic optical properties in NIR range could be observed.
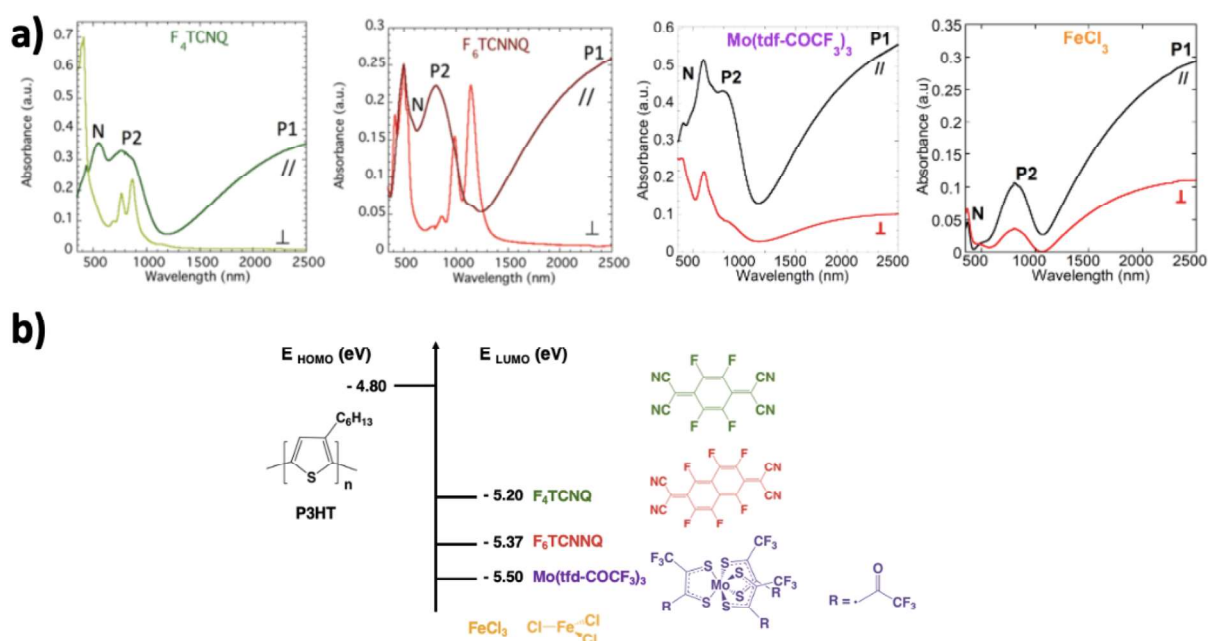
Figure 2. a) Polarized UV-vis-NIR absorbance spectra of oriented P3HT polymers doped with different dopant molecules. The incident light polarization is parallel (//) and perpendicular (⊥) to the rubbing direction. N corresponds to the neutral polymer absorption. P1 and P2 represent polaronic absorption bands. Reproduced from[2,4,6] b) The energy level diagram and chemical structures of various p type dopant molecules: F$_4$TCNQ (green), F$_6$TCNNQ (red), Mo(tdf-COCF$_3$)$_3$ (purple) and FeCl$_3$ (yellow).

b) Impact of doping on the structure and alignment of conjugated polymers

Electron diffraction is well adapted to further investigate the alignment and crystal structure of doped P3HT (**Figure 3a**). For pristine P3HT films, the distance between the P3HT polymer chains separated by alkyl side chains (d_{100}) is around 16.4 Å, and the π-stacking distance is 3.75 Å. Doping P3HT with various dopants including F_4TCNQ, F_6TCNNQ, $FeCl_3$, $Mo(tfd-COCF_3)_3$ results in slightly expanded d_{100} periodicities and reduced π-stacking distance.[2,4,6] The results demonstrated that these dopant molecules incorporate into the layers of alkyl side chains of the P3HT crystalline phase. In addition, the F_4TCNQ-doped film preserves a high order similar to the undoped film. As compared to F_4TCNQ, P3HT doped with F_6TCNNQ presents larger d_{100} periodicities and additional h 0 1 reflections that are absent in the undoped P3HT films. Although the doping with F_6TCNNQ has substantially modified the crystal structure of pristine P3HT, the alignment is well maintained in the doped films. In the case of $FeCl_3$-doped P3HT, $FeCl_4^-$ and $FeCl_2$ molecules of small molecular volume intercalate into side chain layers and the chain orientation is persevered after doping. However, the intensity of ED reflections significantly decreased at high doping concentrations, suggesting some loss of crystallinity and alignment upon doping. This is consistent with the decreased dichroic ratio in the polarized UV-Vis-NIR spectra of oriented P3HT doped with $FeCl_3$. Regarding the films doped with $Mo(tfd-COCF_3)_3$, the ED pattern shows a splitting of the h 0 0 reflections (h= 1-3), indicating that the films are composed of undoped and doped crystallites aligned along the rubbing direction. In summary, the alkyl chain sublattice of P3HT is particularly loose and thus can host various dopant molecules upon adapted lattice expansion in the side chain direction. This intercalation of dopant molecules generally results in a structural reorganization of P3HT chains within π-stacks so as to create "cavities" to host dopant molecules. Consequently, the reorganization of the lattice of P3HT implies to slide P3HT chains in the chain direction so as to group side chains together and simultaneously expand the lattice along the side chain direction, creating the cavities to host dopant molecules (**Figure 3b,c**).[4] Despite this rather important structural reorganization, the P3HT chain alignment obtained by rubbing is almost fully maintained upon doping.

In this chapter, we will study the aligned P3HT films doped with a new dopant: tris(4-bromophenyl)ammoniumyl hexachloro-antimonate, also called magic blue (MB). This dopant possesses an EA of 5.8 eV[20] that is higher than F_4TCNQ (EA≈ 5.20 eV), F_6TCNNQ (EA≈ 5.37 eV)

and Mo(tfd-COCF$_3$)$_3$ (EA≈ 5.5 eV).
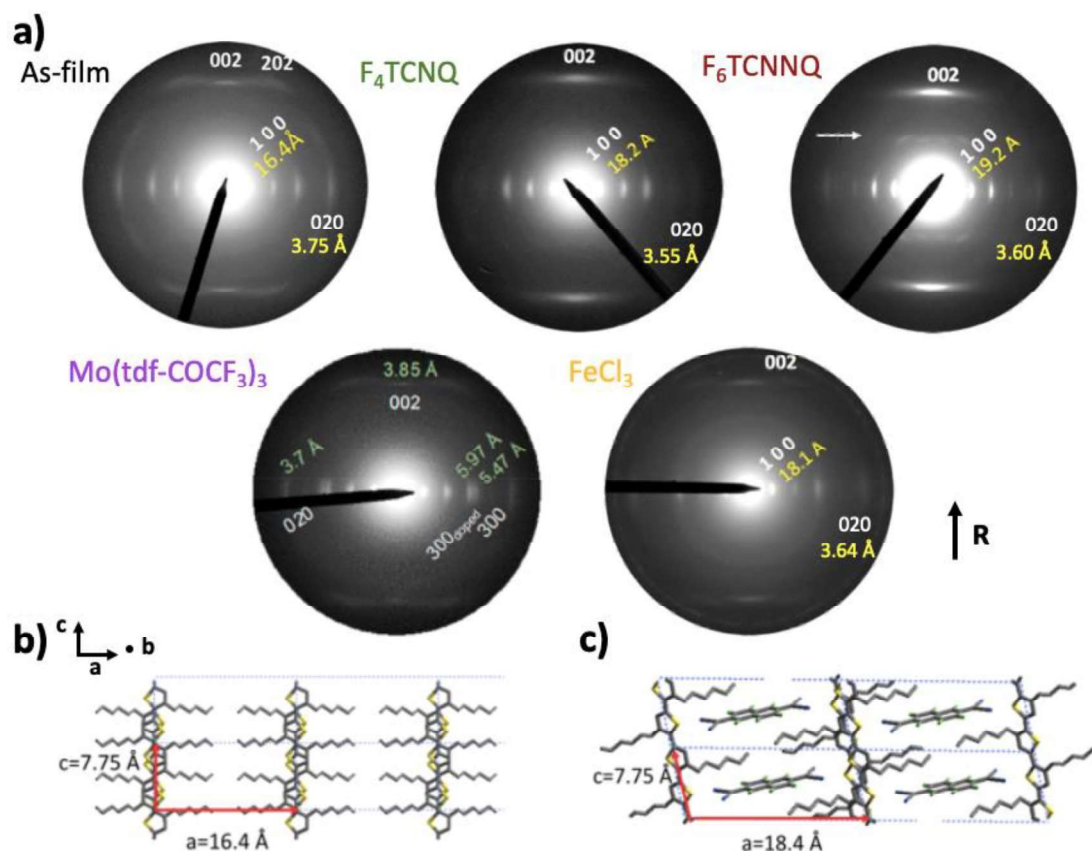
Figure 3. *a) ED patterns for pristine oriented P3HT films and oriented P3HT films doped with various dopants. R stands for the rubbing direction. Reproduced from*[2,4,6]. *Structural models of crystal structures in b) a pristine P3HT polymer and c) a P3HT polymer doped with F$_6$TCNNQ. Adapted from*[4].

6.2.3 Doping P3HT with MB

MB is extensively used as a dopant owing to a good stability in air. Doping conjugated polymers such as P3HT with MB was recently reported by Müller et al.[21] Their results show that doping P3HT with MB gives rise to the appearance of polaronic absorption peaks in the NIR range and a reduced neutral polymer absorption in the visible region (**Figure 4**). Upon doping, an electron is transferred from the P3HT polymer backbone to the tris(4-bromophenyl)ammoniumyl radical cation, producing the neutral tris(4-bromophenyl)amine that is optically transparent. Meanwhile, SbCl$_6^-$ becomes the counter ion and enters the polymer matrix to neutralize the charges. SbCl$_6^-$ is also colorless. Therefore, MB-doped P3HT films show a high transmission in the visible spectrum. This property is of great interest for PSLMs to enhance the transparency of the devices.

In this work, the P3HT polymers are initially aligned by HTR and subsequently doped by the ICD method with MB. These films are probed by polarized UV-Vis-NIR spectroscopy, ED patterns, conductivity and RBS measurements.
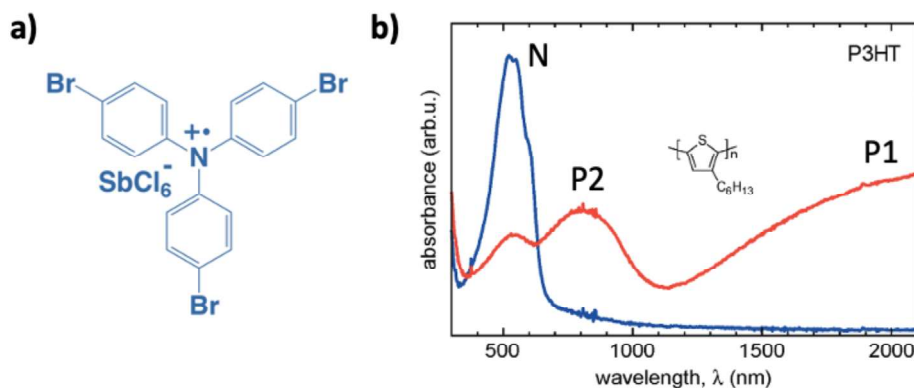
Figure 4. a) Chemical structure of the MB dopant. b) UV-vis-NIR absorbance spectra for undoped (blue line) and doped P3HT films using MB (red line). Inset: Chemical structure of P3HT. Reproduced from[21].

6.3 Materials and methods

Orientation and doping of thin films: Regio-regular P3HT was purchased from Merck (M_w = 43.6 kDa, PDI = 1.8). MB as well as anhydrous solvents (99%) used for doping (acetonitrile) and film preparation (ortho-dichlorobenzene) were purchased from Sigma-Aldrich. The orientation of the films by high temperature rubbing followed the protocol described in previous publications.[5,22] The film thickness was extracted from the UV–vis absorbance using the calibration given in reference [6]. The doping of P3HT films with MB was performed following the incremental concentration doping (ICD) procedure with full sample immersion for 40-60 s in the dopant solution of increasing concentration.[4,23] The doped films were not rinsed with the pure solvent to avoid de-doping of the films. Both doping and rubbing were performed in a glovebox.

Structural Analysis by TEM

Oriented P3HT films were coated with a thin amorphous carbon film using an Edwards Auto306 evaporator to avoid charging under the electron beam. The films were removed from the glass substrate by floating on distilled water and recovered on TEM copper grids. The samples on copper grids were subsequently doped by the ICD procedure. A CM12 Philips

microscope (120 kV) equipped with a MVIII (Soft Imaging System) charge-coupled device camera TEM was used for the structural analysis of the films (bright field and diffraction modes). The 0 0 2 reflection of P3HT at 3.85 Å is not sensitive to the doping of the polymer and is therefore used as an internal calibration to calculate the d_{100} and d_{020} reticular distances in the ED patterns. Beam exposure was set to a minimum using the low dose system to avoid de-doping under the electron beam when the same zone is exposed for a prolonged period of time.

Polarized UV–Vis–NIR Absorption

A Varian Cary 5000 spectrometer with polarized incident light (spectral resolution of 1 nm) was used to probe the level of film orientation and the effect of film doping with MB (350-2500 nm) as a function of doping time and MB concentrations. The incident light polarization is parallel (//) and perpendicular ($\perp$) to the rubbing direction, i.e., polymer chains orientation.

Charge Conductivity

All devices were fabricated on glass substrates cleaned by ultrasonication in acetone, ethanol, hellmanex, and deionized water (×3 times). The cleaned substrates were dried under nitrogen and exposed to plasma prior to film deposition. Gold electrical contacts (40 nm thick) in a four-point probe geometry (1 mm spacing between electrodes, 5 mm length) were deposited via controlled thermal evaporation through a shadow mask, at an average rate of 4–6 Å. s^{-1}. The geometry of gold electrodes allows to measure both the charge transport and thermopower on the same substrate in both parallel and perpendicular directions to the rubbing. Oriented films of P3HT were floated on water and carefully recovered on the device with pre-deposited gold electrodes. They were subsequently doped using the ICD protocol.

Rutherford Backscattering Spectroscopy (RBS)

Rutherford Backscattering Spectroscopy (RBS) is an ion scattering technique, generally used to analyze the elemental composition in thin films or to determine film thicknesses. During the analysis, high-energy He^+ ions (i.e., α particles) are directed onto the sample and backscattered He^+ ions are measured by a detector. The collision between He^+ ions and target atoms relate to the elastic Coulomb scattering of two positive nuclei charges.[24] The mass of the scattering element can be identified though the energy and momentum conservation laws. And the

elemental composition can be quantified since the scattering cross-section is known. The RBS measurements can be achieved without the use of reference standards.[25] More importantly, in our case, the polymer matrix possesses relatively light elements including S, C and H, whereas the dopant molecules contain a heavy element Sb that allows for a good sensitivity using RBS spectroscopy.

The RBS measurements have been performed by Dominique Muller on the 4 MV Van de Graaff accelerator of the ACACIA platform at ICube with a He$^+$ beam, as illustrated in **Figure 5**. An energy of 2 MeV and a scattering angle of 160° are chosen to have good mass separation of the various elements present in the layer. The probed area has a diameter of 800 μm. The statistical error in the determination of the elemental composition is 6%. To avoid local heating by the beam, a current of 3 nA is used. The incident beam is perpendicular to the surface of the sample.
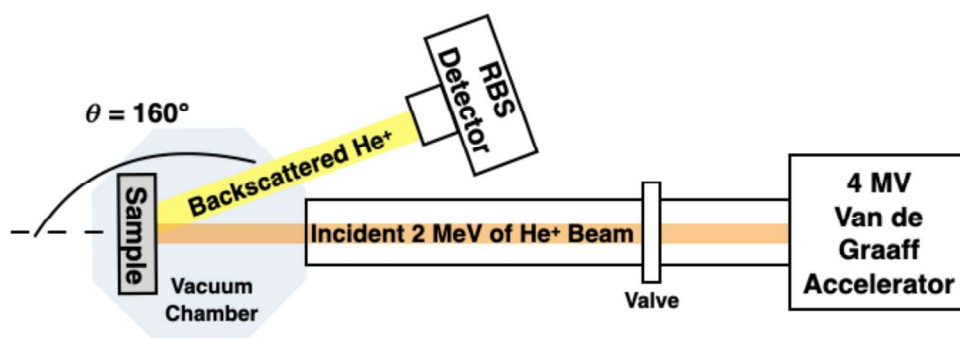
Figure 5. *Schematic illustration of RBS measurement setup.*

Internal integrating sphere

The transmittance and reflectance of doped polymers were measured using a Cary 5000 (Agilent) UV-Vis-NIR spectrophotometer equipped with an integrating sphere (Internal Diffuse Reflectance Accessory DRA 2500). The transmittance measurement was described in Chapter 4. For reflectance measurements (**Figure 6**), the baselines were separately recorded with the PTFE reference disk (R= 100 %) and glass substrate (R= 0%) covering the reflectance port. Then, the sample was placed in the reflectance port of the integrating sphere. As a result, the measured reflectance of the sample is relative to the PTFE disk and takes into account the reflectivity of the bare glass substrate.
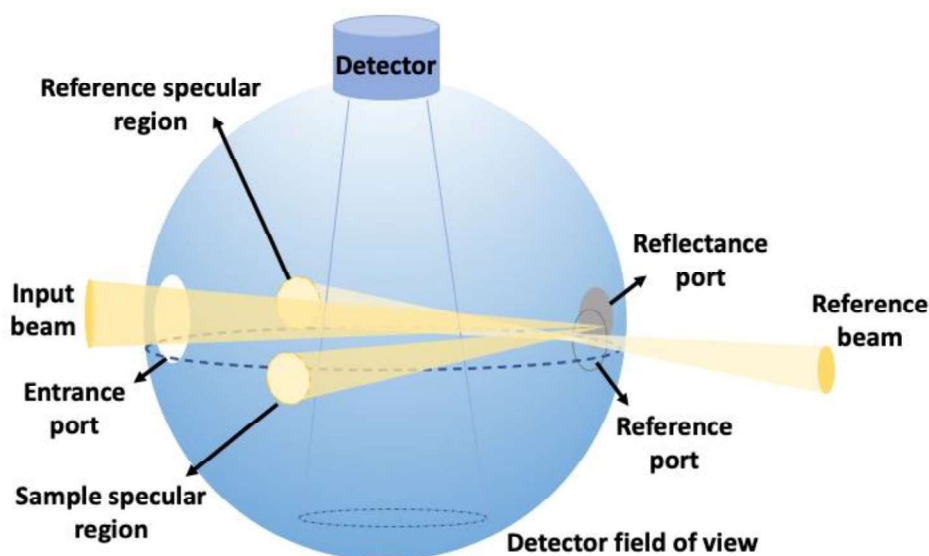
Figure 6. *Schematic illustration of integrating sphere for reflectance measurements.*

6.4 Results and discussion

6.4.1 Anisotropic electric properties

Transparent and conducting ITO substrates are widely used in optoelectronic devices, and in particular also for the fabrication of PSLMs. However, ITO technologies involve a high-cost sputtering deposition at high-temperature. In parallel, ITO shows limited flexibility which hinders its practical application in bendable organic electronics.[26] More importantly, Indium is moreover a high cost and rare element on earth. Thus, new transparent conducting materials such as metal nanowires,[27,28] graphene[29,30] and conducting polymers[31–33] have been developed as substitutes to ITO electrodes. Among them, conducting polymers are considered as promising candidates owing to their high flexibility and moderate price. An ITO-free organic solar cell using a PEDOT: PSS polymer as anode was reported by Kim et al.[31] The PEDOT: PSS polymer with a conductivity of ~550 S.cm^{-1} was used to replace ITO and the corresponding OPV devices show good photovoltaic performances (PCE=3.27 %) comparable to the ITO-based devices (PCE=3.66 %). This result demonstrated that conductive polymers can effectively replace ITO substrates. Furthermore, the orientation of conducting polymers leads to a significant increase in charge conductivity and might be used to further guide the orientation of organic layers deposited atop.[2,4,6] For these reasons, we investigated the fabrication of highly oriented P3HT polymers doped with MB.

137

For the preparation of highly oriented conducting polymers, P3HT films were initially aligned by high temperature rubbing at 186 °C. A highly oriented semi-crystalline structure made of alternating crystalline lamellae and amorphous zones is thus obtained with a total lamellar periodicity of 28 nm.[22,34] The lamellae are made of a majority of face-on crystals with some edge-on domains. Sequential doping of these films deposited on patterned substrates for conductivity measurements was performed with solutions of MB in acetonitrile (ACN) of increasing concentration for 40 s to 1 min in a glove box. The incremental concentration doping (ICD) of P3HT films leads to an improvement of electric properties based on a progressive intercalation of dopants in the pristine polymer structure as compared to direct doping using dopant solutions of high concentration.[4,23,35] The same oriented film was thus dipped in solutions of MB/ACN of increasing concentration [MB] and the anisotropic conductivity was measured along (//) and normal ($\perp$) directions to the rubbing, as shown in **Figure 7a**.

Doping with [MB] $\leq$ 0.05 g. L^{-1} results in poor charge conductivities below 0.02 S.cm^{-1}. Conductivity starts to increase for [MB] = 0.1 g. L^{-1} and a record conductivity $\sigma_{//}$ = 3460 $\pm$ 600 S.cm^{-1} is achieved for oriented P3HT doped with [MB] = 0.2 g. L^{-1}. Further doping of the films results in a slight reduction of the conductivity to 2900 $\pm$ 300 S.cm^{-1} for [MB] = 1.0 g. L^{-1}. The observed conductivity is much larger than that reported for non-oriented films doped in ambient conditions. Also, the saturation of the conductivity sets in at a very low dopant concentration as compared to F$_4$TCNQ or F$_6$TCNNQ. As seen in **Figure 7b**, doping non-oriented P3HT films in a controlled atmosphere in a glove box already improves substantially the conductivity of the doped films by a factor of more than one order of magnitude (σ can reach up to 430 S.cm^{-1}) as compared to films doped in ambient.[21] This is consistent with previous reports for F$_4$TCNQ-doped P3HT.[35] However, orientation is necessary to increase charge conductivity to 3000 S.cm^{-1}. This value is much larger than the reported conductivity of PEDOT: PSS used for the ITO-free OSCs.[31], making it possible to replace ITO electrode by aligned P3HT doped with MB, provided such films show the long term stability necessary for such a use. These results are interesting and evidence a peculiar behavior when oriented P3HT films are doped with MB. Polarized UV–vis–NIR spectroscopy was subsequently used to clarify these trends versus [MB].
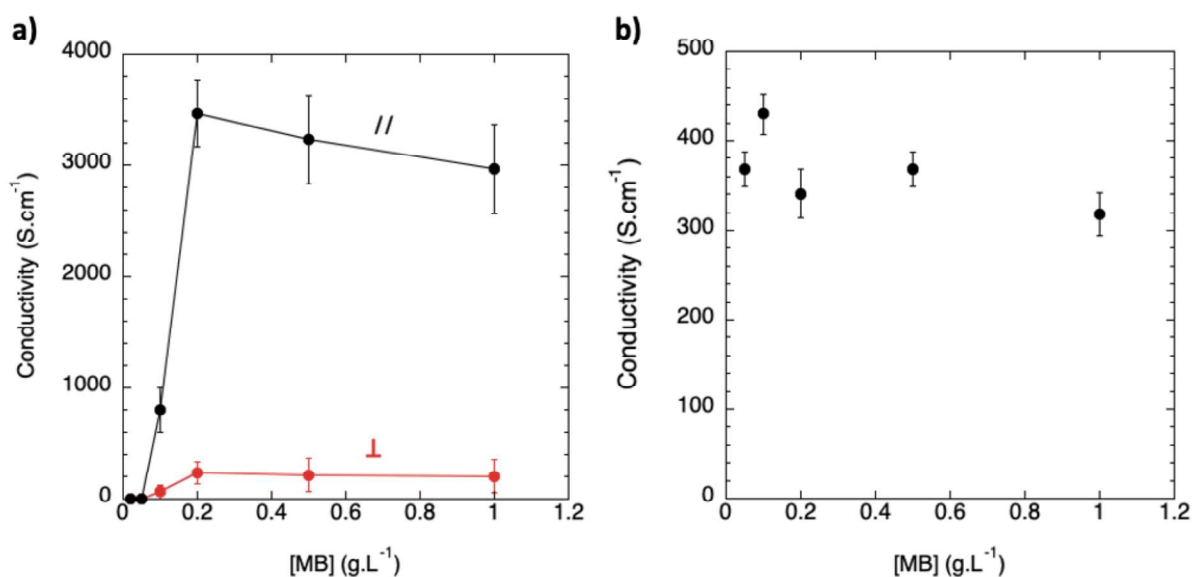
Figure 7. *a) Evolution of the charge conductivity of oriented P3HT thin films doped with magic blue (MB) as measured in the directions parallel (black dots) and perpendicular (red dots). The film thickness was 38 nm. b) Evolution of the conductivity of non-oriented P3HT films versus dopant concentration.*

6.4.2 Anisotropic optical properties

Contrary to the conductivity showing important changes for [MB] ≥ 0.2 g.L^{-1}, the UV–vis–NIR spectra of oriented P3HT with POL//R evidences characteristic doping signatures at very low doping concentrations (0.05 g.L^{-1}): I) the bleaching of the neutral P3HT absorption, and II) the appearance of polaronic bands P1 and P2 (**Figure 8a**). Accordingly, there is evidence for doping of crystalline P3HT domains. Evidence for a first isosbestic point at 650 nm between the neutral and P2 bands is found. For [MB] = 0.2 g. L^{-1}, the neutral P3HT absorption is fully bleached. For higher [MB] = 1.0 g. L^{-1}, the presence of excess dopant on the film surface is manifested by an additional absorption peak at 703 nm (band noted with a black asterisk in **Figure 8a,b**). Very interesting is the situation observed for POL⊥R (**Figure 8b**). The absorption band of amorphous interlamellar zones of P3HT at 500 nm shows also a bleaching upon doping. This effect was not observed when oriented P3HT films were doped with F$_4$TCNQ or F$_6$TCNNQ. As for the crystalline fraction of P3HT, the films doped with [MB] = 0.2 g. L^{-1} show a full bleaching of the absorption band of amorphous P3HT and the presence of well-defined polaronic bands P1 and P2. Both features indicate that MB dopes amorphous P3HT, in strong contrast to F$_4$TCNQ and F$_6$TCNNQ that cannot dope amorphous P3HT (the absorption of amorphous P3HT is

unaffected by doping and no polaronic bands are seen for POL⊥R). Polarized UV–vis–NIR spectroscopy indicates therefore that both oriented P3HT crystals and amorphous interlamellar zones are doped by MB.

The evolution of the UV–vis–NIR spectrum of oriented P3HT with increasing [MB] shows another marked difference with respect to the films doped with F_4TCNQ and F_6TCNNQ. This difference is obvious when plotting the ratio of the absorbances of the polaronic bands P2 at 700nm and P1 at 2500 nm. In the case of MB, for [MB] ≤ 0.1 g. L^{-1}, the ratio r is close to 1 and identical to that observed for F_4TCNQ and F_6TCNNQ. This is characteristic of the presence of polarons in the doped polymers. However, r decreases and saturates to a value of 0.35 when doping with MB up to 5 g. L^{-1}, whereas r remains unchanged whatever the doping concentration of F_6TCNNQ. Most interestingly, the UV–vis–NIR spectra show the existence of a second isosbestic point close to 947 nm between the P2 and the so-called P1 bands, suggesting that the polaronic specie formed at lower [MB] transforms into a different specie at higher doping concentration. This behavior is typical of the transformation of the polarons that are dominant for [MB] ≤ 0.1 g. L^{-1} to bipolarons for [MB] ≥ 0.2 g. L^{-1}. This observation is consistent with the results of Enengl et al. for P3HT films doped by electrochemical oxidation.[15] The increase of the oxidation potential of P3HT thin films leads to a similar decrease of the ratio r = P2/P1 (**Figure 8c**) and was attributed to a transformation of polarons to bipolarons as evidenced by electron spin resonance. This interpretation is also consistent with the blue shift of the P1 band position with increasing dopant concentration (**Figure 8d**). Incidentally, the highest conductivity is observed in the oriented films of P3HT for [MB] = 0.2 g. L^{-1}, i.e., when the ratio P2/P1 is almost constant and the population of bipolarons is established. This result is similar to that reported by Neusser et al.[36] on electrochemical doping of P3HT where the charge conductivity increases upon formation of bipolarons and reaches a plateau at high charge carrier concentration of 10^{21} cm^{-3}. Most importantly, when F_4TCNQ and F_6TCNNQ dope the only P3HT crystalline phase, no important population of bipolarons is observed and the ratio P2/P1 is close to 1. Conversely, as demonstrated by TEM (vide infra), when the dopant is mainly located in the amorphous zones of P3HT, bipolaron formation is favored. In other words, the ratio of polaron and bipolaron absorption bands is a priori related to the preferential location of dopants in crystalline or amorphous phases of P3HT, respectively.
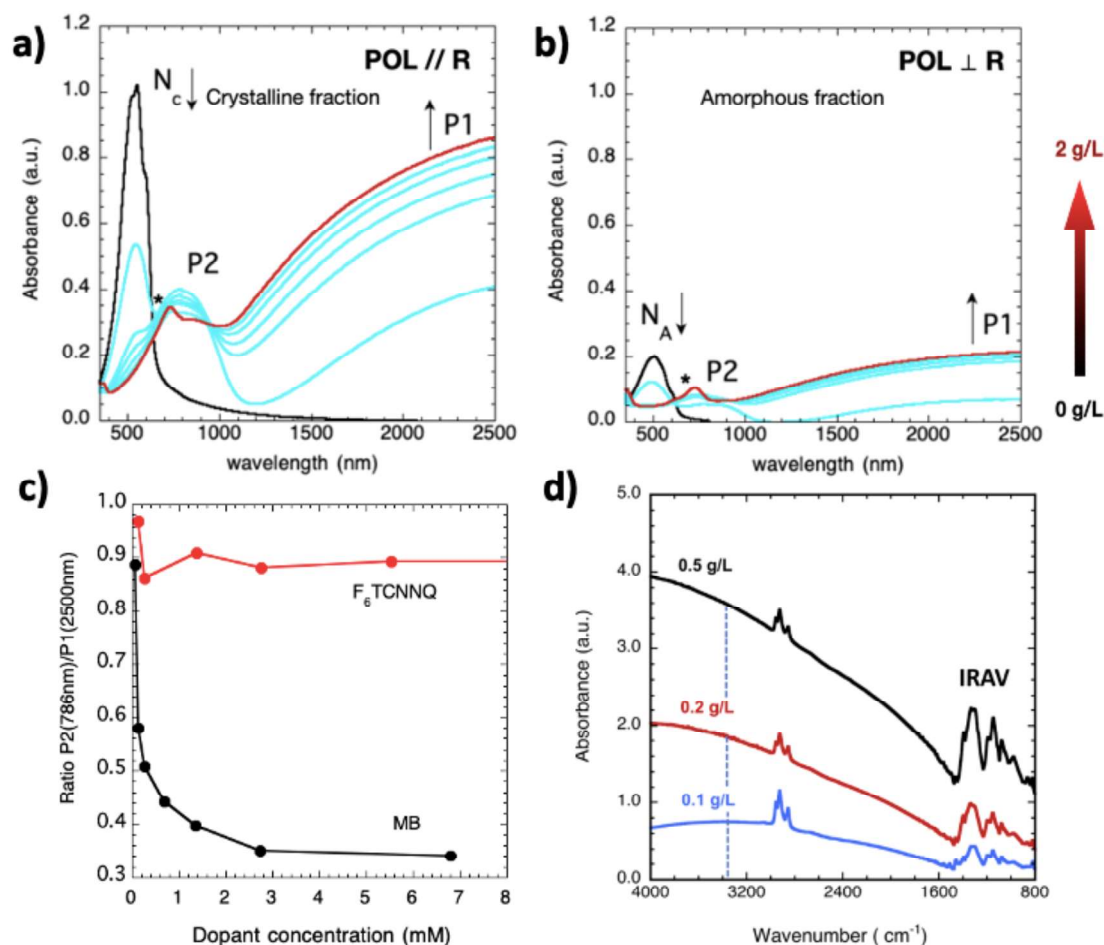
Figure 8. *Evolution of the UV–vis–NIR spectra of oriented P3HT thin films (T_r = 186 °C) measured for a) light polarization (POL) oriented parallel and b) perpendicular to the chain direction. The red asterisk points at the absorption band of excess MB. N_A highlights the absorption band of amorphous P3HT, whereas N_c corresponds to the absorption of neutral crystalline P3HT. P1 and P2 correspond to polaronic bands of doped P3HT. The spectra in black (red) correspond to undoped (doped, 2 g. L⁻¹) oriented P3HT. c) Evolution of the ratio r between P2 and P1 band absorbances as a function of increasing [MB] and comparison with the result obtained for films doped with F6TCNNQ (from reference). d) Evolution of Fourier-transform infrared spectroscopy (FTIR) spectra of oriented P3HT films doped at different concentrations. The dotted line highlights the maximum of the polaronic P1 band for [MB]=0.1 g.L⁻¹. It is clear that this maximum shifts to higher energies when [MB] increases.*

6.4.3 Determination of the doping level

Further insight into the doping of P3HT with MB was obtained by Rutherford backscattering spectroscopy (RBS) that helps quantify the amount of MB present in the thin films. For the P3HT films doped with MB, RBS can probe the presence of the dopant counterion SbCl₆⁻ via Sb atoms versus sulfur atoms for P3HT (**Table 1**). The atomic ratio Sb/S was determined for three

samples doped at 0.2, 0.5, and 1.0 g. L^{-1} (the samples doped at 0.5 and 1.0 g. L^{-1} were doped at all lower concentrations following the ICD method). Regarding RBS data, we do observe an increase in the presence of Sb in the films when [MB] increases but the correlation between [MB] and Sb/S is not linear indicating that the doping is more effective at low [MB], in agreement with charge conductivity measurements.

Beside Sb and S, RBS identifies also the presence of Br in the thin films (**Figure 9**). It can be associated with two species, namely excess of MB crystals on the film surface or to tris(4-bromophenyl) amine inside the P3HT films. Excess of MB crystals is visible only for [MB] ≥ 1.0 g. L^{-1}. This observation suggests that the presence of Br in the RBS spectra of doped P3HT is most likely due to tris(4-bromophenyl)amine present in the bulk of the doped P3HT thin films.

Table 1. *Sb/S atomic ratio measured by RBS measurements versus dopant concentrations.*

[MB] (g.L^{-1})	Sb/S atomic ratio (%)	$\sigma_{//}$ (S.cm^{-1})	$\sigma_{\perp}$ (S.cm^{-1})
0.2	6.7 ± 0.4	3460 ± 300	233 ± 100
0.5	7.2 ± 0.4	3250 ± 400	213 ± 150
1.0	10.2 ± 0.6	2970 ± 400	201 ± 150
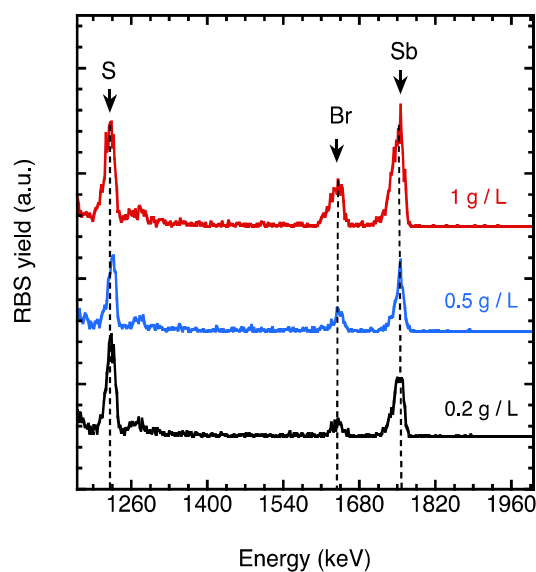
Figure 9. *Evolution of the RBS spectra of oriented P3HT films doped with MB at different concentration.*

6.4.4 Impact of doping on the oriented structure of P3HT

Electron diffraction is a simple means to follow the structural changes in aligned thin films of P3HT upon doping. **Figure 10a** exemplifies the evolution of the ED pattern of oriented P3HT (T_R = 186 °C) as a function of the concentration of MB. **Figure 10b,c** collect the variations of d_{100} and π-stacking periodicity as a function of increasing dopant concentration for the five dopants investigated so far. From a general point of view, the ED pattern of MB-doped P3HT shows limited changes with increasing dopant concentration. Alignment is fully maintained upon doping whatever the concentration of doping. The π-stacking and d_{100} periodicities show virtually no change when the films are doped with MB (only a slight increase of d_{100} is seen at 0.2 g. L^{-1}) as compared to other dopants.

Previous studies have shown that dopant intercalation results in the expansion of the crystal lattice along the side chains of P3HT (a-axis) and a contraction of the π-stacking distance (b axis). Such changes in crystal lattice are indeed well observed for the dopants F_4TCNQ, F_6TCNNQ, $FeCl_3$ and $Mo(tdf-COF_3)_3$ (**Figure 10c**). Accordingly, the situation is clearly different for P3HT doped with MB. Doping of P3HT with MB leaves h 0 2 reflections (h = 0,1,2) almost unchanged in position and intensity even for high MB concentrations. Previous studies have demonstrated that the evolution of the h 0 2 reflections (h = 0,1,2) with doping is a fingerprint of the dopant intercalation in the P3HT crystal lattice.[4,35] Intercalation of dopants inside P3HT crystals results in the disappearing of the 1 0 2 and 2 0 2 reflections and a streaking of the 0 0 2 reflection whose intensity increases substantially. These changes are the fingerprints of a re-organization of P3HT backbones within individual π-stacks. The recent structural refinement for F_6TCNNQ-doped P3HT has shown that doping P3HT with F_6TCNNQ induces a shift of P3HT backbones so as to group alkyl side chains and create cavities to host the dopant molecules in the crystal.[4]

The present results demonstrate that doping with MB does not induce such a structural reorganization within π-stacks. There is thus evidence that MB is only marginally intercalated inside the P3HT lattice. Taken altogether, these results support the idea that doping of P3HT with MB leaves the crystal structure of P3HT mostly unchanged, contrary to all other investigated dopants.
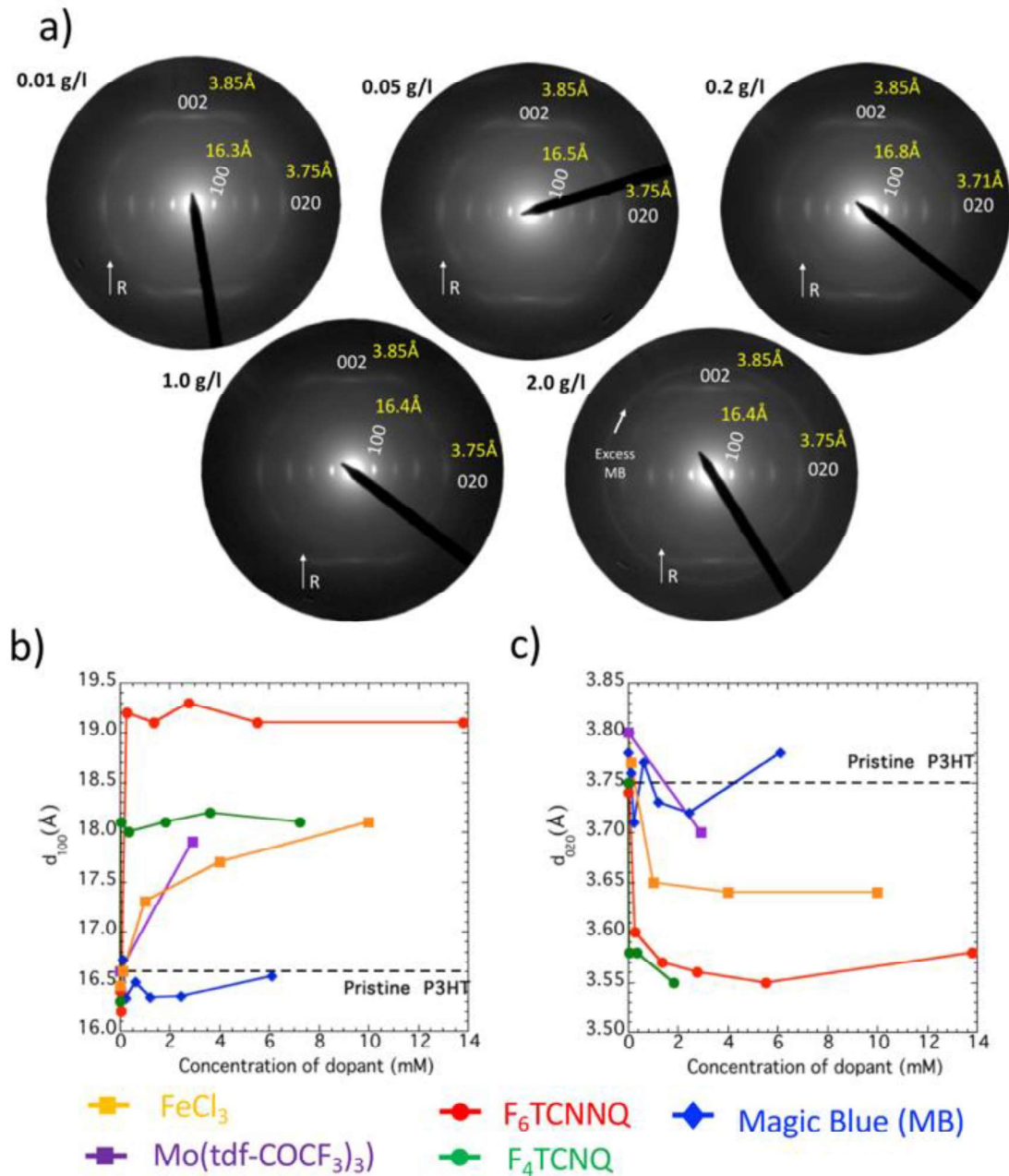
Figure 10. a) Structure evolution in oriented P3HT thin films doped with magic blue (MB) as obtained by low dose TEM. Electron diffraction patterns of doped P3HT film upon sequential doping with MB in acetonitrile from low to high doping concentration: The asterisk marks a Scherrer ring from excess MB on the surface of the doped P3HT film. R represents the rubbing direction. b) and c) Evolution of the layer spacing along the alkyl side chain direction d_{100} b) and the π-stacking periodicity d_{020} c) as a function of the doping concentration for different dopants. The dotted lines highlight the values of the layer spacings d_{100} and d_{020} of undoped P3HT. d) Various doped P3HT microstructures: doping of the crystalline domains for F_4TCNQ and F_6TCNNQ; doping of both crystalline and amorphous zones for $FeCl_3$ and $Mo(tdf-COCF_3)_3$ and doping of the amorphous zones for MB.

6.4.5 Doping kinetic of crystalline and amorphous P3HT

Further understanding of the doping mechanism is gained by following the kinetics of doping by polarized UV–vis–NIR spectroscopy (**Figure 11a,b**). Working on oriented thin films helps investigate the doping kinetics for both crystalline and amorphous domains simply by selecting the incident light polarization. For POL//R, the UV–vis–NIR spectrum of rubbed P3HT films is dominated by the oriented crystalline fraction of P3HT and by the polaronic features P1 and P2 resulting from the doping (**Figure 11a**). For POL⊥R, the UV–vis–NIR spectra of pristine oriented films is dominated by the absorption of non-oriented and amorphous P3HT (**Figure 11b**). Thus, by selecting the light polarization, one can choose to follow the apparent doping kinetics of either the crystalline or the amorphous fractions of P3HT. Our results show a very clear bleaching of the absorption bands of crystalline (POL//R) and amorphous (POL⊥R) fractions with increasing doping time indicating that both crystalline and amorphous P3HT domains are doped. In addition, the polaronic bands P1 and P2 are visible for both light polarizations, increasing in absorbance with increasing doping time and saturating after 1 min. To be more quantitative, we decided to probe the doping kinetics of both crystalline and amorphous P3HT phases by following the variation of the P1 absorbance at 2500 nm as a function of doping time for POL//R and POL⊥R (**Figure 11c,d**). For the amorphous phase, the doping kinetics was also directly determined from the bleaching of the amorphous absorption peak near 500 nm (**Figure 11e**). Similar to our previous work, the doping kinetics can be adjusted using the following equation[3]:

$$A(t) = A_0 \left(1 - \exp\left(-\frac{\sqrt{Dt}}{l} \right) \right) \qquad \textit{Eq.6.1}$$

where A(t) is the absorption at wavelength 2500 nm of the polaron at time t. A_0 is the absorbance of the polaron at saturation, l is the film thickness and D is a fitting parameter that has the dimensions of a diffusion constant. As a consequence, plotting the doping kinetics versus $t^{1/2}/l$ leads to a representation that is independent of film thickness and allows to extract the value of D for the two light polarizations (**Table 2**).

From **Figure 11c,d**, it turns out that the kinetics of both crystalline and amorphous zones are characterized by almost identical D values. In addition, the extracted values are remarkably close to the diffusion constant of iodine into P3HT, i.e., 2.5×10^{-11} cm^2.s^{-1} determined by Maliakal using attenuated total reflectance infrared (ATR-IR) spectroscopy.[37] It would therefore be tempting to claim that the similar values of D for POL//R and POL⊥R are due to similar

diffusion coefficients of MB into amorphous and crystalline domains. However, TEM clearly shows that MB molecules do not enter the P3HT crystals even though spectroscopy demonstrates that they are doped. This apparent contradiction is solved by considering that the oriented P3HT crystals are doped from their interface with the surrounding amorphous zones that contain MB molecules. Hence, the apparent doping kinetics observed for POL//R does not correspond to a diffusion kinetics of the dopants into P3HT crystals. It rather corresponds to the formation kinetics of polarons in P3HT crystals determined by the diffusion of MB into amorphous zones. This is why the fitting parameter D extracted for POL//R and POL⊥R are almost identical.

Table 2. *Fitting parameter D (Equation 1) describing the doping kinetics of oriented P3HT with MB observed with light polarized parallel (//) or perpendicular (⊥) to the P3HT chains.*

Light polarization	Film thickness (nm)	D (cm^2. s^{-1}) (x 10^{-11})
//	109 ± 5	2.5 ± 0.4
	212 ± 11	2.8 ± 0.3
⊥	109 ± 5	2.2 ± 0.6
	212 ± 11	1.8 ± 0.6
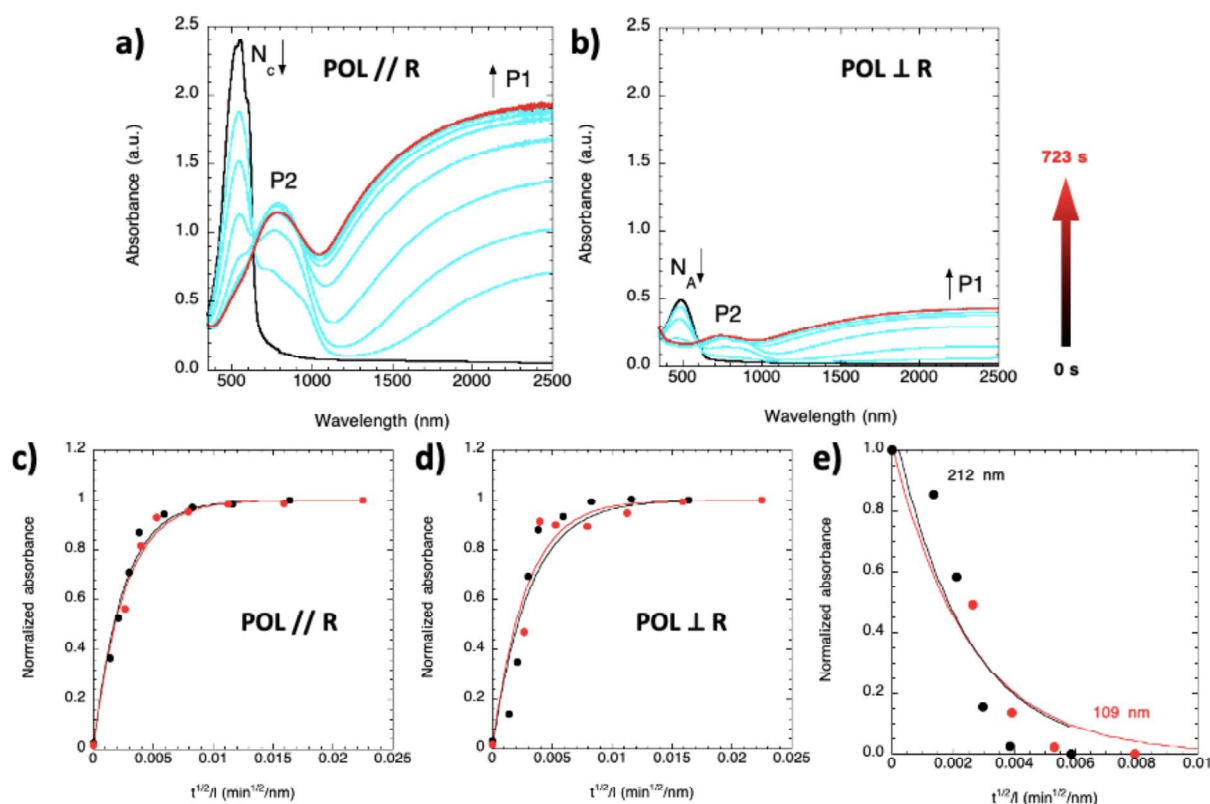
Figure 11. *Evolution of the UV–vis–NIR spectrum of oriented P3HT (T_r = 186 °C, thickness of 212 ± 11 nm) with doping time from 0s (black line) to 723s (red line) for light polarized parallel a) and perpendicular b) to the polymer chain direction. N_C and N_A correspond to the absorbance of the neutral P3HT in crystalline and amorphous form, respectively. P1 and P2 refer to the polaronic absorption bands. c) and d) Evolution of the P1 absorbance at 2500 nm as a function of √t/l with t the doping time and l the film thickness for oriented films of P3HT of thickness 109 ± 5 nm (red dots) and 212 ± 11 nm (black dots) and for light polarized parallel c) and perpendicular d) to the polymer chain direction. The full lines in red and black correspond to the fits of the experimental data points using Equation 1. The extracted doping constants are collected in Table 1.e) kinetics of doping of oriented P3HT versus doping time with MB in acetonitrile as measured from the change in absorbance of the amorphous P3HT absorption band. The two full lines correspond to the fits of the normalized absorbance versus √t/l.*

6.4.6 Comparing MB with other dopants

A synoptic analysis of doping results obtained by TEM and polarized UV–vis–NIR spectroscopy in oriented P3HT thin films with various dopants helps identify three different situations illustrated in **Figure 12**. For dopants with E_A ≤ 5.4 eV such as F_4TCNQ and F_6TCNNQ, doping of the only crystalline P3HT domains is observed because the electron affinity of the dopants is

not sufficient to ensure charge transfer with the coiled P3HT chains present in the amorphous phase.[35] This is a clear-cut result from the polarized UV–vis–NIR spectroscopy showing that the absorption of amorphous P3HT is not at all bleached upon doping with these dopants (**Figure 2**). The consequence is that charge conductivity is rather limited in such systems with a maximum $\sigma_{//} = 520$ S.cm^{-1} for F$_6$TCNNQ along the chain direction. For stronger oxidants such as FeCl$_3$ and Mo(tdf-COCF$_3$)$_3$, both crystalline and amorphous phases are doped. Doping of amorphous P3HT domains is manifested in the polarized UV–vis–NIR spectra by the presence of the polaronic bands P1 and P2 for POL⊥R and bleaching of the absorption of amorphous P3HT (**Figure 2**). The highest charge conductivities reach a value of 570 S.cm^{-1}, close to the values observed for films doped with F$_6$TCNNQ. For both these dopants, the increase of dopant concentration results in a saturation of the doping level evidenced by a saturation of the d$_{100}$ value and of the absorbance of the polaronic bands. However, the diffraction patterns at high dopant concentration witness a substantial loss of packing order within P3HT crystals (loss of h 0 2 reflections and reduced intensity of the reflections).

The case of MB-doped P3HT films is clearly different. From the point of view of the film structure, TEM shows minor changes in lattice parameters and the overall ED patterns of P3HT remain almost unaltered upon doping. Despite unchanged crystal structure, polarized UV–vis–NIR spectroscopy demonstrates the effective doping of crystalline and amorphous P3HT domains with MB. This suggests that the P3HT nanocrystals must be doped via the surrounding amorphous/crystal interface and that the polarons can be delocalized inside the crystals. This last possibility would further imply that the distance between the polaronic charge and the counterions can be large, hence coulombic interactions can be reduced, explaining large mobility of the polarons delocalized in P3HT nanocrystals. As a result, a higher conductivity along chain direction for MB-doped P3HT was observed comparing to that doped with other dopants.

It is important to further analyze which conditions in the choice of the polymer/dopant pair ensure such a situation. A priori the E$_A$ of the dopant must be sufficiently high to dope readily amorphous areas of the polymer with a higher HOMO than crystalline regions. This is the case for dopants such as FeCl$_3$, Mo(tdf-COCF$_3$)$_3$ and MB. However, there is a marked difference between MB and these other two dopants since they are able to intercalate into P3HT crystals. The absence of MB molecules inside P3HT crystals as opposed to FeCl$_3$-doped films must somehow relate to the geometry and molecular dimensions of the dopants. The molecular

volume of $SbCl_6^-$ (129 Å³) is not substantially larger than $FeCl_4^-$ (90 Å³) or $FeCl_2$ and cannot explain the absence of MB in P3HT crystals. The latter species are very small and may diffuse readily in the crystals of P3HT. However, RBS results indicate that tris(4-bromophenyl) amine is present in the P3HT films doped with MB. Tris(4- bromophenyl)amine has a volume of 260 Å.[38] If associated with $SbCl_6^-$ during diffusion, its substantially larger molecular volume in comparison to $FeCl_4^-$ should hinder effective diffusion into P3HT crystals and conversely promote the preferential location of MB into amorphous P3HT areas.

The case of P3HT/MB reminds PEDOT:PSS in various aspects such as i) the predominance of bipolarons as indicated by UV–vis–NIR spectroscopy, ii) the fact that counterions onto PSS chains surround the PEDOT nanocrystals and iii) the fact that so-called secondary crystallization induced by, e.g., ethylene glycol helps to phase-separate PSS and PEDOT and hence improve the charge conductivity.[39,40] From this perspective, the intrinsic semicrystalline nanostructuration of P3HT can be used as a scaffold for the selective nano-scale doping of the polymer.
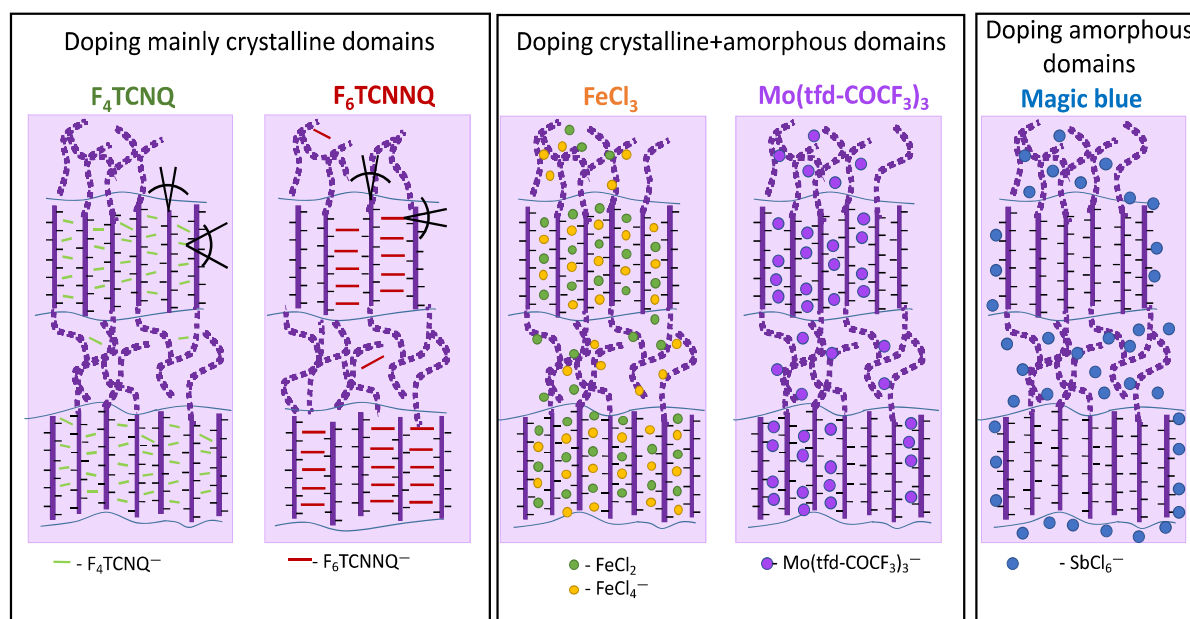
Figure 12. *Various doped P3HT microstructures: doping of the crystalline domains for F₄TCNQ and F₆TCNNQ; doping of both crystalline and amorphous zones for FeCl₃ and Mo(tdf-COCF₃)₃ and doping of the amorphous zones for MB.*

6.4.7 Reflectivity of P3HT doped with MB

Taking long-term stability of PSLMs into consideration, "NIR polarizers" should reflect NIR light

rather than absorb it. High reflectivity should prevent the organic layers in PSLMs from overheating due to prolonged exposure to sunlight. For this reason, we measured the reflectivity of oriented P3HT films doped with MB. The oriented P3HT film with a thickness of 212 ± 11 nm was dipped in a MB solution with a concentration of 0.5 g. L^{-1}. At this doping level, different species including polarons and bipolarons coexist. The reflectance (R) and transmittance (T) of doped P3HT films were probed by polarized UV-Vis-NIR spectroscopy equipped with an integrating sphere (**Figure 13a,b**). We first measured the R and T of a glass substrate without doped polymer, setting the R of glass to 0 % and the T of glass to 100%. Then, the R and T for doped films/glass were measured. According to the measured spectra, the net absorption spectrum (**Figure 13c**) can be obtained through the following equation:[41]

$$T(\%) + R(\%) + Abs(\%) = 100\% \qquad Eq.6.2$$

All spectra show a strong anisotropy of optical properties. For POL//R, a low transmittance in the NIR region was observed due to the formation of P1 and P2 band upon doping. Interestingly, the P1 band at 800 nm displays a large reflectivity ($\sim$ 74%) and a small absorption ($\sim$ 18%). On the contrary, the P2 transition at 2200 nm shows a large absorption ($\sim$ 71%) and little reflectivity ($\sim$ 15%). This observation is interesting since it indicates that only the P1 band at 2200 nm is responsible for a strong reflectivity. This result suggests also that delocalized charge carriers responsible for strong metallic-like NIR reflectivity are involved for the only P1 band transition, not for the P2 transition that may correspond to more localized charge carriers. A similar study on the transmittance and reflectance of various polythiophene films including poly(3,4-ethylenedioxythiophene) (PEDOT), poly(3,4-propylenedioxythiophene) (PProDOT) and poly(3,4-(2,2-dimethylpropylenedioxy)thiophene) (PProDOT-Me$_2$) in three different states (neutral, lightly doped and fully doped) was reported by Hwang et al.[42] For all three polymers, the lightly doped films show polarons, with a decrease of neutral polymer absorption and the presence of two new bands (i.e., polaronic absorption P1 and P2). In the fully doped state, the neutral polymer absorption is completely bleached and a single broad band is observed in NIR range which is associated with the bipolaron formation. More importantly, the NIR reflectance of the P1 band significantly increases due to the appearance of bipolarons. This result is consistent with that observed in MB-doped P3HT films for which bipolarons form at high MB concentration with a high NIR reflectance at around 2000~2200 nm. However, these doped

polythiophene films are not showing a strong reflectivity in the NIR close to 1000 nm as required for PSLM devices to play the role of NIR reflectors for sun light. Since the largest fraction of solar heating is distributed in the 700 - 1000 nm range, it is important to develop oriented doped polymers that show a high reflectivity in this range and thus efficiently prevent solar heating.

For POL⊥R, both absorption of P1 and P2 band are larger than their reflectivity. The low reflectivity is probably attributed to more strongly localized charge carrier in the amorphous fraction of P3HT. This is consistent with the reduced charge mobilities observed in amorphous P3HT versus highly crystalline P3HT.[43]

To conclude this part, MB-doped P3HT does not show the high NIR reflectivity necessary for PSLM devices since the observed NIR reflectivity is strong only for the spectral range beyond 2000 nm. The comparison of absorption and reflectivity measurements clearly shows that strong NIR-reflectivity is only observed for the P1 band transition when highly delocalized bipolaronic (multipolaronic? polaronic band?) states are formed. One strategy to use doped PSCs as NIR reflector would be to shift the P1 band more to the blue, possibly by engineering the chemical structure to obtain a wide band-gap polymer.[44] A blue shift of the P1 band seems however difficult to achieve as it implies that the energetic level of the polaron state would be less favorable for effective charge conductivity and metallic-like states.
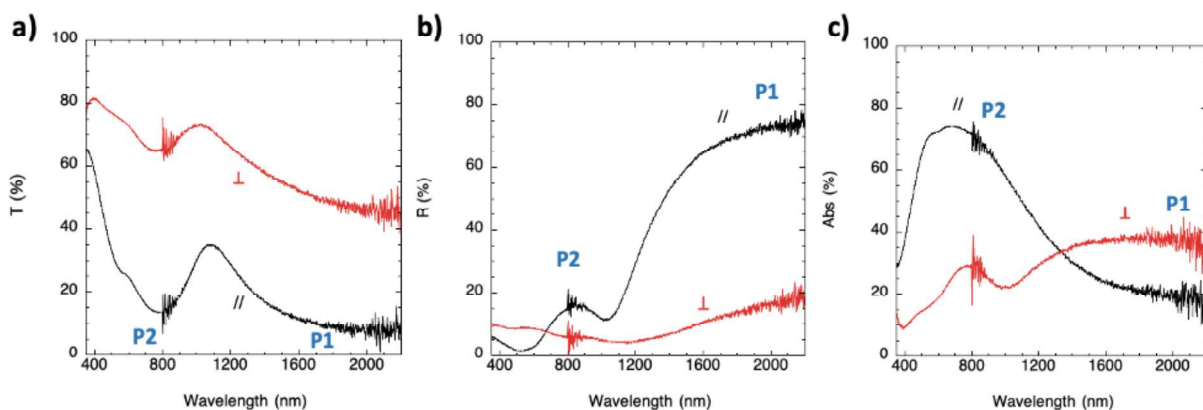
Figure 13. a) Transmittance, b) reflectance and c) Net absorption spectrum of oriented P3HT polymers (212 ± 11 nm) doped with MB ([MB]=0.5 g.L^{-1}). The incident light polarization is parallel and perpendicular to the rubbing direction. The pure absorption spectrum was plotted by the equation expressed as T + R + Abs = 1. Where the measured R contains reflectivity and diffusion of the oriented doped films.

6.4.8 PSLM using highly oriented conducting polymers

As demonstrated in the polarized transmittance spectra (**Figure 13a**), the oriented MB-doped P3HT films display anisotropic optical properties in the NIR range. With such NIR polarizers, we will test the optical response of a self-powered PSLM. The transparent ITO electrodes employed for PSLMs are characterized by a high absorption in the IR range beyond 1100 nm, preventing the modulation of NIR light. Moreover, the majority of solar heating distribution is located in the range 700-1000 nm. For these reasons, we focused on the fabrication of aligned P3HT doped with MB showing the highest optical absorption from 800 to 1000 nm. In other words, we looked for a high polaronic absorption band P2 by tuning the doping level. According to the evolution of UV-Vis-NIR as a function of doping concentration (**Figure 7a,b**), we conclude that the P3HT neutral absorption is fully bleached when [MB] $\geq$ 0.2 g. L^{-1}, minimizing the visible light absorption. However, at the same time, the formation of bipolarons leads to a decrease in the absorbance of P2 band. Therefore, [MB] = 0.1 g. L^{-1} was identified as the best condition to prepare NIR polarizers, despite of a more limited transmittance in the visible range.

The transmittance of two "NIR polarizers" in parallel (black lines) and in perpendicular (red lines) was first measured, as illustrated in **Figure 14a,b**. Two oriented doped polymer films, parallel or perpendicular to each other, both exhibit a high transmittance in the visible range. A slight difference between black and red lines in NIR range indicates that the doped oriented films have the ability to polarize NIR light.

A PM6-based PSLM which can operate in the self-powered regime, was subsequently placed between two crossed "NIR polarizers" (**Figure 14c**), and its optical response was measured by switching between the OFF state (blue line) and ON state (green line). As illustrated in **Figure 14d,** with the doped and aligned P3HT films, despite of modest DR (DR≈5 at 800 nm measured by UV-visible spectroscopy), PSLM displays a small but significant optical modulation in the NIR range, along with a negligible visible light modulation in the range 400-650 nm. This result indicates that using the doped oriented polymers limits the optical modulation of PSLM to the NIR range. For the comparison, **Figure 14e** shows the optical response of PM6-based PSLM using commercial polarizers. In the case of commercial polarizers, when switching PSLM from the OFF state to ON state, the device transmittance is reduced to less than 1% in both visible and NIR range. The average visible transmittance (AVT) (in the range of 380-780 nm) of

PM6-based PSLM in the OFF state using different polarizers were determined by *Eq.4.1* (Chapter 4) and summarized in **Table 3**. The combination of device with doped oriented polymers leads to a significant improvement in the transparency (AVT≈15%) in the OFF state. Furthermore, the amplitude of optical modulation (I_{OFF}/I_{ON}) at 800 nm is around 1.4 that is very close to the theoretical value ($I_{OFF}/I_{ON} \approx 1.8$ at 800 nm) determined by *Eq.5.1*.

Table 3. *AVT of a PM6-based PSLM in the OFF state with commercial polarizers (Thorlabs WP25M-UP) and with two crossed oriented conducting polymers.*

PM6-based PSLM with different polarizers	AVT* (%)
Commercial polarizers	9.2
Oriented conducting polymers	14.9

*AVT is calculated by an equation: $AVT = \frac{\int T(\lambda)P(\lambda)S(\lambda)d\lambda}{\int P(\lambda)S(\lambda)d\lambda}$, where T is transmittance, P is the human eyes photonic response (380 nm-780 nm), S is solar radiance spectrum (AM 1.5G) and λ is the wavelength.
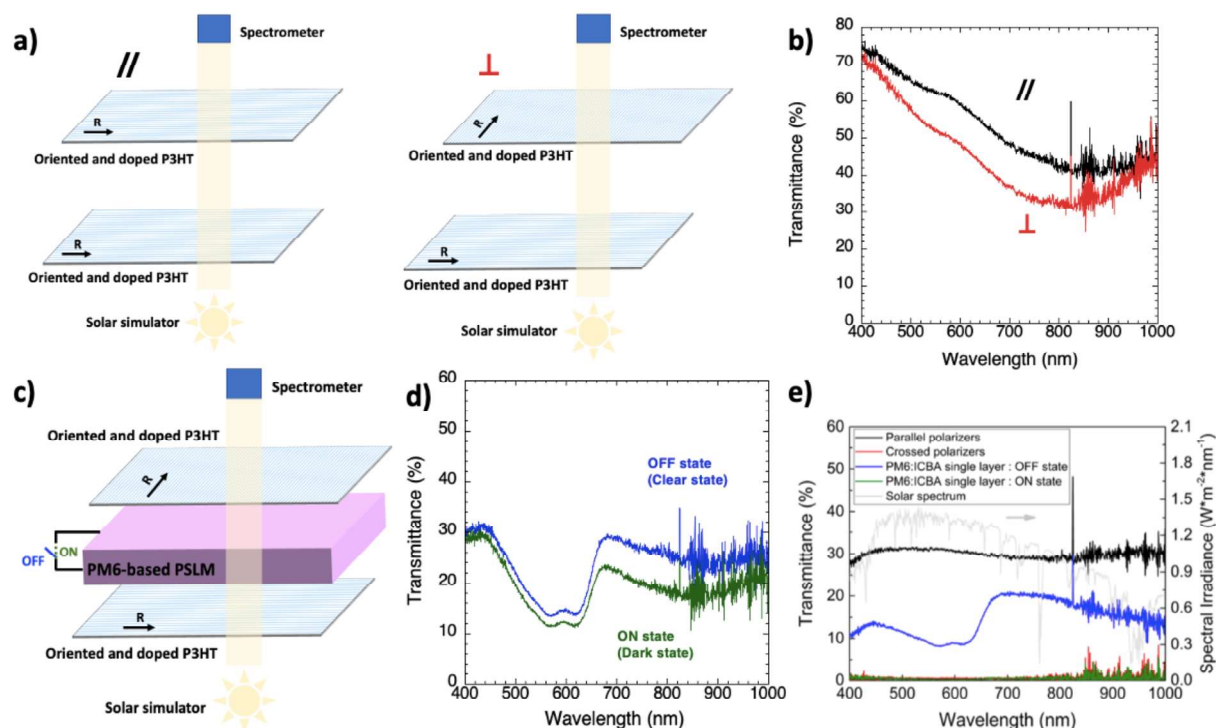
Figure 14. *a) Schematic illustration of transmittance measurements for 'NIR polarizers' in parallel (black) and in perpendicular (red). R is rubbing direction. b) Transmittance of two oriented doped polymers (109 ± 5 nm) in*

parallel (dark line) and in perpendicular (red line). c) Schematic illustration of transmittance measurements for a PM6-based PSLM with two crossed "NIR polarizers" switching between the OFF state and the ON state. d) Transmittance of PM6-based PSLM in the OFF state (blue line) and ON state (green line) using two crossed "NIR polarizers". e) Transmittance of two wire-grid polarizers (Thorlabs WP25M-UP) in parallel (dark line) and in perpendicular (red line) and PM6-based PSLM in the OFF state (blue line) and ON state (green line) using wire-grid polarizers. The gray line corresponds to the solar spectrum.

6.5 Conclusion

In this chapter, the conductivities, optical properties, crystal structure of oriented P3HT polymers doped with MB were first studied. Doping P3HT with MB results in a high charge conductivity along the polymer chains direction around 3000 S.cm^{-1}. Such large conductivities and high transparency in the visible range make MB-doped/oriented P3HT films an interesting alternative to replace transparent ITO electrodes in devices provided such doped PSC films show sufficient long-term stability. Structural studies by TEM indicate that both the alignment and crystal structure of rubbed P3HT is preserved upon doping. A combination of TEM and polarized UV-vis spectroscopy demonstrates that MB dopant molecules do not intercalate into P3HT crystals as observed for other dopants such as F_4TCNQ or $FeCl_3$. The doping of both crystalline and amorphous zones of P3HT occurs through the amorphous phase that hosts preferentially the dopants i.e., $SbCl_6^-$ counterions. High conductivities in MB-doped P3HT are thus explained by the fact that crystalline P3HT domains retain their pristine structure and are doped from their interface with the surrounding amorphous phase where the dopants are located. Augmenting the distance between polarons in crystals and counterions in amorphous zones might be an effective strategy to reduce polaron localization through coulombic trapping by dopant counterions and thus to improve the charge conductivities in doped-PSCs.

The doped oriented films show anisotropic optical properties in NIR range of interest for PSLM devices when such layers are used as NIR polarizers. With increasing the doping concentration, the formation of bipolaron is evidenced, which is associated with a decrease of the ratio P2/P1. Therefore, in order to gain polaronic P2 absorption, the oriented conductive polymers were prepared at low doping concentration and served as 'NIR-polarizer' for PM6-based PSLMs. The PSLM devices fabricated with such 'NIR-polarizer' show increased transparency in the visible range and optical modulation in the NIR range. A small light intensity modulation was attributed to a modest DR of oriented conductive polymers at 800 nm. Nevertheless, this result

demonstrated that it is possible to keep the high transmittance of PSLMs in the visible range and only modulate the NIR light. More interestingly, the doped films along the chain direction show a high reflectivity at $\lambda \geq 2500$ nm and a high optical absorption at 800 nm. However, the reduced reflectivity and the high absorbance of the P2 band in MB-doped P3HT is not optimal for PSLM applications since the doped PSC films will heat upon solar light exposure. To include doped-PSCs in PSLMs, new strategies are necessary to tune the P1 and P2 band positions and match solar spectrum specifications. One could for instance play with the modulation of the P1 and P2 band positions by adapting the electronic structure of alternated p(D-A) polymers along with the choice of the right dopant and doping method.

References

(1)   Khandelwal, H.; Schenning, A. P. H. J.; Debije, M. G. Infrared Regulating Smart Window Based on Organic Materials. *Adv. Energy Mater.* **2017**, *7* (14), 1602209.

(2)   Vijayakumar, V.; Zhong, Y.; Untilova, V.; Bahri, M.; Herrmann, L.; Biniek, L.; Leclerc, N.; Brinkmann, M. Bringing Conducting Polymers to High Order: Toward Conductivities beyond 10^5 S Cm^{-1} and Thermoelectric Power Factors of 2 MW m^{-1} K^{-2}. *Adv. Energy Mater.* **2019**, *9* (24), 1900266.

(3)   Vijayakumar, V.; Zaborova, E.; Biniek, L.; Zeng, H.; Herrmann, L.; Carvalho, A.; Boyron, O.; Leclerc, N.; Brinkmann, M. Effect of Alkyl Side Chain Length on Doping Kinetics, Thermopower, and Charge Transport Properties in Highly Oriented F$_4$TCNQ-Doped PBTTT Films. *ACS Appl. Mater. Interfaces* **2019**, *11* (5), 4942–4953.

(4)   Untilova, V.; Zeng, H.; Durand, P.; Herrmann, L.; Leclerc, N.; Brinkmann, M. Intercalation and Ordering of F$_6$TCNNQ and F$_4$TCNQ Dopants in Regioregular Poly(3-Hexylthiophene) Crystals: Impact on Anisotropic Thermoelectric Properties of Oriented Thin Films. *Macromolecules* **2021**, *54* (13), 6073–6084.

(5)   Hamidi-Sakr, A.; Biniek, L.; Bantignies, J.-L.; Maurin, D.; Herrmann, L.; Leclerc, N.; Lévêque, P.; Vijayakumar, V.; Zimmermann, N.; Brinkmann, M. A Versatile Method to Fabricate Highly In-Plane Aligned Conducting Polymer Films with Anisotropic Charge Transport and Thermoelectric Properties: The Key Role of Alkyl Side Chain Layers on the Doping Mechanism. *Adv. Funct. Mater.* **2017**, *27* (25), 1700173.

(6)   Untilova, V.; Hynynen, J.; Hofmann, A. I.; Scheunemann, D.; Zhang, Y.; Barlow, S.; Kemerink, M.; Marder, S. R.; Biniek, L.; Müller, C.; Brinkmann, M. High Thermoelectric Power Factor of Poly(3-Hexylthiophene) through In-Plane Alignment and Doping with a Molybdenum Dithiolene Complex. *Macromolecules* **2020**, *53* (15), 6314–6321.

(7)   Zhong, Y.; Untilova, V.; Muller, D.; Guchait, S.; Kiefer, C.; Herrmann, L.; Zimmermann, N.; Brosset, M.; Heiser, T.; Brinkmann, M. Preferential Location of Dopants in the Amorphous Phase of Oriented Regioregular Poly(3-hexylthiophene-2,5-diyl) Films Helps Reach Charge Conductivities of 3000 S Cm^{-1}. *Adv. Funct. Mater.* **2022**, *32* (30), 2202075.

(8)   Shirakawa, H.; Louis, E. J.; MacDiarmid, A. G.; Chiang, C. K.; Heeger, A. J. Synthesis of Electrically Conducting Organic Polymers: Halogen Derivatives of Polyacetylene, (CH) x. *J. Chem. Soc. Chem. Commun.* **1977**, No. 16, 578.

(9)   Lüssem, B.; Keum, C.-M.; Kasemann, D.; Naab, B.; Bao, Z.; Leo, K. Doped Organic Transistors. *Chem. Rev.* **2016**, *116* (22), 13714–13751.

(10)   Fahlman, M.; Fabiano, S.; Gueskine, V.; Simon, D.; Berggren, M.; Crispin, X. Interfaces in Organic Electronics. *Nat. Rev. Mater.* **2019**, *4* (10), 627–650.

(11)   Bubnova, O.; Khan, Z. U.; Malti, A.; Braun, S.; Fahlman, M.; Berggren, M.; Crispin, X. Optimization of the Thermoelectric Figure of Merit in the Conducting Polymer Poly(3,4-Ethylenedioxythiophene). *Nat. Mater.* **2011**, *10* (6), 429–433.

(12)   Russ, B.; Glaudell, A.; Urban, J. J.; Chabinyc, M. L.; Segalman, R. A. Organic Thermoelectric Materials for Energy Harvesting and Temperature Control. *Nat. Rev. Mater.* **2016**, *1* (10), 16050.

(13)   Kroon, R.; Mengistie, D. A.; Kiefer, D.; Hynynen, J.; Ryan, J. D.; Yu, L.; Müller, C. Thermoelectric Plastics: From Design to Synthesis, Processing and Structure–Property Relationships. *Chem. Soc. Rev.* **2016**, *45* (22), 6147–6164.

(14)   Pingel, P.; Neher, D. Comprehensive Picture of p -Type Doping of P3HT with the Molecular Acceptor F 4 TCNQ. *Phys. Rev. B* **2013**, *87* (11), 115209.

(15) Enengl, C.; Enengl, S.; Pluczyk, S.; Havlicek, M.; Lapkowski, M.; Neugebauer, H.; Ehrenfreund, E. Doping-Induced Absorption Bands in P3HT: Polarons and Bipolarons. *ChemPhysChem* **2016**, *17* (23), 3836–3844.

(16) Li, W.; Yang, L.; Tumbleston, J. R.; Yan, L.; Ade, H.; You, W. Controlling Molecular Weight of a High Efficiency Donor-Acceptor Conjugated Polymer and Understanding Its Significant Impact on Photovoltaic Properties. *Adv. Mater.* **2014**, *26* (26), 4456–4462.

(17) Salleo, A.; Kline, R. J.; DeLongchamp, D. M.; Chabinyc, M. L. Microstructural Characterization and Charge Transport in Thin Films of Conjugated Polymers. *Adv. Mater.* **2010**, *22* (34), 3812–3838.

(18) Duong, D. T.; Wang, C.; Antono, E.; Toney, M. F.; Salleo, A. The Chemical and Structural Origin of Efficient P-Type Doping in P3HT. *Org. Electron.* **2013**, *14* (5), 1330–1336.

(19) Sirringhaus, H.; Brown, P. J.; Friend, R. H.; Nielsen, M. M.; Bechgaard, K.; Langeveld-Voss, B. M. W.; Spiering, A. J. H.; Janssen, R. A. J.; Meijer, E. W.; Herwig, P.; de Leeuw, D. M. Two-Dimensional Charge Transport in Self-Organized, High-Mobility Conjugated Polymers. *Nature* **1999**, *401* (6754), 685–688.

(20) Zhang, S.; Hill, H. M.; Moudgil, K.; Richter, C. A.; Hight Walker, A. R.; Barlow, S.; Marder, S. R.; Hacker, C. A.; Pookpanratana, S. J. Controllable, Wide-Ranging N-Doping and P-Doping of Monolayer Group 6 Transition-Metal Disulfides and Diselenides. *Adv. Mater.* **2018**, *30* (36), 1802991.

(21) Hofmann, A. I.; Kroon, R.; Zokaei, S.; Järsvall, E.; Malacrida, C.; Ludwigs, S.; Biskup, T.; Müller, C. Chemical Doping of Conjugated Polymers with the Strong Oxidant Magic Blue. *Adv. Electron. Mater.* **2020**, *6* (8), 2000249.

(22) Hamidi-Sakr, A.; Biniek, L.; Fall, S.; Brinkmann, M. Precise Control of Lamellar Thickness in Highly Oriented Regioregular Poly(3-Hexylthiophene) Thin Films Prepared by High-Temperature Rubbing: Correlations with Optical Properties and Charge Transport. *Adv. Funct. Mater.* **2016**, *26* (3), 408–420.

(23) Vijayakumar, V.; Durand, P.; Zeng, H.; Untilova, V.; Herrmann, L.; Algayer, P.; Leclerc, N.; Brinkmann, M. Influence of Dopant Size and Doping Method on the Structure and Thermoelectric Properties of PBTTT Films Doped with F_6TCNNQ and F_4TCNQ. *J. Mater. Chem. C* **2020**, *8* (46), 16470–16482.

(24) Mi, B.; Coronell, O.; Marinas, B.; Watanabe, F.; Cahill, D.; Petrov, I. Physico-Chemical Characterization of NF/RO Membrane Active Layers by Rutherford Backscattering Spectrometry☆. *J. Membr. Sci.* **2006**, *282* (1–2), 71–81.

(25) Jose Chirayil, C.; Abraham, J.; Kumar Mishra, R.; George, S. C.; Thomas, S. Instrumental Techniques for the Characterization of Nanoparticles. In *Thermal and Rheological Measurement Techniques for Nanomaterials Characterization*; Elsevier, 2017; pp 1–36.

(26) Fan, X.; Wang, J.; Wang, H.; Liu, X.; Wang, H. Bendable ITO-Free Organic Solar Cells with Highly Conductive and Flexible PEDOT:PSS Electrodes on Plastic Substrates. *ACS Appl. Mater. Interfaces* **2015**, *7* (30), 16287–16295.

(27) Lee, J.-Y.; Connor, S. T.; Cui, Y.; Peumans, P. Solution-Processed Metal Nanowire Mesh Transparent Electrodes. *Nano Lett.* **2008**, *8* (2), 689–692.

(28) Yu, Z.; Zhang, Q.; Li, L.; Chen, Q.; Niu, X.; Liu, J.; Pei, Q. Highly Flexible Silver Nanowire Electrodes for Shape-Memory Polymer Light-Emitting Diodes. *Adv. Mater.* **2011**, *23* (5), 664–668.

(29) Kim, K. S.; Zhao, Y.; Jang, H.; Lee, S. Y.; Kim, J. M.; Kim, K. S.; Ahn, J.-H.; Kim, P.; Choi, J.-Y.; Hong, B. H. Large-Scale Pattern Growth of Graphene Films for Stretchable Transparent Electrodes. *Nature* **2009**, *457* (7230), 706–710.

(30) Becerril, H. A.; Mao, J.; Liu, Z.; Stoltenberg, R. M.; Bao, Z.; Chen, Y. Evaluation of Solution-

Processed Reduced Graphene Oxide Films as Transparent Conductors. *ACS Nano* **2008**, *2* (3), 463–470.

(31) Na, S.-I.; Kim, S.-S.; Jo, J.; Kim, D.-Y. Efficient and Flexible ITO-Free Organic Solar Cells Using Highly Conductive Polymer Anodes. *Adv. Mater.* **2008**, *20* (21), 4061–4067.

(32) Zhang, F.; Johansson, M.; Andersson, M. R.; Hummelen, J. C.; Inganäs, O. Polymer Photovoltaic Cells with Conducting Polymer Anodes. *Adv. Mater.* **2002**, *14* (9), 662–665.

(33) Po, R.; Carbonera, C.; Bernardi, A.; Tinti, F.; Camaioni, N. Polymer- and Carbon-Based Electrodes for Polymer Solar Cells: Toward Low-Cost, Continuous Fabrication over Large Area. *Sol. Energy Mater. Sol. Cells* **2012**, *100*, 97–114.

(34) Brinkmann, M.; Wittmann, J.-C. Orientation of Regioregular Poly(3-Hexylthiophene) by Directional Solidification: A Simple Method to Reveal the Semicrystalline Structure of a Conjugated Polymer. *Adv. Mater.* **2006**, *18* (7), 860–863.

(35) Untilova, V.; Biskup, T.; Biniek, L.; Vijayakumar, V.; Brinkmann, M. Control of Chain Alignment and Crystallization Helps Enhance Charge Conductivities and Thermoelectric Power Factors in Sequentially Doped P3HT:F$_4$TCNQ Films. *Macromolecules* **2020**, *53* (7), 2441–2453.

(36) Neusser, D.; Malacrida, C.; Kern, M.; Gross, Y. M.; van Slageren, J.; Ludwigs, S. High Conductivities of Disordered P3HT Films by an Electrochemical Doping Strategy. *Chem. Mater.* **2020**, *32* (14), 6003–6013.

(37) Maliakal, A. J. Characterization of Dopant Diffusion within Semiconducting Polymer and Small-Molecule Films Using Infrared-Active Vibrational Modes and Attenuated Total Reflectance Infrared Spectroscopy. *ACS Appl. Mater. Interfaces* **2013**, *5* (17), 8300–8307.

(38) *Organic Electronics Materials and Devices*; Ogawa, S., Ed.; Springer: Tokyo, 2015.

(39) Kim, N.; Kee, S.; Lee, S. H.; Lee, B. H.; Kahng, Y. H.; Jo, Y.-R.; Kim, B.-J.; Lee, K. Highly Conductive PEDOT:PSS Nanofibrils Induced by Solution-Processed Crystallization. *Adv. Mater.* **2014**, *26* (14), 2268–2272.

(40) Takano, T.; Masunaga, H.; Fujiwara, A.; Okuzaki, H.; Sasaki, T. PEDOT Nanocrystal in Highly Conductive PEDOT:PSS Polymer Films. *Macromolecules* **2012**, *45* (9), 3859–3865.

(41) Dresselhaus, M.; Cronin, S. B.; Dresselhaus, G.; Gomes Souza Filho, A. *Solid State Properties: From Bulk to Nano*, 1st ed. 2018.; Graduate Texts in Physics; Springer Berlin Heidelberg : Imprint: Springer: Berlin, Heidelberg, 2018.

(42) Hwang, J.; Tanner, D. B.; Schwendeman, I.; Reynolds, J. R. Optical Properties of Nondegenerate Ground-State Polymers: Three Dioxythiophene-Based Conjugated Polymers. *Phys. Rev. B* **2003**, *67* (11), 115205.

(43) Alberga, D.; Perrier, A.; Ciofini, I.; Mangiatordi, G. F.; Lattanzi, G.; Adamo, C. Morphological and Charge Transport Properties of Amorphous and Crystalline P3HT and PBTTT: Insights from Theory. *Phys. Chem. Chem. Phys.* **2015**, *17* (28), 18742–18750.

(44) McCall, R. P.; Ginder, J. M.; Roe, M. G.; Asturias, G. E.; Scherr, E. M.; MacDiarmid, A. G.; Epstein, A. J. Massive Polarons in Large-Energy-Gap Polymers. *Phys. Rev. B* **1989**, *39* (14), 10174–10178.

Chapter 7 Conclusion and Outlooks

In this thesis, a novel smart glazing system, called Photovoltaic Spatial Light Modulator (PSLM), was introduced, opening up a new direction for the development of self-powered smart windows. However, there are still many scientific and technical challenges that need to be addressed before PSLMs can be applied to smart windows. In particular, the transparency remains quietly low in the OFF state mainly due to the optical absorption of external polarizers and PV layers employed for PSLMs. Therefore, various strategies have been tried in this thesis to improve the transparency of devices: I) selecting a semi-transparent photovoltaic layer II) using the oriented photovoltaic layers and III) using oriented conducting polymer films as "NIR polarizers" for PSLMs.

- **Semi-transparent PV layer:** The optical absorption of organic semiconductors can be tailored by molecular engineering. In this work, we explored a new wide-bandgap material ($E_g \approx 2.8$ eV) composed of two triazatruxene (TAT) end-groups, linked by a π-conjugated carbazole (Cbz) unit. The thin film of TAT-Cbz exhibits optical absorption mainly in the near-ultraviolet (NUV) region. NUV light harvesting PV layers were fabricated by blending TAT-Cbz with $PC_{60}BM$. The blend films showed a high transmittance in the visible range and produced a photovoltage higher than threshold voltage (V_{th}) of LC molecules. By using such semi-transparent PV layers, we managed to increase the transparency of PSLM from 9% to 15% of AVT in the OFF state. Although solar cells based on the TAT-Cbz/$PC_{60}BM$ show a modest PV performance (PCE=0.12-0.13%), PSLMs still show a 32% drop in the transmittance when switching from the OFF state to the ON state. This study demonstrates that a photovoltage delivered by PV layer exceeding V_{th} of LC molecules ($V_{ph} > V_{th}$) is a necessary and sufficient condition for self-powered operation of PSLMs. On the other hand, we demonstrated that the photocurrent produced by PV layer have a strong influence on the response time of devices.

    The self-powered device shows a modest sensitivity due to the photovoltage delivered by TAT-Cbz/$PC_{60}BM$ close to V_{th}. The semi-transparent PV layers with a higher V_{ph} are able to further improve the performance of device. The OSC based on the TAT-Cbz/Indene-C_{60} Bisadduct (ICBA) was fabricated in our works, producing around 1 eV of V_{oc}. However, this result was not reproducible, part of ICBA-based devices showed a

remarkable leakage current probably due to poor film-forming properties. A semi-transparent polymer might be added into this BHJ layer to improve the quality of the films and fabricate a ternary solar cell. Besides TAT-Cbz/PC$_{60}$BM or TAT-Cbz/ICBA small molecules, other pairs of wide-bandgap materials such as BF-DPB/B4PYMPM with a V$_{oc}$ of ~2 eV would be worthy to test with PSLMs.

- **Oriented photovoltaic layers:** High temperature rubbing is an effective and reproducible method to orient many conjugated polymers such as P3HT, C12-pBTTT and P(NDI2OD-T2)).[1–3] In previous work of Brinkmann's group, they demonstrated that both rubbing temperature and molecular weight distribution of polymers have a strong impact on the alignment of films. Our results indicate that the rubbing force has also an influence on the alignment and crystal structure of P3HT films. Stronger rubbing force led to better orientation and crystallinity in rubbed P3HT films whereas the roughness increases only slightly. Oriented PV layer with a quasi-bilayer structure was fabricated by orienting P3HT polymer and solution deposition of PC$_{60}$BM layer atop the oriented film. Such PV layers display anisotropic optical (DR=3) and PV properties (J$_{sc///}$J$_{sc\perp}$=1.5). However, they deliver a low photovoltage with V$_{oc}$≈0.46 V < V$_{th}$ that cannot switch the LC orientation necessary for a self-powered PSLM. A second strategy was proposed to prepare polarized OSC and produce a higher photovoltage using an inverted structure. In this case, the oriented PV layer was composed of PBnDT-FTAZ and N2200 polymers. Blend films were successfully aligned by rubbing and thermal annealing. We demonstrated that the thermal annealing helps improve the crystallinity of both polymers and their alignment. To fabricate a polarized OSC, a very thin and non-aligned FTAZ:N2200 blend film (l≈35 nm) was deposited on the top of oriented FTAZ:N2200 blend film to overcome short circuit caused by pinholes and scratches created by rubbing. A larger active area (0.12 cm^2) of polarized OSC was obtained in comparison with that reported in the previous publication (0.0314 cm^2). Interestingly, the polarized OSC eventually shows a J$_{sc}$ ratio of 1.5 and a DR of 4.

  The thermal evaporation of small donor molecules such as α-sexithiophene (6T) on the rubbed PV layer might be an alternative method to overcome pinholes in the films while maintaining the alignment of the underlying blend films. Most importantly, 6T

can orient uniaxially on the oriented polymer substrates. Tanigaki et al. have successfully oriented 6T molecules onto polythiophene (PT) film prepared by friction transfer and fabricated a polarized OPV device with a configuration: ITO/PEDOT: PSS/oriented PT/oriented 6T/PC$_{60}$BM/ bathocuproine/LiF/Al.[4] The oriented PT/6T film exhibits a DR of 6.3 at maximum absorption wavelength of 6T. The OPV device based on such oriented 6T display a dichroic PV effect. That could be beneficial for their integration in PSLMs. It is also worth mentioning that another alternative to fabricate polarized OSCs could be to orient rod-like acceptor molecules[5] on rubbed P3HT.

- **Oriented conducting polymers** Doping oriented P3HT polymers with MB leads to a charge conductivity reaching up to 3000 S.cm^{-1} along the chain direction, that is the highest conductivity reported for doped P3HT, making it possible to replace the ITO electrodes. The unchanged crystal structure of P3HT upon doping reveals that MB dopants are intercalated into the amorphous phase, reducing the polaron localization in the crystal domains and thereby boosting the charge mobilities. Doped oriented P3HT films show a high transmittance in the visible region and anisotropic NIR absorption and reflectivity. They can act as 'NIR polarizers' for PSLMs. We demonstrated that a self-powered PSLM combining these 'NIR polarizers' improves the transparency of PSLMs while restricting the optical modulation to the NIR range. We proved that oriented doped polymers display a high conductivity and have a potential as 'NIR polarizer' for PSLMs. Yet there are still many open questions and issues to be tackled.

    - One challenge is NIR reflectivity of oriented conducting polymers. In this work, the MB-doped oriented P3HT polymers exhibit a large optical absorption in the range of 700-1200 nm and a high reflectivity in the range of 1200-2500 nm along the chain direction. However, the most fraction of solar heating is distributed in the 700~1000 nm range. Such "NIR polarizer" cannot be considered as an ideal "NIR reflector". In the doped polythiophene films, the NIR reflectivity is partly associated with the presence of bipolarons. However, the correlation between optical reflectance and polaronic bands in doped organic films has been seldom discussed. We proposed one possibility for gaining a reflectivity in 1000 nm is to shift the

polaronic band P1 more to the blue. This strategy might be achieved with a wide bandgap polymer. An in-depth study of the reflectivity of polaronic species is crucial to apply oriented doped polymers to smart window applications.

- Another issue is stability of the oriented doped polymers in practical applications. Unlike inorganic doping where the host materials and dopants are bound by strong covalent bonds, organic doping involves a weak coulombic attraction between conjugated polymers and dopant molecules.[6] The systems are labile and de-doping often occurs, either by physico-chemical mechanism (desorption, dopant evaporation) or by chemical aging. The charge-transfer reaction for doping polymers is intrinsically reversible equilibrium process. Some factors such as light, heat and chemical reaction can modify the molecular energy levels and affect the equilibrium until dedoping occurs.[7] Chemical reactions might occur due to external environment (such as oxygen and water vapor) or intrinsic instability of doped polymers.[8] Such dedoping causes a significant decrease in polaronic absorption and conductivity. However, to date, dedoping mechanisms are poorly understood. It is possibly attributed to the physical diffusion or/and the chemical degradation. Identifying the dedoping mechanism would help us to find strategies for preventing the doped film degradation, e.g., an appropriate material for encapsulation to enhance the environmental stability.

The semi-transparent PV layers and MB-doped oriented P3HT films have been proved to enhance the transparency of PSLM device (AVT≈ 15% in both cases). An alternative strategy to further improve the device transparency is to investigate more transparent AL layer to replace P3HT film or blend the P3HT polymer with the near UV-absorbing materials such as $PC_{60}BM$ to reduce the visible light absorption. An ideal AL layer should have a high transmittance in the visible range while induce a high-quality LC alignment. Moreover, it should be able to neutralize the accumulated ion (that is residual ions in LC layer) at the AL/LC interface that impacts negatively on the optical response of PSLMs. Combining the "NIR polarizer" with a PSLM based on a semi-transparent PV layer and transparent AL should lead to PSLMs with improved transparency.

In addition to the transparency of PSLM devices, there are still other obstacles that need to be

tackled such as large-scale fabrication and long-term stability. At present, a self-powered PSLMs based on a tandem structure with an active area of 15 cm^2 was achieved by a fabrication process similar to that of small-scale devices.[9] The larger devices exhibit a longer response time due to increased resistive-capacitive time constant. Such large devices might be fabricated by spray coating technology. As for long-term stability, using LC molecules with a higher purity may improve the stability of PSLMs. However, such LC molecules commonly possess a higher V_{th}. In other words, a higher V_{oc} delivered by PV layer would be required for self-powered PSLMs.

References

(1)   Biniek, L.; Leclerc, N.; Heiser, T.; Bechara, R.; Brinkmann, M. Large Scale Alignment and Charge Transport Anisotropy of PBTTT Films Oriented by High Temperature Rubbing. *Macromolecules* **2013**, *46* (10), 4014–4023.

(2)   Hamidi-Sakr, A.; Biniek, L.; Fall, S.; Brinkmann, M. Precise Control of Lamellar Thickness in Highly Oriented Regioregular Poly(3-Hexylthiophene) Thin Films Prepared by High-Temperature Rubbing: Correlations with Optical Properties and Charge Transport. *Adv. Funct. Mater.* **2016**, *26* (3), 408–420.

(3)   Brinkmann, M.; Gonthier, E.; Bogen, S.; Tremel, K.; Ludwigs, S.; Hufnagel, M.; Sommer, M. Segregated *versus* Mixed Interchain Stacking in Highly Oriented Films of Naphthalene Diimide Bithiophene Copolymers. *ACS Nano* **2012**, *6* (11), 10319–10326.

(4)   Mizokuro, T.; Takeuchi, K.; Heck, C.; Aota, H.; Tanigaki, N. Orientation Management of α-Sexithiophene Layer for the Application in Organic Photovoltaic Devices. *Org. Electron.* **2012**, *13* (12), 3130–3137.

(5)   Matsidik, R.; Komber, H.; Brinkmann, M.; Schellhammer, K. S.; Ortmann, F.; Sommer, M. Evolution of Length-Dependent Properties of Discrete n-Type Oligomers Prepared via Scalable Direct Arylation. *J. Am. Chem. Soc.* **2023**, jacs.3c00058.

(6)   Li, J.; Rochester, C. W.; Jacobs, I. E.; Friedrich, S.; Stroeve, P.; Riede, M.; Moulé, A. J. Measurement of Small Molecular Dopant F4TCNQ and $C_{60}F_{36}$ Diffusion in Organic Bilayer Architectures. *ACS Appl. Mater. Interfaces* **2015**, *7* (51), 28420–28428.

(7)   Jacobs, I. E.; Moulé, A. J. Controlling Molecular Doping in Organic Semiconductors. *Adv. Mater.* **2017**, *29* (42), 1703063.

(8)   Wang, Y.; Rubner, M. F. Stability Studies of the Electrical Conductivity of Various Poly(3-Alkylthiophenes). *Synth. Met.* **1990**, *39* (2), 153–175.

(9)   Fall, S.; Wang, J.; Regrettier, T.; Brouckaert, N.; Ibraikulov, O. A.; Leclerc, N.; Lin, Y.; Elhaj, M. I.; Komitov, L.; Lévêque, P.; Zhong, Y.; Brinkmann, M.; Kaczmarek, M.; Heiser, T. Self-Powered Dynamic Glazing Based on Nematic Liquid Crystals and Organic Photovoltaic Layers for Smart Window Applications. *ACS Appl. Mater. Interfaces* **2023**, *15* (3), 4267–4274.

Annex

Chapter 5

We assumed that LC molecules rotates perfectly by 90° in PSLMs. In this case, the OFF state corresponds to the two crossed polarizers and the ON state corresponds to the two polarizers in parallel. In the OFF state, the transfer matrix is given by:

$$\begin{pmatrix} A \\ A \end{pmatrix} \begin{pmatrix} \alpha_{//} & 0 \\ 0 & \alpha_{\perp} \end{pmatrix} \begin{pmatrix} \alpha_{//} & 0 \\ 0 & \alpha_{\perp} \end{pmatrix}$$

Where $\begin{pmatrix} A \\ A \end{pmatrix}$ is the amplitude of unpolarized light with two components, one component is parallel to the polarizer, another component is perpendicular to the polarizer and α is attenuation coefficient for amplitude of light through the polarizer in parallel (//) or in perpendicular ($\perp$).

The light intensity through the PSLM in the OFF state can be simplified to:

$$I_{OFF} = \left(A_{//} + A_{\perp}\right)^2 = \left[\left(\alpha_{//}^2 + \alpha_{\perp}^2\right)\right]^2 A^2$$

In the ON state, the transfer matrix can be written by:

$$\begin{pmatrix} A \\ A \end{pmatrix} \begin{pmatrix} \alpha_{//} & 0 \\ 0 & \alpha_{\perp} \end{pmatrix} \begin{pmatrix} \alpha_{\perp} & 0 \\ 0 & \alpha_{//} \end{pmatrix}$$

The light intensity through across the PSLM in the ON state can be simplified to:

$$I_{ON} = \left(A_{//} + A_{\perp}\right)^2 = \left[\left(2\alpha_{//}\alpha_{\perp}\right)\right]^2 A^2$$

The dichroic ratio for light intensity can be expressed by: $DR = \left(\dfrac{\alpha_{//}}{\alpha_{\perp}}\right)^2$

As a result, the ratio of the light intensities between in the OFF state and the ON state can be written as:

$$\frac{I_{OFF}}{I_{ON}} = \frac{\left(1 + \frac{1}{DR}\right)^2 \times DR}{4}$$
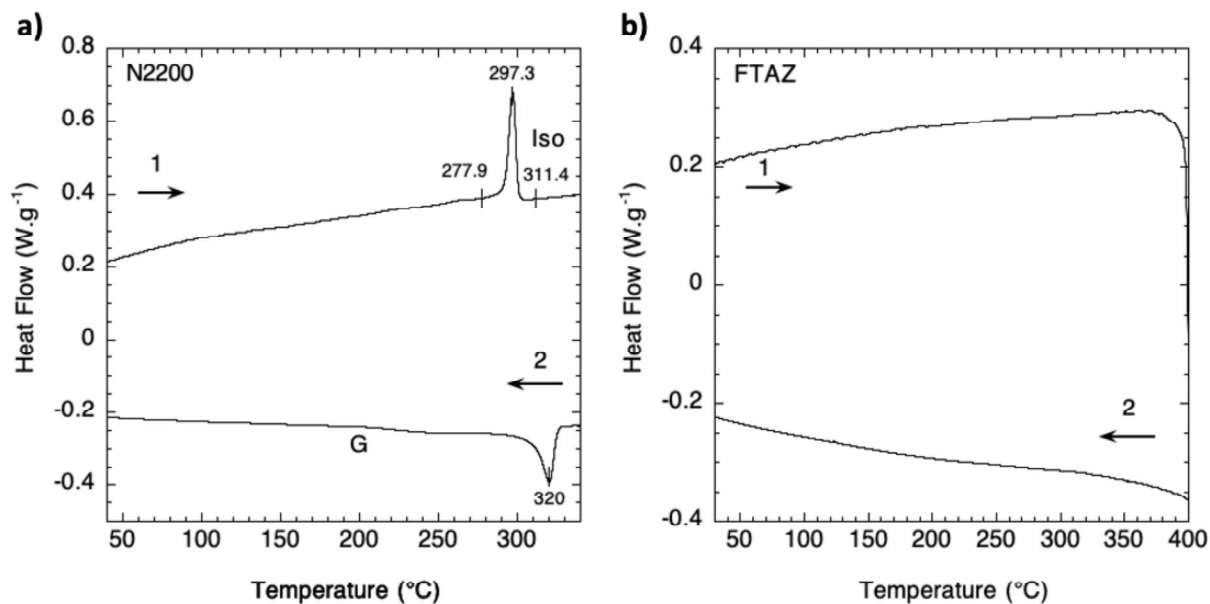
Figure S1. *DSC of a) N2200 polymers and b) FTAZ polymers. G is glassy state and Iso corresponds to isotropic liquid phase. Both heating and cooling rates are 10°C/min. The DSC measurements were performed under N₂ atmosphere.*

Résumé en français

Introduction

Suite aux crises climatiques et économiques, l'intérêt public mondial grandit pour une consommation d'énergie raisonnée, et particulièrement celle liée aux bâtiments. Selon l'observatoire européen du patrimoine immobilier, il est estimé que les bâtiments représentent environ 40 % de la consommation d'énergie et 36 % des émissions de gaz à effet de serre.[1] Actuellement, la plupart des bâtiments sont énergétiquement inefficaces. Un des axes possibles pour améliorer l'efficacité énergétique des bâtiments, est d'envisager des vitres dites « intelligentes », qui peuvent contrôler le rayonnement solaire et réduire la consommation d'énergie pour l'éclairage et la climatisation. Les matériaux optiques dynamiques, dont la transparence peut être modulée par des stimuli externes, sont des éléments importants pour les vitrages intelligents. Différentes technologies ont été développées, notamment les matériaux électrochromes, photochromes et thermochromes.[2,3] Toutefois, leur utilisation généralisée est encore limitée par leur efficacité énergétique et leur temps de réponse. Le projet de cette thèse se concentre sur un nouveau concept, appelé « Photovoltaic Spatial Light Modulator » (PSLM), qui a le potentiel de surmonter certains verrous technologiques qui limitent actuellement l'intégration de vitrages intelligents dans les bâtiments.[4]

Un dispositif PSLM est composé d'une couche de cristaux liquides nématiques torsadés (TNLC) comprise entre deux lames de verre conductrices (ITO), comme le montre la figure 1. Les deux couches d'alignement (AL) sont déposées sur les verres ITO. Elles sont mutuellement perpendiculaires, ce qui permet aux TNLC molécules de se tordre de 90° d'un côté à l'autre côté. La multicouche photovoltaïque organique (OPV) est placée entre la couche TNLC et l'une des lames de verre ITO, elle est capable de générer le champ électrique sous l'illumination.

Ce dispositif fonctionne entre un polariseur et un analyseur. La lumière incidente est polarisée linéairement par le polariseur, qui est orienté parallèlement aux orientations de TNLC sur la surface éclairée. Comme le montre la figure 1a, à l'état OFF (état clair), aucun champ électrique n'est produit à travers la couche TNLC. Par conséquent, la polarisation de la lumière est tournée de 90° par les molécules de TNLC, passant à travers l'analyseur qui est perpendiculaire au polariseur initial. Cela conduit à un état transparent. Dans le cas d'état ON (état sombre), représenté à la figure 1b, il y a les chutes de tension dans la couche TNLC. Si cette tension

dépasse la tension de seuil V_{th} (Fréedericksz transition), les molécules de TNLC commencent à modifier d'orientation, la polarisation de la lumière va être bloquée par l'analyseur, ce qui entraîne une diminution de la transmittance du dispositif.
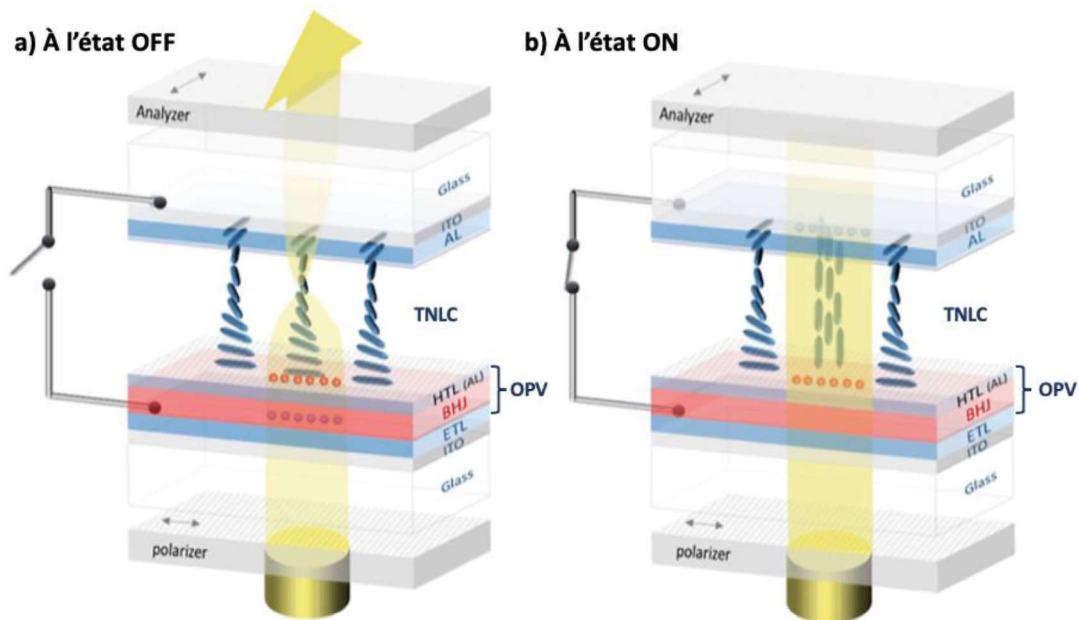
Figure 1. *Illustration schématique des dispositifs PSLM a) à l'état OFF (L'état clair) et b) à l'état ON (l'état sombre). Reproduit de la référence [4].*

Le premier dispositif PSLM a été démontré en 2017 au laboratoire ICube, en collaboration avec le professeur M. Kaczmarek de l'Université de Southampton. À cette époque, une réduction de 20 % de la transparence auto-activée sous une lumière monochromatique de 0,1 W/cm^2 a pu être obtenue. Cependant, de nombreux obstacles scientifiques et techniques empêchent encore le développement de vitrages intelligents basés sur la technologie PSLM. Par exemple, la transparence à l'état OFF est inférieure à 10 %, principalement en raison de l'utilisation de polariseurs externes et de couches photovoltaïques opaques. L'objectif de cette thèse est d'améliorer la transparence du PSLM, I) en étudiant des matériaux à large bande interdite pour absorber plus de la lumière UV et réduire l'absorption dans le visible[5]; II) en utilisant des couches photovoltaïques orientées comme polariseur "interne" : les couches photovoltaïques avec des propriétés optiques anisotropes peuvent polariser la lumière incidente et aussi convertir la lumière absorbée en phototension[6]; III) en développant des polariseurs dans le proche infrarouge (NIR), basés sur des polymères conducteurs orientés et dopés. Le dispositif

PSLM final devrait être i) plus transparent dans le domaine visible et ii) absorber la lumière UV tout en permettant de contrôler la lumière proche infrarouge.

Selon les différentes méthodes pour améliorer la transparence des PSLMs, le manuscrit de cette thèse s'organise en trois chapitres qui concernent : I) les matériaux à large bande interdite ; II) les couches photovoltaïques orientées ; III) les polariseurs proche infrarouge.

I) Des matériaux à large bande interdite :

Ce chapitre se divise en deux parties. La première partie présente l'étude d'une nouvelle molécule donneurs d'électrons à large bande interdite, qui se compose de l'unité triazatruxene (TAT) et le groupe carbazole (Cbz).[7] Les propriétés optiques des molécules TAT-Cbz et couche photovoltaïque à base de TAT-Cbz ont été étudiées par spectroscopie UV-Visible. Une couche photovoltaïque a été réalisée par les molécules TAT-Cbz en mélange avec un dérivé fullerène (PC$_{60}$BM) comme accepteur d'électrons. Le spectre de transmission pour la couche photovoltaïque montre une transparence élevée. Les cellules solaires à base de TAT-Cbz/PC$_{60}$BM ont étés fabriquées pour étudier leurs propriétés photovoltaïques. Il a été démontré que la phototension délivrée par la couche active est cruciale pour le fonctionnement autonome des PSLMs, et que le photocourant a une influence sur le temps de réponse des PSLMs. Les résultats indiquent que la phototension délivrée par la couche de TAT-Cbz/PC$_{60}$BM est suffisamment élevée pour modifier l'orientation de cristaux liquides (LC) dans le dispositif PSLM.

Dans la deuxième partie de ce chapitre, les couches actives de TAT-Cbz/PC$_{60}$BM ont été intégrées dans le dispositif PSLM. La transparence à l'état OFF a été améliorée de 9% à 15% en utilisant ces molécules à larges bandes interdites. Nous avons aussi démontré que les PSLMs semi-transparents peuvent fonctionner de manière autonome, même si la cellule solaire organique à base de TAT-Cbz présente un faible rendement de conversion (PCE=0,12-0,13 %). Cela élargit considérablement le choix des matériaux semi-conducteurs organiques adaptés aux dispositifs PSLMs.

II) Des couches photovoltaïques orientées :

Dans cette partie, nous avons utilisé une technique de brossage à haute température afin de fabriquer les couches actives alignées. La machine de brossage utilisée est constituée d'un

169

cylindre de brossage recouvert par un tissus microfibre et d'autre part d'un porte-objet chauffant portant le film polymère à brosser. Dans un premier temps, nous avons travaillé avec une bicouche de poly(3-hexylthiophene) (P3HT) /PC$_{60}$BM. Les films de P3HT ont été orientés avec différentes forces de brossage. L'alignement des films et les structures cristallines ont été observées par spectroscopie UV-visible polarisée et microscopie électronique en transmission (diffraction des électrons). Nos résultats indiquent qu'une force de brossage plus forte permet d'améliorer l'orientation des films et d'augmenter les cristallinités des films. Ensuite, une couche de PC$_{60}$BM est déposée sur le film orienté de P3HT pour combler les trous et former une bicouche. Les molécules de PC$_{60}$BM diffusent dans les polymères de P3HT sans influence sur l'alignement de P3HT. Les cellules solaires à la base des bicouches alignées montrent une anisotropie optique. Cependant, elles délivrent une faible phototension avec $V_{oc} \approx 0{,}46$ V $< V_{th}$ qui ne permet pas de modifier l'orientation de LC dans les dispositifs PSLM.

Pour cette raison, nous avons proposé d'orienter une couche en hétérojonction constituée du mélange PBnDT-FTAZ (donneur)/P(NDIT2OD-T2) (accepteur) qui peut générer une phototension plus élevée. Les polymères ont été d'abord orientés par la machine de brossage, et puis recuits à haute température. Nous avons démontré que le recuit thermique permet de croître les cristallinités des deux polymères et améliorer leur alignement. Les cellules solaires comprenant les couches actives orientées ont été fabriquées et étudiées. Cependant, les films orientés ont généralement des trous ou rayures créés par le brossage mécanique. Cela conduit à des courants de fuite dans les cellules solaires. Pour résoudre ce problème, nous avons déposé un film mince non orienté de PBnDT-FTAZ/P(NDIT2OD-T2) sur les films orientés de PBnDT-FTAZ/P(NDIT2OD-T2). Dans ce cas, les cellules solaires montrent une absorption optique anisotrope (DR≈4) ainsi qu'un effet photovoltaïque dichroïque ($J_{sc//}/J_{sc\perp} \approx 1.5$). Ces stratégies devraient permettre de fabriquer des cellules solaires polarisées et sont applicables à nos dispositifs PSLM.

III) Des polariseurs proche infrarouges :

Le dopage de polymères semi-conducteurs conduit généralement à une absorption optique dans la région NIR.[8] Les polymères semi-conducteurs hautement orientés présentent des propriétés optiques anisotropes.[9,10] Pour ces raisons, nous avons envisagé l'élaboration de polymères conducteurs orientées pour servir de "polariseurs NIR" dans les dispositifs PSLM.

Dans cette partie, les polymères P3HT dopées avec tris(4-bromophenyl) amoniumyl hexachloroantimonate (*magic blue*, MB) ont été étudiés. MB est un oxydant puissant et il possède une bonne stabilité dans l'air.[8] De plus, ces molécules dopantes sont incolores. Par conséquent, l'ajout de ces molécules dopantes n'influence pas la transparence de films. Pour fabriquer les polymères conducteurs orientées, les films de P3HT sont d'abord alignés par brossage à haute température, puis dopés dans une solution de MB. Le niveau de dopage est contrôlé via le temps de dopage et de la concentration de MB en solution. La spectroscopie UV-vis-NIR polarisée permet de confirmer l'orientation des polymères dopés. Les résultats indiquent que le dopage de P3HT avec MB est efficace et que les films orientés et dopés présentent des propriétés optiques anisotropes, notamment dans le domaine proche infra-rouge avec des bandes polaroniques bien définies. Les données de diffraction obtenues par TEM et de spectroscopie polarisée démontrent la localisation préférentielle du MB dans la phase amorphe du P3HT, les dopants étant absents des cristaux de P3HT.[11] La conséquence de cette structure est une conductivité très élevée du P3HT dopé avec MB (3000 S/cm). Nous avons ensuite testé un dispositif PSLM autonome avec les polymères conducteurs orientés utilisés comme polariseurs externes. Par rapport aux polariseurs commerciaux, les polariseurs à base de polymères conducteurs orientés augmentent la transparence dans le visible du PSLM (~ 15%) tout en permettant une modulation de la transmittance dans le domaine proche infra-rouge. L'amplitude de modulation de la lumière NIR reste cependant assez faible (~9%) en raison du faible rapport dichroïque dans la gamme de 700~1000 nm du P3HT dopé et orienté. Ce résultat indique néanmoins qu'il est possible de conserver une transmittance élevée et de moduler uniquement la lumière dans le proche infrarouge dans notre dispositifs PSLM.

Conclusion

Pour conclure, trois méthodes distinctes pour améliorer la transmission des dispositifs PSLM à l'état OFF ont été étudiées dans ce projet. Avec la 1ère méthode, la transparence de PSLM a été améliorée en utilisant des molécules TAT-Cbz à large bande interdite. Les dispositifs réalisés fonctionnent de façon autonome, sans application de tension électrique externe. En plus, nous avons pu démontrer qu'une photo-tension supérieure à une tension seuil (propriété du cristal liquide) est suffisante pour obtenir des dispositifs PSLMs autonomes, indépendamment du

rendement de conversion énergétique de la couche photovoltaïque. Avec la 2ème méthode, nous avons fabriqué avec succès des cellules solaires polarisées. Les cellules solaires montrent un effet photovoltaïque dichroïque et peuvent produire des photo-tensions suffisamment élevées pour modifier l'orientation des cristaux liquides. La prochaine étape consistera à renforcer l'absorption optique anisotrope des cellules solaires et intégrer les couches actives alignées dans nos dispositifs PSLM. Avec la dernière méthode, les films de P3HT dopés et orientés pour les dispositifs PSLMs, conduisent à une augmentation de la transmission dans la région visible tout en permettant une petite modulation dans la région proche infra-rouge. Néanmoins les films P3HT orientés dopés avec MB absorbent plus qu'ils ne réfléchissent la lumière, ce qui à terme peut être un inconvénient (augmentation de la température). La prochaine étape consistera à étudier d'autres matériaux capables de réfléchir davantage la lumière dans le proche infrarouge.

Références

(1)   D'Agostino, D.; Mazzarella, L. What Is a Nearly Zero Energy Building? Overview, Implementation and Comparison of Definitions. *J. Build. Eng.* **2019**, *21*, 200–212. https://doi.org/10.1016/j.jobe.2018.10.019.

(2)   Ke, Y.; Chen, J.; Lin, G.; Wang, S.; Zhou, Y.; Yin, J.; Lee, P. S.; Long, Y. Smart Windows: Electro-, Thermo-, Mechano-, Photochromics, and Beyond. *Adv. Energy Mater.* **2019**, *9* (39), 1902066. https://doi.org/10.1002/aenm.201902066.

(3)   Baetens, R.; Jelle, B. P.; Gustavsen, A. Properties, Requirements and Possibilities of Smart Windows for Dynamic Daylight and Solar Energy Control in Buildings: A State-of-the-Art Review. *Sol. Energy Mater. Sol. Cells* **2010**, *94* (2), 87–105. https://doi.org/10.1016/j.solmat.2009.08.021.

(4)   Fall, S.; Wang, J.; Regrettier, T.; Brouckaert, N.; Ibraikulov, O. A.; Leclerc, N.; Lin, Y.; Elhaj, M. I.; Komitov, L.; Lévêque, P.; Zhong, Y.; Brinkmann, M.; Kaczmarek, M.; Heiser, T. Self-Powered Dynamic Glazing Based on Nematic Liquid Crystals and Organic Photovoltaic Layers for Smart Window Applications. *ACS Appl. Mater. Interfaces* **2023**, *15* (3), 4267–4274. https://doi.org/10.1021/acsami.2c21727.

(5)   Davy, N. C.; Sezen-Edmonds, M.; Gao, J.; Lin, X.; Liu, A.; Yao, N.; Kahn, A.; Loo, Y.-L. Pairing of Near-Ultraviolet Solar Cells with Electrochromic Windows for Smart Management of the Solar Spectrum. *Nat. Energy* **2017**, *2* (8), 17104. https://doi.org/10.1038/nenergy.2017.104.

(6)   Zhu, R.; Kumar, A.; Yang, Y. Polarizing Organic Photovoltaics. *Adv. Mater.* **2011**, *23* (36), 4193–4198. https://doi.org/10.1002/adma.201101514.

(7)   Mahmoudi, C.; Muzuzu, W.; Fall, S.; Zhong, Y.; Mélart, C.; Lévêque, P.; Heiser, T.; Jaballah, N. S.; Majdoub, M.; Leclerc, N. Near Ultra-Violet Absorbers for Transparent Organic Solar Cells. *Dyes Pigments* **2022**, *207*, 110752. https://doi.org/10.1016/j.dyepig.2022.110752.

(8)   Hofmann, A. I.; Kroon, R.; Zokaei, S.; Järsvall, E.; Malacrida, C.; Ludwigs, S.; Biskup, T.; Müller, C. Chemical Doping of Conjugated Polymers with the Strong Oxidant Magic Blue. *Adv. Electron. Mater.* **2020**, *6* (8), 2000249. https://doi.org/10.1002/aelm.202000249.

(9)   Hamidi-Sakr, A.; Biniek, L.; Fall, S.; Brinkmann, M. Precise Control of Lamellar Thickness in Highly Oriented Regioregular Poly(3-Hexylthiophene) Thin Films Prepared by High-Temperature Rubbing: Correlations with Optical Properties and Charge Transport. *Adv. Funct. Mater.* **2016**, *26* (3), 408–420. https://doi.org/10.1002/adfm.201504096.

(10)   Tremel, K.; Fischer, F. S. U.; Kayunkid, N.; Pietro, R. D.; Tkachov, R.; Kiriy, A.; Neher, D.; Ludwigs, S.; Brinkmann, M. Charge Transport Anisotropy in Highly Oriented Thin Films of the Acceptor Polymer P(NDI2OD-T2). *Adv. Energy Mater.* **2014**, *4* (10), 1301659. https://doi.org/10.1002/aenm.201301659.

(11)   Zhong, Y.; Untilova, V.; Muller, D.; Guchait, S.; Kiefer, C.; Herrmann, L.; Zimmermann, N.; Brosset, M.; Heiser, T.; Brinkmann, M. Preferential Location of Dopants in the Amorphous Phase of Oriented Regioregular Poly(3-hexylthiophene-2,5-diyl) Films Helps Reach Charge Conductivities of 3000 S Cm^{-1}. *Adv. Funct. Mater.* **2022**, *32* (30), 2202075. https://doi.org/10.1002/adfm.202202075.

Yuhan ZHONG

New strategies to improve the transparency of photovoltaic spatial light modulators for self-powered dynamic glazing

Université de Strasbourg

École doctorale
Mathématiques,
sciences de l'information
et de l'ingénieur | ED 269
Université de Strasbourg

Résumé

Le PSLM (ou "Photovoltaic Spatial Light Modulators") est un nouveau type de verre dynamique qui a le potentiel d'être utilisé dans les vitres "intelligentes" pour contrôler l'irradiation solaire à l'intérieur des bâtiments et ainsi d'améliorer leur efficacité énergétique. Le dispositif se compose principalement d'un cristal liquide nématique, dont le directeur influe sur la transparence et la biréfringence du PSLM, et d'une multicouche organique photovoltaïque. Lorsque le PSLM est exposé à la lumière, un champ électrique apparaît par effet photovoltaïque qui modifie l'orientation des cristaux liquides. Cet effet permet au PSLM de changer de teinte en fonction de l'intensité de la lumière, sans nécessiter d'alimentation externe. La transparence du dispositif à l'état "clair" est l'un des paramètres clés qu'il convient d'améliorer en vue d'applications telles que les fenêtres intelligentes.

Dans le cadre de cette thèse, nous nous sommes focalisés sur trois stratégies complémentaires pour améliorer la transparence des PSLMs : I) en utilisant une couche photovoltaïque contenant un matériau semi-conducteur à large bande interdite pour réduire l'absorption de la lumière dans le domaine du visible ; II) en développant des couches photovoltaïques optiques anisotropes et en les utilisant comme "polariseurs internes" dans le PSLM. Pour cela, nous avons utilisé une technique de brossage à haute température de la couche photovoltaïque ; et III) en utilisant des films de polymères dopés et orientés comme "polariseurs infrarouge". La combinaison d'un dispositif PSLM autonome avec ce type de polariseurs augmente la transmittance dans le domaine visible tout en limitant la modulation optique au domaine infrarouge.

Mots clés : PSLM, transparence du dispositif, matériau à bande interdite élevée, propriétés optiques anisotropes, polariseurs NIR.

Résumé en anglais

A Photovoltaic Spatial Light Modulator (PSLM) is a new class of switchable glazing that has the potential to be used in smart windows for controlling indoor solar radiation and improving the energy efficiency in buildings. The device consists mainly of a nematic liquid crystal which determines its optical properties (transparency, birefringence), and an organic photovoltaic (PV) layer. The latter generates an electric field under illumination that changes the orientation of the liquid crystal director and allows the device to change its tint under light without requiring an external power supply. The device transparency in the clear state is one of the key parameters for smart windows applications.

In this thesis, we focused on three complementary strategies to improve the clear state transparency of a PSLM: I) using a PV layer containing a high band gap material to avoid photon absorption in the visible.; II) developing anisotropic optical PV layers by high temperature rubbing that can be used simultaneously as "internal polarizer", and III) using oriented and doped polymer films as near infrared (NIR) polarizers. Combining a self-powered PSLM with NIR polarizers increases its transparency in the visible region while restricting the optical modulation to the NIR range.

Keywords: Photovoltaic Spatial Light Modulator, device transparency, high band gap materials, anisotropic optical properties, NIR polarizers.